Discovery and Characterization of Earthquakes on Immature Faults with InSAR

by

Israporn Sethanant

B.Sc., Chulalongkorn University, 2016
M.Sc., Oregon State University, 2019

A Dissertation Submitted in Partial Fulfillment of the
Requirements for the Degree of

DOCTOR OF PHILOSOPHY

in the School of Earth and Ocean Sciences

© Israporn Sethanant, 2024
University of Victoria

All rights reserved. This dissertation may not be reproduced in whole or in part,
by photocopying or other means, without the permission of the author.

I acknowledge and respect the Lək̓ʷəŋən (Songhees and Esquimalt) Peoples
on whose territory the university stands, and the Lək̓ʷəŋən and W̱SÁNEĆ Peoples
whose historical relationships with the land continue to this day.

Discovery and Characterization of Earthquakes on Immature Faults with InSAR

by

Israporn Sethanant

B.Sc., Chulalongkorn University, 2016
M.Sc., Oregon State University, 2019

Supervisory Committee

Dr. Edwin Nissen, Supervisor
(School of Earth and Ocean Sciences)

Dr. Lucinda Leonard, Departmental Member
(School of Earth and Ocean Sciences)

Dr. Kelin Wang, Departmental Member
(School of Earth and Ocean Sciences)

Dr. Tuna Onur, Outside Member
(Department of Civil Engineering)

ABSTRACT

Fault structural maturity describes how fault zones evolve with incremental slip, and may control certain aspects of earthquake rupture behaviour. Immature faults are harder to identify and characterize than mature faults by virtue of their subtle to non-existent topographic and geophysical expressions, and thus pose distinct hazards and risks. Nonetheless, the advent of satellite-borne Interferometric Synthetic Aperture Radar (InSAR) surface deformation mapping has revolutionized our ability to characterize large earthquakes that occur on these hidden faults. By doing so, we can start to recognize common attributes to immature faults that may have important implications for seismic hazard. This is the central theme of this dissertation.

After introducing how InSAR works, I describe how to interpret surface deformation maps for various faulting styles. To explore relations between structural maturity and rupture behaviour, I then employ InSAR to characterize recent earthquakes along immature strike-slip faults in two contrasting tectonic settings: the Eastern California Shear Zone/Walker Lane of California and Nevada, USA, and the Shan Plateau in Laos, Thailand and Myanmar. The main foci are the 2020 M_w 6.5 Monte Cristo Range, Nevada earthquake and the 2019 M_w 6.2 Sainyabuli, Laos earthquake, respectively. In both cases, I tried to characterize the full complexity of the earthquakes by working with collaborators to incorporate independent seismological constraints.

We found certain rupture behaviours common to the Monte Cristo Range and Sainyabuli earthquakes that may be linked to fault maturity. Both mainshocks had short ($\sim$20–30 km) fault lengths and pronounced ($\sim$80–90%) shallow slip deficits (SSD) that may reflect off-fault deformation $\sim$5–10 km from the primary faults, consistent with relocated aftershocks. However, InSAR slip profile comparisons with other strike-slip earthquakes suggest that SSD is controlled more by earthquake magnitude than maturity, with smaller events having the greatest range in SSD and larger ones propagating to the surface with more consistency. The Monte Cristo Range earthquake also involved an unusual configuration of crossing faults, likely due to the early evolution stage of the host fault zone.

The limited geomorphic expression along modelled faults of the Monte Cristo Range and Sainyabuli events raises an alarming concern for seismic hazard assessment (SHA). Since immature faults are hard to map, they are often overlooked in hazard calculations. However, SHA practitioners may benefit from knowledge of rupture geometries and behaviours provided by observational studies like this dissertation, to help define seismic sources and select appropriate ground motion models for regional and site-specific SHA.

Contents

Supervisory Committee **ii**

Abstract **iii**

Table of Contents **iv**

List of Tables **viii**

List of Figures **ix**

Acknowledgements **xii**

1 Introduction **1**

1.1 The Importance of Studying Earthquakes 1

1.2 Influence of Fault Structural Maturity on Rupture Behaviours 2

1.3 Studying Earthquakes with InSAR 3

1.3.1 Synthetic Aperture Radar (SAR) 3

1.3.2 How InSAR Works 6

1.3.3 InSAR Application to Earthquakes and its Limitations 8

1.4 Dissertation Structure 9

2 The InSAR Lookbook: an illustrated guide to earthquake interferograms **11**

2.1 Author Names, Affiliations, and Roles 11

2.2 Abstract 11

2.3 Plain Language Summary 12

2.4 Introduction 12

2.5 Why coseismic interferograms look as they do 14

2.5.1 Strike-slip earthquakes 14

2.5.2 Dip-slip earthquakes 17

2.6 Introducing the InSAR Lookbook . . . 19
2.6.1 Model Set-up and Displacement Sense Convention . . . 19
2.6.2 Model Fault Configurations . . . 20
2.6.3 How to Use the Lookbook . . . 20
2.6.4 Extrapolating and Interpolating the Lookbook Models . . . 22
2.6.5 Limitations . . . 23
2.7 The InSAR Lookbook . . . 24
2.7.1 Strike-slip Earthquakes . . . 34
2.7.2 Moderate Angle Dip-slip Earthquakes . . . 34
2.7.3 Low-angle Thrust and Normal Faulting earthquakes . . . 36
2.7.4 Oblique-slip Earthquakes . . . 37
2.7.5 Lookbook Summary . . . 37
2.8 Real Earthquake Comparisons . . . 39
2.8.1 Strike-slip Examples . . . 39
2.8.2 Dip-slip Examples . . . 42
2.8.3 Low-angle Thrust Examples . . . 45
2.8.4 Oblique-slip Examples . . . 47
2.9 Conclusions . . . 49
2.10 Data and Resources . . . 49
2.11 Supplemental Material . . . 50

3 The 2020 M_w 6.5 Monte Cristo Range (Nevada) earthquake: anatomy of a crossing-fault rupture through a region of highly-distributed deformation 73
3.1 Author Names, Affiliations, and Roles . . . 73
3.2 Abstract . . . 74
3.3 Plain Language Summary . . . 75
3.4 Introduction . . . 75
3.5 Regional Context . . . 79
3.6 Data and Methodology . . . 80
3.6.1 Surface Faulting Observations . . . 80
3.6.2 Geodetic Slip Modeling . . . 81
3.6.3 Seismological Analysis . . . 84
3.7 Results . . . 86
3.7.1 Mainshock Surface Ruptures . . . 86
3.7.2 Mainshock Source Model and Mechanisms . . . 88

3.7.3 Aftershock Distribution and Mechanisms . . . 93
3.7.4 Comparisons with other Geodetic Slip Models and Seismological Observations . . . 94
3.7.5 Evidence of Previous Ruptures and Cumulative Offset . . . 99
3.8 Discussion . . . 101
3.8.1 Fault Kinematics and Complexity Revealed by Combining Geodesy, Seismology, and Field Observations . . . 101
3.8.2 Characteristics of Structural Immaturity in the MCRE and Implications for Seismic Hazard Assessment . . . 105
3.8.3 Shallow Slip Deficit in the MCRE . . . 107
3.8.4 Are Shallow Slip Deficits Governed by Fault Structural Maturity? . . . 110
3.9 Conclusions . . . 111
3.10 Data and Resources . . . 114
3.11 Acknowledgments . . . 115
3.12 Supplemental Material . . . 115

4 Recent earthquakes on unmapped faults highlight hidden seismic hazards within the Golden Triangle region of Laos, Thailand, and Myanmar 141
4.1 Author Names, Affiliation, and Roles . . . 141
4.2 Abstract . . . 142
4.3 Introduction . . . 143
4.4 Data and Methods . . . 148
4.4.1 InSAR Data Processing and Source Modelling . . . 148
4.4.2 Earthquake Relocation . . . 152
4.4.3 Waveform Modelling . . . 155
4.5 The 2019–2021 Sainyabuli, Laos Earthquakes . . . 155
4.5.1 The 2019 Sainyabuli Mainshock Kinematics . . . 155
4.5.2 The 2021 Sainyabuli Earthquake . . . 161
4.5.3 Other Earthquakes of the Sainyabuli Sequence . . . 162
4.6 The 2022 and 2023 Keng Tung, Myanmar Earthquakes . . . 162
4.7 Other Notable Earthquakes . . . 166
4.7.1 The 2014 Mae Lao, Thailand Earthquake . . . 166
4.7.2 The 2011 Tarlay, Myanmar Earthquake . . . 168
4.7.3 The 2007 Bokeo, Laos Earthquake . . . 168
4.8 Discussion . . . 169

4.8.1 Seismogenic Layer Thickness and Earthquake Rupture Mechanics . 169
4.8.2 Fault Structural Immaturity and Implications for Seismic Hazards . 171
4.9 Conclusions 173
4.10 Acknowledgement 173
4.11 Data and Resources 174
4.12 Supplemental Material 175

5 Conclusions **192**

Bibliography **196**

List of Tables

Table 2.1 Lookbook index and model fault plane parameters 21
Table 2.2 List of real earthquakes used as lookbook comparisons 40

Table 3.1 InSAR imagery parameters for modelling the Monte Cristo Range earthquake 81
Table 3.2 Parameters of our preferred, two fault InSAR-GNSS uniform and distributed slip models 91
Table 3.3 List of earthquakes, shallow slip deficits, and cumulative geological offsets for the events profiled in Figure 3.13 113
Table 3.4 Fault parameter search bounds used in the uniform slip modeling . . 116
Table 3.5 One-dimensional velocity model used in the *mloc* relocation 117
Table 3.6 Uniform slip parameter configurations and results for the northern fault in the three-fault modeling scenario 117
Table 3.7 Parameters of the InSAR-GNSS distributed slip model sub-fault patches 127
Table 3.8 Calibrated hypocenters from *mloc* 131
Table 3.9 Regional moment tensor solutions for the 90 best-recorded events . . 138

Table 4.1 InSAR imagery details for the five largest events studied here 149
Table 4.2 Earthquake source parameters of the five earthquakes studied here . 151
Table 4.3 One-dimensional velocity model used in the *mloc* relocation 153
Table 4.4 Relocated hypocenters of the five largest events studied here 159
Table 4.5 Reference points for the moment tensor inversions 185
Table 4.6 Best deviatoric moment tensor solutions 185
Table 4.7 Distributed slip model parameters of the 2019 Sainyabuli mainshock 186
Table 4.8 Calibrated hypocenters from *mloc* 188

List of Figures

Figure 1.1 Schematic illustration of radar satellite acquisition geometry 5

Figure 2.1 3-D displacement fields and interferograms for a left-lateral strike-slip earthquake 15
Figure 2.2 3-D displacement fields and interferograms for a normal faulting earthquake 18
Figure 2.3 InSAR lookbook: forward model interferograms for ten faulting types (subfigures a–j), varying strike 24
Figure 2.4 InSAR deformation lobe pattern summary chart 38
Figure 2.5 Interferogram comparisons between real strike-slip earthquakes and lookbook models 41
Figure 2.6 Interferogram comparisons between real dip-slip earthquakes and lookbook models 44
Figure 2.7 Interferogram comparisons between real low-angle thrust earthquakes and lookbook models 46
Figure 2.8 Interferogram comparisons between real oblique-slip earthquakes and lookbook models 48
Figure 2.9 InSAR lookbook: unwrapped interferograms for ten faulting types (subfigures a–j), varying strike 51
Figure 2.10 InSAR lookbook: forward model interferograms for twelve fault strikes (subfigures a–l), varying rake 61

Figure 3.1 Tectonic setting of the 2020 Monte Cristo Range earthquake 78
Figure 3.2 Observed and model interferograms of the uniform and distributed slip inversions 82
Figure 3.3 InSAR-GNSS model faults with surface offsets and cracks mapped in the field 87
Figure 3.4 Photos and InSAR signals of pebble clearing phenomena from cracks and its direction of clearing 89

Figure 3.5 Observed and model interferograms of the third, northern model fault along the northern fault zone 92
Figure 3.6 Three-dimensional view of our preferred InSAR-GNSS distributed slip model, model slip and aftershock depth profiles 93
Figure 3.7 Relocated hypocenters, their focal mechanisms, and cross-sectional views of both along the western and eastern model faults 95
Figure 3.8 Comparison of the Monte Cristo Range earthquake geodetic model slip profiles from our paper and other studies 98
Figure 3.9 Hillshade topography maps and field photos showing evidence of previous ruptures 100
Figure 3.10 Paleoseismic trench across the northern fault zone of the Monte Cristo Range earthquake surface rupture 102
Figure 3.11 Hillshaded topography and multispectral imagery along the western and eastern model faults 103
Figure 3.12 Three, competing, interpreted cross-sections of the fault structure and kinematics in the western rupture area 106
Figure 3.13 Slip profiles from InSAR-derived coseismic slip models of twenty-eight large (M_w 6.4–7.9), strike-slip, continental earthquakes 112
Figure 3.14 GNSS coseismic surface displacements in the Monte Cristo Range earthquake 118
Figure 3.15 Cluster vectors of the relocated epicenters and raypaths used for direct calibration 118
Figure 3.16 Theoretical and observed arrival times at all distances 119
Figure 3.17 Arrival times at different epicentral distances 120
Figure 3.18 Unwrapped interferograms of our preferred two-fault model 121
Figure 3.19 Western model fault plane parameters yielded by the 500 Monte Carlo restarts of the two-fault slip inversion 122
Figure 3.20 Eastern model fault plane parameters yielded by the 500 Monte Carlo restarts of the two-fault slip inversion 123
Figure 3.21 Interferograms of a non-crossing fault configuration. 124
Figure 3.22 Comparison of our centroid and focal depths of the 90 best-recorded events 125
Figure 3.23 Focal mechanisms categorized by their rake values 126

Figure 4.1 Tectonic setting of the Shan Plateau within the broader India-Eurasia collision zone . . . 144
Figure 4.2 Mapped active faults and earthquake focal mechanisms from across the Shan Plateau . . . 145
Figure 4.3 *mloc* cluster vector and station map, and arrival time fit curves . . . 154
Figure 4.4 Interferograms of the 2019 Sainyabuli mainshock . . . 157
Figure 4.5 Three-dimensional distributed slip model and slip profile of the 2019 Sainyabuli mainshock . . . 158
Figure 4.6 Relocated epicenters by focal depth and focal depth histogram . . . 159
Figure 4.7 Zoomed in maps and histograms for each earthquake sequence . . . 160
Figure 4.8 Interferograms of the 2021 Sainyabuli aftershock . . . 161
Figure 4.9 Relocated epicenters by event year and tectonic terranes . . . 163
Figure 4.10 Moment tensor solutions of the five earthquakes studied here . . . 164
Figure 4.11 Interferograms of the 2022 Keng Tung mainshock . . . 165
Figure 4.12 Interferograms of the 2023 Keng Tung mainshock . . . 167
Figure 4.13 Third interferogram of the 2019 Sainyabuli mainshock . . . 176
Figure 4.14 Interferograms of the conjugate model fault of the 2021 Sainyabuli aftershock . . . 177
Figure 4.15 Interferograms of the conjugate model fault of the 2022 Keng Tung mainshock . . . 177
Figure 4.16 Location shift map of the relocation cluster . . . 178
Figure 4.17 Theoretical and observed arrival times at different epicentral distances 179
Figure 4.18 Waveform fits for the best deviatoric moment tensor solution for the 2019 Sainyabuli foreshock . . . 180
Figure 4.19 Waveform fits for the best deviatoric moment tensor solution for the 2019 Sainyabuli mainshock . . . 181
Figure 4.20 Waveform fits for the best deviatoric moment tensor solution for the 2021 Sainyabuli aftershock . . . 182
Figure 4.21 Waveform fits for the best deviatoric moment tensor solution for the 2022 Keng Tung mainshock . . . 183
Figure 4.22 Waveform fits for the best deviatoric moment tensor solution for the 2023 Keng Tung mainshock . . . 184

ACKNOWLEDGEMENTS

They say having a supportive supervisor in graduate school is like winning a lottery; I think I did. I cannot find enough words to express my gratitude to my supervisor, Ed. Our discussion over countless croissants and espresso have shaped me into the careful scientist I am today. Ed's positivity is also contagious and I always feel uplifted when we meet. I am grateful for his mentorship not only in research but in life as well, for his kindness, encouragement, support, and for setting such a beautiful example of the type of researcher/person I aspire to be. It has been a great pleasure working with you and getting to know you.

To my collaborators, Eric Bergman, Harley Benz, Léa Pousse-Beltran, Ezgi Karasözen, Sarah Jaye Oliva, Ian Pierce—I could not have reached this point without your immense support; thank you for the fun times we had working together! Thank you for always sharing your knowledge and experience with me, even before some of us finally met in person. Léa, you were a huge part of the first interferogram I ever processed and many more that followed; it has been wonderful working with you. Sarah, I am forever grateful for your presence in Victoria, your mentorship, and more importantly, friendship. Eric, you are so kind and always take the time to explain difficult concepts to me; you inspire me to uphold this value and help others whenever I can.

I am deeply grateful to my committee members, Dr. Lucinda Leonard, Dr. Kelin Wang, and Dr. Tuna Onur, for their support throughout my endeavors. Their constructive feedback has broadened and sharpened my expertise and inspired me to become comfortable in speaking engineering, geophysics, and geodynamics languages. Their influence has made me more courageous, creative, and confident. I feel incredibly fortunate and thankful to have learned from all of you. I would also like to thank the SEOS faculty and staff who supported me in many ways throughout my program.

To my TEARS cohort, Pacific Geoscience Centre colleagues, visiting students, and SEOS peers, I am truly glad to have met you all and I thank you for your support. Our team's energy were special and I feel lucky to have been a part of it! Special thanks to Élyse Gaudreau and Theron Finley, my late night office buddies, for bouncing ideas, laughing at my jokes, and just being exceptional friends. To my late lunch buddies, Camille Febvre and Jia-Xuan, thank you for the priceless times spent together, whether at the library, kitchen, or on the boulder. Thank you for the stretch routines after long office hours, for being a great listener, and boosting my confidence in challenging times. Your brightness lights up the room and thank you for sharing that light with me. I would like to thank UVic's Speakers Bureau Program, Mandy Crocker, Anna Diederichs, Megumi Patchett, Camille Brillon, and Ross Stein, who had been an important part of my outreach journey.

Last but not least, to my family and friends in Victoria (Fai, Na'Boom, P'L, and many more), Corvallis, and back home in Thailand—thank you for always believing in me and being close to my heart. In particular, to my parents and brother: your love and powerful blessings have made my heart strong throughout this path. Also, I express my deepest gratitude to my spiritual teachers, past and present, and LP Hermitage friends, for guiding me to develop the *right view*.

Chapter 1

Introduction

1.1 The Importance of Studying Earthquakes

Active faulting plays a significant role in sculpting the landscapes of large parts of the world (e.g., Jackson, 2001), including here in the Pacific Northwest. From mountain peaks that draw adventure seekers to valleys and basins where most towns and cities are situated, much of the topography around us is built along or above active faults. However, once in a while, these faults host large earthquakes, generating strong ground shaking and sometimes a cascade of other hazards including liquefaction, landsliding, seiches, and tsunamis. Since earthquakes on any single fault happen infrequently—often recurring over hundreds to thousands of years—they usually catch us unprepared, even in countries with long histories of damaging earthquakes.

In the past decade, records show that earthquakes annually affect millions of people worldwide, leading to hundreds to thousands of fatalities and even larger numbers impacted by injury, displacement, and the need for assistance. These consequences can vary widely from region to region, with economic costs worst when populous parts of wealthy countries are struck, but social impacts usually highest when more vulnerable populations are affected, often exposing inequalities in disaster relief (Bilham, 2009). Studying earthquakes is crucial to help mitigate these impacts. On a basic level, this involves investigating where earthquake ruptures occur, how they start and stop, what controls the extent of damaging ground shaking, and how often they recur (Morell et al., 2020). Through such studies, we can better anticipate earthquakes and their effects, enabling us to allocate limited resources wisely for preparedness, response, reconstruction, and recovery.

Building this resilience is a collective effort between earthquake scientists, engineers,

social scientists, government agencies such as seismological bureaus and emergency management, first responders, and the general public. Seismic hazard models are used to quantify the likelihood of specific levels of ground shaking across a region of interest, with scientists providing much of the data, and engineers and governmental agencies the main end users. Specifically, seismology researchers contribute by providing information on active fault geometries, slip rates, and earthquake source characteristics such as depths and magnitudes. However, a significant challenge lies in the fact that not all faults with the potential to generate large earthquakes have been investigated, or even discovered (England and Jackson, 2011; Jackson, 2001). This owes to the fact that structurally immature faults—defined below—tend to have limited, or even completely lacking, surface expressions. This absence of clear surface faulting precludes much of the information critical to seismic hazard models from being gathered.

1.2 Influence of Fault Structural Maturity on Rupture Behaviours

Fault structural maturity is a qualitative term that encapsulates the progression of fault zone evolution (Choy and Kirby, 2004). As a fault evolves with incremental offset, several changes occur to its structure. The fault core (containing slip surfaces, gouge, cataclasites and breccias) forms and thickens (Robertson, 1983; Scholz, 1987; Hull, 1988; Childs et al., 2009), and a fractured or pulverized damage zone develops within the adjacent rock volume (Shipton and Cowie, 2001; Finzi et al., 2009; Faulkner et al., 2011; Savage and Brodsky, 2011; Aben et al., 2016). The fault surface trace straightens and simplifies as fault segments coalesce, geometrical asperities are smoothed out, and strain becomes more localized (Walsh and Watterson, 1988; Wesnousky, 1988; Peacock and Sanderson, 1991; Childs et al., 1995; Stirling et al., 1996; Frost et al., 2009; Wechsler et al., 2010; Brodsky et al., 2011; Zinke et al., 2015; Hatem et al., 2017). Structural maturity is typically parameterized by the total, cumulative fault offset, though fault age, slip rate, fault length, and surface trace complexity are sometimes used as alternate proxies (Manighetti et al., 2007, 2021).

Structural maturity is of interest to seismologists in part because it is thought to govern important aspects of fault rupture behaviour. Some observations and simple conceptual models suggest that earthquakes along structurally mature faults exhibit more localized deformation and narrower aftershock distributions than those along immature faults

(Powers and Jordan, 2010; Perrin et al., 2021), as well as faster rupture velocities (Perrin et al., 2016; Chounet et al., 2018), more persistent rupture directivity (Kane et al., 2013; Aderhold and Abercrombie, 2015), proportionally more surface slip (or lower shallow slip deficit) (Dolan and Haravitch, 2014), and larger amounts of aseismic afterslip (Johanson et al., 2006; Feng et al., 2010; Thomas et al., 2014; Li et al., 2020b; Pousse-Beltran et al., 2020). It has also been hypothesized that earthquakes along mature faults have a greater propensity to break through segment boundaries to achieve larger rupture lengths (Manighetti et al., 2007), perhaps explaining their smaller overall stress drops (Choy and Kirby, 2004; Hecker et al., 2010) and in turn their weaker near-field ground motions (Radiguet et al., 2009) and lower rates of dynamic aftershock triggering (Gomberg, 1996). Mature faults may also exhibit steadier interseismic strain accumulation (Wang et al., 2021) and more regular recurrence intervals (Berryman et al., 2012; Thakur and Huang, 2021). These relationships illustrate how fault structural maturity could have an important bearing on seismic hazard, and raise the possibility of incorporating easily-observed metrics for structural maturity (such as cumulative offset) in hazard assessments and earthquake early warning algorithms (Dolan and Haravitch, 2014; Perrin et al., 2016; Hutchison et al., 2020).

However, due to the inherent challenges in identifying immature faults and the relative infrequency of earthquakes along them, many of these proposed relationships are based on limited data. Therefore, it is crucial that when large earthquake sequences do strike immature faults, they are thoroughly investigated. This dissertation seeks to characterize recent large earthquakes that occurred on immature faults in two different parts of the world with distinct geology and tectonics. A commonality in these studies is the use of advanced satellite measurements and slip modelling to characterize faulting even when blind, and its integration with more traditional instrumental datasets. In particular, the proliferation of satellite-borne Interferometric Synthetic Aperture Radar (InSAR) over the past two decades has facilitated the routine acquisition of extensive surface deformation datasets for almost all large, onshore earthquakes (Bürgmann et al., 2000; Elliott et al., 2016).

1.3 Studying Earthquakes with InSAR

1.3.1 Synthetic Aperture Radar (SAR)

Synthetic Aperture Radar (SAR) is a technique used to produce high-resolution images of Earth's surface, usually from satellites in low Earth orbit (altitudes of 600–800 km). These

platforms deploy side-looking radio detection and ranging (radar) antennae that illuminate the Earth with electromagnetic signals, usually in microwave frequencies ($\sim$1 mm to 30 cm wavelength), and record the back-scattered energy (Rosen et al., 2000). SAR platforms usually transmit in the L-band (15–30 cm), C-band (3.75–7.5 cm), or X-band (2.5–3.75 cm) of the microwave range. At these wavelengths the atmosphere is at its lowest opacity and the signal can penetrate cloud cover and water vapour with only minor path delays, making it all-weather. The active source means that images can be collected day or night, although in practice the satellites follow sun-synchronous orbits designed such that the platform's solar panels are always illuminated by sunlight. These capabilities make SAR extremely versatile, and it is widely used across for geoscience, forestry and agriculture, polar science, marine surveillance, hazard monitoring, urban mapping, and for other purposes.

Beam divergence over the great distance travelled by the radar signal results in footprints several kilometers wide on the Earth's surface. However, information carried by the back-scattered waves can be used to distinguish smaller pixels from within this footprint, allowing an image to be generated. The image has two parts to it: the amplitude, a function mostly of surface roughness, and the phase, which for a single image is effectively random (Massonnet and Feigl, 1998). Just like how the aperture of a camera controls the amount of light it receives, the radar antenna length determines how much back-scattered energy is collected, and in turn both the image footprint and resolution. However, it is impractical to place a very large antenna on a satellite platform. The is where the 'synthetic aperture radar' comes in: SAR involves simulating an extremely long antenna by combining successive radar returns as the satellite travels along its path (Bürgmann et al., 2000; Rosen et al., 2000) (Figure 1.1). Every point on the ground is imaged multiple times, and this time series is post-processed to form a single image with both a broad footprint and a fine spatial resolution.

The image resolution further depends on a number of other factors. Because the satellite is moving along its orbital track as it emits its signal, the echoes received at the antenna are phase-shifted from their original wavelength. SAR uses this frequency shift to determine the along-track, or azimuth, coordinate of the pixel. The azimuth resolution of a SAR image is theoretically half of the real antenna dimension (Massonnet and Feigl, 1998). In general, resolutions are achieved at 1–2 m for airborne SAR systems and 5–50 m for the more common spaceborne ones (European Space Agency , nd), sufficient for studying long-wavelength ground deformation from tectonics, earthquakes, volcanoes, and larger landslides. Perpendicular to the along-track direction, pixels can be located in the cross-

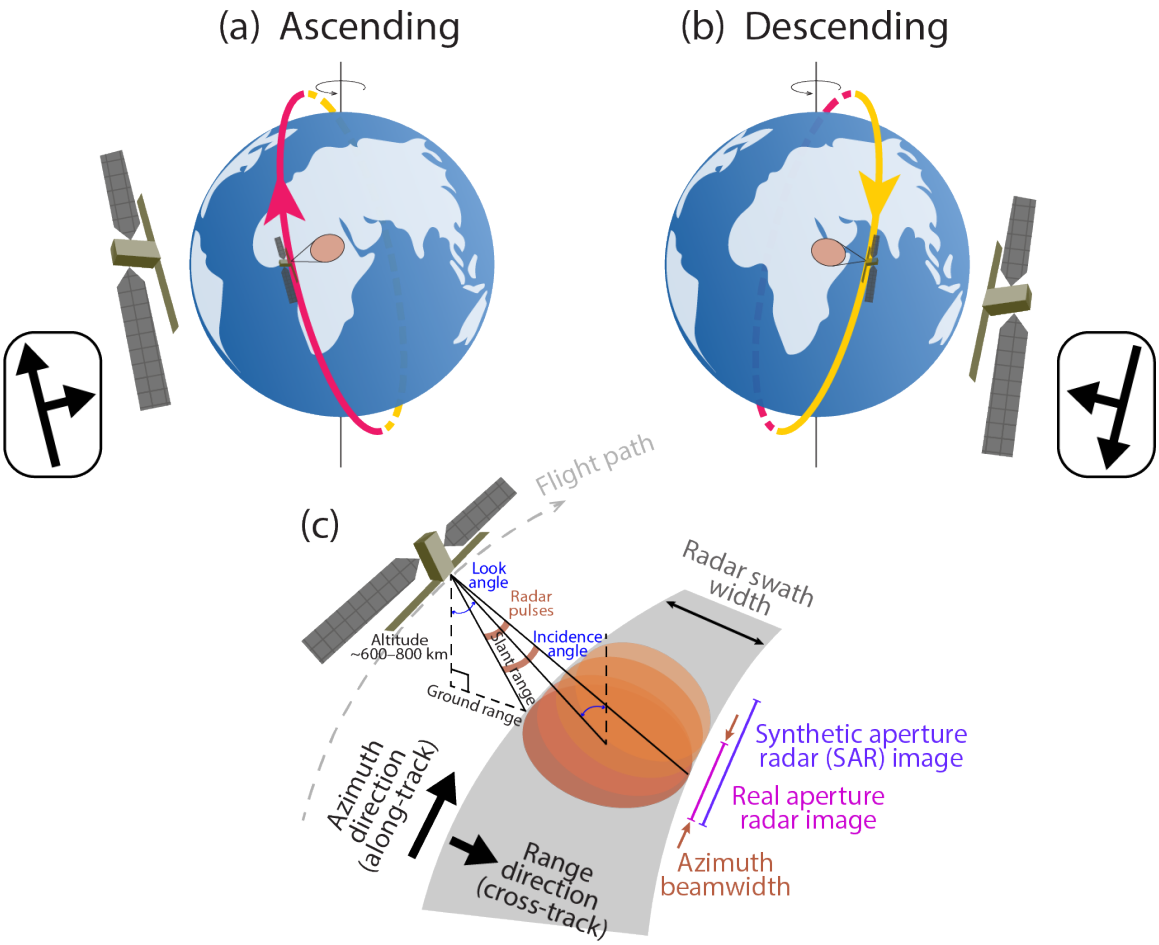


Figure 1.1: Schematic illustration of radar satellite (a) ascending and (b) descending paths, showing a right-side looking system. (c) Radar satellite acquisition geometry showing footprints of real aperture and Synthetic Aperture Radar (SAR) images. Conjugate thick arrows denote the azimuth and range directions.

track or range direction by the two way travel time of the radar pulse. The range resolution is primarily controlled by the radar pulse duration rather than the antenna size. Two closely spaced elements can be distinguished on the basis of travel times, if their two-way travel times are greater than the pulse duration. A higher range resolution can be achieved by a shorter pulse duration.

There are several SAR satellites used for Earth observation. The Japan Aerospace Exploration Agency (JAXA)'s Advanced Land Observing Satellites, ALOS-1 and ALOS-2, operated between 2006–2011 and 2014–present, respectively. Their longer wavelength, L-band SAR images are less disrupted by atmospheric conditions (e.g., cloud, rain, snow, dust), allowing for the most robust, all-weather observations. The larger wavelength of

the L-band also penetrates vegetation, advantageous for surveying densely vegetated regions (including, naturally, Japan). Depending on the acquisition mode, the spatial resolution ranges between ∼3–100 m. The revisit time at a given location of is 46 days for ALOS-1 and 14 days for ALOS-2. The Canadian Space Agency (CSA)'s RADARSAT-1 (1995–2013) and RADARSAT-2 (2007–recent) satellites image the Earth's surface at a shorter, C-band wavelength (5.6 cm), at spatial and temporal resolutions of 1–100 m and 24 days, respectively. In 2019, CSA launched three more identical SAR satellites under the RADARSAT Constellation Mission (RCM), shortening the revisit time to only four days. The European Space Agency (ESA) has the longest running SAR satellite series, all C-band (5.6 cm), starting with ERS-1 (1991–2000), ERS-2 (1995–2011), and ENVISAT (2002–2012), and culminating in the identical Sentinel-1A (2014–present) and Sentinel-1B (2016–2021). Sentinel-1 imagery has an unprecedentedly broad swath width of ∼250 km, spatial resolutions of 5–40 m, and revisit times of 12 days for each satellite, or 6 days when the pair was working in tandem.

All of the platforms listed above deploy right-side looking antennae from sun-synchronous Low Earth Orbits. On the ascending orbital tracks, the satellites travel from SSE to NNW and acquire imagery looking to the ENE and down (the 'line-of-sight') (Figure 1.1a). After traversing near to the north pole, the satellites follow descending orbital tracks from NNE to SSW, collecting imagery looking to the WNW and down (Figure 1.1b). This geometry is crucial when considering surface deformation mapped from repeat SAR images, a technique known as interferometry.

1.3.2 How InSAR Works

Interferometric Synthetic Aperture Radar (InSAR) refers to differencing SAR phase images collected from approximately the same position but at different times. While the individual phase images are essentially random noise, differencing them creates a coherent interference pattern known as an interferogram. The phase change for an individual pixel reflects several factors (Eq. 1.1) including the difference between the antenna position for the two images (known as the baseline), which in practice is never quite the same on successive orbits; a resultant, perspective effect of Earth's topography; atmospheric path delays to either image; any changes to back-scatters contained within the pixel between the two acquisition dates; and finally, any Earth surface deformation.

$$\begin{aligned}\text{Interferometric phase} = {} & \Delta\text{Orbital} + \Delta\text{Topography} + \Delta\text{Atmosphere} \\ & + \Delta\text{Pixel} + \Delta\text{Deformation}\end{aligned} \tag{1.1}$$

Changes in the baseline across an interferogram result in a linear pattern of fringes known as an orbital ramp (ΔOrbital) which is easily removed during processing, while the topographic phase (ΔTopography) can be removed using a digital elevation model (DEM). Ignoring atmospheric delays (ΔAtmosphere) and pixel effects (ΔPixel) for the time being, these corrections result in a map of Earth surface deformation resolved in the satellite line-of-sight (ΔDeformation). In raw form, this is displayed as color cycles ('fringes'), each of which represents a contour of one half-wavelength of ground motion, with the order of color change indicating whether motion is towards or away from the satellite. Much like the elevation contours on a topographic map, closely-spaced and compact fringes indicate steeper line-of-sight displacement gradients, while wider fringes reflect gentler or absent deformation. Fringes can also be added up into a map of cumulative LOS displacement, a process called phase unwrapping, though doing so can introduce errors, particularly in regions of partial decorrelation. To estimate the total line-of-sight displacement, the number of fringes can be multiplied by one-half wavelength, as shown in Eq. 1.2. However, deformation is often easiest to visualize with the fringe contouring of the original (wrapped) interferograms.

$$\begin{aligned}\text{Line-of-sight displacement (cm)} = {} & \text{number of fringes} \\ & \times \text{one-half wavelength of radar signal (cm)}\end{aligned} \tag{1.2}$$

In reality, noise is introduced to all interferograms by changes in the medium through which the radar signal propagates. Water vapor present in the troposphere, the lowest layer of Earth's atmosphere, can refract radar waves and generate fringes (ΔAtmosphere) unrelated to earthquake deformation. This noise is usually worse in humid tropical, temperate, and coastal regions, and better in dryer, inland, desert environments. In addition, there are typically greater water vapor signals in the thicker stratospheric columns above lowlands than in the thinner ones above mountains. Where high relief is generated along dip-slip faults, both the tectonic and atmospheric signals may therefore correlate with topography. This renders one approach to improving signal-to-noise, by stacking interferograms (e.g., Elliott et al., 2008). Corrections using global weather models are an alternate and increasingly popular means of reducing this atmospheric noise (e.g., Yu et al., 2017, 2018b,a).

Lastly, coherent interferograms rely on pixel back-scattering characteristics remaining unchanged between the two satellite passes (or put another way, if ΔPixel is non-zero, then the phase change is effectively random). Perhaps the most important cause of this decorrelation is growing vegetation. Thus, InSAR works best in regions with arid climate

and less in temperate and especially tropical rainforest (though there are approaches to improve coherence in these environments, e.g., Zheng et al., 2021), contrasts that will be well evident in the two case studies presented in this dissertation. Other common causes of pixel decorrelation include agriculture, other land use changes, snow cover, flooding, and water saturation. Such changes are rarely reversible, so interferograms spanning shorter intervals are usually more coherent than those spanning longer ones, especially in regions with fast-growing vegetation; this is one reason why the Sentinel-1 pair, with its shorter revisit times, has had better success in tropical regions than earlier C-band sensors (e.g., Funning and Garcia, 2019).

There are some additional causes of decorrelation implicated in large earthquakes and which are relevant to this dissertation. Pixel coherence can be compromised by surface rupturing, liquefaction, landsliding, building collapse, and even the strong ground accelerations themselves, which when greater than 1 g vertically can cause individual pixel scatterers to shift (e.g., Funning et al., 2005). Finally, decorrelation can sometimes occur without changes to pixel back-scattering being implicated: namely, whenever and wherever the fringe spacing becomes closer than the width of a pixel. This effect is often observed in steep, mountainous topography, due the close spacing of topographic fringes (i.e., the ΔTopography contribution), especially at long perpendicular baselines. However, it can also occur amongst steep deformation gradients (i.e. the ΔDeformation contribution), most commonly along earthquake surface ruptures. This limits the efficacy of mapping near fault surface deformation with InSAR, as explained further below.

1.3.3 InSAR Application to Earthquakes and its Limitations

Since its first application to the 1992 Landers, California earthquake (Massonnet et al., 1993), and acceleration from the launch of Sentinel-1A in 2014, InSAR has become perhaps *the* prevalent technique for mapping surface deformation in large continental earthquakes, and interpreting and modelling the causative fault mechanisms and slip distributions. Large earthquakes appear in wrapped interferograms as lobate fringe patterns, with typically between one and five discrete, long-wavelength (kilometers to 10s of km) deformation lobes. For surface rupturing events, these lobes are arranged around an elongate zone of closely-packed fringes or decorrelation along the fault trace. In the simplest approach, consideration of the relative motion of each lobe (whether it has moved towards or away from the satellite) in both the ascending and descending interferograms allows one to infer the relative ground motion on either side of the fault, and thus the

fault kinematics. A more quantitative approach involves forward or inverse elastic dislocation modelling, where unwrapped InSAR displacements are used to solve for source parameters such as strike, dip, rake, fault plane location and dimensions, and slip. This modelling is especially important for larger earthquakes, where first-order observations of the interferogram might not adequately capture geometric fault complexities such as multiple-fault or conjugate ruptures.

InSAR remains applicable even for buried earthquakes occurring on immature faults, since the deformation lobes can be detected even if the earthquake does not rupture to the surface, with patterns of motion towards or away from the satellite still indicative of the slip mechanism. However, the detectability of deformation lobes is conditioned upon the earthquake being large and shallow enough, with moment magnitudes (M_w) greater than $\sim$5.5 for hypocentral depths less than $\sim$10 km being a good rule of thumb (e.g., Liu et al., 2021a; Wright et al., 2003). For larger, surface rupturing events, decorrelation near the fault trace can often obscure the shallow slip distribution. In these cases, other geodetic imaging techniques such as optical image correlation and differential lidar can be used to add near-field displacement observations and map surface offsets (e.g., Gaudreau et al., 2023; Milliner et al., 2015) and through joint inversion with InSAR data, improve the resolution of slip models at shallow depths (Scott et al., 2019).

1.4 Dissertation Structure

The overarching goal of this dissertation is to investigate earthquake deformation with InSAR, with a focus on characterizing continental strike-slip ruptures on hidden and immature faults. There are three main projects structured as journal manuscripts. One of them (Chapter 3) is based on a journal article that is already peer-reviewed and published, and the other two (Chapters 2 and 4) are based on submitted manuscripts. Though InSAR is central to all of the work, each chapter has its own research questions, introduction and background information, results and conclusions, and supplemental materials. In Chapters 3 and 4, and with help from collaborators, I also incorporate seismological observations and methods, which are introduced there.

Below, I summarize the remaining chapters of this dissertation and how they contribute to the overarching goal.

Chapter 2 is an illustrated guide on how to interpret InSAR signals. Disseminating inteferograms has become more and more prevalent after large earthquakes, yet outside of specialists there is limited understanding in what the InSAR signals mean, and there so far

lacks a single study showcasing a complete suite of fringe patterns. In this chapter, I deconstruct InSAR signals and explain why the final interferograms look the way they do. I produce sets of model interferograms for different earthquake types, to demonstrate how the InSAR signal changes with varying fault kinematics and strike orientations. Users (general public, scientists, engineers, etc.) can utilize this lookbook by matching theoretical and real world event InSAR patterns to help interpret the rupture mechanism.

Chapter 3 is the first of two main case studies, in which I use InSAR to characterize the 2020 M_w 6.5 Monte Cristo Range earthquake in arid Nevada, USA. The mainshock involved previously unmapped faults, presenting an ideal opportunity to explore rupture behaviours potentially linked to structural immaturity. In this study, I integrated seismological and field observations through collaborative efforts, yielding a more comprehensive understanding of the rupture complexity of this earthquake. InSAR analysis revealed a compound source fault geometry, and I argue that, unusually, the two faults even cross one other. Additionally, by comparing my slip model with those compiled from several of InSAR studies of strike slip earthquakes, I highlight that earthquake magnitude plays a more significant role than fault structural maturity in controlling the shallow slip deficit.

Chapter 4 is a second main case study, in which I showcase the utilization of InSAR for characterizing moderate-sized earthquakes in a tropical region. I look at five significant seismic events of M_w 5.5–6.2 in the Golden Triangle region spanning Laos, Thailand, and Myanmar. Unlike in the first case study, this area is characterized by dense forests, a humid climate, and rugged topography; but like Chapter 3, I show that the earthquakes occurred on previously unrecognized, immature faults. I emphasize the importance of coupling InSAR measurements to high-precision multi-event relocations in earthquake research within such challenging environments. Given the proximity of these earthquakes to critical infrastructure and important cultural and historical sites, I hope to spur improvements to regional seismic hazard assessment by highlighting the capacity for short, hidden faults to generate substantial ruptures.

Chapter 5 concludes the dissertation by summarizing rupture behaviours common to both case studies that may be linked to fault structural immaturity. I highlight how InSAR is an important tool to understand differences in earthquake behaviour between mature and immature faults. Since previously unrecognized faults were able to generate sizeable earthquakes in both case studies, I emphasize the importance of considering hidden, immature faults in seismic hazard assessments, so that we can be more prepared for these types of events.

Chapter 2

The InSAR Lookbook: an illustrated guide to earthquake interferograms

2.1 Author Names, Affiliations, and Roles

I. Sethanant[1] and E. Nissen[1]

[1]School of Earth and Ocean Sciences, University of Victoria, British Columbia, Canada

This chapter is based on a manuscript submitted to Seismica. I undertook all InSAR modelling and analysis, produced all figures, and wrote the first draft of the text. Dr. Edwin Nissen supervised this work and provided manuscript edits and figure suggestions.

2.2 Abstract

Interferometric Synthetic Aperture Radar (InSAR) is a powerful and increasingly popular method for mapping onshore earthquake deformation and characterizing the causative faulting. Following notable large earthquakes, InSAR images (interferograms) are quickly disseminated across the scientific community and often into the media. However, outside of InSAR specialists, there remains a lack of general understanding of how to interpret them. This chapter aims to fill this gap by providing an illustrated guide to earthquake InSAR signals. By forward modelling three-dimensional surface displacement fields, we elucidate how the combination of horizontal and vertical movements, viewed from ascending or descending satellites, determines the general fringe formation. We then synthesize interferograms for a comprehensive suite of faulting styles, including strike-slip, reverse,

normal, low-angle thrust, low-angle normal, and oblique-slip faults. We outline the most common InSAR fringe patterns and demonstrate that strike-slip earthquakes tend to exhibit 2- or 4-lobed InSAR signals (resembling butterfly wings and four-leaf clovers), while dip-slip ruptures usually produce 2- or 3-lobed signals (resembling bow ties). However, more complex 5-lobed shapes (resembling balloon model animals) are possible at certain strike angles. We offer guidelines for utilizing the lookbook to estimate earthquake mechanisms visually and to pick the causative fault plane from any two seismological nodal planes. By comparing modelled interferograms and real-world earthquakes, we showcase the broad applicability of the lookbook, even for complex multiple segment ruptures. Lastly, we suggest potential applications of the lookbook beyond the scientific community.

2.3 Plain Language Summary

InSAR is a method that uses repeat satellite radar images to map shifts in the ground surface, and has become popular for analyzing onshore earthquakes. With some basic guidelines, both the location and style of faulting can quickly be inferred from InSAR images, called interferograms. In this study, we explain the link between 3-dimensional ground displacements and the patterns seen in the InSAR images. We then produce a 'lookbook' of model interferograms that showcase the range of deformation patterns characteristic of earthquakes of different fault styles and orientations. For example, faults that slide sideways generate patterns resembling butterfly wings or four-leaf clovers, while those that involve angled thrusting or stretching produce rounded double or triple deformation lobes. Our lookbook can be used to characterize real world earthquakes quickly, without the need for specialized modelling.

2.4 Introduction

After any large onshore earthquake, it is nowadays customary for earthquake scientists to map the resulting coseismic surface deformation with InSAR as soon as the post-event radar images are acquired. These interferograms are increasingly processed automatically and made publicly available at short notice, for example through the LiCSAR platform (Lazecký et al., 2020; Watson et al., 2023) and Alaska Satellite Facility (Kennedy et al., 2021; Meyer et al., 2017). Thereafter, the images are often quickly shared with first responders working in the field (e.g., earthquake geologists, structural engineers, and emergency managers) and disseminated among the geoscience community and general public

through media and social media platforms (Watson et al., 2023; Meyer et al., 2017; Xu et al., 2020; Barnhart et al., 2019b).

To a trained eye, coseismic interferograms are particularly helpful in identifying the rupture location and mechanism, in doing so solving the nodal plane ambiguity inherent in seismological focal mechanisms. InSAR imagery can also capture other critical features of an earthquake (sometimes uniquely), including rupture extents, off-fault deformation, liquefaction, and even building collapse (Funning et al., 2005; Fielding et al., 2005). However, to our knowledge there is not yet a one stop, go-to guide for how to "read" or interpret interferograms. In our experience, earthquake scientists trained primarily in field geology or instrumental seismology sometimes struggle to interpret these images, and even for InSAR specialists, certain types of earthquakes at particular strike angles can produce complicated signals that are difficult to understand at first glance.

The central aim of this study is to provide an illustrated guide to interpreting InSAR signals through a comprehensive suite of model interferograms spanning a wide range of fault types and orientations. Our work builds upon an earlier, interactive, web-based tool for simulating interferograms, called 'Visible Earthquakes' (Funning and Cockett, 2012), sadly now discontinued. Using an elastic dislocation model, we first illustrate how three-dimensional deformation in an earthquake is resolved into the line-of-sight (LOS) displacements to which InSAR is sensitive, a vital concept for understanding why InSAR signals look the way they do (Section 2.5). We then describe our forward modelling set-up for the lookbook itself (Section 2.6). Then, we present our lookbook of InSAR signals, which captures end-member faulting styles including left- and right-lateral strike-slip (Section 2.7.1), reverse, normal, low-angle thrust, and low-angle normal slip (Sections 2.7.2, 2.7.3), as well as some of the most common types of oblique-slip mechanism (Section 2.7.4). For each fault type, interferograms are arranged radially by fault strike (and later, rake) such that the reader can visually assess its influence on the observed InSAR fringe patterns. Finally, we show how this lookbook can help assess real-world earthquakes using a number of examples (Section 2.8). Beyond the application of earthquake science, this lookbook may serve as educational material for introducing Earth surface imaging to students and the public, or as an outstanding communication tool within sectors like insurance companies, surveys and land management agencies, which involve personnel with diverse expertise.

2.5 Why coseismic interferograms look as they do

To help illustrate why earthquake interferograms appear as they do, we use a simple elastic dislocation model to demonstrate how 3-D coseismic displacements map into satellite LOS displacements at different orientations. In this section, we follow a similar line of reasoning to that used by Funning et al. (2005) to explain fringe patterns in the 2003 Bam, Iran earthquake. We use the same modelling set-up as for the main lookbook (described in Section 2.6) with the left-lateral strike-slip and moderately-dipping (45°) normal fault parameters from Table 2.1. A 45°-dipping reverse faulting earthquake would generate the same deformation pattern as the normal faulting earthquake, except with the exact opposite horizontal and vertical displacement sense.

2.5.1 Strike-slip earthquakes

In Figure 2.1a (left panel), we plot the theoretical 3-D displacement field for a N-trending left-lateral strike-slip earthquake. Horizontal displacement vectors are plotted at regular intervals over a color map of vertical displacement, with red indicating uplift and blue subsidence. In the near field, horizontal displacement vectors are longest, and parallel to the fault, on either side of the fault center, while they are shorter, and at oblique angles, around the fault tips. Horizontal displacement vectors also shorten with increasing distance from the fault, in every direction. Vertical displacements for a strike-slip fault are small, but non-negligible, especially around the fault endpoints where horizontal contraction and extension results in uplift and subsidence, respectively. SW and NE of the fault trace, horizontal displacement vectors are shortening, explaining the two regions of uplift, whereas NW and SE of it, vectors are lengthening, leading to stretching and subsidence. The sense of vertical displacement is therefore anti-symmetric both along the fault and perpendicular to it.

In Figure 2.1a (center and right panels), we separate the horizontal displacement vectors into their distinct N–S and E–W components, still superimposing these onto the vertical deformation color map. The large, lateral displacements parallel to the strike-slip fault are captured in the N–S displacement field (Figure 2.1a, center panel) while the smaller motions perpendicular to the fault are captured in the E–W displacement field (Figure 2.1a, right panel). Since InSAR satellites follow near polar orbital tracks and look downwards and to the right, they have very little sensitivity to the N–S displacements (the vectors in the center panel), but much stronger sensitivity to both the E–W and vertical displacements (Figure 2.1a, right panel).

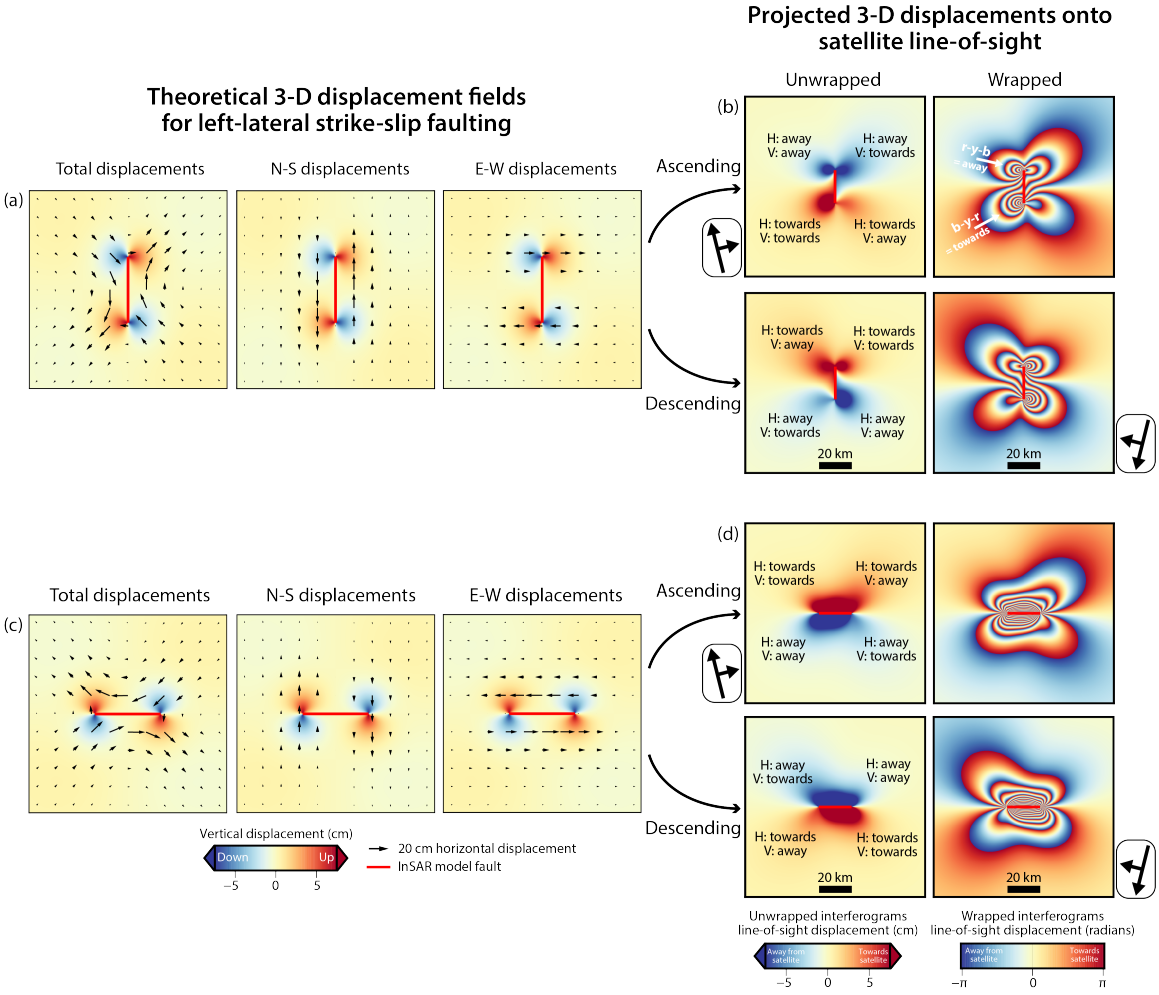


Figure 2.1: (Left) 3-D displacement fields and (right) unwrapped and wrapped interferograms for a (a, b) N–S-oriented and (c, d) E–W-oriented left-lateral strike-slip earthquake (model fault shown by thick solid red line). On the left side of the figure (a, c), horizontal motions (black vectors) are overlain on a color map of vertical displacement (red is uplift and blue subsidence). The left panels shows full horizontal displacements while the center and right panels split these into their N-S and E-W components, respectively. On the right side of the figure (b, d), the 3-D displacements are projected onto the satellite LOS to produce (top) ascending and (bottom) descending (left) unwrapped and (right) wrapped interferograms. As is convention, satellite geometries are denoted by conjugate arrows, with the long arrows indicating satellite azimuths and the short one indicating horizontal components of the LOS vector. Annotations in the unwrapped interferograms denote the horizontal (H) and vertical (V) components of LOS displacement.

In an ascending track interferogram, the InSAR look vector is roughly equal parts towards the ENE and downwards (Figure 2.1b, top panels). The NW quadrant of the displacement field thus comprises motions that are horizontally away (eastward) and vertically

away (downward) from the satellite, adding constructively into a strong LOS displacement away from the satellite (Figure 2.1b, top left) and resulting in densely packed fringes in the wrapped interferogram (Figure 2.1b, top right). In the NE quadrant, displacements are horizontally away (eastward) but vertically towards (upward) the satellite, mostly cancelling out for a weaker LOS displacement away from the satellite and fewer fringes. In the SW quadrant, westward and upward displacement combines into a strong LOS displacement towards the satellite, while in the SE quadrant the westward and downward motions mostly cancel each other out for a weak LOS displacement towards the satellite. Thus, the combinations of E–W and vertical motions in the four quadrants of the ascending interferogram produce two northern deformation lobes with motion away from the satellite and two southern lobes with motion towards the satellite, with stronger LOS displacements and more densely packed fringes in the western lobes and weaker LOS displacements with fewer fringes in the eastern ones (Figure 2.1b, top right).

On its descending track, the satellite observes the same displacement field differently, looking in equal parts to the WNW and downwards (Figure 2.1b, bottom panels). In the NW quadrant, motions are horizontally towards (eastward) but vertically away (downward) from the satellite, mostly cancelling out (Figure 2.1b, bottom left). In the NE quadrant, displacements are horizontally towards (eastward) and vertically towards (upward) the satellite, adding to strong LOS displacements towards the satellite. Likewise, motions in the SW quadrant mostly cancel out, while those in the SE quadrant constructively interfere to generate strong LOS displacement away from the satellite. Therefore, the descending interferogram also generates two lobes each of motion towards and away from the satellite, but this time LOS displacements are strongest and fringes most densely packed on the eastern side of the fault (Figure 2.1b, bottom right), opposite to the ascending interferogram.

Next, we repeat the exercise for an E–W-trending left-lateral strike-slip earthquake. The 3-D displacement field is the same as for the N–S earthquake, but rotated 90° (Figure 2.1c). The large, lateral displacements parallel to the strike-slip fault are now captured in the E–W displacement field (Figure 2.1c, right panel), to which InSAR is highly sensitive, whereas the smaller fault-perpendicular motions are captured in the N–S displacement field (Figure 2.1c, center panel), to which InSAR is mostly insensitive. In the ascending track interferogram, the strong westward motion N of the fault interferes constructively with uplift in the NW quadrant but destructively with subsidence in the NE quadrant, merging into a single, lopsided lobe with LOS displacement toward the satellite (Figure 2.1d, top panels). Similar interference on the S side of the fault, where eastward

lateral motion dominates, results in a single, lopsided lobe containing LOS displacement away from the satellite. There are therefore two deformation lobes, towards the satellite in the North and away from it in the South (Figure 2.1d, top left), with the densest fringes in the west and the longest wavelengths in the east, appearing to 'skew' the fringe patterns in this direction (Figure 2.1d, top right). Following the same reasoning, the descending track interferogram is a double mirror image of the ascending one, with single northern and southern lobes containing displacement away from and towards the satellite, respectively, both skewed westwards (Figure 2.1d, bottom panels). This demonstrates an important point: that asymmetric lobe shapes often simply reflect InSAR look geometries, rather than variations in slip along strike as might seem intuitive.

2.5.2 Dip-slip earthquakes

The 3-D displacement field for a N-striking normal faulting earthquake is dominated by vertical subsidence in the hanging wall east of the fault, with a much smaller amount of uplift in the footwall west of it (Figure 2.2a, left panel). Horizontal displacements are greatest either side of the fault center, where they are perpendicular to the fault, and smaller towards the fault tips, where they include increasing fault-parallel components, pointing radially outwards west of the fault and inwards east of it. The E–W displacement field, to which InSAR is sensitive, captures the large, fault-perpendicular displacements (Figure 2.2a, right panel), while the N–S displacements, to which InSAR is insensitive, includes the smaller fault-parallel motions (Figure 2.2a, center panel).

In the near-field of the hanging wall east of the fault, LOS displacements are dominated by subsidence, leading to motion away from the satellite in both ascending and descending interferograms (Figure 2.2b, left panels). The deformation lobe is narrow, with closely packed fringes in the wrapped interferograms centered directly above the eastward-dipping fault plane (Figure 2.2b, right panels). Further east, far-field displacements comprise eastward motions that are away from the ascending satellite and towards descending one (Figure 2.2b, left panels). In the ascending interferogram, the near- and far-field hanging wall lobes are both negative, thus merging together, whereas in the descending interferogram they are of opposite displacement sense, staying as separate near-field negative and far-field positive lobes. In the footwall west of the fault, both interferograms are dominated by fault perpendicular westward motion, forming a single deformation lobe moving towards the ascending satellite but away from the descending one. Overall, the ascending interferogram thus contains two distinct lobes, and the de-

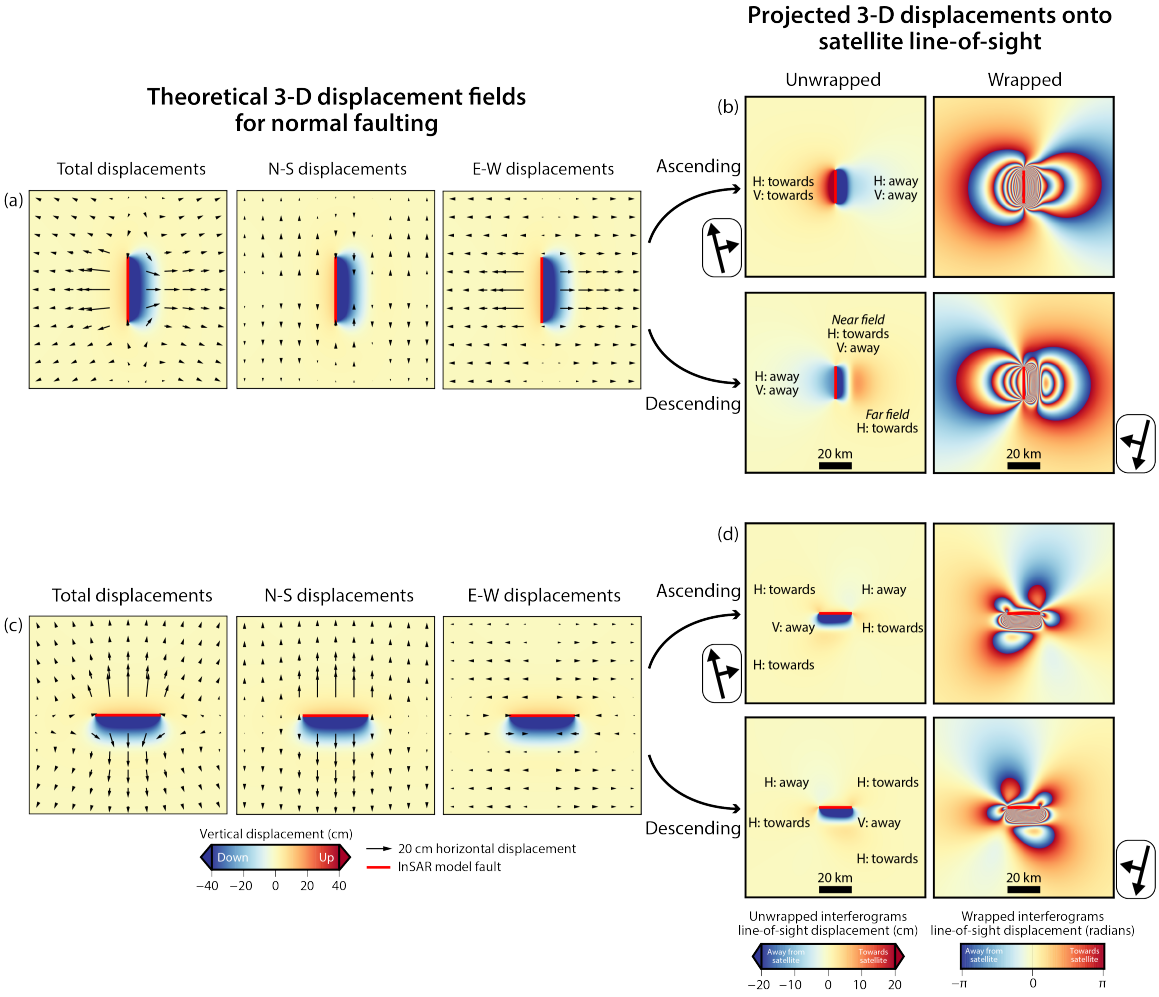


Figure 2.2: (Left) 3-D displacement fields and (right) unwrapped and wrapped interferograms for a (a, b) N-striking and (c, d) E-striking normal faulting earthquake (surface trace in red). On the left side of the figure (a, c), horizontal motions (black vectors) are overlain on a color map of vertical displacement (red is uplift and blue subsidence). The left panels shows full horizontal displacements while the center and right panels split these into their N-S and E-W components, respectively. On the right side of the figure (b, d), the 3-D displacements are projected onto the satellite LOS to produce (top) ascending and (bottom) descending (left) unwrapped and (right) wrapped interferograms. As is convention, satellite geometries are denoted by conjugate arrows, with the long arrows indicating satellite azimuths and the short one indicating horizontal components of the LOS vector. Annotations in the unwrapped interferograms denote the horizontal (H) and vertical (V) components of LOS displacement.

scending interferogram three.

For an E-striking normal faulting earthquake, the large, lateral displacements per-

pendicular to the normal fault are now captured in the N–S displacement field, to which InSAR is mostly insensitive, whereas the smaller fault-parallel motions are captured in the E–W displacement field, which the InSAR picks up (Figure 2.2c). Near-field LOS displacements in the hanging wall south of the fault are still dominated by vertical motion away from the satellite, resulting in a narrow lobe centered above the dipping fault in both the ascending and descending interferograms (Figure 2.2d). In the footwall north of the fault, LOS deformation mostly reflects the smaller, fault-parallel motions around the fault tips. These result in an arrangement of smaller lobes (three positive, one negative) surrounding the dense, central lobe in both interferograms, which are mirror images of one another about the N–S axis.

2.6 Introducing the InSAR Lookbook

2.6.1 Model Set-up and Displacement Sense Convention

We used the formulae of Okada (1985) implemented in Oksar software (Wright et al., 1999) to generate displacement fields for earthquakes represented as uniform slip on planar, rectangular dislocations embedded in an elastic half-space. For each earthquake configuration (described below), 3-dimensional displacements were mapped across a 150 km $\times$ 150 km region at a 100 m spatial resolution. These were then projected into the ascending and descending satellite line-of-sight, using a local Earth radius of 6,370 km, a satellite height of 700 km, and satellite azimuths of 350.1° (ascending) and 190.7° (descending). These parameters are based upon European Space Agency (ESA) Sentinel-1 orbits at mid latitudes, and we chose a center scene incidence angle of 38.3°, equivalent to the middle of a Sentinel-1 Interferometric Wide Swath scene at the same latitude (European Space Agency, nd). Angles at higher or lower latitudes and along the swath edges differ by only a few degrees, with minimal discernible changes to the resultant model interferograms. Finally, we wrapped the LOS displacements using the Sentinel-1 half-wavelength of 2.77 cm.

Unfortunately, there is no settled protocol amongst the InSAR community on how to represent the sense of ground displacement (whether towards or away from the satellite) in interferograms, and so we first establish our own convention and terminology. For unwrapped interferograms, we use red and blue colours to refer to motion towards and away from the satellite, respectively: this seems intuitive to most geologists and is the common convention in the seismology literature. For wrapped interferograms, it is easiest

to think first of the far-field deformation as approximating zero, and then to consider the color order as one approaches the earthquake signal from any one side of it. Here, we use the convention that when crossing fringes in the order blue through yellow to red (abbreviated as blue–yellow–red), motion is increasingly towards the satellite. For simplicity and brevity, we call these fringes 'positive lobes'. If, approaching the fault, the colours instead cycle red–yellow–blue, then motions are increasingly away from the satellite, and we call the region a 'negative lobe'.

2.6.2 Model Fault Configurations

We forward modelled ten types of earthquake at each of twelve different strike orientations (at 30° increments from 0° to 330°), producing four interferograms for each configuration: ascending and descending, wrapped and unwrapped. The ten faulting types incorporate rake values of 0°, 45°, 90° (in both reverse and low-angle thrust configurations), 135°, 180°, −135°, −90° (in both normal and low-angle normal configurations), and −45° (Table 2.1). We used dips of 90° for strike-slip faults, 45° for normal and reverse faults, 67.5° for oblique-slip faults (an average of the dip-slip and strike-slip values), and 10° for low-angle thrust and low-angle normal faulting. The reverse and normal fault dip of 45° is based on a global survey of continental dip-slip focal mechanisms (Middleton and Copley, 2014; Collettini and Sibson, 2001). In all cases, we used a 20 km-long and 10 km-wide fault plane with uniform slip of 1 m for consistency with fault length scaling relationships (Wells and Coppersmith, 1994). For most earthquake types, the fault top depth is zero; the fault bottom depths therefore differ according to dip angle, but the length to width ratio is a constant 2 to 1 (Table 2.1). The exceptions are our low-angle thrust and low-angle normal faulting earthquakes, whose purpose is to represent slip on décollements or detachments; these faults are centered at just below 10 km depth. For the half-space, we used elastic Lamé parameters λ and μ of 3.2×10^{10} Pa, which together with fault area and slip yield a seismic moment of 6.4×10^{18} Nm, equivalent to a moment magnitude (M_w) of 6.5.

2.6.3 How to Use the Lookbook

The overarching goal of the lookbook is to help readers interpret real coseismic interferograms. When InSAR images of an earthquake become available, users can match them with model interferograms plotted in the lookbook to make a first order interpretation or estimation of the rupture mechanism.

Table 2.1: An index listing all suites of model earthquakes presented in the lookbook, their underlying source parameters, and where the model interferograms are plotted; the first figure listed is the (w)rapped interferogram and the second figure is the (u)nwrapped one. All model earthquakes involve 1.0 m of uniform slip on a 20 km-long, 10 km-wide, rectangular, planar fault.

Earthquake descriptor	**Strike**	**Dip**	**Rake**	**Depth** (km)	**Fig.** (w/u)
Left-lateral strike-slip	variable	90°	0°	0–10	2.3a/2.9a
Right-lateral strike-slip	variable	90°	180°	0–10	2.3b/2.9b
Reverse	variable	45°	90°	0–7.07	2.3c/2.9c
Normal	variable	45°	−90°	0–7.07	2.3d/2.9d
Low-angle thrust	variable	10°	90°	10–11.74	2.3e/2.9e
Low-angle normal	variable	10°	−90°	10–11.74	2.3f/2.9f
Left-lateral/reverse oblique-slip	variable	67.5°	45°	0–9.24	2.3g/2.9g
Right-lateral/reverse oblique-slip	variable	67.5°	135°	0–9.24	2.3h/2.9h
Left-lateral/normal oblique-slip	variable	67.5°	−45°	0–9.24	2.3i/2.9i
Right-lateral/normal oblique-slip	variable	67.5°	−135°	0–9.24	2.3j/2.9j
N-striking	0°	variable	variable	variable	2.10a
NNE-striking	30°	variable	variable	variable	2.10b
ENE-striking	60°	variable	variable	variable	2.10c
E-striking	90°	variable	variable	variable	2.10d
ESE-striking	120°	variable	variable	variable	2.10e
SSE-striking	150°	variable	variable	variable	2.10f
S-striking	180°	variable	variable	variable	2.10g
SSW-striking	210°	variable	variable	variable	2.10h
WSW-striking	240°	variable	variable	variable	2.10i
W-striking	270°	variable	variable	variable	2.10j
WNW-striking	300°	variable	variable	variable	2.10k
NNW-striking	330°	variable	variable	variable	2.10l

We provide Table 2.1 to help the reader navigate to the appropriate figure within the lookbook. Two types of figures are listed. In the top half of the table, there is a figure for each fixed style of faulting, in which ascending/descending interferogram pairs are plotted radially at 30° increments of strike (Figures 2.3a–2.3j). This type of figure will be most useful when the style of faulting is either known (for example, from an independent seismological focal mechanism, such as those often made available well before the first InSAR imagery by agencies such as the United States Geological Survey National Earthquake Information Center, USGS NEIC), or suspected (for example, using knowledge of the tectonic setting). Often, this will help narrow the search for the relevant InSAR signal in the lookbook to one of two possibilities, representing each nodal plane. The lookbook may then help users distinguish the fault plane from the auxiliary plane of the focal mechanism (though even with InSAR imagery to hand, there is sometimes still a nodal plane ambiguity).

In the bottom half of Table 2.1, there is a figure for each fixed orientation of fault strike, in which ascending/descending interferogram pairs are plotted radially at 45° increments of rake (Figures 2.10a–2.10l). These figures are more appropriate for when the style of faulting is unknown, but they do require an estimation of the fault strike. Often, the strike can be estimated directly from the interferogram, using any observed displacement discontinuity or linear zone of image decorrelation, such as are expected along earthquake surface ruptures.

2.6.4 Extrapolating and Interpolating the Lookbook Models

Naturally, the model earthquakes in the lookbook represent a tiny fraction of all source parameter space, and ultimately inverse models are needed to determine the best-fitting fault geometry and slip distribution. Readers should therefore use the lookbook models only as first order approximations of real interferograms. However, equipped with a feel for how each variable impacts the deformation field, they can also interpolate or extrapolate the lookbook model faults to approximate the source parameters of a real earthquake from a set of observed interferograms.

For example, earthquake ruptures striking at 10° or 20° will generate fringe patterns roughly intermediate to those of our 0°- and 30°-striking forward models. Variations in dip or rake away from our fixed series of values will skew the relative amplitudes and/or positioning of InSAR deformation lobes, without changing the essential pattern. Preventing slip from reaching the surface by burying the fault top depth will remove the LOS displacement discontinuity along the fault surface trace, replacing it with closely spaced fringes, but will not impact far field deformation. Similarly, extending the bottom of the fault to greater depths will increase far-field displacements without impacting those along the fault trace. Lengthening the fault stretches the fringes in the along-strike direction, without altering those around the fault ends. Fault slip, the only parameter in linear relation to surface deformation, controls the number of fringes but not the pattern; for example, an earthquake with half or double the moment of one of our models will simply half or double the number of fringes. Similarly, wrapped interferograms generated from satellites with longer wavelengths than Sentinel-1 (e.g., ALOS-2) will have fewer fringes than our forward models, but retain the same shape.

2.6.5 Limitations

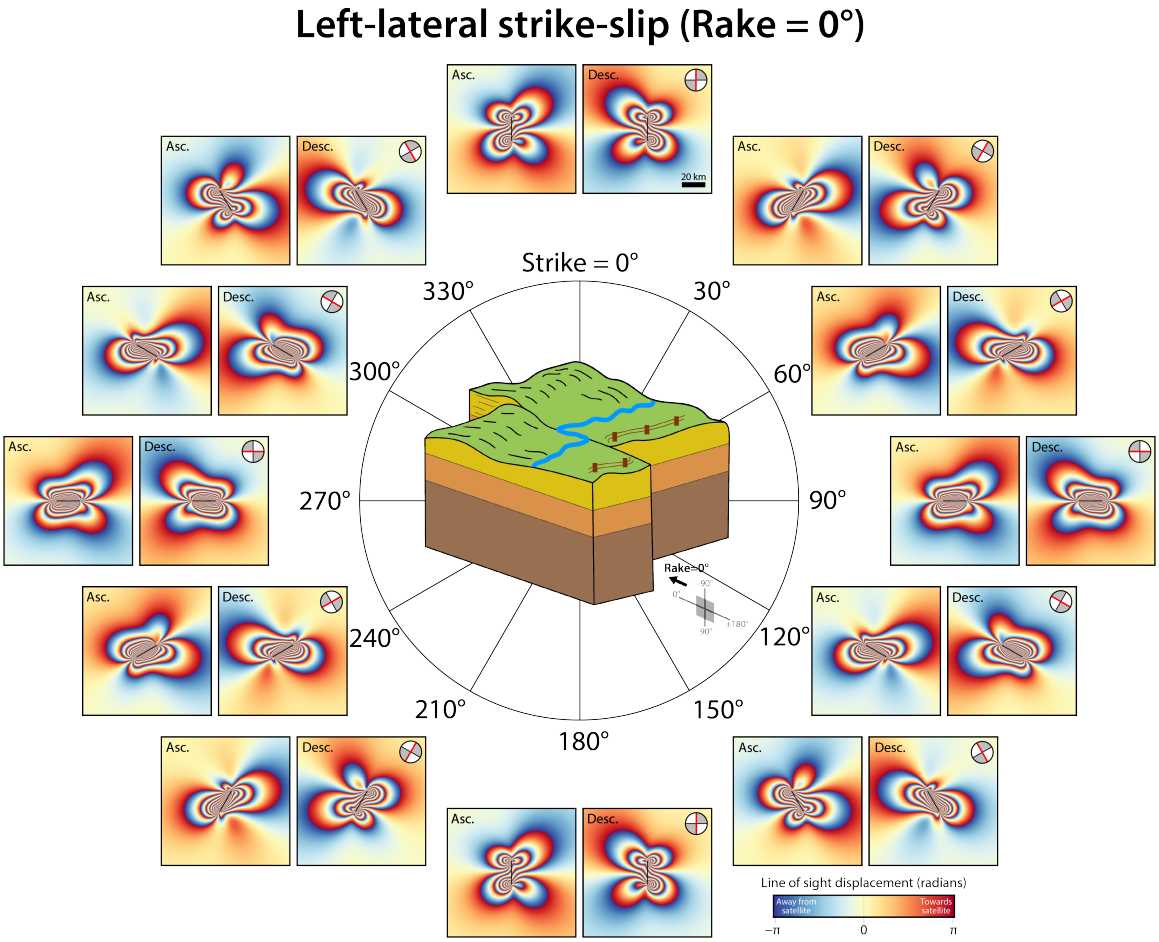
Real earthquakes involve variations in slip and rake over the fault surface, which may not be planar. The longest continental ruptures often display multiple slip asperities along strike, giving rise to 'string of pearl' InSAR fringe patterns that surpass the simplicity of our lookbook interferograms. A good example of this phenomenon was the 2008 M_w 7.9 Wenchuan, China earthquake, which exhibited four (or more), separate patches of multi-meter ($\sim$5–8 m) slip along the $\sim$250 km-long fault (Tong et al., 2010; Wan et al., 2017). Multi-fault ruptures are a separate class of earthquake involving near-simultaneous failure of more than one discrete fault, and naturally cannot be modelled closely using a single dislocation. Notable examples include the 2010 M_w 7.1 Darfield and 2016 M_w 7.8 Kaikoura earthquakes, both in New Zealand, the 2010 M_w 7.2 El Mayor-Cucapah earthquake in Mexico, and the 2019 M_w 7.1 Ridgecrest earthquake in California. To fit InSAR data closely, published models of these earthquakes incorporate up to a dozen discrete fault segments with widely variable geometries and kinematics (Elliott et al., 2012; Hamling et al., 2017; Wei et al., 2011; Magen et al., 2020). The uniform slip models in our lookbook cannot feasibly capture such complexities, underscoring the importance of modelling source geometries and slip distributions, especially for the largest events.

However, it is also encouraging to us that coseismic interferograms for most earthquakes smaller than about M_w 7 can be fit quite satisfactorily with simple, rectangular, uniform slip planes. Indeed, doing so remains a routine first stage in InSAR inverse modelling studies, with the second stage (solving for slip and rake distributions) often yielding only marginal differences in modelled surface deformation. Generally these differences are greatest along the fault surface trace, particularly for earthquakes that fail to rupture fully to the surface, introducing a shallow slip deficit (see e.g., Chapter 3). For earthquakes with simple slip distributions—where slip is concentrated in a single region and tapers towards the fault ends—the observed fringe patterns tend to align closely with our established uniform slip templates.

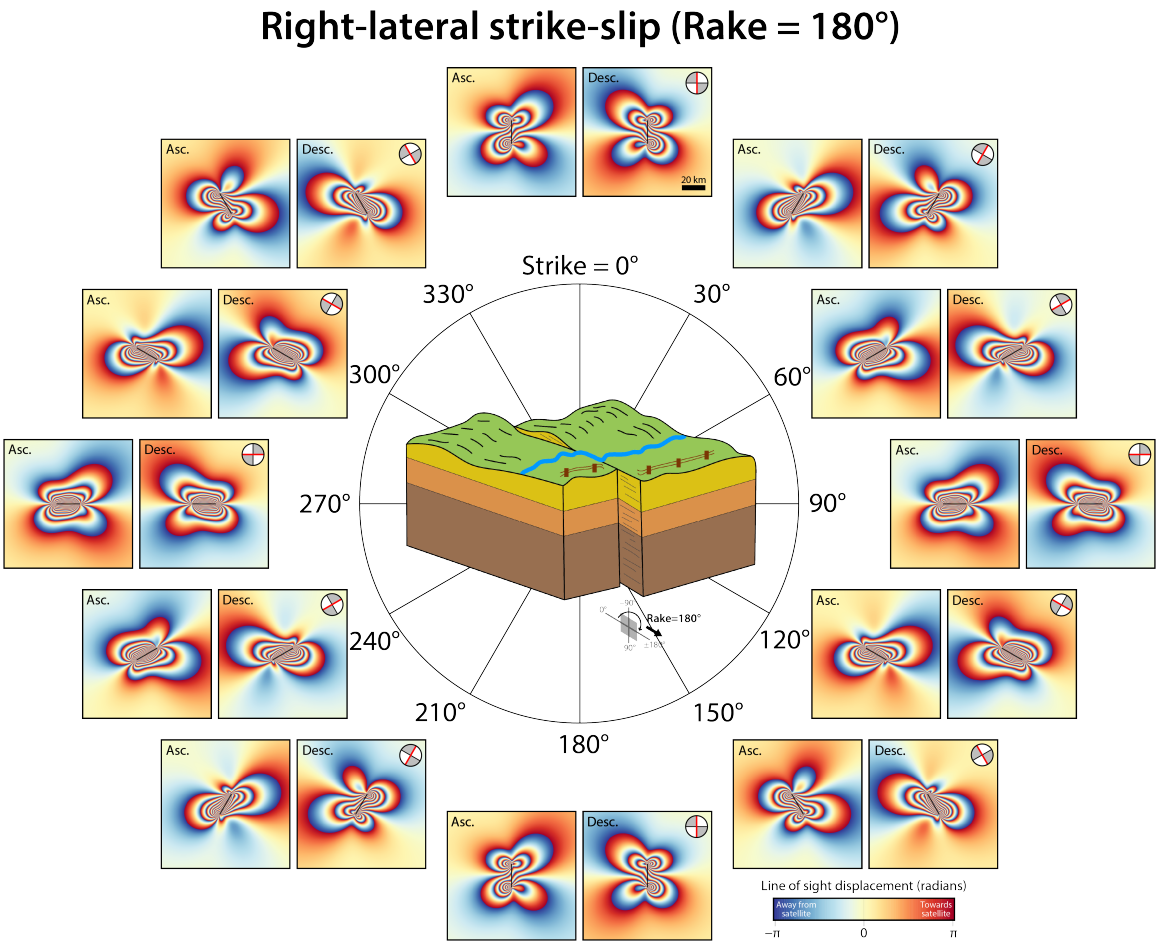
Finally, at certain fault geometries, it can be difficult to discriminate the causative fault plane from the conjugate nodal plane using InSAR data. This is very similar to the nodal plane ambiguity in seismological focal mechanisms, and is especially problematic for buried earthquakes or where near-field deformation is decorrelated in the interferogram (as is often the case for large, shallow earthquakes in steep topography). We will discuss this limitation both as we introduce our lookbook interferograms (Section 2.7) and as we examine some real earthquake data (Section 2.8.2).

2.7 The InSAR Lookbook

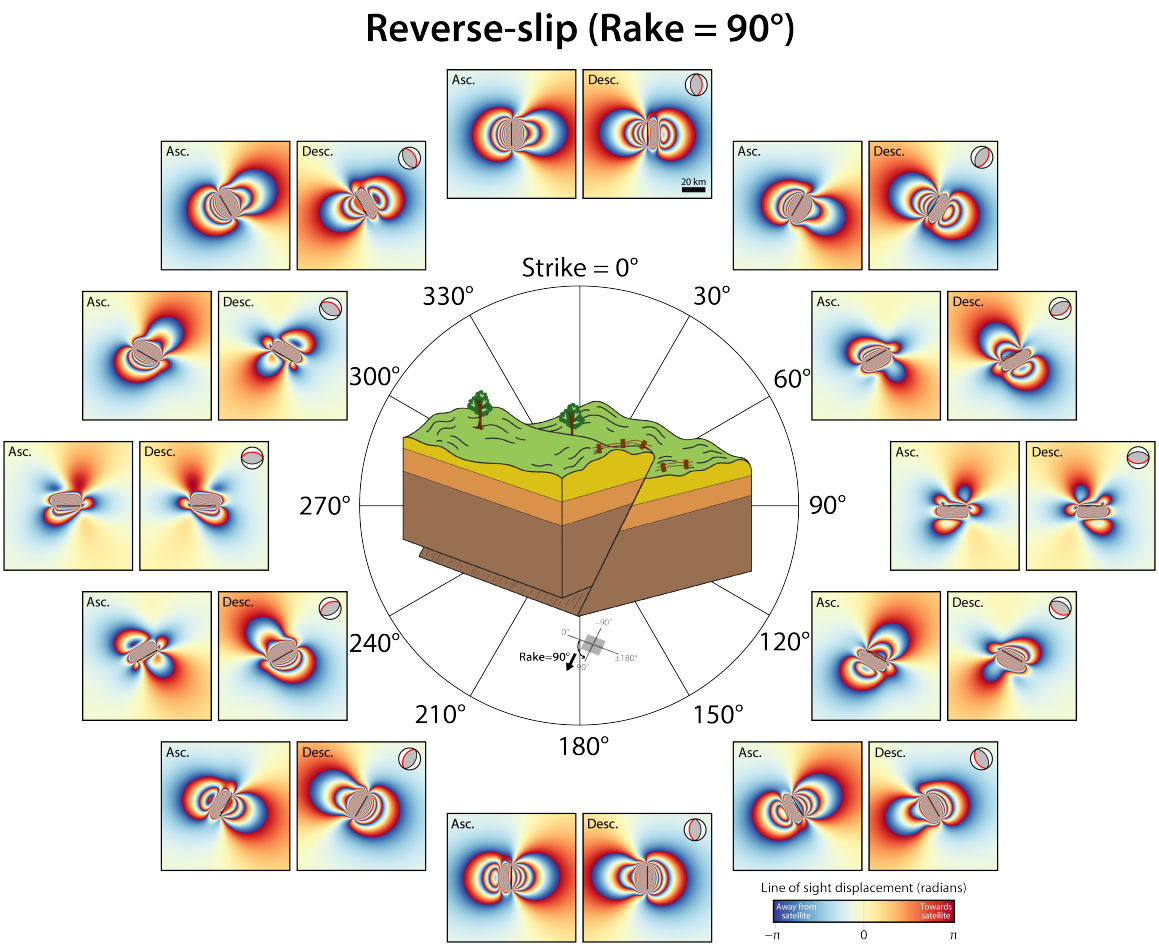
Figure 2.3: The InSAR lookbook. In each panel (a) to (j), ascending and descending interferogram pairs are plotted radially at 30° increments in fault strike around a block diagram illustrating the displayed faulting. Solid black lines mark the 20 km-long model fault trace; for non-vertical faults, a dashed rectangle marks the model fault itself. In all panels, we use the convention that when crossing fringes in the order blue–yellow–red, motion is increasingly towards the satellite, and when crossing fringes in the order red–yellow–blue, motion is increasingly away from the satellite. The beach ball is the earthquake focal mechanism, with the fault plane outlined in red.



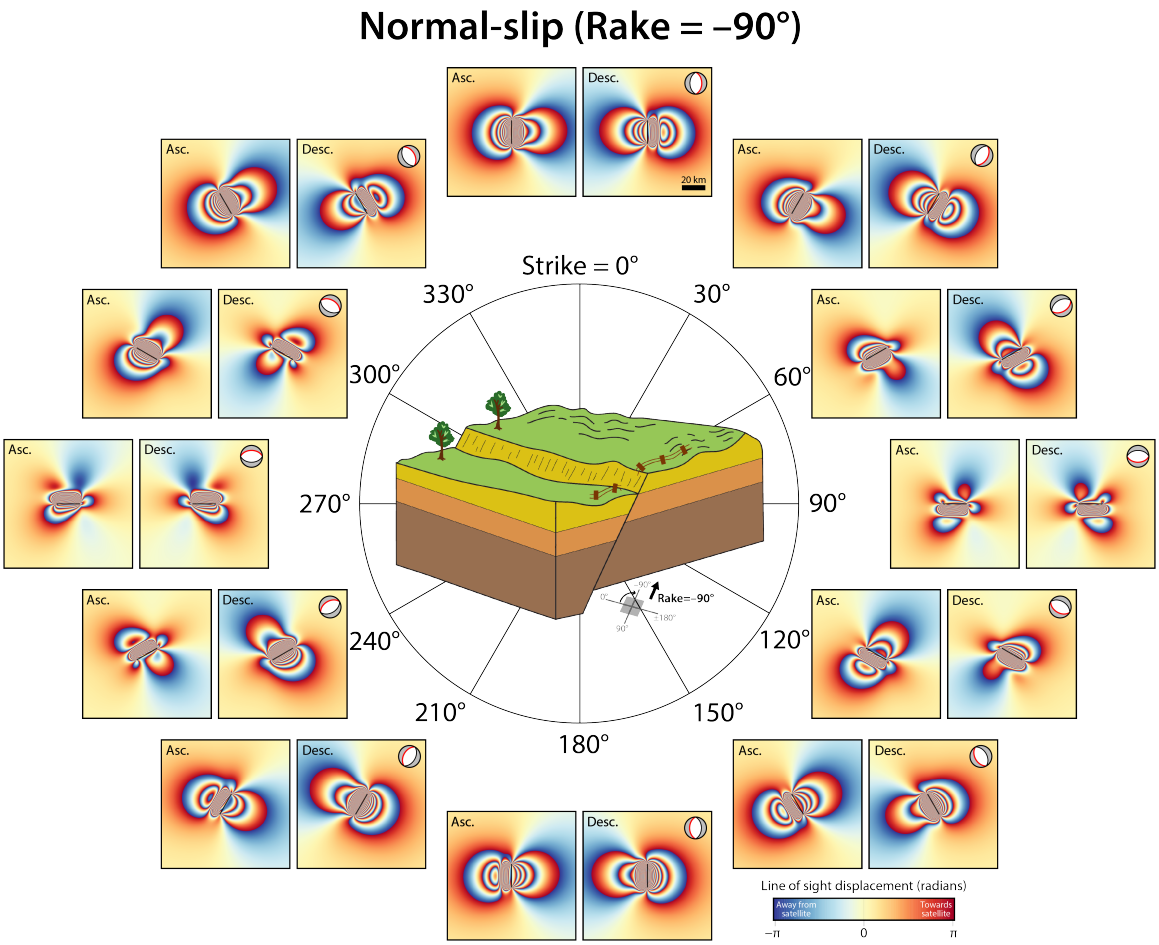
a InSAR forward model wrapped interferograms for variably striking left-lateral strike-slip earthquakes (dip 90°, rake 0°).



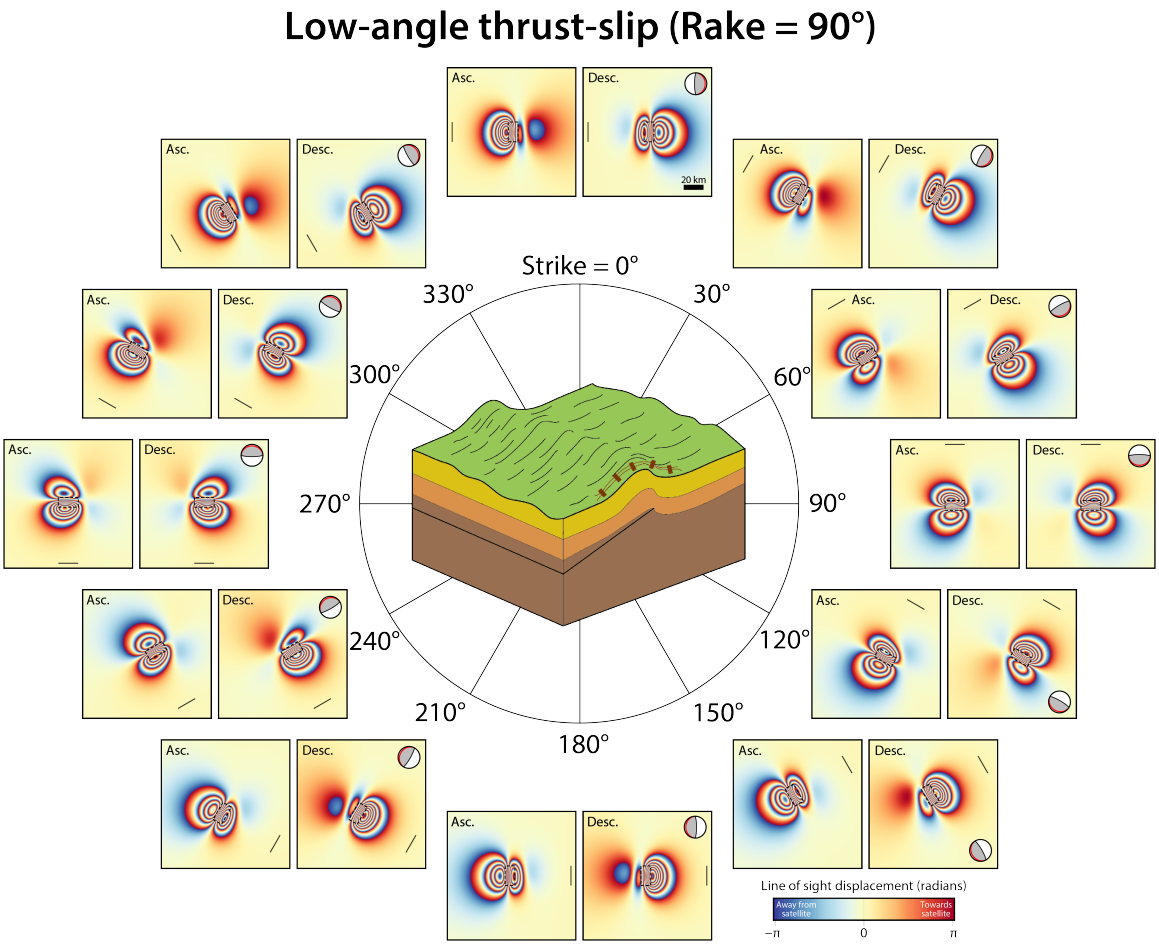
b InSAR forward model wrapped interferograms for variably striking right-lateral strike-slip earthquakes (dip 90°, rake 180°).



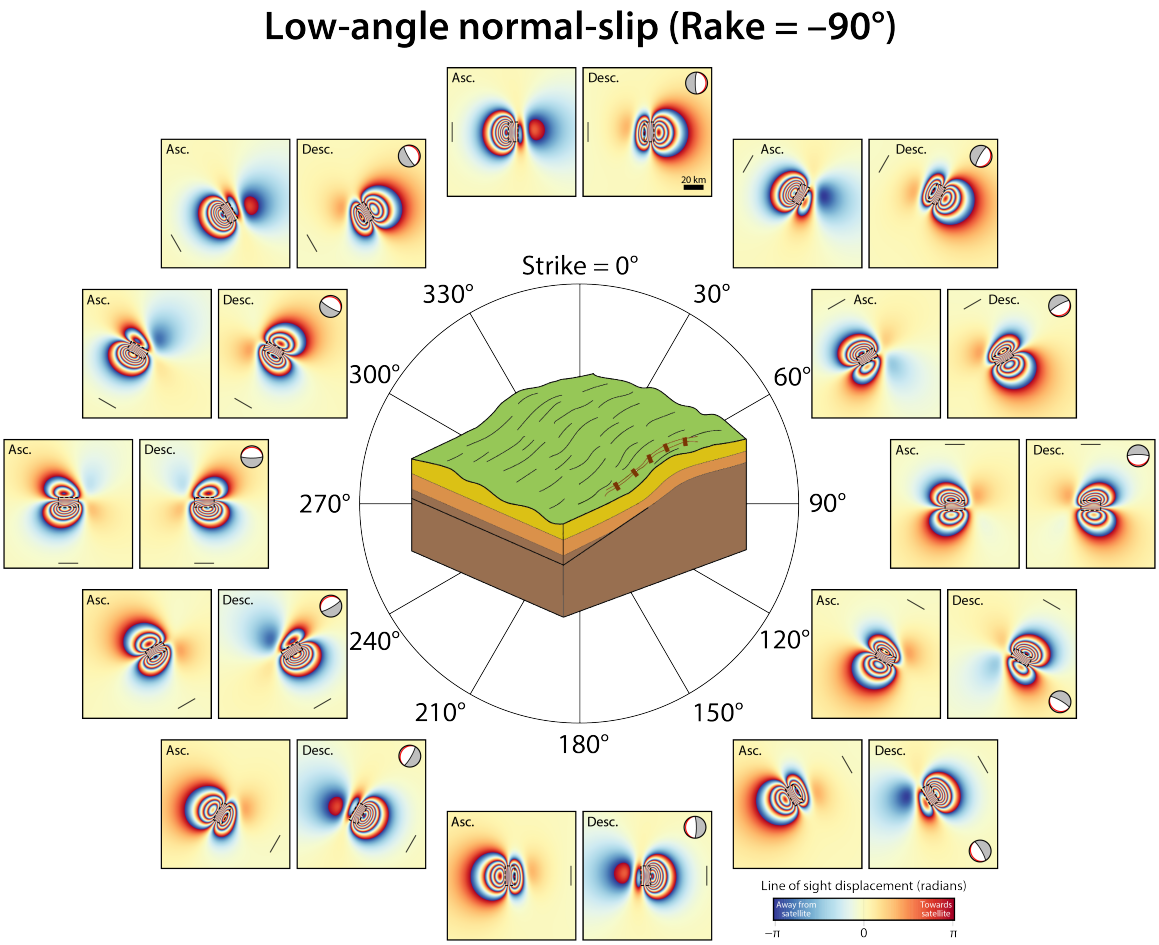
c InSAR forward model wrapped interferograms for variably striking reverse faulting earthquakes (dip 45°, rake 90°).



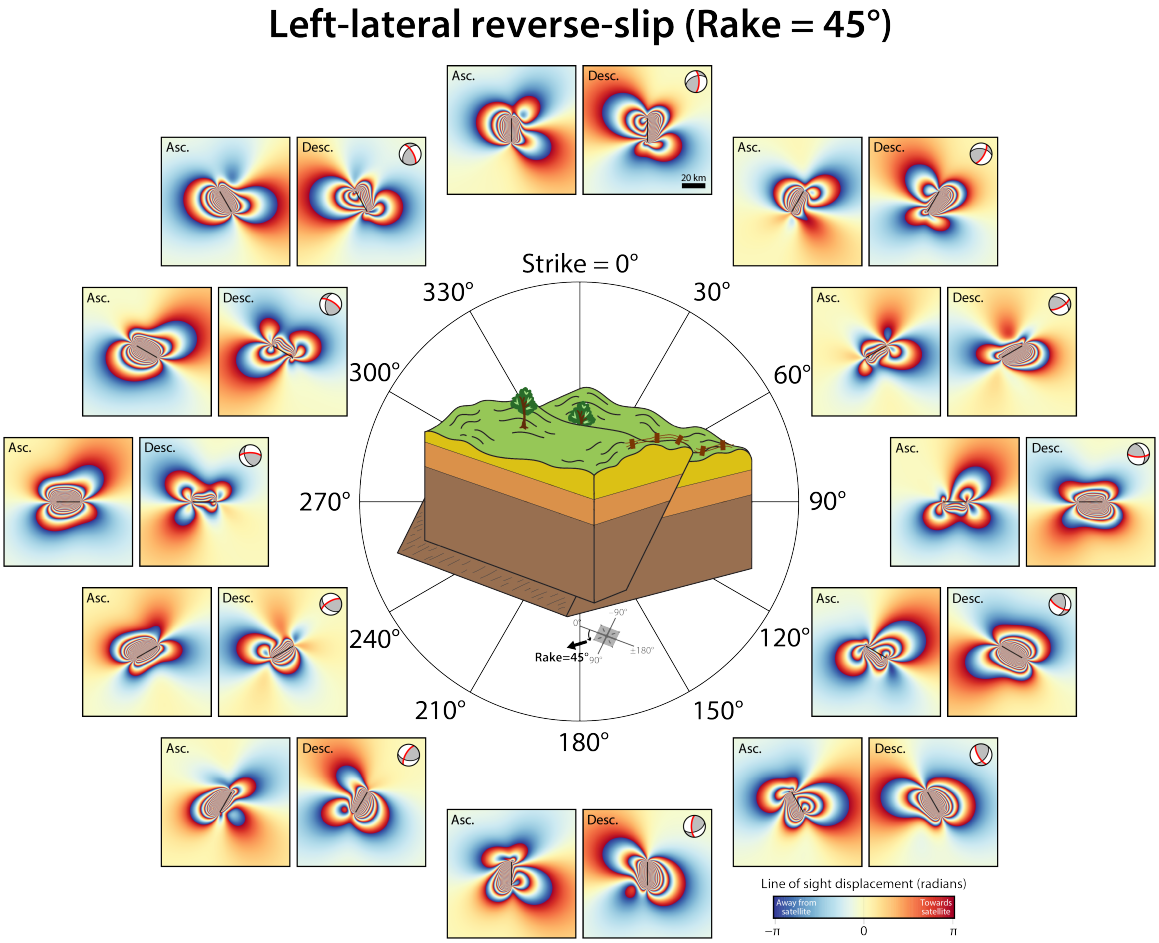
d InSAR forward model wrapped interferograms for variably striking normal faulting earthquakes (dip 45°, rake −90°).



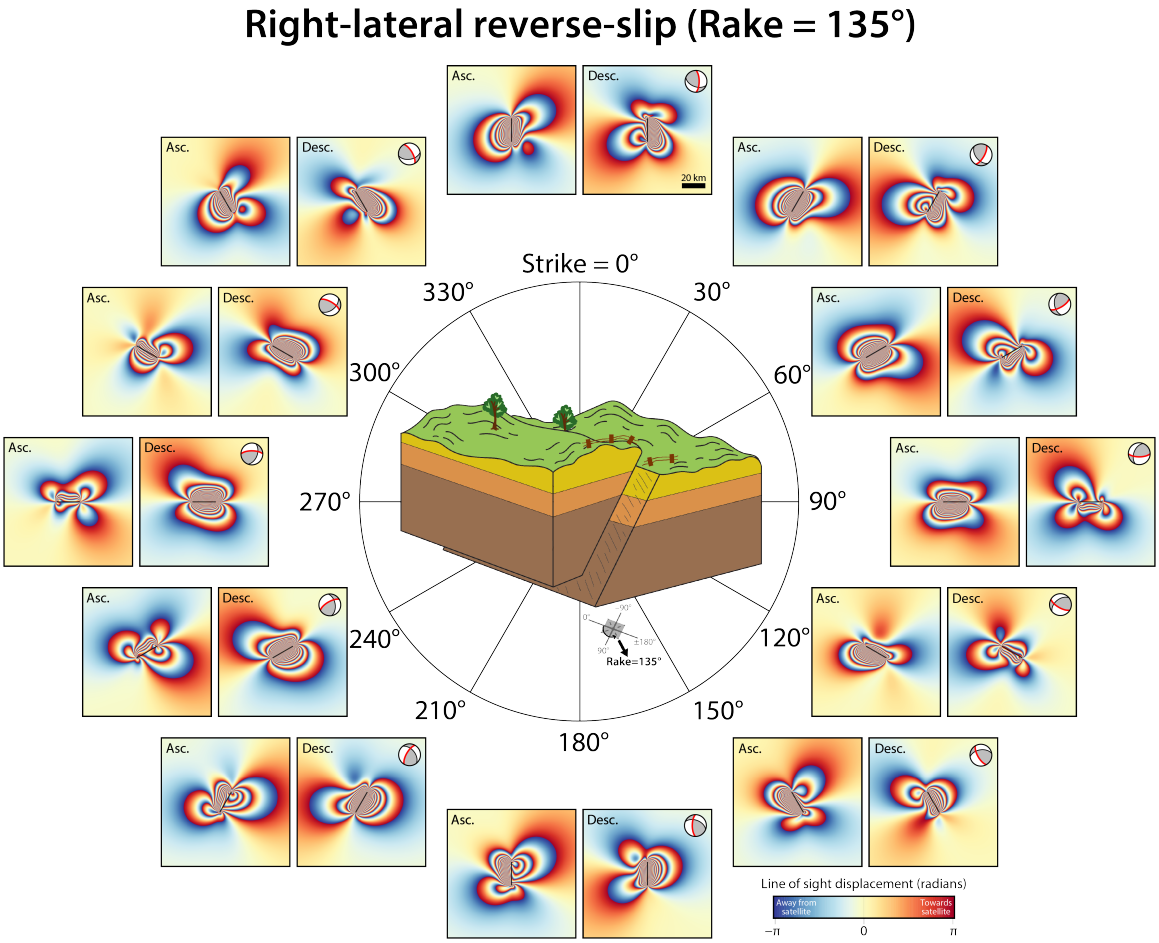
e InSAR forward model wrapped interferograms for variably striking, buried, low-angle thrust faulting earthquakes (dip 10°, rake 90°).



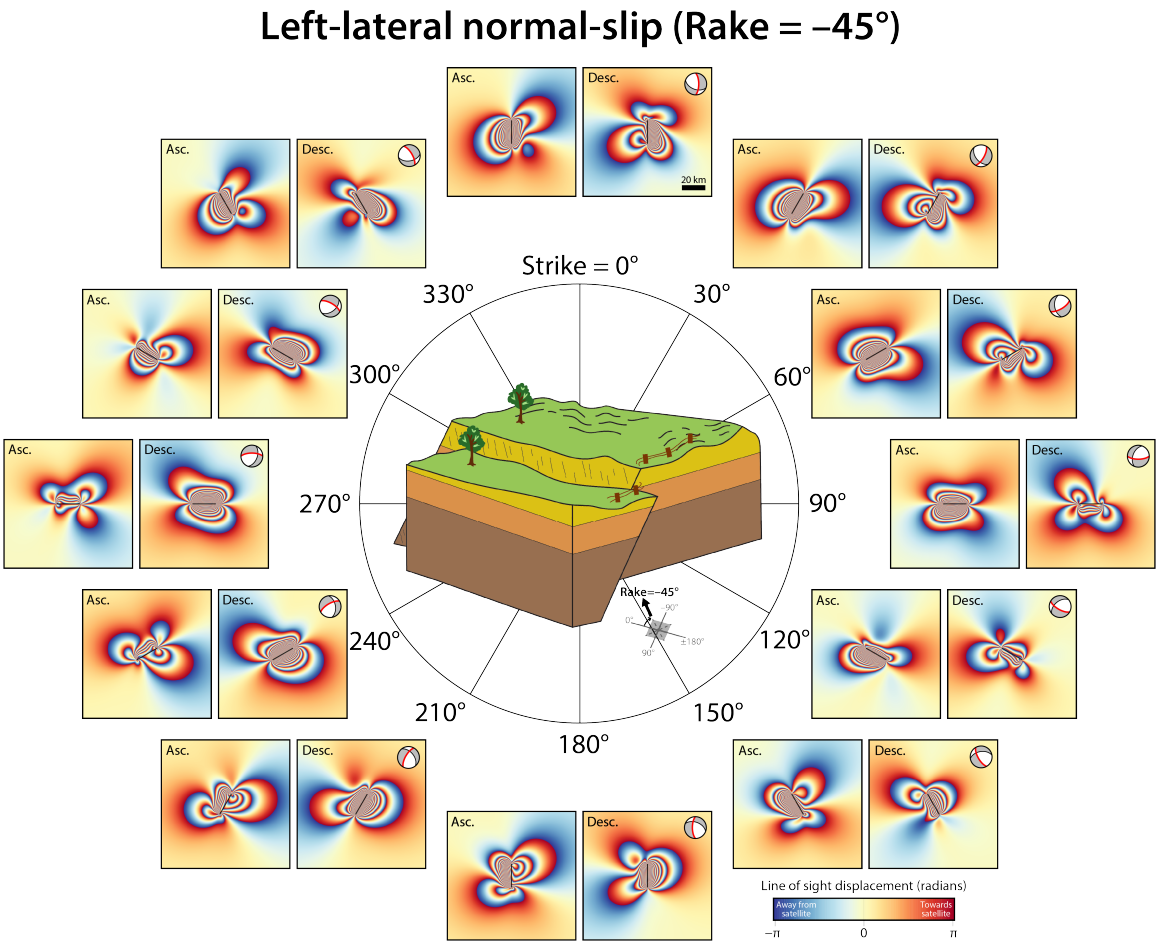
f InSAR forward model wrapped interferograms for variably striking, buried, low-angle normal faulting earthquakes (dip 10°, rake −90°).



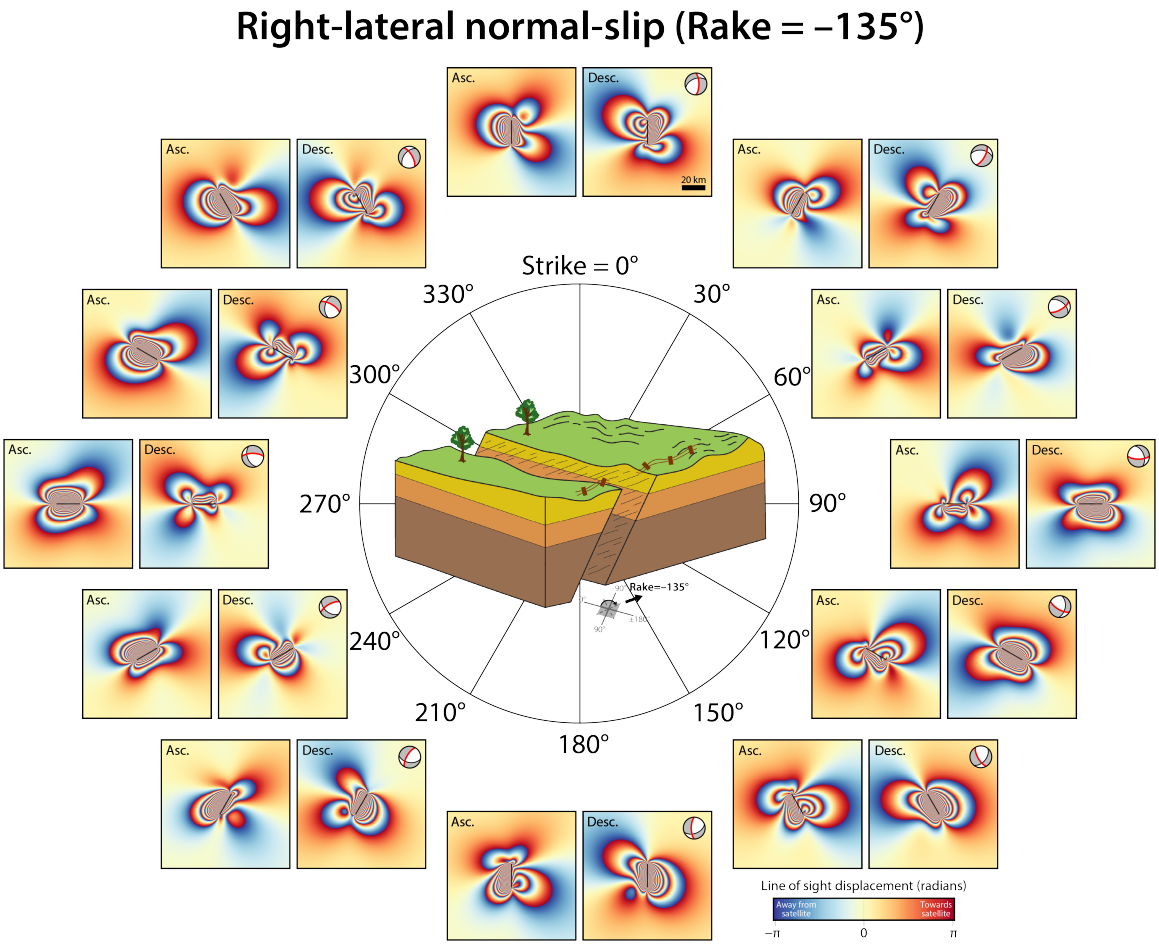
g InSAR forward model wrapped interferograms for variably striking, left-lateral/reverse, oblique-slip earthquakes (dip = 67.5°, rake = 45°).



h InSAR forward model wrapped interferograms for variably striking, right-lateral/reverse, oblique-slip earthquakes (dip = 67.5°, rake = 135°).



i InSAR forward model wrapped interferograms for variably striking, left-lateral/normal, oblique-slip earthquakes (dip = 67.5°, rake = −45°).



j InSAR forward model wrapped interferograms for variably striking, right-lateral/normal, oblique-slip earthquakes (dip = 67.5°, rake = −135°).

2.7.1 Strike-slip Earthquakes

Interferograms for left-lateral and right-lateral strike-slip earthquakes are plotted radially by fault strike in Figures 2.3a–2.3b. Because our model strike-slip faults are vertical, interferograms for strikes 0°–150° are identical to those for strikes 180°–330°, but we include the duplication for consistency with later figures for dipping geometries. The left- and right-lateral interferograms mimic one another, but with the sense of displacement (whether toward or away from the satellite) switched.

As described in Section 2.5, strike-slip earthquakes generate the simplest patterns of deformation when oriented E–W. Here, there is a broad, positive deformation lobe on one side of the fault mirrored by a broad, negative lobe on the other side, together giving rise to a distinctive butterfly shape. The ascending and descending interferograms give rise to similar patterns but with fully opposing senses of displacement, a diagnostic characteristic of dominantly strike-slip earthquakes. As the faulting rotates away from E–W to WNW or ENE, the lobes become skewed in opposite directions along strike, with the distortion more pronounced in whichever of the ascending or descending interferograms looks more obliquely to fault strike. At NNW and NNE orientations, a second, smaller pair of lobes emerges at the opposite fault ends to the larger pair. This four-leaf clover pattern becomes more evident still when the fault strikes N–S, with lobes on one side of the fault broader but of lower amplitude than those on the other, for the reasons explained in Section 2.5. The northern two lobes have the same displacement sense as one another, and the southern two lobes are both of the opposite sense. Merging of the northern two lobes across the strike of the fault, and of the southern two lobes, can therefore give rise to far-field fringes that closely resemble those of a conjugate strike-slip fault (for example, compare far-field deformation for the N–S-trending left-lateral earthquake in Figure 2.3a with that for the E–W-trending right-lateral earthquake in figure 2.3b). Thus, in the absence of positive identification of fault strike (for example due to decorrelation or fault burial), it can be difficult to discriminate the fault plane from the auxiliary plane for strike-slip earthquakes (e.g., Biggs et al., 2006).

2.7.2 Moderate Angle Dip-slip Earthquakes

For reverse and normal faulting earthquakes at moderate dip angles (we use 45° in our models), 3-D deformation fields will comprise roughly equal parts horizontal and vertical displacement. Horizontal deformation is dominated by displacement perpendicular to the fault trace: towards the fault in the reverse case (reflecting shortening) and away

from it in the normal case (reflecting extension). Adjacent to the fault center, horizontal displacement is only towards or away from the fault, while around the fault ends, there are also smaller fault-parallel components. While InSAR will always be sensitive to the vertical component, how much of the horizontal component is also captured will thus depend on the fault orientation, which governs the balance of visible E–W and invisible N–S deformation.

Interferograms for earthquakes involving reverse faulting (rake = 90°) and normal faulting (rake = −90°) are plotted radially by strike in Figures 2.3c and 2.3d, respectively. These sets of interferograms are exact copies of one another but with the sense of displacement flipped. All of these interferograms exhibit a condensed, central deformation lobe directly over the dipping fault, in which strong vertical deformation manifests in both ascending and descending interferograms as displacement toward the satellite in the reverse case and displacement away from it in the normal case. In real interferograms, this central area is often substantially decorrelated by the close fringe spacing (e.g., Wright et al., 1999).

The central area is surrounded by variable numbers of broader, longer wavelength deformation lobes. Dip slip earthquakes at northerly and southerly strikes have the simplest far-field lobe patterns, with two roughly equally-sized lobes extending W and E of the fault in both ascending and descending interferograms. These far-field lobes are dominated by horizontal motion toward the fault in the reverse case (Figures 2.3c) and away from the the fault in the normal case (Figures 2.3d), explaining why they exhibit the opposite displacement sense at ascending and descending viewing angles. For example, for reverse faulting earthquakes, the western lobe is negative in the ascending interferogram and positive in the descending intergerogram, and the eastern lobe is positive in the ascending interferogram but negative in the descending interferogram. Together, the broad far field lobes either side of a condensed central lobe somewhat resemble a bow-tie.

At more easterly or westerly fault strikes, the InSAR fringe patterns become more complicated. While the condensed, central deformation patterns above the fault planes remain, the broader, far field lobes characteristic of N–S dip-slip faulting become much less pronounced. This reflects that as fault strike approaches E or W, far field displacement towards the reverse fault and away from the normal fault is manifest more and more as N–S deformation, to which InSAR is insensitive. One or more smaller lobes appear around either end of the condensed central patch, reflecting localized E–W deformation around the tips of the fault. These produce a complicated four or five lobed deformation pattern, somewhat resembling a balloon animal. A diagnostic characteristic of E- and

W-striking dip slip earthquakes is that the ascending and descending interferograms are mirror images of one another, about an axis perpendicular to the fault center.

Another notable feature of the dip-slip earthquake interferograms is the similarity in fringe patterns between conjugate fault pairs at 90° angles to one another, but striking in similar azimuths. This explains why it is often difficult to differentiate the fault and auxiliary planes in real dip slip earthquakes, especially when faulting is buried (Zhang et al., 2021). Solving this ambiguity may require independent constraints on dip direction, such as from a relocated hypocenter (Karasözen et al., 2018), an alignment of one nodal plane with prominent fault traces (Elliott et al., 2011; Nissen et al., 2022), or triggering relations with other nearby earthquakes (Lohman and Barnhart, 2010).

2.7.3 Low-angle Thrust and Normal Faulting earthquakes

To mimic InSAR signals for thrust and normal faulting earthquakes on low-angle décollements or detachments, we use a model fault dipping at 10° and centered at around 10 km depth. The resulting 3-D deformation is dominated by horizontal displacements at right angles to fault strike; the interferograms will therefore capture this best at northerly or southerly fault strikes. InSAR is also sensitive to smaller amounts of uplift or subsidence, particularly that centered directly above the thrust or normal slip plane.

Figures 2.3e and 2.3f show our model low-angle thrust and normal faulting interferograms, plotted radially by strike. The two sets of interferograms are of the exact opposite displacement sense to one another. Each interferogram contains two or three main lobes arranged above and around the fault. A diagnostic feature at northerly or southerly strikes is that the largest and most prominent deformation lobe appears on the opposite side of the fault in the ascending interferogram to the descending one. As the fault rotates away from N or S, a second deformation lobe on the opposite side of the fault grows in prominence and a third lobe may emerge at one of the two viewing geometries. For E- and W-striking faults, the prominent negative and positive far-field lobes are roughly evenly sized, and in the same arrangement (one on each side of the fault) in the ascending and descending interferograms; although the lobe directly above the fault plane still contains the most fringes. Faint lobes appear to the East (ascending) and West (descending), forming a four-leaf clover pattern. As with the moderate dip-slip earthquakes, when the strike is exactly E or W, the ascending and descending interferograms are mirror images of one another reflected about a N–S axis through the fault center.

2.7.4 Oblique-slip Earthquakes

We model four types of oblique-slip earthquake, each one dipping at 67.5°, in other words intermediary between our vertical strike-slip and 45° dip-slip faults. The resulting interferograms (Figures 2.3g–2.3j) thus combine aspects of those presented earlier for strike-slip and moderate dip-slip earthquakes. We acknowledge that other types of oblique-slip earthquake are possible, including ones involving lower angle fault planes (e.g., Nissen et al., 2019; Cheloni et al., 2024), and that these will exhibit different deformation patterns to the models presented here.

The interferograms exhibit up to five main deformation lobes, reflecting the complex combinations of vertical and lateral displacements that typify oblique-slip earthquakes (Figures 2.3g–2.3j). However, at certain fault strike and radar illumination angles, simpler butterfly-shaped fringe patterns emerge. For example, left-lateral/reverse oblique-slip faults that strike W produce butterfly lobes in the ascending interferogram, while those that strike E produce butterfly lobes in the descending interferogram (Figure 2.3g). These happen to be the fault strike and radar illumination angles at which vertical and E–W deformation components match one another in both location and displacement sense, thus avoiding complicated interference patterns between positive vertical and negative horizontal displacements, and vice versa. However, whereas for ∼E–W vertical strike-slip faults the butterfly patterns are produced simultaneously in the ascending and descending interferograms (Figures 2.3a and 2.3b), here they are produced in just one of the two. This appears to be a diagnostic characteristic of oblique-slip earthquakes.

2.7.5 Lookbook Summary

Figure 2.4 summarizes the deformation patterns of our lookbook earthquakes in a single, simplified chart. We can make a few generalizations from this. Strike-slip earthquakes exhibit butterfly shapes when striking E–W, four-leaf clover shapes when striking N–S, and distorted intermediaries at angled orientations. The lobes have the opposite sense of displacement in the ascending and descending interferograms.

Moderate angle dip-slip earthquakes that strike N or S generate a two-lobed ∞ shaped deformation pattern at one viewing angle and a three-lobed bow-tie pattern at the other. There is condensed deformation of consistent displacement sense directly above the fault (in the hanging wall), but the far field lobes are of the opposite displacement sense in the ascending and descending interferograms. Those that strike E–W are multi-lobed, resembling balloon model animal shapes, and the ascending and descending interferograms are

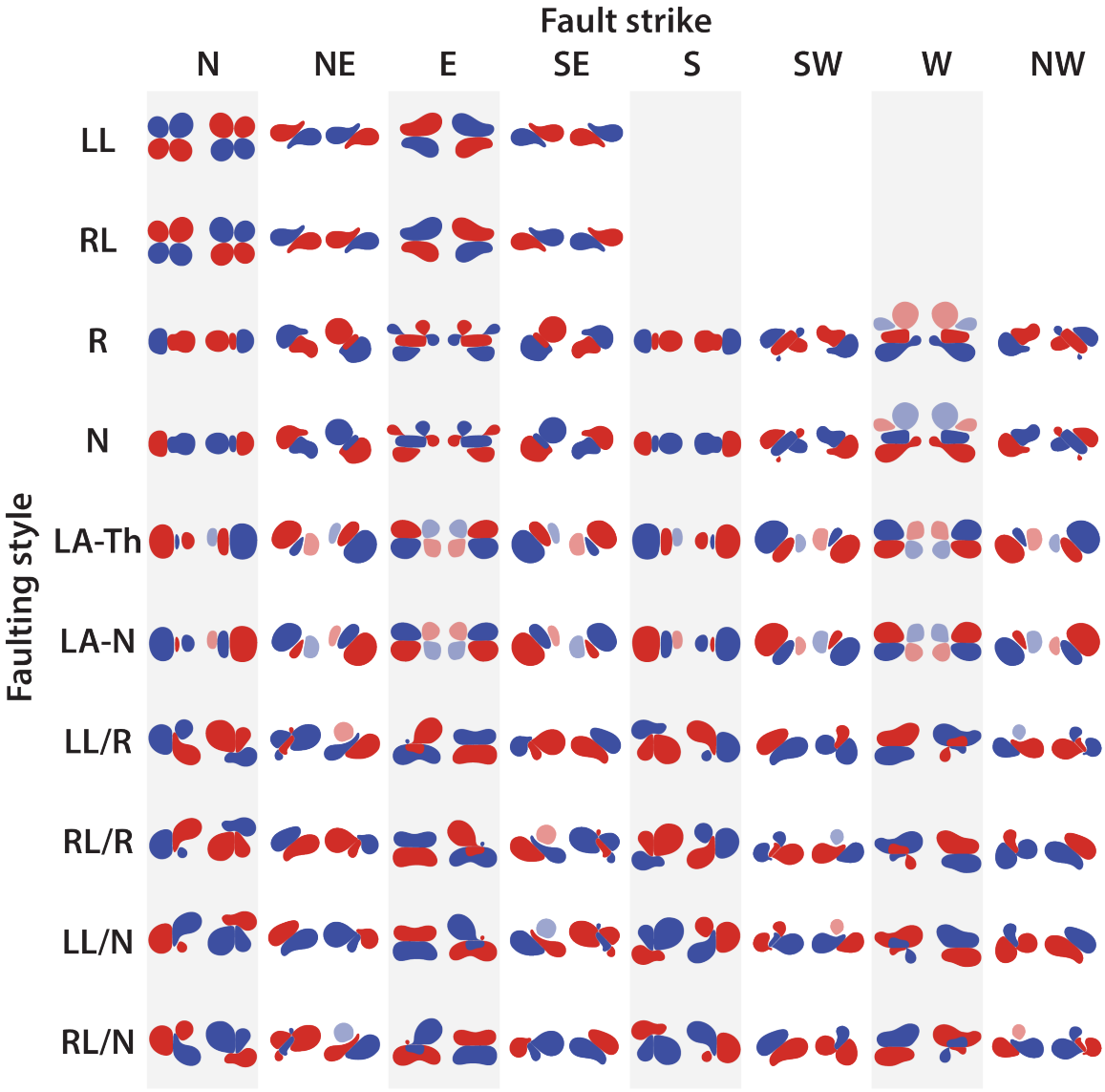


Figure 2.4: A chart summarizing InSAR deformation lobe patterns by earthquake fault type and orientation. Rows represent the ten earthquake fault types (LL = left-lateral, RL = right-lateral, R = reverse, N = normal, LA = low angle, Th = thrust) and columns show eight strikes at 45° increments from North. For each combination of earthquake type and strike, we plot simplified ascending track (left) and descending track (right) lobe patterns, with red and blue indicating motion towards or away from the satellite, respectively. Faded colours are used where lobes are prominent in our wrapped interferograms, but contain less than a full fringe cycle. Because our model strike-slip earthquakes are on vertical faults, deformation at strikes of S, SW, W and NW mimics that at strikes of N, NE, E and SE, respectively.

mirror images of one another about an axis perpendicular to the fault center.

Buried, low-angle thrust and normal earthquakes generate simpler patterns in which a single large lobe is characteristic of northerly and southerly strikes (located on the opposite side of the fault in ascending and descending interferograms), and two main lobes are characteristic of westerly and easterly strikes (with mirror imaging as for their moderate angle equivalents).

Lastly, a diagnostic characteristic of oblique-slip earthquakes is the stark difference in lobe patterns between the ascending and descending interferograms, reflecting the complex interplay between vertical and horizontal displacements as resolved by the differing radar illumination angles.

2.8 Real Earthquake Comparisons

To demonstrate the application of our InSAR lookbook, we now compare our model interferograms with those of sixteen, real world earthquakes (Table 2.2). These were selected firstly because they all display clear InSAR fringe patterns for comparison with our synthetic interferograms, and secondly because they span a wide range of mechanisms and orientations. Some of the events have published InSAR fault slip models, which we discuss later in this section. Most of the interferograms were obtained from the COMET LiCSAR portal (Lazecký et al., 2020; Watson et al., 2023), which provides Sentinel-1 interferograms of large earthquakes since 2019 (see Data and Resources); for two of the earthquakes we obtained them from published studies (Funning et al., 2005; Kim and Han, 2023). We scaled the real earthquake interferograms to match our lookbook model interferograms in size on the page, and applied the same LOS displacement convention (see Section 2.6.1). Therefore, the real earthquake deformation lobes may differ from the lookbook comparison models in both size and amplitude, according to the earthquake magnitude and depth. However, as described in Section 2.6.3, the purpose is to compare the general lobe patterns taking into account their LOS displacement sense.

2.8.1 Strike-slip Examples

The 2003 M_w 6.6 Bam, Iran earthquake generated the four-leaf clover deformation pattern characteristic of N–S right-lateral strike-slip faulting (Figure 2.5a). Though the earthquake occurred in a region of previously sparse seismicity, it was also directly along strike from the major, N–S Gowk right-lateral fault system (Walker and Jackson, 2002), so the fault

Table 2.2: Real earthquakes used as lookbook comparisons. Dates of earthquakes and ascending and descending InSAR acquisitions are listed as dd.mm.yr in Coordinated Universal Time (UTC). Fault refers to our interpretation from the lookbook, given as strike followed by kinematics (LL = left-lateral, RL = right-lateral); question marks indicate where the conjugate nodal plane could equally be the fault. We know of no examples of InSAR observations of earthquakes on low-angle normal faults. Unless noted otherwise by asterisks, interferograms were obtained from the COMET LiCSAR Sentinel-1 database (see Data and Resources).

Earthquake	Date	M_w	Fault	Ascending	Descending
Strike-slip (Figure 2.5)					
Bam, Iran	26.12.03	6.6	N, RL	16.11.03–25.01.04*	03.12.03–11.02.04*
Menyuan, China	07.01.22	6.7	ESE, LL	05.01.22–17.01.22	29.12.21–10.01.22
Petrinja, Croatia	29.12.20	6.4	NW, RL	18.12.20–30.12.20	17.12.20–04.01.21
Murghob, Tajikistan	23.02.23	6.9	NNE?, LL	03.02.23–23.03.23	21.02.23–05.03.23
Dip-slip (Figure 2.6)					
Hotan, China	25.06.20	6.3	S?, Normal	22.06.20–04.07.20	17.06.20–29.06.20
Nima, China	22.07.20	6.3	NNE?, Normal	18.07.20–30.07.20	02.07.20–26.07.20
Thessaly, Greece	03.03.21	6.3, 6.0†	NW, Normal	25.02.21–09.03.21	03.03.21–09.03.21
Herāt, Afghanistan	07.10.23	6.3, 6.3	W, Reverse	25.09.23–07.10.23	26.09.23–08.10.23
Low-angle thrust (Figure 2.7)					
Jiashi, China	19.01.20	6.0	W, Thrust	16.01.20–28.01.20	10.01.20–22.01.20
Hormozgan, Iran	14.11.21	6.0, 6.4	E, Thrust	13.11.21–25.11.21	09.11.21–03.12.21
Ganaveh, Iran	18.04.21	5.8	NW, Thrust	02.04.21–20.05.21	10.04.21–22.04.21
Marrakesh-Safi, Morocco	08.09.23	6.8	ENE?, Thrust	03.09.23–15.09.23	04.09.23–16.09.23
Oblique slip (Figure 2.8)					
Mindanao, Philippines	15.12.19	6.8	NW, LL/Reverse	13.12.19–25.12.19	13.12.19–19.12.19
Khövsgöl, Mongolia	11.01.21	6.7	NNW, RL/Normal	21.06.20–20.06.21**	07.01.21–19.01.21
Wushi, China	22.01.24	7.0	WSW, LL/Reverse	14.01.24–26.01.24	13.01.24–25.01.24
Monte Cristo Range, USA	15.05.20	6.5	ENE, LL/Normal	11.05.20–29.05.20	11.05.20–29.05.20

*Both Envisat interferograms (half-wavelength of 2.77 cm) are from Funning et al. (2005).
**The ALOS-2 ascending interferogram (half-wavelength of ∼12 cm) is from Kim and Han (2023).
†The second earthquake occurred on 04.03.21.

style and orientation were not surprising. The interferograms also display a narrow, N–S trend of decorrelation which marks a surface rupture (Funning et al., 2005). A dense fringe lobe on the east side of the surface rupture and in between the larger deformation lobes, a feature not evident in our simpler model, partly reflects right-lateral/reverse oblique slip on a shallow splay off the main right-lateral fault (Funning et al., 2005).

The 2022 M_w 6.7 Menyuan, China earthquake in the Qilian Shan mountains is characterized by butterfly-shaped deformation lobes that are symmetric in the descending interferogram but skewed in the ascending one, closely mimicking our lookbook interferograms for WNW–ESE, left-lateral strike-slip earthquakes (Figure 2.5b). The earthquake

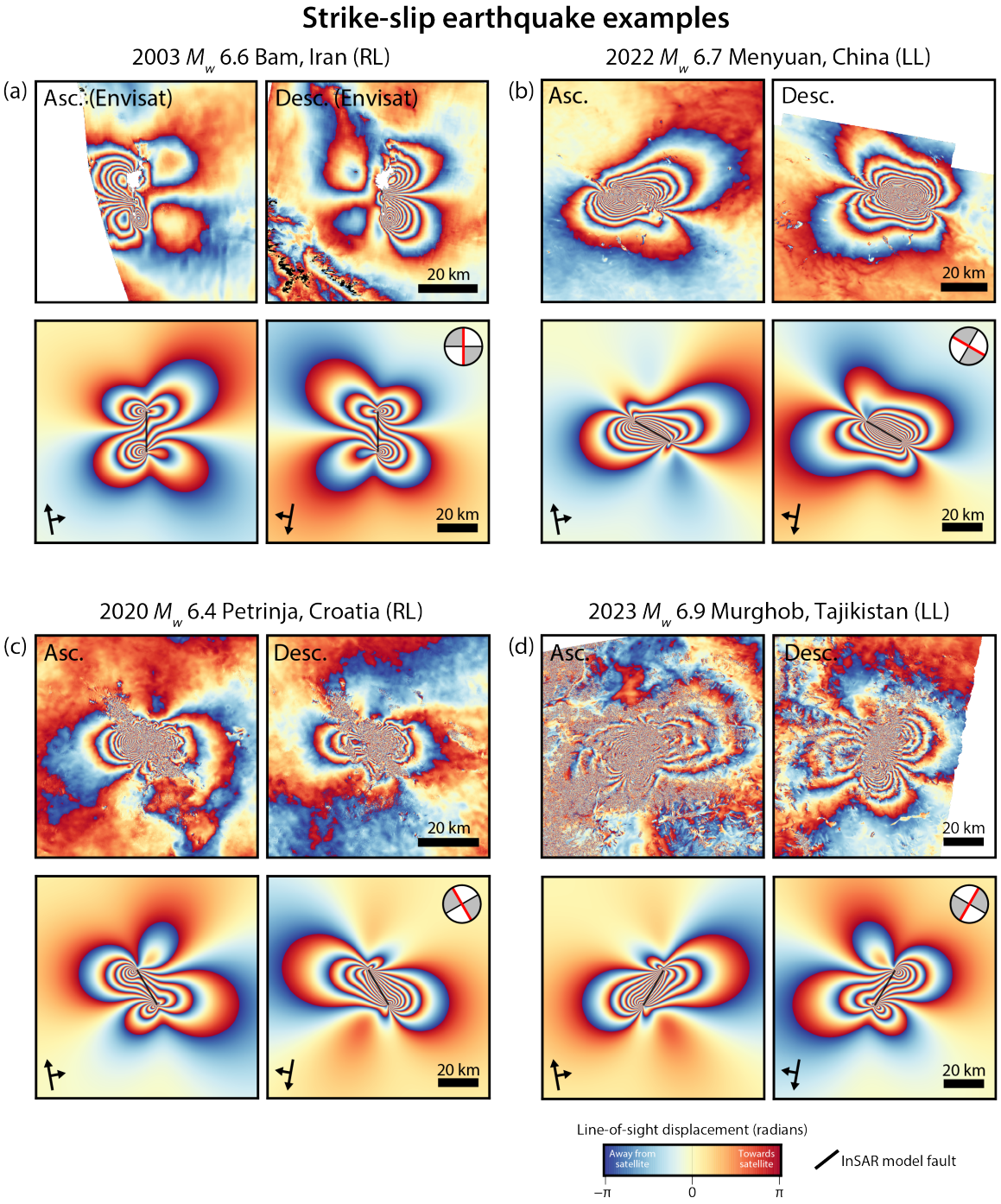


Figure 2.5: Interferograms comparing real strike-slip earthquakes (top rows) and our lookbook models (bottom rows) of the (a) 2003 M_w 6.6 Bam, Iran, (b) 2022 M_w 6.7 Menyuan, China, (c) 2020 M_w 6.4 Petrinja, Croatia, and (d) 2023 M_w 6.9 Murghob, Tajikistan earthquakes (see Table 2.2 for earthquake details). Left and right columns are ascending and descending interferograms, respectively. For the Bam earthquake, the Envisat interferograms half-wavelength is 2.77 cm (panel a, top row) similar to our models. Thick black lines indicate our model faults and conjugate arrows denote the satellite azimuth and line-of-sight. The beach ball is the earthquake focal mechanism of our InSAR model, with the fault plane outlined in red.

epicenter lies on the well known, ESE-trending, left-lateral Haiyuan fault (Li et al., 2023), so the relevant lookbook model would have been easily anticipated. The pattern arises because the Haiyuan fault is exactly perpendicular to the descending look vector but slightly oblique to the ascending one.

The 2020 M_w 6.4 Petrinja, Croatia earthquake differs from the earlier examples in that it was the first event of $M_w \geq 6.0$ in its region since modern records began (USGS NEIC). An elongate zone of decorrelation masks details of the near-field deformation but hints at an approximately NW–SE-trending rupture (Figure 2.5c). Without an expectation for the fault kinematics, lookbook users could instead utilize our fixed strike models for 150°- or 330°-striking faults (Figures 2.10f and 2.10l) to find the closest rupture mechanism. The observed pattern duly matches that for a rake of 180°, indicating a right-lateral strike-slip earthquake, consistent with both rapid moment tensor solutions and subsequently published InSAR slip models (Xiong et al., 2022).

The 2023 M_w 6.9 Murghob, Tajikistan earthquake in the Pamir mountains exhibits a skewed butterfly fringe pattern in the ascending interferogram and a four-leaf clover in the descending one, closely resembling our model interferograms for a NNE–SSW left-lateral earthquake (Figures 2.5d). The NNE trend is hinted at in a zone of decorrelation, though coherence is rather poor across the entire interferogram, likely owing to steep topography and/or snow cover. Published InSAR slip models confirm our inference of NNE-trending left-lateral faulting (Liu et al., 2024; Shi et al., 2023).

2.8.2 Dip-slip Examples

The 2020 M_w 6.3 Hotan, China earthquake occurred in the northwestern Tibetan plateau, a region of widespread ∼E–W-directed extension (e.g., Fang et al., 2024). There is some disagreement on its source mechanism, with the USGS W-phase model suggesting pure normal slip on a NNE- or SSW-striking plane, and the Global Centroid Moment Tensor (GCMT) catalog indicating oblique slip on a N-striking right-lateral/normal fault or a SW-striking left-lateral/normal fault. This is a good test of whether the lookbook can resolve such an ambiguity. We find that the closest lookbook solutions to the USGS and GCMT nodal planes (Figures 2.3d, 2.3i, 2.3j) are a poor match to the observed InSAR deformation (Figure 2.6a). Instead, our lookbook interferograms for a S-striking normal fault seem to match the data best. This is borne out by published InSAR slip models with strike 186°, a few degrees off our lookbook value (Zhu et al., 2021; Yu et al., 2021). However, N-striking normal faulting will produce a rather similar fringe pattern and, with the condensed cen-

tral lobe and parts of the western far-field lobe significantly decorrelated, we consider the fault and auxiliary planes to be ambiguous in this case.

The 2020 M_w 6.3 Nima, China earthquake in the central Tibetan plateau illustrates a similar deformation pattern, with a dense, near-field fringe ellipse in both interferograms, and two (ascending) or three (descending) deformation lobes in total (Figure 2.6b). Our NNE-striking normal fault model (strike, dip, and rake of 30°, 45°, and $-90°$) reproduces the data best, but a SSW-striking normal fault is also a reasonably close match. The preferred mechanism compares well with a published InSAR inversion that yields strike, dip and rake of 28°, 48°, and $-87°$ (Li et al., 2021a). Other source inversions involve additional geometric complexities beyond the scope of our lookbook. For example, Liu et al. (2023) propose a three-segmented fault model and Gao et al. (2022) suggest an S-shape geometry with varying strike and dip angles.

The 2021 M_w 6.3 and 6.0 Thessaly, Greece earthquake doublet exhibits a more convoluted fringe pattern than the Tibetan normal faulting events described above, owing in part to the fact that its fault strike is deviating away from N–S (Figure 2.6c). Both interferograms contain a condensed, NW-trending fringe ellipse moving away from the satellite, surrounded by two (ascending) or 3–4 (descending) smaller deformation lobes. The signal compares quite well to our lookbook interferograms for a WNW-striking normal faulting earthquake, though the far-field lobes appear somewhat distorted. This, and the elongated condensed fringes, likely owe to the involvement of two along-strike segments separated by a fault bend and stepover, as revealed by published InSAR models (Yang et al., 2022b).

The October 7 2023 Herāt doublet in the Paropamisus mountains of NW Afghanistan involved a pair of M_w 6.3 earthquakes ∼30 minutes apart, and was followed by two more M_w 6.3 events on October 11 and 15 which are not captured in the interferograms presented here. USGS and GCMT moment tensors for the October 7 earthquakes support reverse faulting striking either approximately eastwards and dipping ∼60° S, or approximately westwards and dipping 30° N. Both interferograms contain an elongate (E–W) lobe of deformation towards the satellites in the north, and a broad but subtle lobe of deformation away from the satellites in the south, consistent with a W-striking, N-dipping reverse fault (Figures 2.6d). Upon closer inspection, the ascending and descending interferograms also exhibit small 'tear-drop' lobes at the eastern and western fault tips, respectively, a pattern that closely matches our lookbook summary model in Figure 2.4.

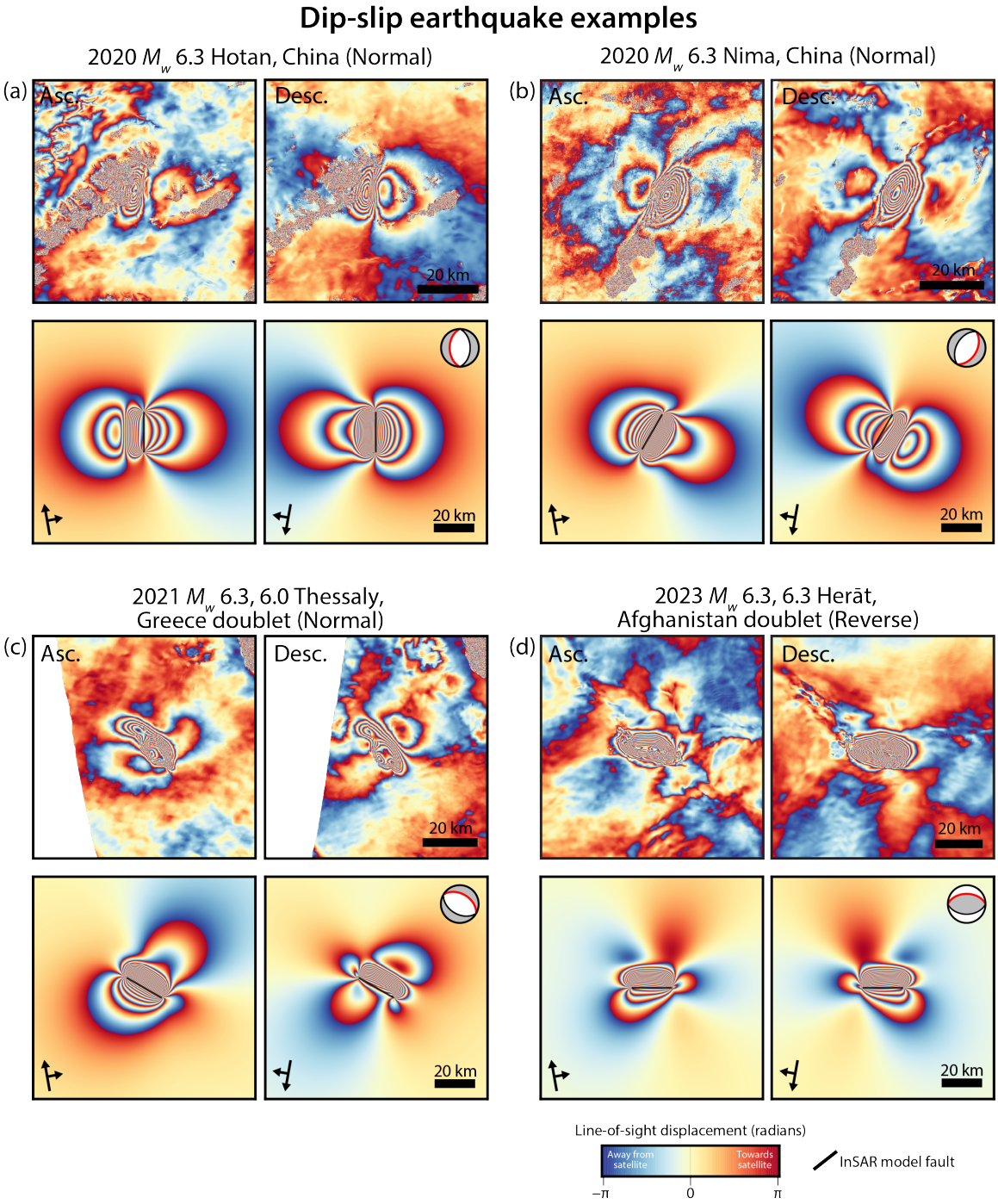


Figure 2.6: Interferograms comparing real dip-slip earthquakes (top rows) and our look-book models (bottom rows) of the (a) 2020 M_w 6.3 Hotan, China, (b) 2020 M_w 6.3 Nima, China, (c) 2021 M_w 6.3, 6.0 Thessaly, Greece (doublet), and (d) 2023 M_w 6.3, 6.3 Herāt, Afghanistan (doublet) earthquakes (see Table 2.2 for earthquake details). Left and right columns are ascending and descending interferograms, respectively. Thick black lines indicate our model faults and conjugate arrows denote the satellite azimuth and line-of-sight. The beach ball is the earthquake focal mechanism of our InSAR model, with the fault plane outlined in red.

2.8.3 Low-angle Thrust Examples

The 2020 M_w 6.0 Jiashi, China earthquake in the southwestern Tian Shan exhibits a pair of elongate, E–W-trending deformation lobes in both ascending and descending interferograms. The northern lobes contain displacements away from the satellite and the southern lobes contain about double those displacements towards the satellite (Figure 2.7a). This pattern is characteristic of a W-striking (N-dipping) low-angle thrust fault centered between the two lobes and projecting to the surface some distance to the South. The elongate fringe pattern reflects that the real earthquake involved a much greater length-to-width ratio than our model value of 2, as confirmed by inverse modelling and aftershock relocations (Wang et al., 2022).

The 2021 Hormozgan, Iran doublet in the frontal Zagros mountains involved M_w 6.0 and 6.4 earthquakes about 90 seconds apart, which cannot be separated by InSAR and whose deformation patterns overlap and merge. Ascending and descending interferograms each exhibit a simple two-lobed shape, with the opposite displacement sense to the Jiashi example: the northern lobes contain displacements towards the satellite and the southern lobes contain less than half those displacements away from the satellite (Figure 2.7b). This pattern is characteristic of an E-striking (S-dipping) low-angle thrust fault. However, North-side-up dip slip on the conjugate, subvertical, W-striking nodal plane (a configuration at odds with Andersonian mechanics and beyond the scope of our lookbook) would generate a similar surface deformation pattern, and cannot be ruled out on the basis of InSAR alone. This is reflected in disagreements over the choice of fault plane amongst three, published studies (Golshadi et al., 2023; Rezapour and Jamalreyhani, 2023; Namdarsehat et al., 2024).

The 2021 M_w 5.8 Ganaveh, Iran earthquake, also in the frontal Zagros, exhibits a principal, NW-trending deformation lobe with displacements towards both ascending and descending satellites (Figure 2.7c). The descending interferogram contains a secondary, northeastern lobe moving away from the satellite; the equivalent lobe in the ascending interferogram is mostly obscured by atmospheric noise. The pattern is consistent with a WNW-striking low-angle thrust fault, in agreement with two published InSAR modelling studies (Jafari et al., 2023; Jamalreyhani et al., 2023).

Interferograms for the 2023 M_w 6.8 Marrakesh-Safi, Morocco earthquake in the Atlas mountains contain more short-wavelength atmospheric noise than those of our other low-angle thrust examples, but a pair of long-wavelength deformation lobes can still be made out (Figure 2.7d). The northern lobe contains displacements towards both ascending and

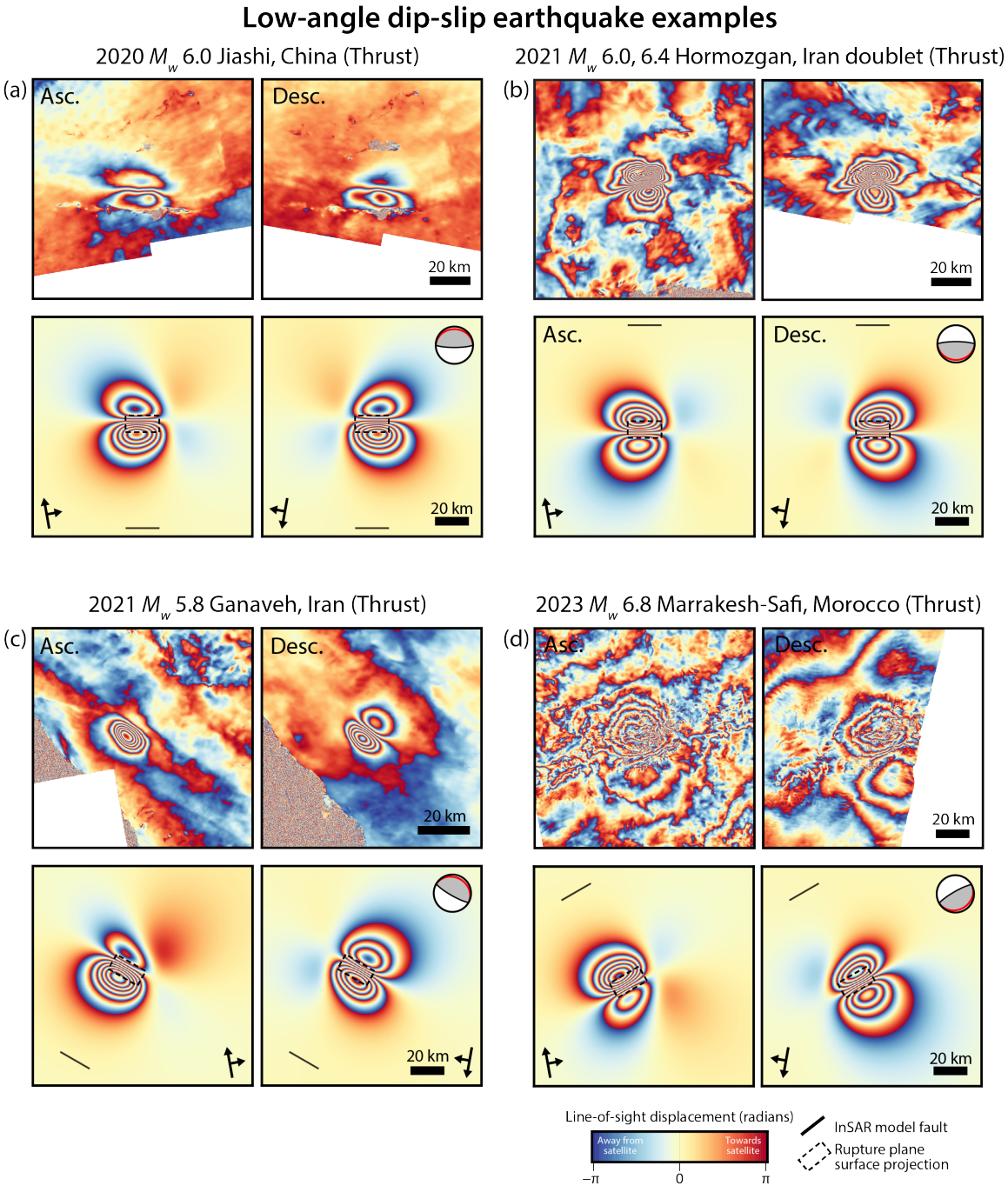


Figure 2.7: Interferograms comparing real low-angle thrust earthquakes (top rows) and our lookbook models (bottom rows) of the (a) 2020 M_w 6.0 Jiashi, China, (b) 2021 M_w 6.0, 6.4 Hormozgan, Iran (doublet), (c) 2021 M_w 5.8 Ganaveh, Iran, and (d) 2023 M_w 6.8 Marrakesh-Safi, Morocco earthquakes (see Table 2.2 for earthquake details). Left and right columns are ascending and descending interferograms, respectively. Thick black lines indicate our model faults and conjugate arrows denote the satellite azimuth and LOS. The beach ball is the earthquake focal mechanism of our InSAR model, with the fault plane outlined in red.

descending satellites but is broader in the ascending interferogram; the southern lobe has the opposite displacement sense but is broader in the descending case. This pattern is consistent with the ENE-striking (SSE-dipping) low-angle thrust model from our lookbook. Modelling of the InSAR by Cheloni et al. (2024) supported oblique, right-lateral/thrust slip on a 22°, SSW-dipping fault plane, a configuration not included in our lookbook. While there are significant strike and rake discrepancies between our closest forward model and Cheloni et al.'s inverse model, both involve NW-directed slip vectors on gently dipping planes, explaining the similarity of deformation.

2.8.4 Oblique-slip Examples

The 15 December 2019 M_w 6.8 Mindanao, Philippines earthquake—the last and largest of a sequence of four major events in late 2019 along the southern Cotabato fault system—produced two lobes in a skewed butterfly pattern in the ascending interferogram and a more complicated three-lobed shape in the descending interferogram, a distinction diagnostic of oblique-slip faulting (Figure 2.8a). A distinct NW–SE discontinuity separating lobes in both satellite geometries hints at the fault orientation, and our NNW-striking left-lateral/reverse faulting interferograms match the deformation well (Figure 2.4). This inference is supported by an inverse model by Li et al. (2020a).

The 2021 M_w 6.7 Khövsgöl, Mongolia earthquake also shows two lobes in the ascending ALOS-2 interferogram (in which fringes represent ∼12 cm increments of LOS displacement) and three lobes in the descending one (Figure 2.8b). The decorrelated region in the SE of the interferograms is Khövsgöl Lake, obscuring much but not all of the southeastern lobe. Altogether, the Khövsgöl interferograms resemble those of the Mindanao earthquake but with opposite sense of motion, matching the NNW-striking right-lateral/normal earthquake in our lookbook (Figure 2.4). This is in broad agreement with published inverse models, suggesting strike, dip, and rake values of 340°–345°, 42°–59°, and −116° to −146°, respectively (Kim and Han, 2023; He et al., 2022; Liu et al., 2021b, 2022).

The 2024 M_w 7.0 Wushi, China earthquake in the southwestern Tian Shan generated a butterfly-shaped deformation pattern in the ascending interferogram and a three-lobed shape in the descending one (Figure 2.8c). In general, the satellite look vector that yields the simpler, butterfly pattern gives away the fault orientation—a clear ENE–WSW lineament in this case. We utilize the fixed strike (variable rake) model interferograms at 60° and 240° (Figures 2.10c and 2.10i) to confirm a match with a WSW-striking left-lateral/re-

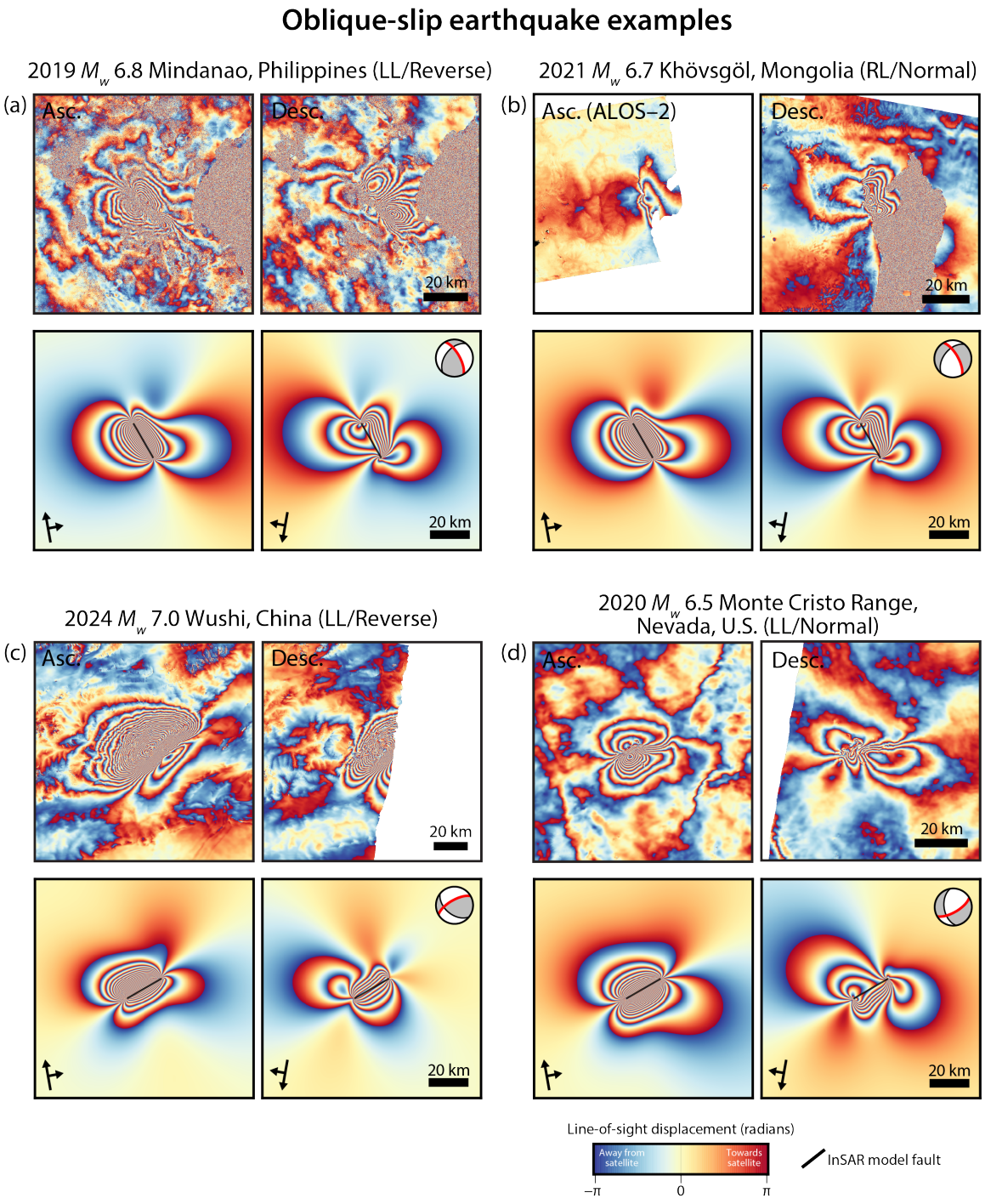


Figure 2.8: Interferograms comparing real oblique-slip earthquakes (top rows) with our lookbook models (bottom rows) of the (a) 2019 M_w 6.8 Mindanao, Philippines (b) 2021 M_w 6.7 Khövsgöl, Mongolia, (c) 2024 M_w 7.0 Wushi, China, and (d) 2020 M_w 6.5 Monte Cristo Range, USA earthquakes (see Table 2.2 for earthquake details). Left and right columns are ascending and descending interferograms, respectively. For the Khövsgöl earthquake, the ALOS-2 ascending interferogram half-wavelength is ∼12 cm (panel b, top left). Thick black lines indicate our model faults and conjugate arrows denote the satellite azimuth and line-of-sight. The beach ball is the earthquake focal mechanism of our InSAR model, with the fault plane outlined in red.

verse faulting interferogram. This is consistent both with automated USGS NEIC and GCMT moment tensors and with the kinematics of the WSW-striking Maidan fault, which likely hosted the earthquake (Wu et al., 2019; Guo et al., 2024).

Lastly, the 2020 M_w 6.5 Monte Cristo Range earthquake in the Mina deflection zone, part of the Walker Lane of California-Nevada, produced two deformation lobes in the ascending interferogram and three in the descending one (Figure 2.8d). Similar to the Wushi earthquake, the simpler butterfly pattern in the ascending interferogram suggests faulting parallel to the ENE look vector, and our lookbook summary (Figure 2.4) supports ENE-striking, left-lateral/normal faulting (rake = -45°). However, published InSAR inverse models reveal a more complicated two-fault geometry, with a shorter left-lateral/normal segment in the west crossing a longer left-lateral segment in the east (see Chapter 3, Sethanant et al., 2023). This is reflected in the southern pair of lobes in the descending interferogram, which have different shapes to those in the lookbook (a squatter SW lobe and an elongate SE lobe). While the lookbook does not capture geometrical complexities, the general lobe patterns are still efficient in providing first order interpretations.

2.9 Conclusions

This lookbook is the first systematic demonstration of the changes in InSAR deformation patterns expected for varying strike and rake angles. By understanding the distinct lobe patterns in both ascending- and descending-track interferograms, the lookbook provides an illustrative guide to estimating earthquake source mechanisms from interferograms without need for sophisticated inverse modelling. With growing numbers of InSAR satellites and availability of pre-processed imagery, this resource will be invaluable for rapid assessment of coseismic interferograms following large, continental earthquakes.

2.10 Data and Resources

Oksar software used for generating displacement fields and forward model interferograms is kindly provided by Dr. Tim Wright. For the earthquakes plotted in Figures 2.5–2.8, Sentinel-1 interferograms were downloaded from the COMET LiCSAR portal (`https://comet.nerc.ac.uk/comet-lics-portal-earthquake-event/`, last accessed on May 31, 2024) while Envisat and ALOS-2 interferograms for the 2003 Bam and 2021 Khövsgöl earthquakes were kindly provided by Dr. Gareth Funning and Dr. Hyangsun Han, respectively. We used the interferogram color scale developed by Watson et al. (2023) and ob-

tained from `https://github.com/comet-licsar/licsar_proc/blob/main/misc/pha.cpt` (last accessed May 31, 2024). Figures were plotted using the Generic Mapping Tools version 6 (Wessel et al., 2019).

2.11 Supplemental Material

Description of Supplemental Material

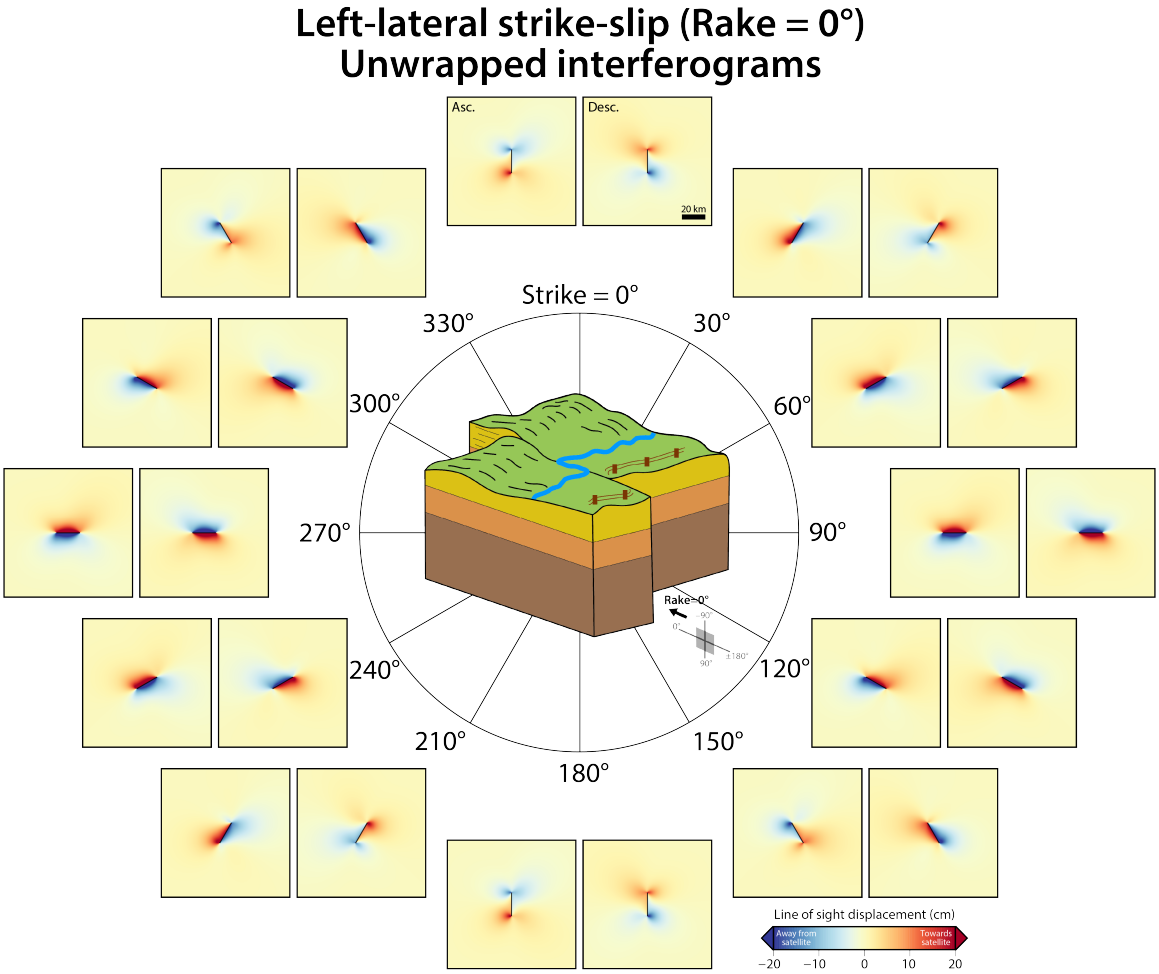
Supplemental materials for the InSAR lookbook consist of twenty-two figures: unwrapped interferograms at variable strike angles for the ten faulting types (Figures 2.9a–2.9j), and wrapped interferograms at fixed strikes and variable rake angles (Figures 2.10a–2.10l). See Table 2.1 in the main text for the fault parameters of all suites of models, and Section 2.6.3 for more details of the application of these figures.

List of Supplemental Figures

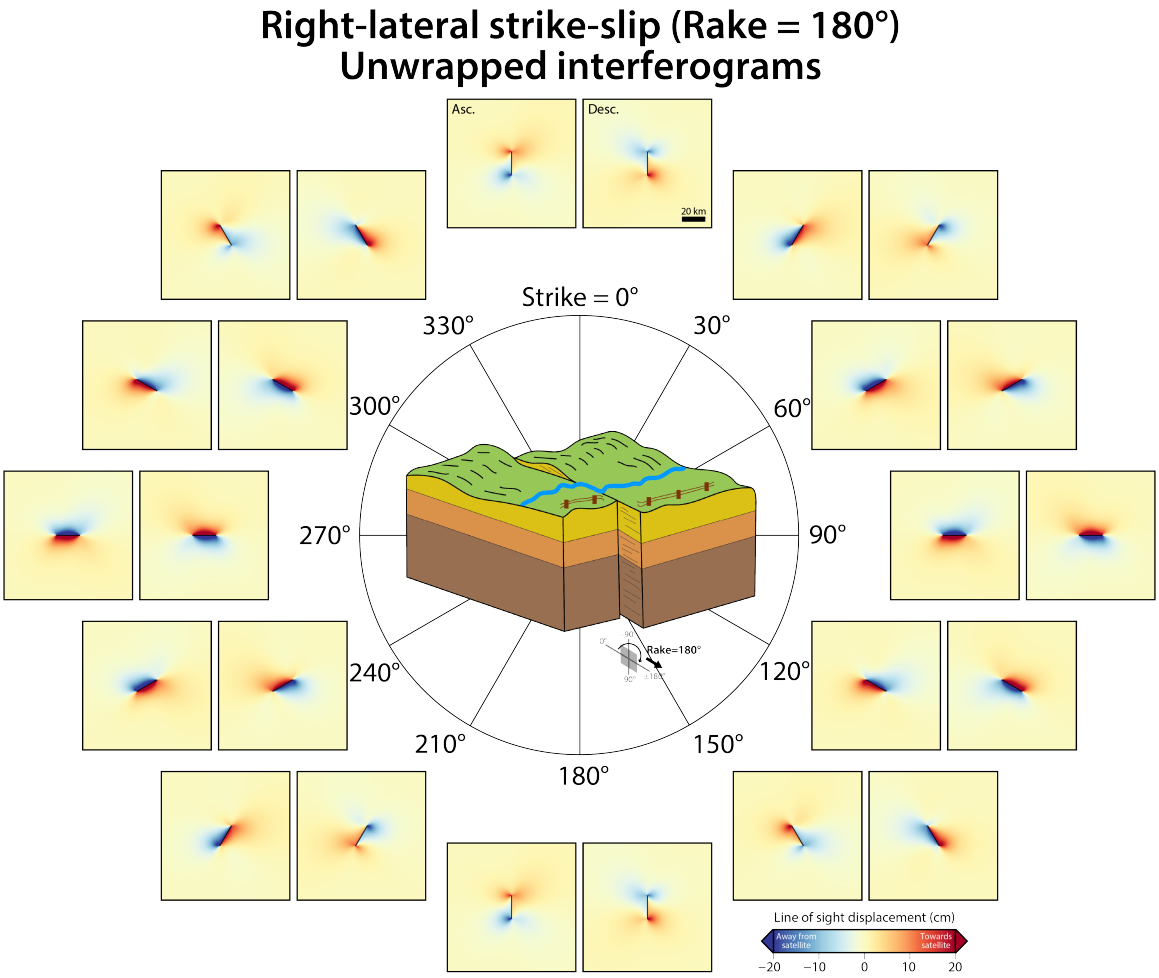
1. Figure 2.9a: Left-lateral strike-slip earthquake unwrapped interferograms
2. Figure 2.9b: Right-lateral strike-slip earthquake unwrapped interferograms
3. Figure 2.9c: Reverse faulting earthquake unwrapped interferograms
4. Figure 2.9d: Normal faulting earthquake unwrapped interferograms
5. Figure 2.9e: Low-angle thrust faulting earthquake unwrapped interferograms
6. Figure 2.9f: Low-angle normal faulting earthquake unwrapped interferograms
7. Figure 2.9g: Left-lateral/reverse oblique-slip earthquake unwrapped interferograms
8. Figure 2.9h: Right-lateral/reverse oblique-slip earthquake unwrapped interferograms
9. Figure 2.9i: Left-lateral/normal oblique-slip earthquake unwrapped interferograms
10. Figure 2.9j: Right-lateral/normal oblique-slip earthquake unwrapped interferograms
11. Figure 2.10a: Interferograms for strike 0° faulting, varying rake
12. Figure 2.10b: Interferograms for strike 30° faulting, varying rake
13. Figure 2.10c: Interferograms for strike 60° faulting, varying rake
14. Figure 2.10d: Interferograms for strike 90° faulting, varying rake
15. Figure 2.10e: Interferograms for strike 120° faulting, varying rake
16. Figure 2.10f: Interferograms for strike 150° faulting, varying rake
17. Figure 2.10g: Interferograms for strike 180° faulting, varying rake
18. Figure 2.10h: Interferograms for strike 210° faulting, varying rake

19. Figure 2.10i: Interferograms for strike 240° faulting, varying rake
20. Figure 2.10j: Interferograms for strike 270° faulting, varying rake
21. Figure 2.10k: Interferograms for strike 300° faulting, varying rake
22. Figure 2.10l: Interferograms for strike 330° faulting, varying rake

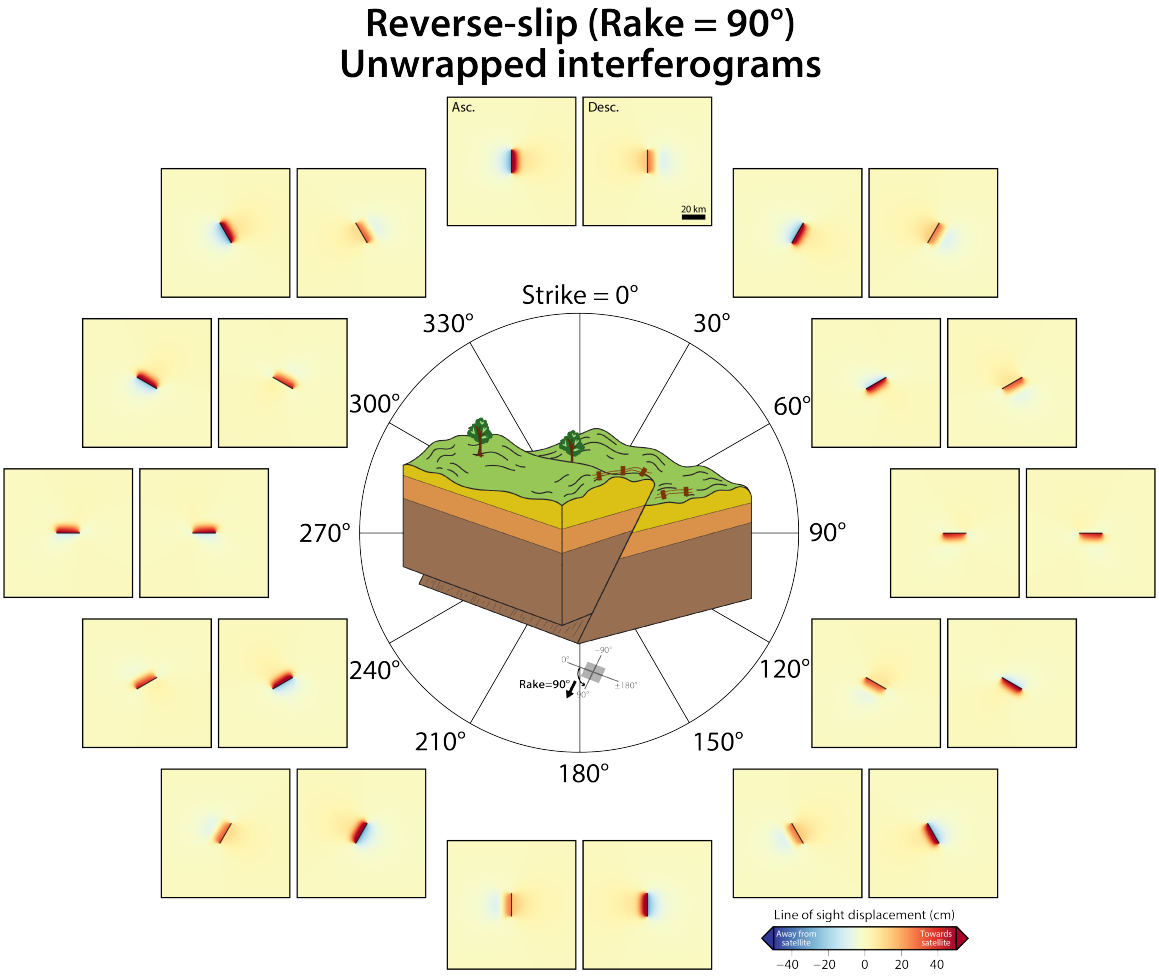
Figure 2.9: In each panel (a) to (j), ascending and descending unwrapped interferogram pairs are plotted radially at 30° increments in fault strike around a block diagram illustrating the displayed faulting. Solid black lines mark the 20 km-long model fault trace; for non-vertical faults, a dashed rectangle marks the model fault itself. In all panels, we use the convention that when crossing fringes in the order blue–yellow–red, motion is increasingly towards the satellite, and when crossing fringes in the order red–yellow–blue, motion is increasingly away from the satellite.



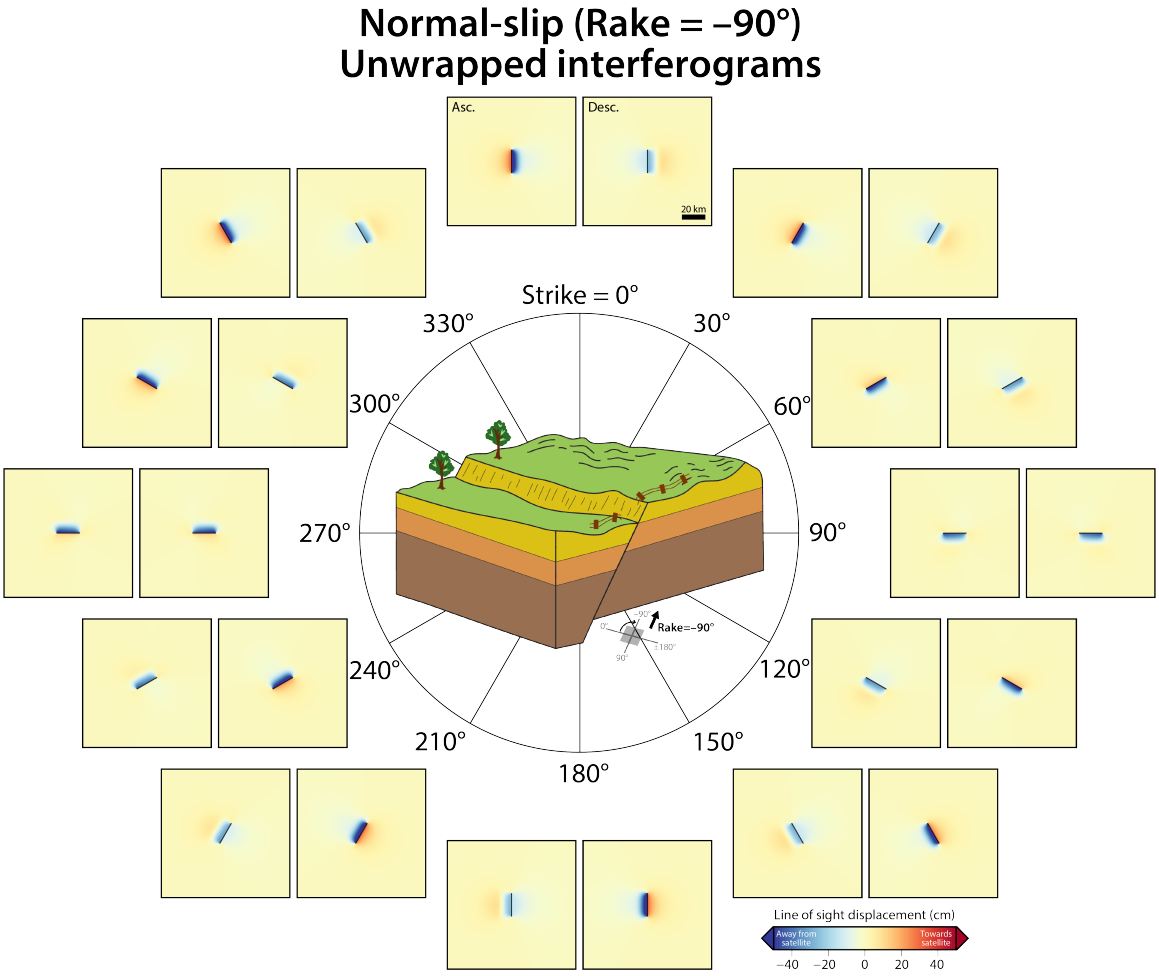
a InSAR forward model unwrapped interferograms for variably striking left-lateral strike-slip earthquakes (dip 90°, rake 0°).



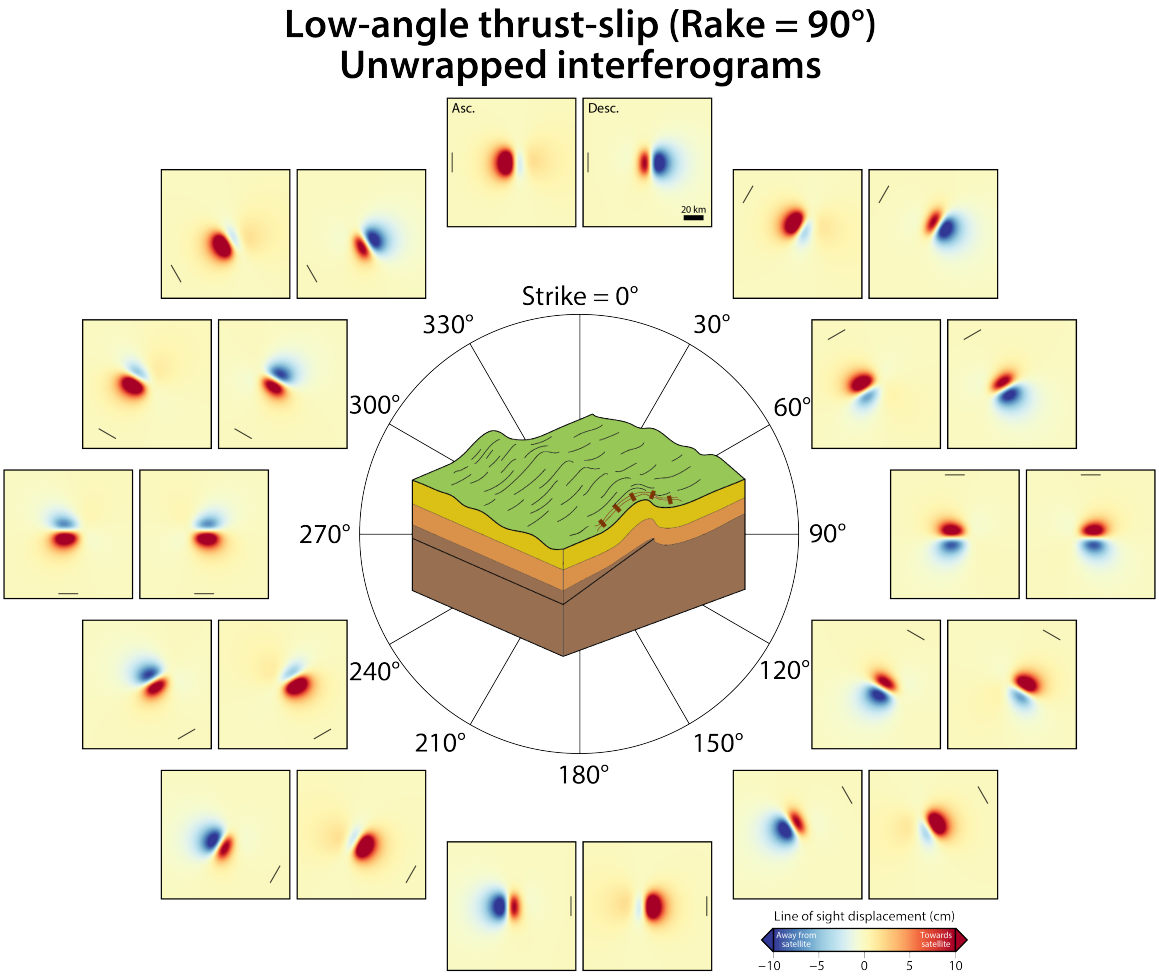
b InSAR forward model unwrapped interferograms for variably striking right-lateral strike-slip earthquakes (dip 90°, rake 180°).



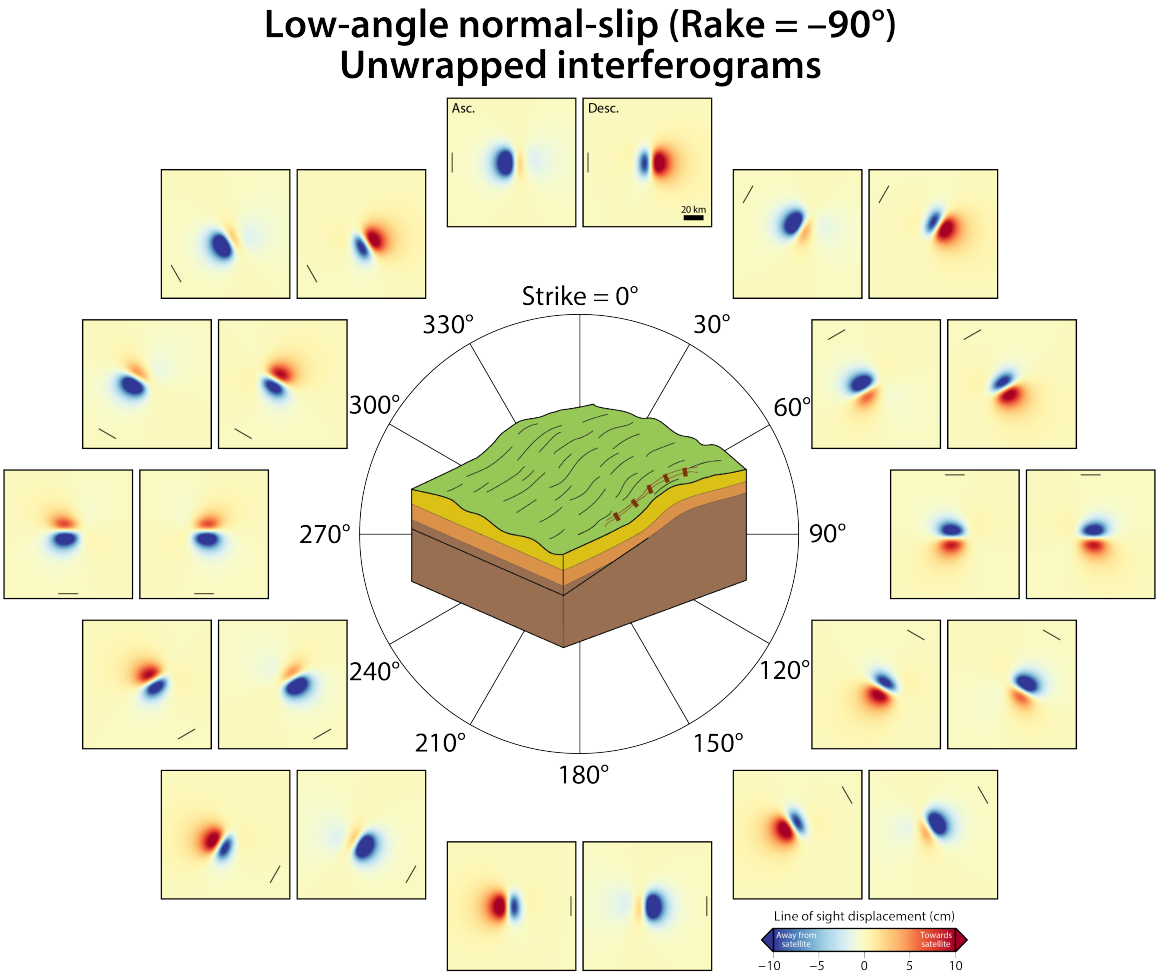
c InSAR forward model unwrapped interferograms for variably striking reverse faulting earthquakes (dip 45°, rake 90°).



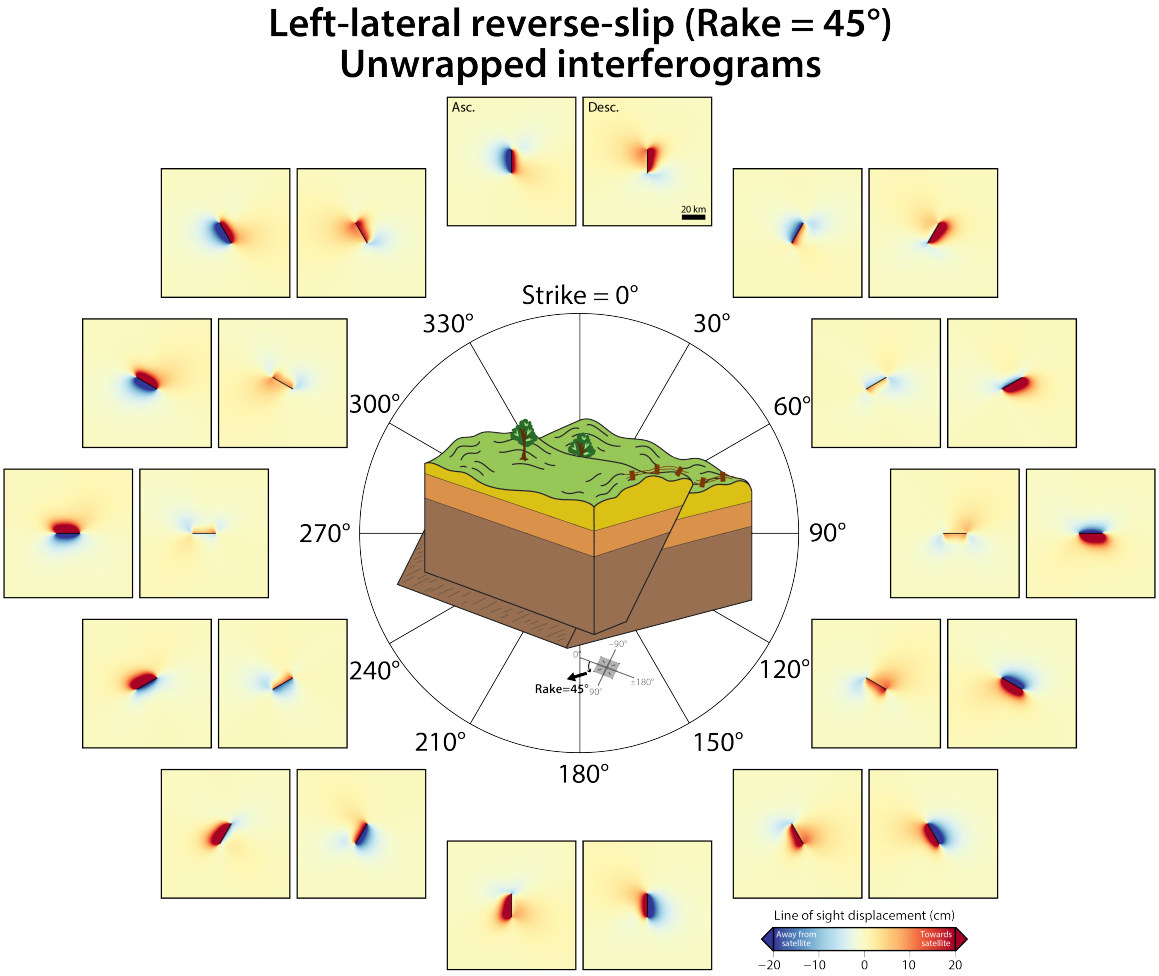
d InSAR forward model unwrapped interferograms for variably striking normal faulting earthquakes (dip 45°, rake −90°).



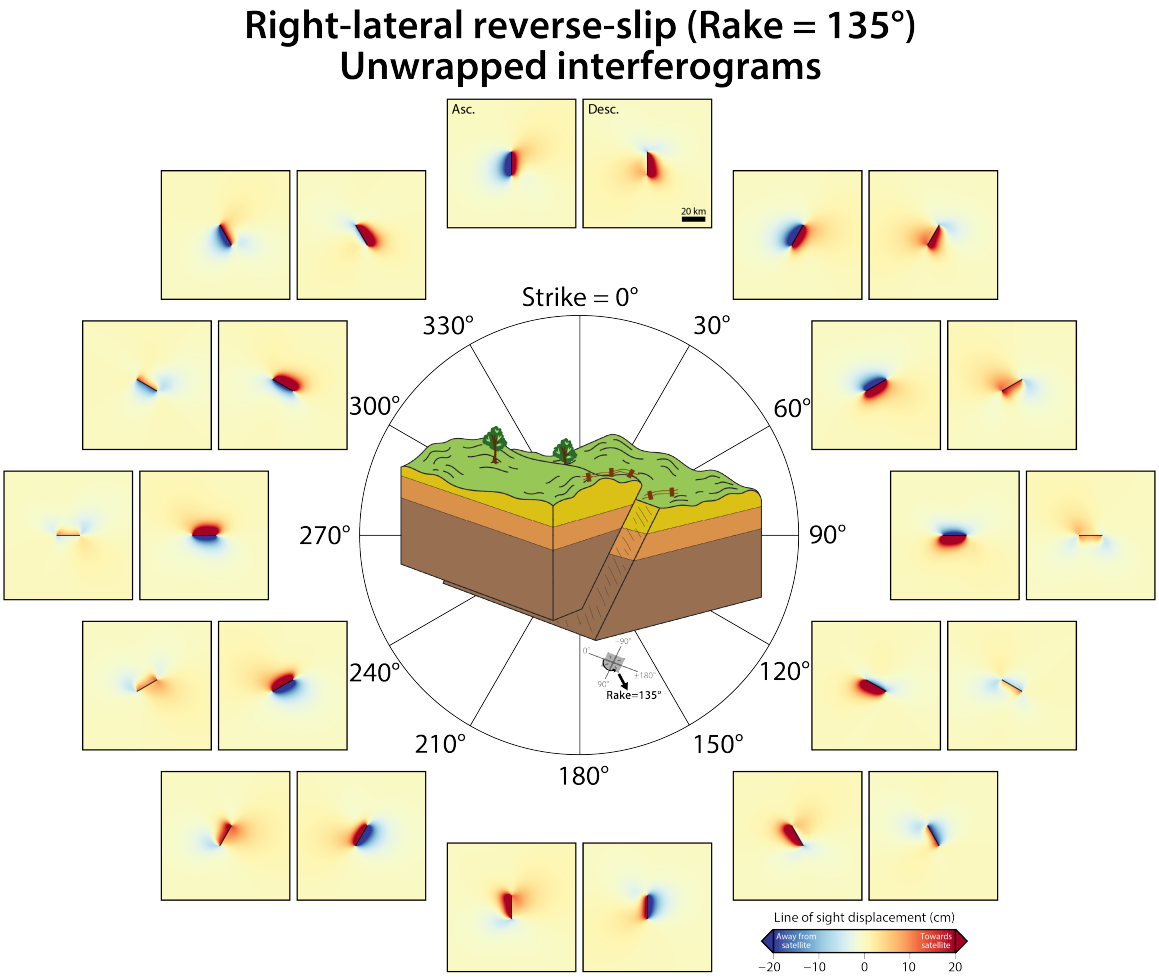
e InSAR forward model unwrapped interferograms for variably striking, buried, low-angle thrust faulting earthquakes (dip 10°, rake 90°).



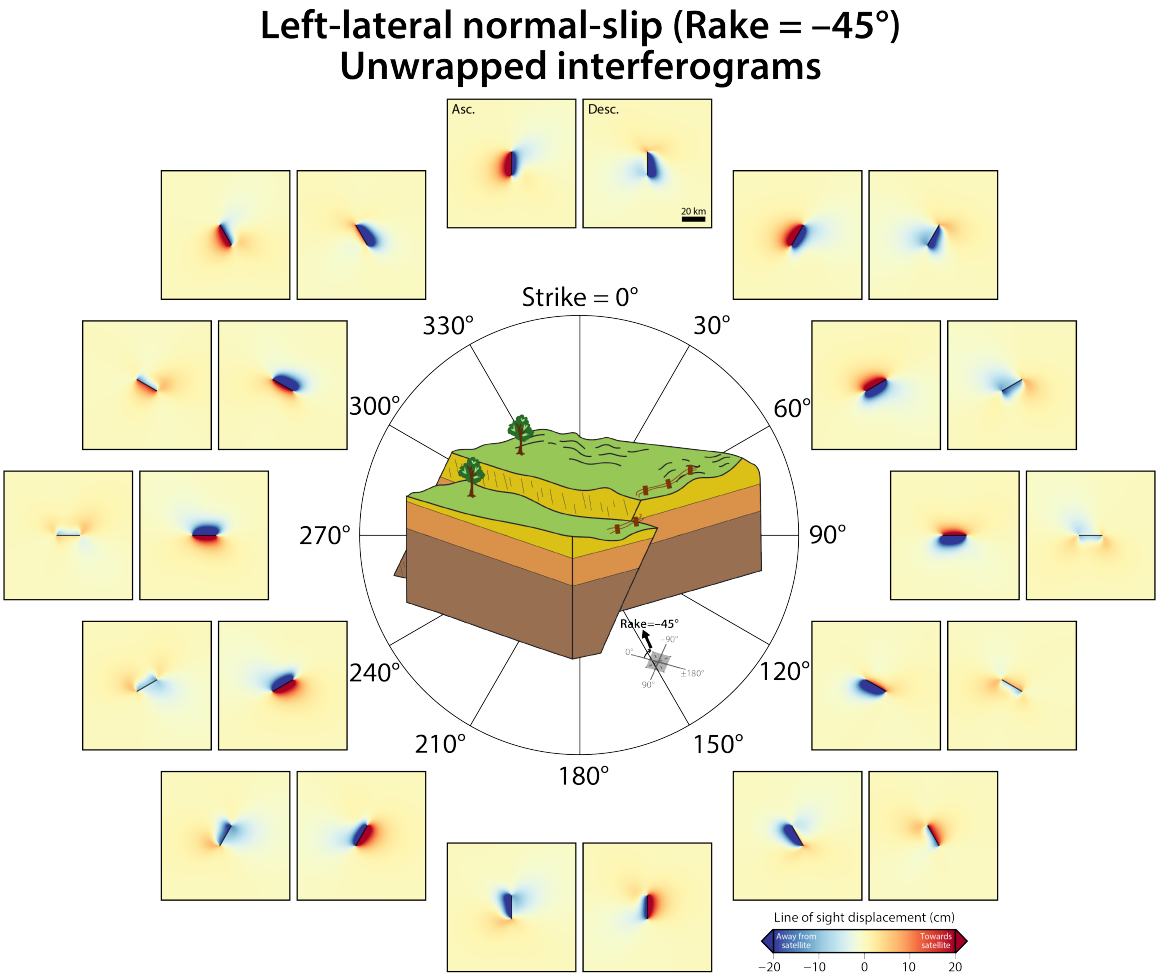
f InSAR forward model unwrapped interferograms for variably striking, buried, low-angle normal faulting earthquakes (dip 10°, rake −90°).



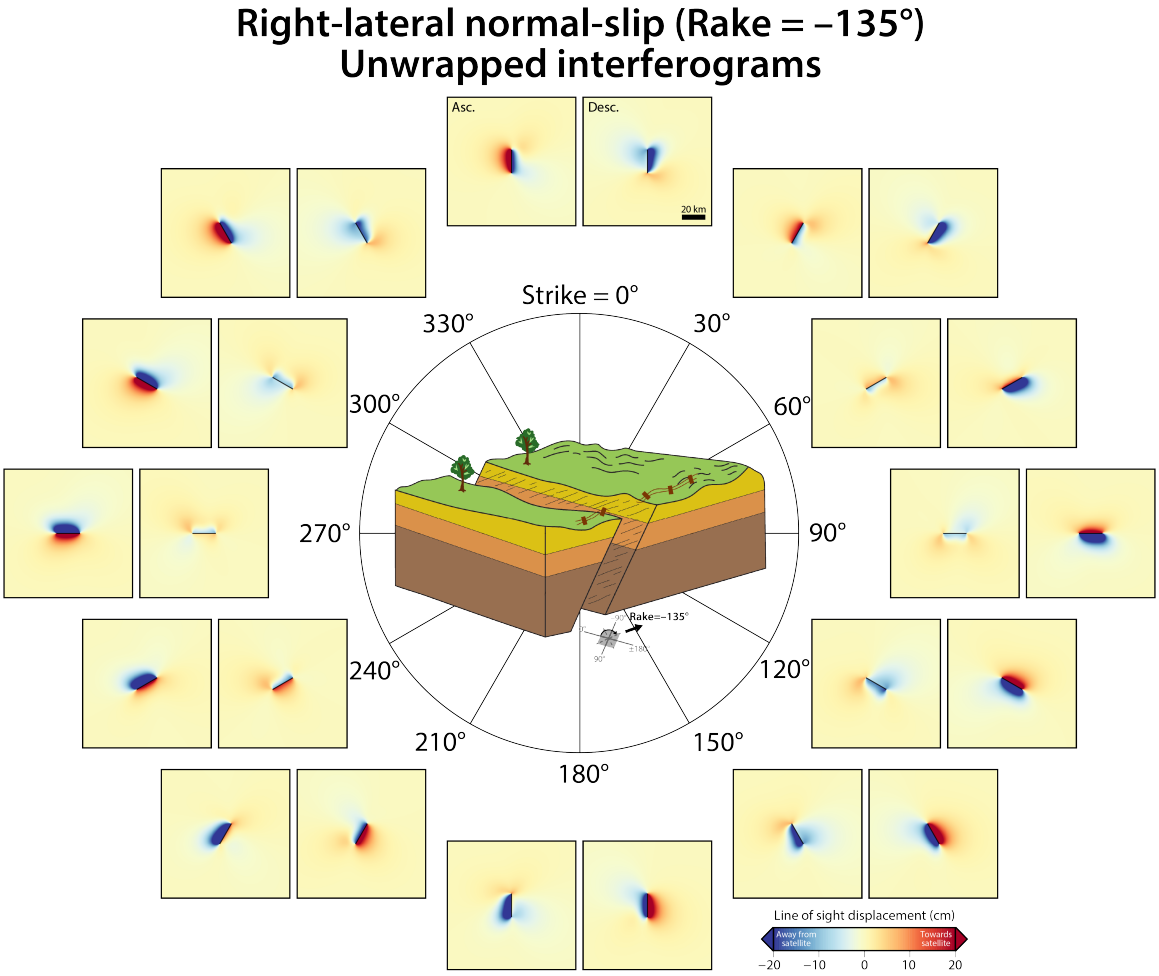
g InSAR forward model unwrapped interferograms for variably striking, left-lateral/reverse, oblique-slip earthquakes (dip = 67.5°, rake = 45°).



h InSAR forward model unwrapped interferograms for variably striking, right-lateral/reverse, oblique-slip earthquakes (dip = 67.5°, rake = 135°).

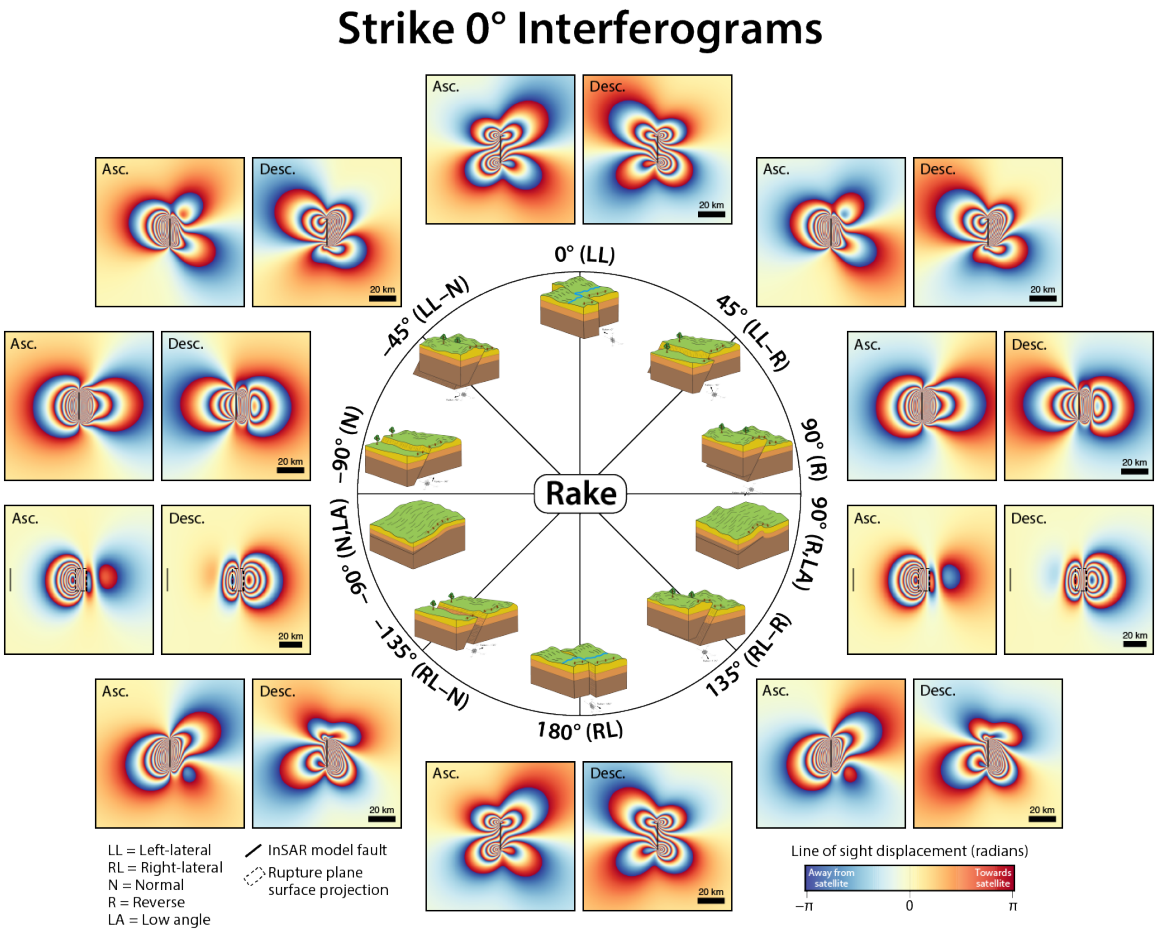


i InSAR forward model unwrapped interferograms for variably striking, left-lateral/normal, oblique-slip earthquakes (dip = 67.5°, rake = −45°).

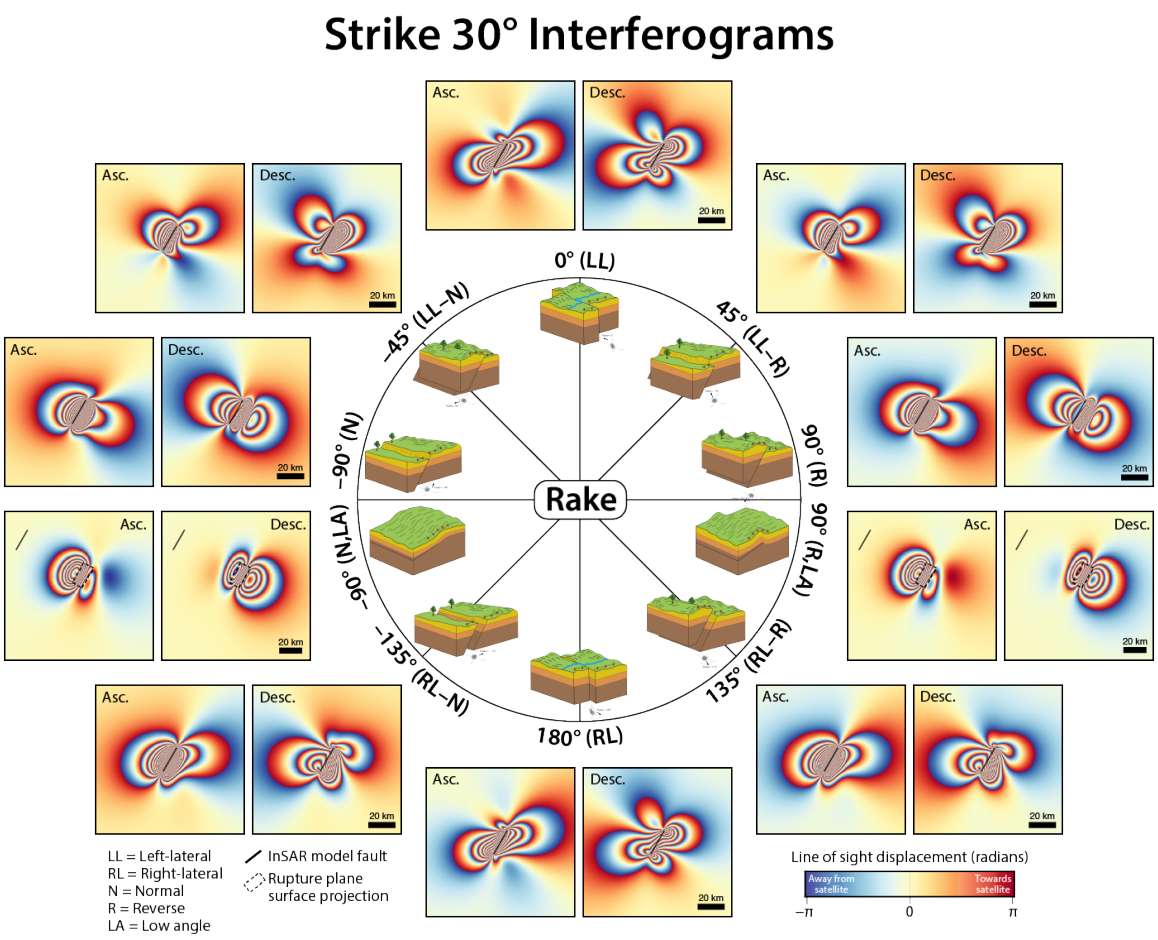


j InSAR forward model unwrapped interferograms for variably striking, right-lateral/normal, oblique-slip earthquakes (dip = 67.5°, rake = −135°).

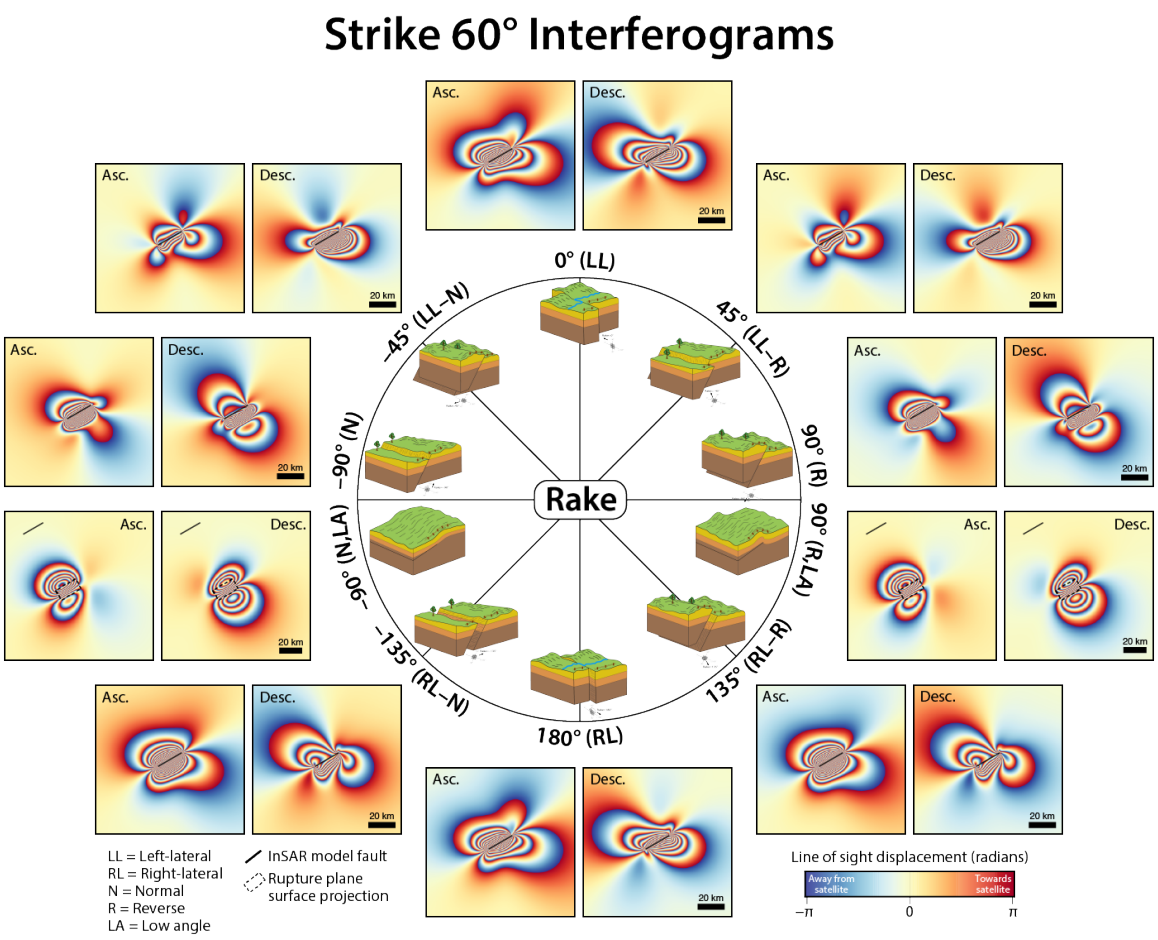
Figure 2.10: In each panel (a) to (l), ascending and descending wrapped interferogram pairs are plotted radially at 45° increments in fault rake. Abbreviations of the kinematics and geometry include: left-lateral (LL), right-lateral (RL), N (normal), R (reverse), and low-angle (LA). At 90° (reverse) and −90° (normal) rake, an additional pair of interferograms for low-angle faulting (dip = 10°) are shown below the moderate-angle pair (dip = 45°). Thick black line denotes the model fault trace and dashed black rectangle indicates the surface projection of the rupture plane in the low-angle faulting scenarios.



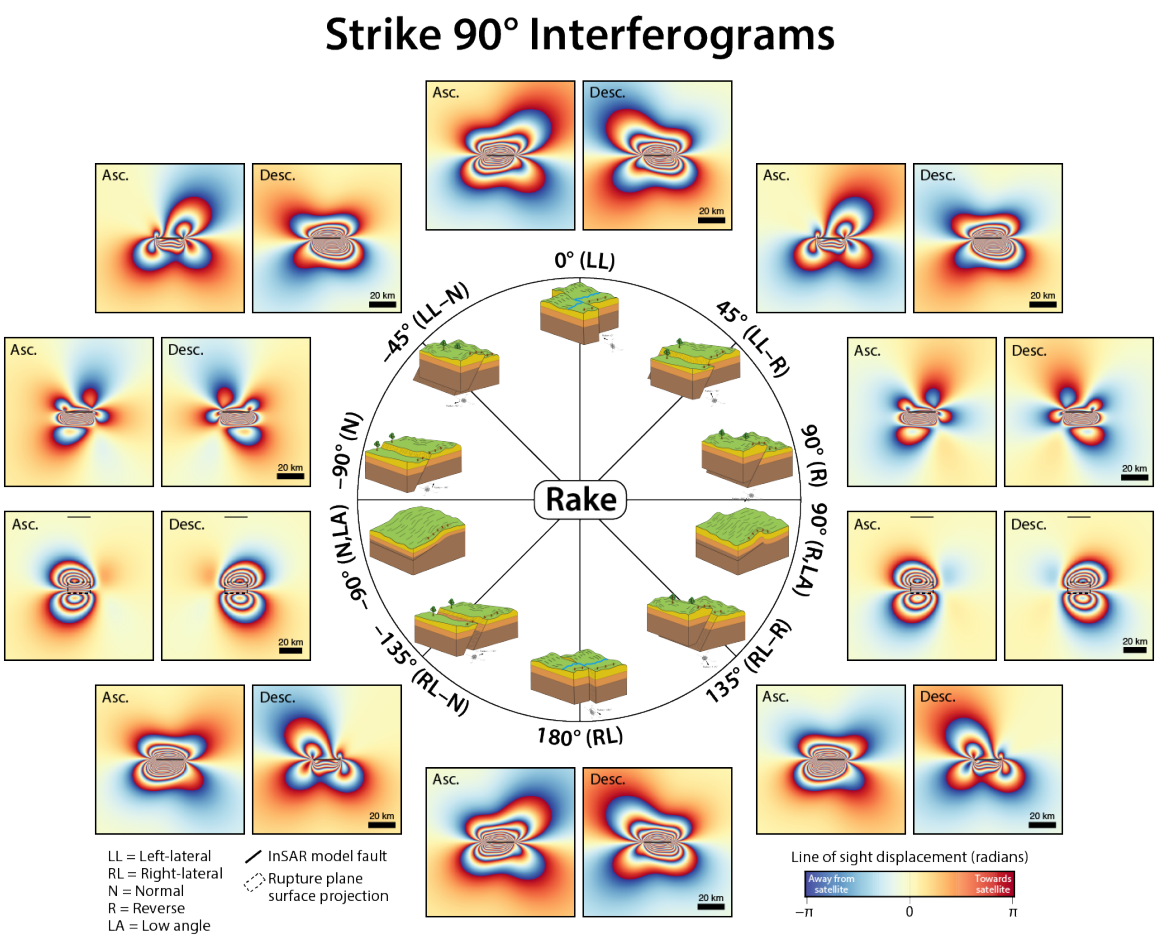
a Wrapped interferograms for strike 0° faulting earthquakes, with variable rake.



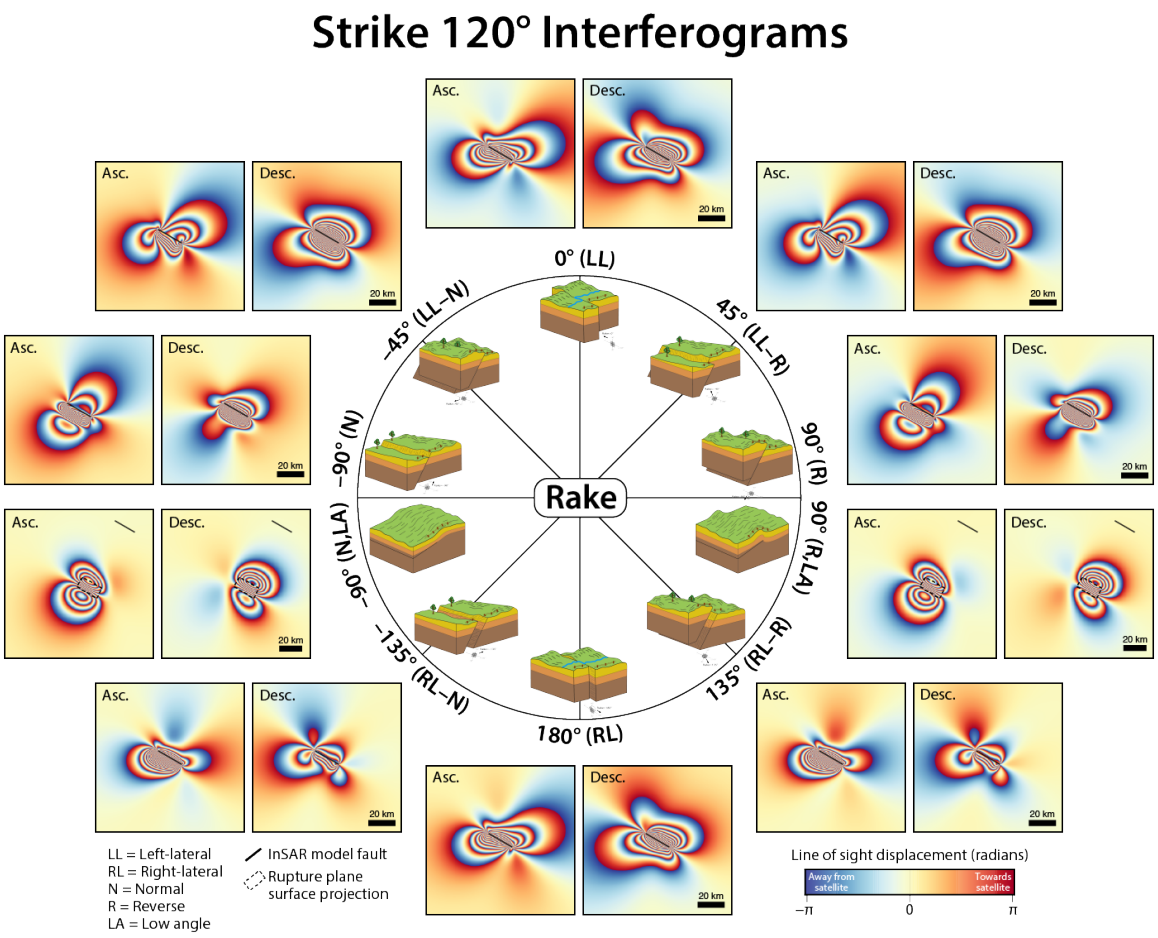
b Wrapped interferograms for strike 30° faulting earthquakes, with variable rake.



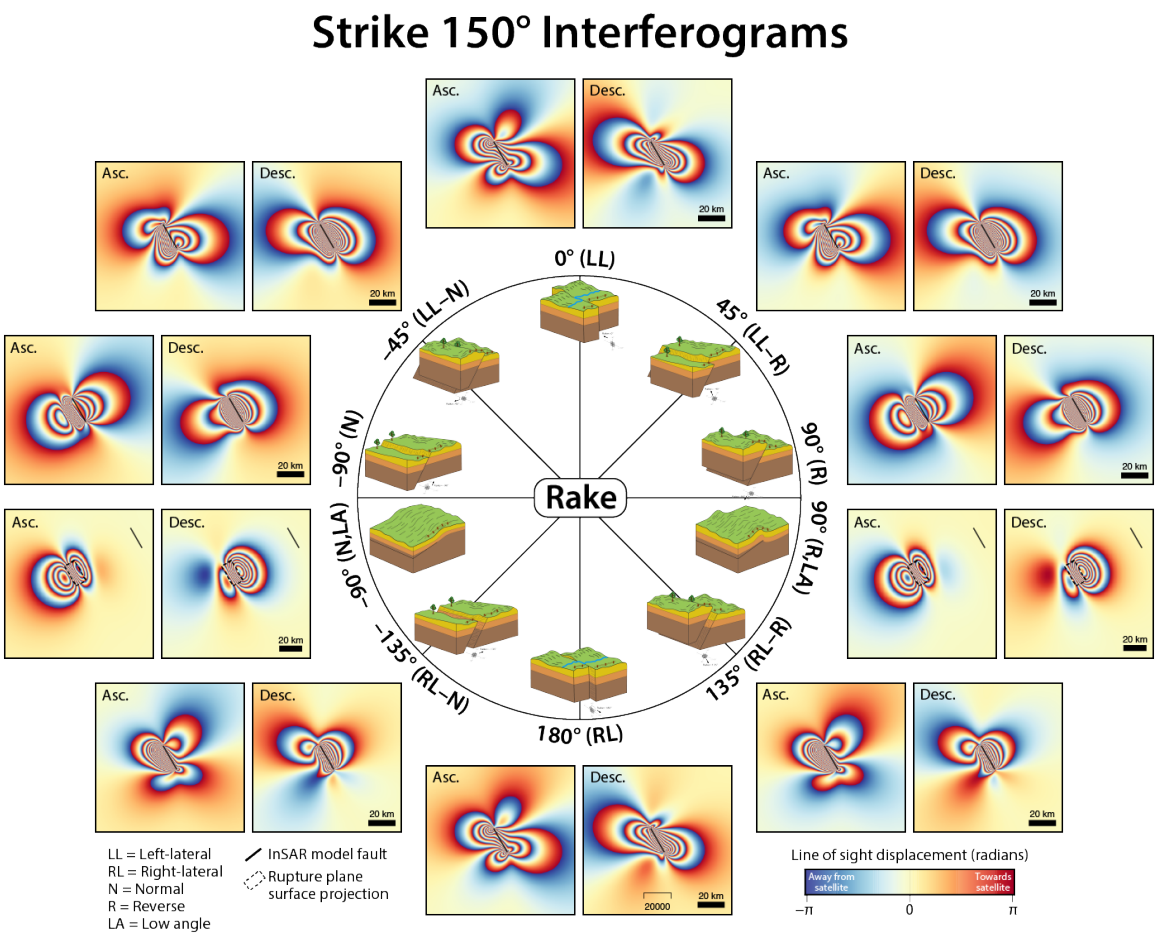
c Wrapped interferograms for strike 60° faulting earthquakes, with variable rake.



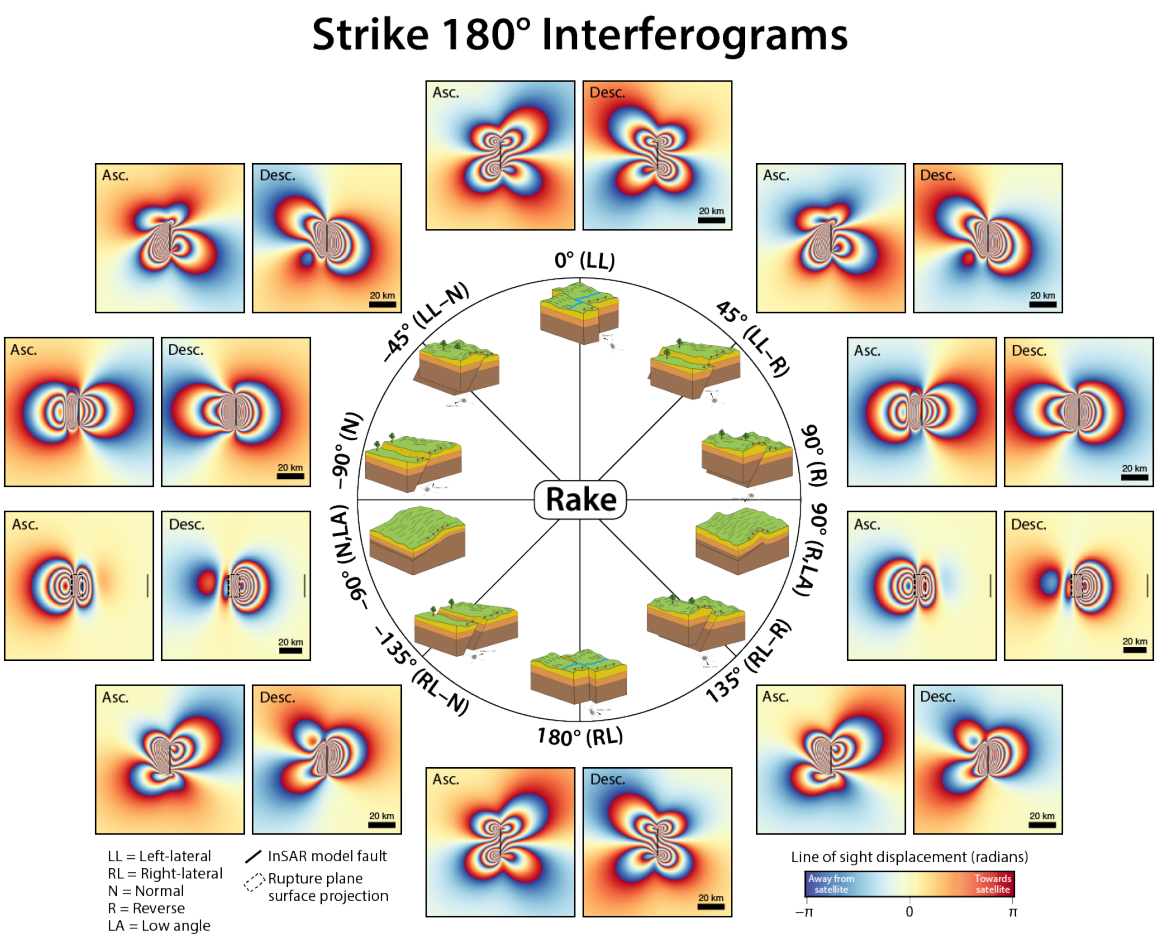
d Wrapped interferograms for strike 90° faulting earthquakes, with variable rake.



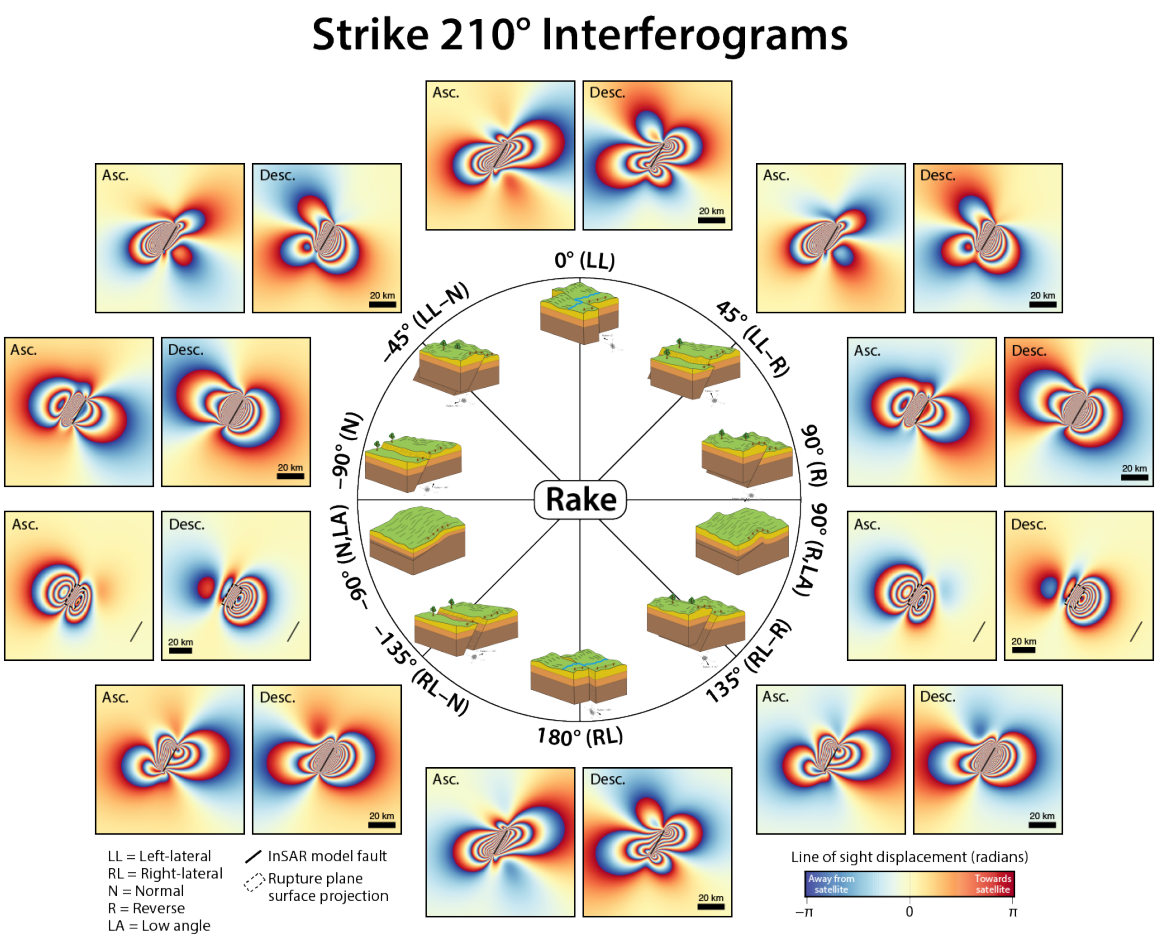
e Wrapped interferograms for strike 120° faulting earthquakes, with variable rake.



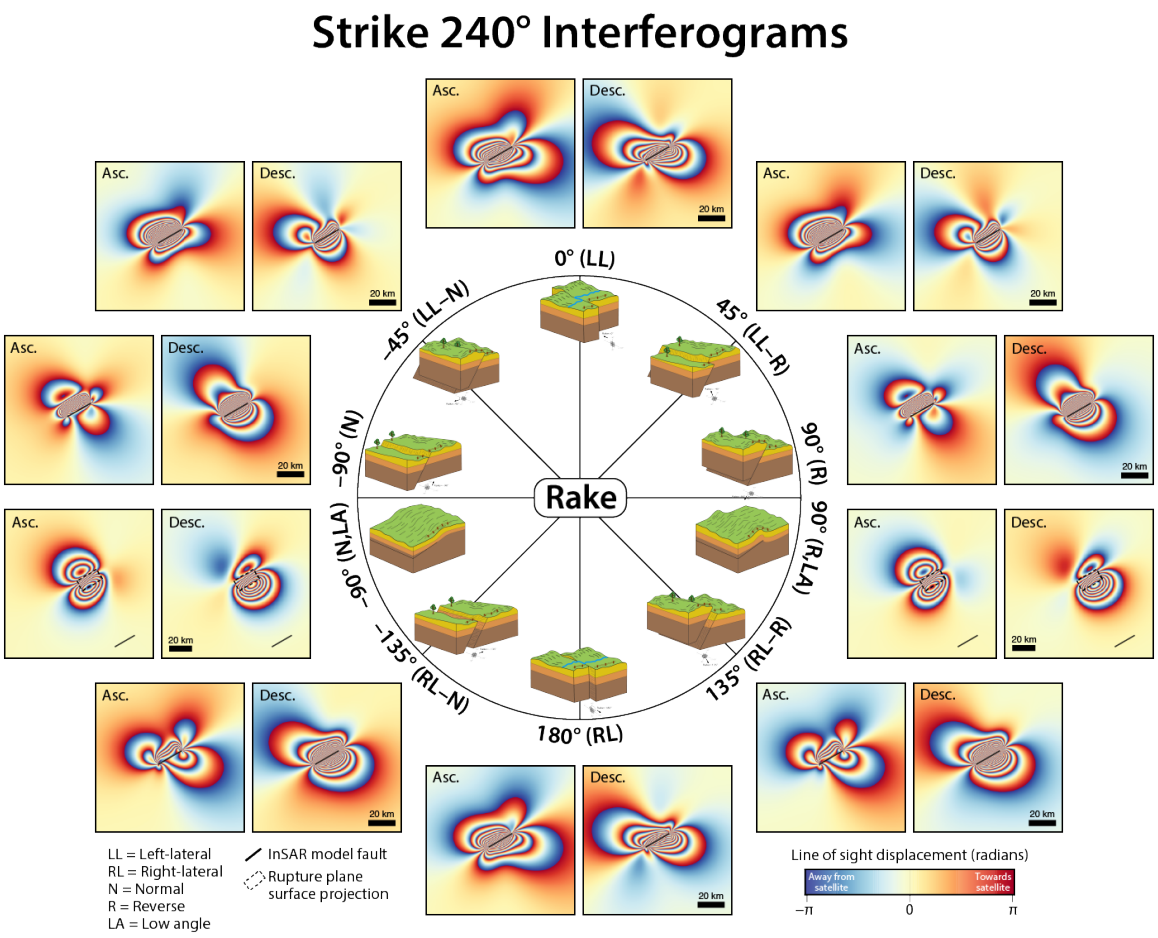
f Wrapped interferograms for strike 150° faulting earthquakes, with variable rake.



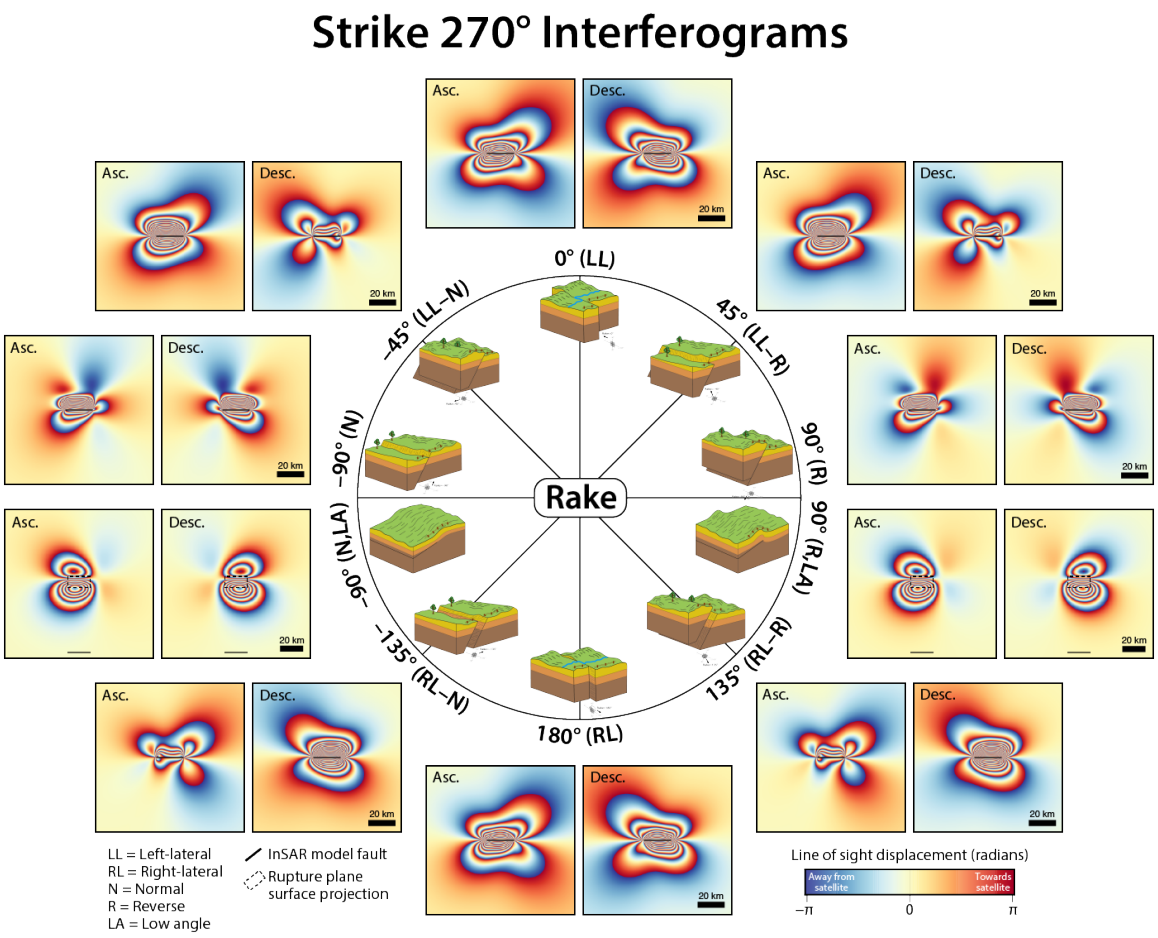
g Wrapped interferograms for strike 180° faulting earthquakes, with variable rake.



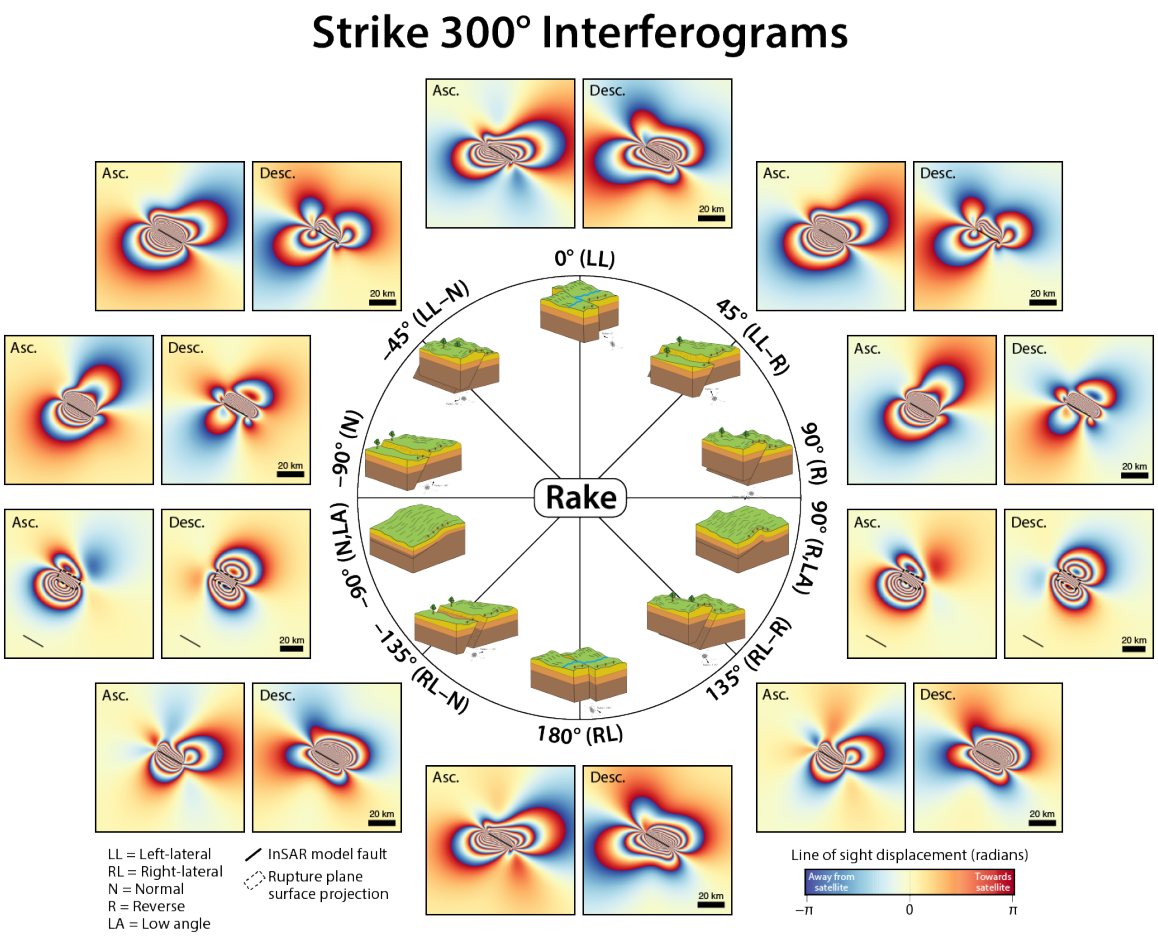
h Wrapped interferograms for strike 210° faulting earthquakes, with variable rake.



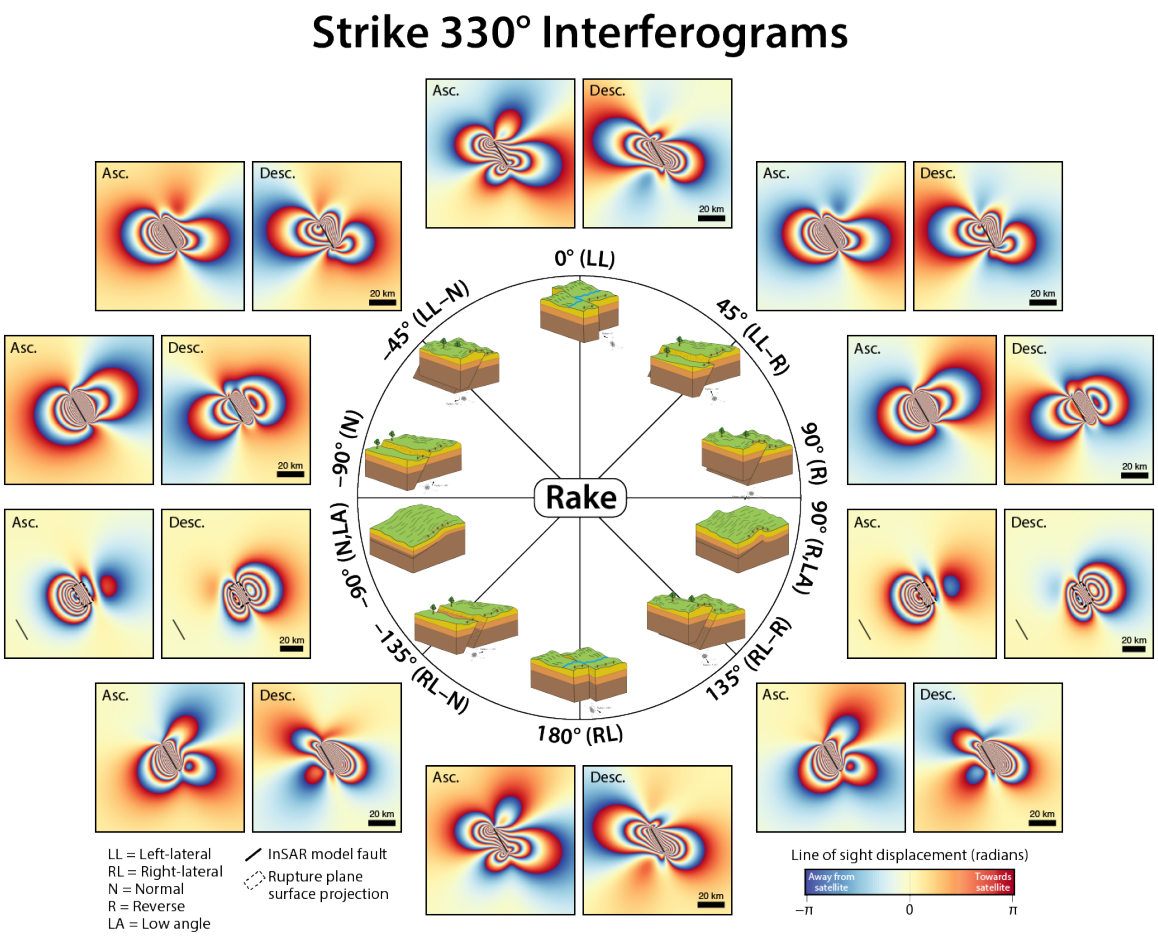
i Wrapped interferograms for strike 240° faulting earthquakes, with variable rake.



j Wrapped interferograms for strike 270° faulting earthquakes, with variable rake.



k Wrapped interferograms for strike 300° faulting earthquakes, with variable rake.



1 Wrapped interferograms for strike 330° faulting earthquakes, with variable rake.

Chapter 3

The 2020 M_w 6.5 Monte Cristo Range (Nevada) earthquake: anatomy of a crossing-fault rupture through a region of highly-distributed deformation

3.1 Author Names, Affiliations, and Roles

I. Sethanant[1], E. Nissen[1], L. Pousse-Beltran[2], E. Bergman[3], I. Pierce[4]

[1]School of Earth and Ocean Sciences, University of Victoria, British Columbia, Canada

[2]Université Grenoble Alpes, Université Savoie Mont Blanc, CNRS, IRD, Université Gustave Eiffel, ISTerre, 38000 Grenoble, France

[3]Global Seismological Services, Golden, Colorado, USA

[4]Department of Earth Sciences, University of Oxford, Oxford, United Kingdom

This chapter was published in the Bulletin of the Seismological Society of America (`https://doi.org/10.1785/0120220166`). The sections, figures, and supplemental materials were renumbered here to accommodate the dissertation format. Published supplemental data files were also reformatted into long tables in this dissertation. I undertook the InSAR modelling and analysis, data curation and formal analysis, created figures, wrote and edited the text. Dr. Edwin Nissen supervised this work and provided

manuscript edits. Dr. Léa Pousse-Beltran supervised InSAR corrections and provided minor manuscript edits. Dr. Eric Bergman conducted the earthquake relocation and provided minor manuscript edits. Dr. Ian Pierce contributed field observation data and minor manuscript edits.

3.2 Abstract

The 15 May 2020 M_w 6.5 Monte Cristo Range earthquake (MCRE) in Nevada, USA is the largest instrumental event in the Mina deflection, a zone of E-trending left-lateral faults accommodating a right step between NW-trending right-lateral faults of the Walker Lane. The MCRE ruptured a highly-distributed faulting area with muted geomorphic expressions, motivating us to characterize the behaviour of an earthquake on a structurally-immature fault system. Inverse modeling of Interferometric Synthetic Aperture Radar (InSAR) and Global Navigation Satellite System (GNSS) displacements reveals left-lateral slip on an E-striking, eastern fault and left-lateral–normal slip on an ENE-striking, western fault. Unusually, the two faults cross one another and ruptured together in the mainshock. Maximum slip of 1 m occurs at 8–10 km depth but less than 0.1 m of slip reaches the surficial model fault patches, yielding a pronounced shallow slip deficit (SSD) of 91$\%$. Relocated hypocenters indicate that the mainshock initiated at 9 km depth and that aftershocks span depths of 1–11 km, constraining the local seismogenic thickness. Our new field observations of fracturing and pebble-clearing in the western MCRE characterize a third, shorter, northern fault that is at the resolution limit of the InSAR-GNSS modeling. The segmented and intersecting fault geometry, off-fault aftershocks with variable mechanisms, distributed surface fractures, limited long-term geomorphic offsets, and a $\sim$600–700 m (cumulative) bedrock offset, are all characteristic of a structurally-immature fault system. However, the large SSD is not unusual for an earthquake of this magnitude, and a larger compilation of InSAR models (twenty-eight $M_w \geq$6.4 strike-slip events) shows that SSDs correlate with magnitude rather than structural maturity. This study demonstrates the importance of integrating geodesy, seismology, and field observations to capture the full complexity of large earthquakes, and further suggests that seismic hazard assessments in shattered crustal regions consider the potential for multi- and cross-fault rupture.

3.3 Plain Language Summary

The 2020 Monte Cristo Range earthquake, western Nevada, ruptured mostly previously unrecognized faults in a highly fractured region of crust in which no single, through-going fault has yet emerged. Understanding earthquake behaviour in such regions is crucial for assessing seismic hazard. We use radar imagery and other satellite measurements to model the fault geometry and how much slip occurred, seismograms to estimate the nucleation depth and aftershock patterns, and field observations to characterize surface rupturing. Results show that the earthquake sequence involved three main faults with differing orientations and movements; unusually, two of the faults cross one another. The segmented fractures, distributed aftershocks and their varied geometries, and the limited record of past earthquakes, are all characteristics of a newly emergent fault zone. However, according to our comparison with twenty-seven other global earthquakes, the small proportion ($\sim$10%) of slip that reached the surface does not relate with the faults being young, but rather the size of the earthquake.

3.4 Introduction

Fault segmentation is known to play an important role in earthquake rupture propagation and arrest. The influential 'characteristic earthquake' model posits that maximum earthquake magnitudes are limited by the lengths of discrete, mapped fault segments and their intervening segment boundaries (Schwartz and Coppersmith, 1984; Wesnousky, 2006). However, in recent years this simple view has been complicated by observations of a number of multi-fault earthquakes that have jumped across major segment boundaries to achieve larger rupture areas and magnitudes than would normally be anticipated (e.g., Hicks and Rietbrock, 2015; Huang et al., 2016; Nissen et al., 2016; Hamling et al., 2017). Fault segmentation is one manifestation of fault structural maturity, a term that describes the evolution of fault zone properties with incremental offset. In this progression, a fault core thickens (e.g., Robertson, 1983; Scholz, 1987; Hull, 1988; Childs et al., 2009), off-fault damage intensifies (e.g., Shipton and Cowie, 2001; Finzi et al., 2009; Faulkner et al., 2011; Savage and Brodsky, 2011; Aben et al., 2016), and the fault trace simplifies as segments coalesce and asperities are smoothed out (e.g., Walsh and Watterson, 1988; Wesnousky, 1988; Peacock and Sanderson, 1991; Childs et al., 1995; Stirling et al., 1996; Frost et al., 2009; Wechsler et al., 2010; Brodsky et al., 2011). Structural maturity may also be important in controlling other aspects of earthquake rupture behavior. Observations suggest that

earthquakes along structurally-mature faults exhibit more localized deformation and narrower aftershock distributions (Powers and Jordan, 2010; Zinke et al., 2015; Hatem et al., 2017; Perrin et al., 2021), faster rupture velocities (Perrin et al., 2016; Chounet et al., 2018), more persistent rupture directivity (Kane et al., 2013; Aderhold and Abercrombie, 2015), proportionally more surface slip (Dolan and Haravitch, 2014), larger amounts of aseismic afterslip (Johanson et al., 2006; Feng et al., 2010; Thomas et al., 2014; Li et al., 2020b), smaller overall stress drops and weaker near-field ground motions (Choy and Kirby, 2004; Manighetti et al., 2007; Radiguet et al., 2009; Hecker et al., 2010), and lower rates of dynamic aftershock triggering (Gomberg, 1996), than those along immature faults. Mature faults may also exhibit steadier interseismic strain accumulation (Wang et al., 2021) and more regular recurrence intervals (Berryman et al., 2012; Thakur and Huang, 2021).

These relationships illustrate how the structural setting of an earthquake, including fault segmentation and structural maturity, could have an important bearing on seismic hazard, for example, by influencing potential rupture lengths and magnitudes, amounts and distributions of slip, and involvement of multiple faults. They raise the possibility of incorporating easily-observed metrics for structural maturity—such as fault cumulative offset, age, slip rate, length, and surface trace complexity (Choy and Kirby, 2004; Manighetti et al., 2007, 2021)—in hazard assessments and earthquake early warning algorithms (Dolan and Haravitch, 2014; Perrin et al., 2016; Hutchison et al., 2020). However, other factors including fault geometry and kinematic style, tectonic environment, and rheology of ruptured material may also influence earthquake behaviour, potentially complicating matters (e.g., Oskin et al., 2012; Teran et al., 2015). To clarify these relations further, careful observations are needed of earthquakes from a range of structural and geological settings and which span the full spectrum of fault structural maturity.

The M_w 6.5 Monte Cristo Range earthquake (MCRE) ruptured on 15 May 2020 at 11:03 UTC (4:03 AM local time) mostly along previously unmapped faults in the Mina deflection zone within the central Walker Lane, Nevada (Wesnousky, 2005) (Figure 3.1). The evolution of the Mina deflection since the Miocene has given rise to a region of conspicuously varied lithology and geometrically complex faulting (Wetterauer, 1977; Oldow et al., 1994, 2008). Fault segments mapped in the western Mina deflection, just west of the MCRE, are relatively short (on average 1–3 km with a maximum segment length of $\sim$10 km), highly distributed, and variably oriented (Dohrenwend, 1982; Oldow et al., 1994), and some of them reactivate inherited structures (Wetterauer, 1977; Oldow et al., 2008). Faults and fault-bounded blocks within the Mina deflection are thought to rotate about vertical axes to accommodate dextral shear transfer across the Walker Lane (Wesnousky,

2005). This crustal rotation potentially diverts the faults away from being favorable to slip, preventing the emergence of a single through-going fault that could attain structural maturity. Following the mainshock, field mapping revealed zones of distributed fractures within an approximately 28 km-long and up to 800 m wide rupture zone (Dee et al., 2021; Koehler et al., 2021). This distributed deformation, together with the slow rupture velocity (on average 1.5 km/s, Liu et al., 2021a), extensive off-fault aftershocks (Ruhl et al., 2021), and the weakly discernible neotectonic landforms indicative of long-term faulting (Dee et al., 2021; Koehler et al., 2021), also suggest that the MCRE may have ruptured a highly-immature fault system.

Several studies have investigated the MCRE rupture kinematics using a variety of data and methods. Dee et al. (2021) and Koehler et al. (2021) collected detailed field observations of surface ruptures and secondary fissures. Bormann et al. (2021) rapidly deployed temporary seismic stations and captured near-field moderate magnitude aftershocks (M_{L} 4–5). Ruhl et al. (2021) relocated the seismicity of the MCRE sequence and inferred that the mainshock and aftershocks ruptured fault-fracture networks that merge at depth. Various geodetic data sets have been inverted for the mainshock fault geometry and slip distribution, including Interferometric Synthethic Aperture Radar (InSAR) interferograms and azimuth offsets, Global Navigation Satellite Systems (GNSS) displacements, and seismic waveforms (Zheng et al., 2020; Sadeghi Chorsi et al., 2021; Cui et al., 2021; Hammond et al., 2021; Li et al., 2021b; Liu et al., 2021a). These published models comprise one to three fault segments and suggest peak coseismic slip of between 0.6–1.7 m.

Our study builds on this previous work by integrating our own geodetic mainshock slip model, aftershock relocations and mechanisms, and new field observations into a single study. Our mainshock model is distinct from previous ones in that model slip is restricted to seismogenic depths that are independently constrained using calibrated aftershock focal depths. Some of our field observations of surface cracking, including the first of pebble-clearing features where pebbles and gravels are cleared unilaterally (on one side only) of surface cracks, also shed new light on the complex block motions within the fault zone. Our discussion of discrepancies between the findings of the different methods highlights the importance of incorporating geodetic, seismological and field data to capture the full complexity of a rupture especially in a shattered crustal zone. Finally, we frame our results in the context of fault structural maturity and show that various attributes of the MCRE are characteristic of rupture within an emergent and highly-distributed fault system.

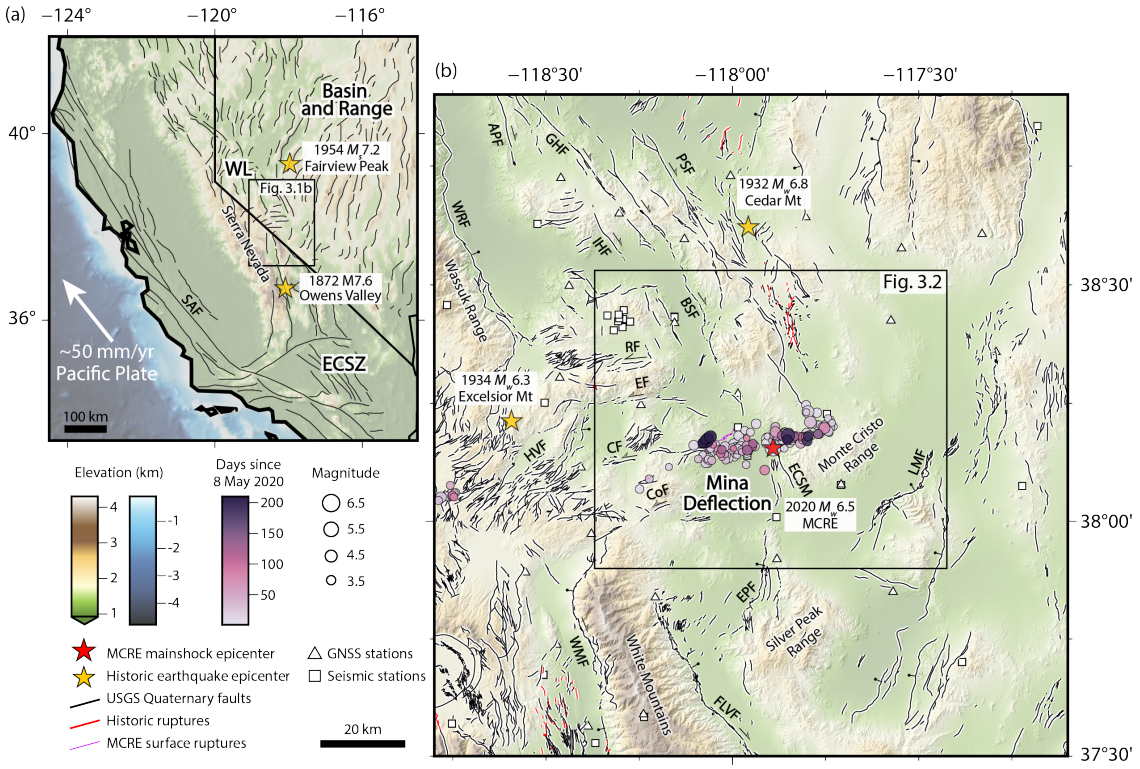


Figure 3.1: Tectonic setting of the 2020 Monte Cristo Range earthquake (MCRE). (a) Regional context of the Eastern California shear zone (ECSZ) and Walker Lane (WL) and (b) a zoom in of the Walker Lane. The red star is our relocated MCRE epicenter and yellow stars indicate historic earthquake epicenters from the National Earthquake Information Center (NEIC) of the United States Geological Survey (USGS) and from Callaghan and Gianella (1935). The circles in (b) are relocated aftershocks of the MCRE, scaled with magnitude, and shaded with the number of days since 8 May 2020. Thin purple lines are the MCRE surface ruptures from Dee et al. (2021) and Koehler et al. (2021). Major faults (black lines) and historic ruptures (red lines) are from the USGS Quaternary fault and fold database (see Data and Resources): APF—Agai Pah fault; BSF—Benton Springs fault; CF—Candelaria fault; CoF—Coaldale fault; ECSM—Eastern Columbus Salt Marsh fault; EF—Excelsior fault; EPF—Emigrant Peak fault; FLVF—Fish Lake Valley fault; GHF—Gumdrop Hills fault; HVF—Huntoon Valley fault; IHF—Indian Head fault; LMF—Lone Mountain fault; PSF—Petrified Springs fault; RF—Rattlesnake fault; SAF—San Andreas fault; WMF—White Mountain fault; WRF—Wassuk Range fault.

3.5 Regional Context

The Walker Lane lies between the Sierra Nevada block and the Basin and Range extensional province (Locke et al., 1940; Stewart and Ernst, 1988) and accommodates ∼20% of the ∼50 mm/yr dextral motion between the Pacific and North America Plates at this latitude (Dokka and Travis, 1990; Bennett et al., 2003). This shear is distributed across arrays of NW-trending right-lateral strike-slip faults, N- to NE-trending normal faults, and NE-striking left-lateral strike-slip faults (Figure 3.1), several of which have hosted large historic earthquakes, including the 1954 M_s 7.2 Fairview Peak, 1932 M_w 6.8 Cedar Mountain, and 1872 M 7.6 Owens Valley earthquakes (Hodgkinson et al., 1996; Wesnousky, 2005).

The Mina deflection zone within the central Walker Lane disrupts the otherwise mostly northerly-oriented structures with a suite of discontinuous E-W, left-lateral faults (Pierce et al., 2021). These accommodate a ∼25–60 km-wide right step that helps transfer dextral slip between the longer, NW-striking, right-lateral White Mountain and Fish Lake Valley fault zones to the southwest and the Benton Springs and Petried Springs faults to the northeast (Wesnousky, 2005; Lee et al., 2009; DeLano et al., 2019). Geologic, geomorphic, geodetic, and paleomagnetic studies suggest that they do so by rotating clockwise around vertical axes, opening small, triangular basins at the fault termini (Wesnousky, 2005; Petronis et al., 2009; Rood et al., 2011; Nagorsen-Rinke et al., 2013; Bormann et al., 2016; Grondin et al., 2016; DeLano et al., 2019; Pierce et al., 2021). From north to south, the most conspicuous of these Mina deflection faults are the Rattlesnake, Excelsior, Candelaria, and Coaldale faults (Figure 3.1), each of which is made up of numerous discrete segments that sum to lengths of up to ∼20 km (Wesnousky, 2005). In general, the faults exhibit alternating north- and south-facing vertical scarps, geomorphic marker offsets, linear fault-bounded ridges, *en echelon* fractures and pressure ridges, and beheaded stream channels within bedrock and Quaternary alluvium, indicative of left-lateral and normal faulting (Wesnousky, 2005; Lee et al., 2006). The only historic earthquake in this area is the 1934 M_w 6.3 Excelsior Mountain earthquake which produced *en echelon* fissures and down-to-the-north vertical scarps along the Excelsior fault, consistent with left-lateral–normal slip (Callaghan and Gianella, 1935; Wesnousky, 2005).

The MCRE is the largest instrumentally-recorded earthquake in the Mina deflection. The mainshock ruptured areas where E-trending Quaternary faults have not been mapped, as well as sections where the rupture projects into the NW-striking Benton Springs and Petrified Springs faults in the north (Koehler et al., 2021). In the west, the MCRE rup-

tured along strike (east) of the mapped Candelaria fault. Although there are no historic earthquakes along the Candelaria fault, it exhibits evidence for surface ruptures in the middle to late Holocene (Wesnousky, 2005), with a net left-lateral–normal slip of ∼900 m since 2.8 Ma, measured from offset markers of Pliocene basalt, for a Quaternary slip rate of ∼0.3 mm/yr (Speed and Cogbill, 1979).

3.6 Data and Methodology

3.6.1 Surface Faulting Observations

Surface Rupture Mapping

One of us (I. P.) visited the MCRE area from May 16 (one day after the earthquake) to June 7, 2020, as part of a larger field team investigating surface faulting. The field observations described here are based upon and augment the sub-centimeter resolution uncrewed aerial system (UAS) imagery, detailed surface rupture mapping, fault offset measurements, and surface crack orientation data collected by this team and published by Dee et al. (2021) and Koehler et al. (2021). We reinterpret these data sets in the context of our InSAR analysis of mainshock faulting (see Sections 3.7.1, 3.8.1).

Paleoseismic Trenching

During this fieldwork, one of us (I. P.) also excavated an exploratory paleoseismic trench to seek evidence for any previous ruptures. The trench was sited along what appeared to us to be one of the pronounced MCRE surface ruptures, and oriented perpendicular to their northeasterly trend. The 4.7 m long by 0.9 m wide by 1.3 m deep trench was excavated by a backhoe, logged, and back-filled on the same day. Both trench walls were photographed with a hand-held camera and an orthomosaic was created using Structure from Motion (see Data and Resources Section). No samples were collected from the trench.

Long-term Fault Offsets

We analyzed satellite multispectral imagery and digital topography to search for and quantify any geologic or geomorphic offsets indicative of long-term faulting or cumulative displacement (a proxy for structural maturity). Using a Sentinel-2B image acquired on May 3, 2022 (see Data and Resources), we generated false color imagery with band combinations 4-3-2 (natural color) and 12-11-2 (false color). We enhanced these with a

standard deviation color stretch to highlight feature contrasts from which apparent cumulative offsets were derived. At fault scarp locations, we extracted topographic profiles from the United States Geological Survey (USGS) 3D Elevation Program (3DEP) 1/3 arc-second (∼10 m) seamless digital elevation model (DEM) in order to estimate vertical separations.

3.6.2 Geodetic Slip Modeling

InSAR and GNSS Data and Processing

We produced three six-day interferograms using SAR images acquired by the European Space Agency's C-band (wavelength 5.6 cm) Sentinel-1 satellites (see Data and Resources). The SAR images were obtained on four dates between 10 May 2020 and 17 May 2020 by two adjacent descending tracks and one ascending track (Table 3.1), offering three looking angles. The interferograms were processed with GAMMA software (Wegmüller et al., 2016). We removed the topographic phase contribution using the 3 arc-second (∼90 m) Shuttle Radar Topography Mission (Farr and Kobrick, 2000) DEM (see Data and Resources). The interferograms were filtered using a power spectrum algorithm (Goldstein and Werner, 1998), unwrapped using the branch-cut algorithm, and georectified to the Universal Transverse Mercator coordinate system (UTM zone 11N) with a 90 m pixel resolution (Figure 3.2). Lastly, we manually fixed unwrapping errors in areas that show spurious phase discontinuities and carefully removed a few patches disconnected from the main interferogram and for which the unwrapping uncertainty is high.

Table 3.1: Details of the InSAR imagery we used to model the 15 May 2020 Monte Cristo Range earthquake. Line-of-sight (LOS) incidence angles (from the vertical) and azimuths (degrees from north) are measured at the mainshock epicenter. Abbreviations: a—ascending track, d—descending track, intf—interferogram.

Interferogram	Track	Date 1	Date 2	LOS incidence (°)	LOS azimuth (°)
intf1	d144	10 May 2020	16 May 2020	33	281
intf2	d71	11 May 2020	17 May 2020	44	280
intf3	a64	10 May 2020	16 May 2020	41	80

We also collated regional GNSS coseismic offsets processed by the Nevada Geodetic Laboratory (NGL) using their updated data set released on 19 June 2020 (Blewitt et al., 2018). The data comprise continuous GNSS stations belonging to the Mobile Array of GPS for Nevada Transtension (MAGNET), Network of the Americas (NOTA), and other

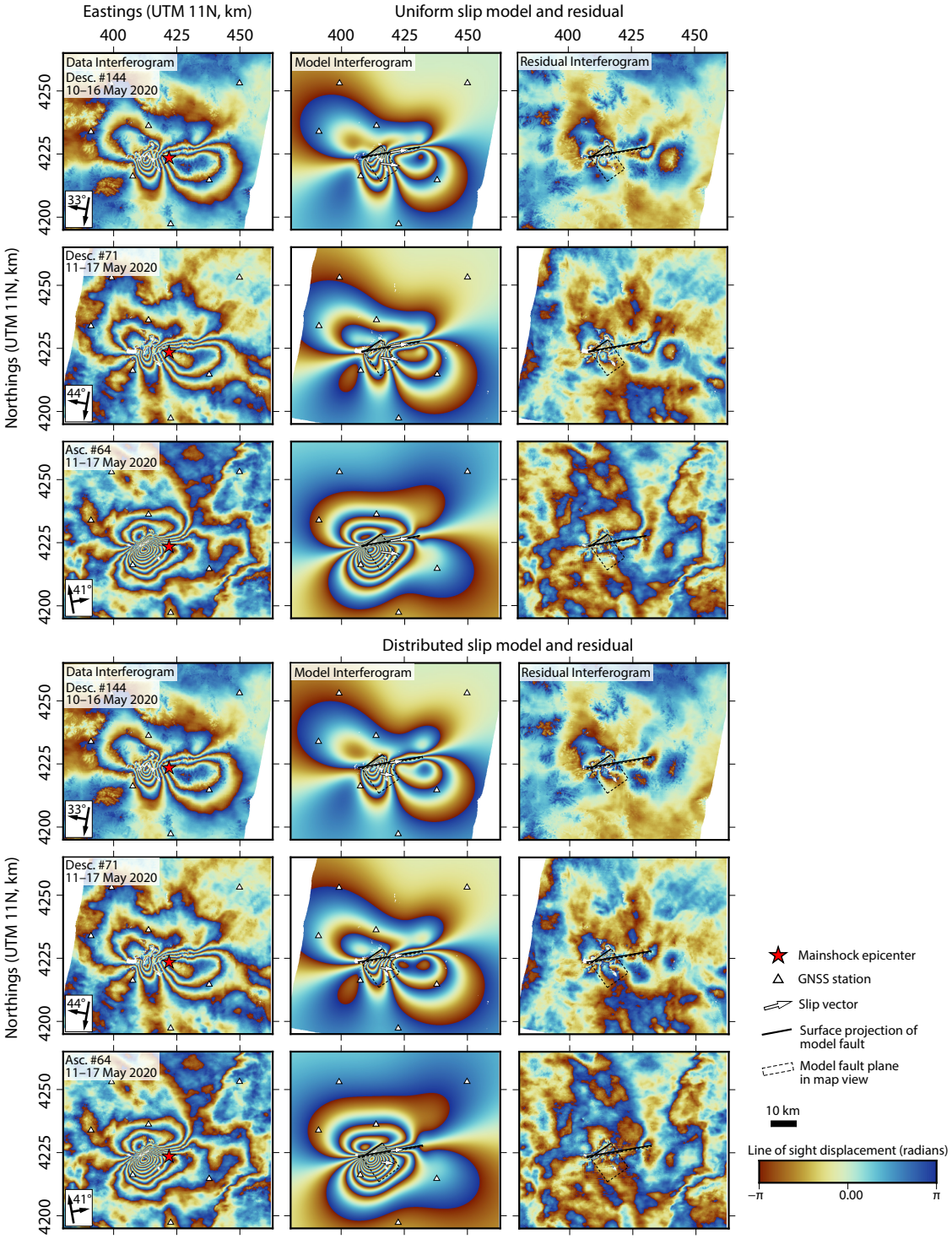


Figure 3.2: Observed, model, and residual wrapped interferograms of the uniform slip and distributed slip inversions. The satellite orbital tracks (desc.—descending, asc.—ascending) are followed by the track number and the interferogram date range. Satellite track and line-of-sight azimuths are given as long and short vectors in the corner of the data interferograms, along with the incidence angle. The thick black lines indicate the surface projection of the model fault, the dashed box illustrates the model fault plane in map view, and the white arrows denote the slip vector of the hanging wall. The red star is the relocated mainshock epicenter and the white triangles are nearby GNSS stations. Unwrapped interferograms are provided in Supplementary Figure 3.18.

networks, which together provide a typical station spacing of ∼20 km across the study area (Supplementary Figure 3.14).

Uniform Slip Modeling

We solved first for the mainshock fault geometry and then for the slip distribution by jointly inverting the three unwrapped interferograms and the GNSS coseismic offsets, using a routine elastic dislocation procedure (e.g., Wright et al., 1999) described in detail below. To prepare the data for inversion, the three interferograms were downsampled using a Quadtree algorithm (e.g., Jónsson et al., 2002; Wright et al., 2003) in which the sampling block size and variance threshold were adjusted such that each downsampled dataset comprised ∼400–600 datapoints concentrated within areas of high phase gradient. We only modeled the 25 GNSS data points within the extent of the InSAR coverage, all within ∼75 km of the mainshock epicenter (Supplementary Figure 3.14). We experimented with using horizontal and vertical offsets or only the horizontal ones; finding little difference in our results, our final model incorporates all three components. Since the two descending interferograms share similar look angles, they are together weighted equally to the single ascending interferogram and the GNSS offset dataset.

We first estimated the fault location and geometry by assuming that the earthquake occurred along a rectangular fault plane in a uniform elastic half-space with Lamé constants λ and $\mu = 3.2 \times 10^{10}$ Pa. We solved the Okada (1985) equations using a downhill simplex algorithm (Press et al., 1992) to obtain fault plane parameters that minimize misfits between data and model surface displacements. We solved for the fault strike, dip, rake, slip, center latitude and longitude, length, top depth, and bottom depth, but kept slip fixed at 0.5 m because of an expected trade-off with fault width. To ensure that a broad parameter space is searched and the global minimum misfit found, we used 500 Monte-Carlo restarts with starting parameters selected randomly from specified ranges (Wright et al., 1999; Funning et al., 2005; Elliott et al., 2012). We started with broad parameter bounds centered upon values estimated directly from the InSAR imagery (strike, location, length, top depth) or from automated mainshock focal mechanisms (dip, rake, bottom depth), and then repeated the inversion with the narrower bounds given in Supplementary Table 3.4 once a satisfactory, preliminary model fault geometry had emerged. For each interferogram, we also solved for 3 nuisance parameters: a translation in line-of-sight (LOS) to account for the uncertainty in LOS at the unwrapping reference point, and E-W and N-S gradients in LOS to account for residual orbital ramps.

We initially modeled the geodetic data with a single, uniform slip fault plane, but the resulting model interferograms did not visually fit the InSAR data well. Adding a second uniform slip plane provided a much better visual and numerical fit, with eastern and western model faults accounting for the distinct fringe patterns observed east and west of the epicenter (Figure 3.2).

Distributed Slip Modeling

Having determined the fault geometry, we next solved for the slip distribution. We started by extending the two uniform slip model fault planes along strike and up- and down-dip, to allow for the possibility of slip outside of the extents of the uniform slip model. Both ends of the western and eastern model faults were extended $\sim$1 km along strike and their bottom depths were increased to 14 km to allow for tapering of slip at the base of the seismogenic zone. This does not exceed 15 km, the local seismogenic thickness inferred from our relocated hypocenters, the deepest of which is 11 km $\pm$ 1–4 km (see Sections 3.6.3, 3.7.3). The extended model fault planes were then each divided into 2 km $\times$ 2 km sub-fault patches, and the slip distribution was estimated using a Laplacian smoothing operator (Wright et al., 2004; Funning et al., 2005) and a slip positivity constraint (Bro and De Jong, 1997). Following Wright et al. (2004), we chose a smoothing constant that maximizes the smoothness of the slip distribution without greatly increasing the model misfit. Full parameters of our final slip model are provided in Supplementary Long table 3.7.

3.6.3 Seismological Analysis

Hypocentral Relocations

In addition to geodesy, we relocated the hypocenter locations of the mainshock and 196 well-recorded foreshock and aftershock events using the *mloc* multi-event relocation software (Bergman and Solomon, 1990; Walker et al., 2011; Karasözen et al., 2019; Benz, 2021). This utilizes arrival time data of multiple earthquake events recorded at multiple stations to minimize biases from unknown Earth velocity structure, and thus obtain calibrated hypocenter parameters. We used arrival time data gathered from the International Seismological Centre (ISC) bulletin and the USGS Advanced National Seismic System (ANSS) Comprehensive Earthquake Catalog (ComCat), for well-recorded events from 8 May 2020 to 3 December 2020 (see Data and Resources Section).

Mloc adopts the hypocentroid decomposition algorithm which separates the relocation into two inverse problems, for which tailored arrival time data can be used. First, the program uses all available arrival time data at all epicentral distances to solve for the relative locations of each hypocenter in the cluster. These cluster vectors connect each event to the hypocentroid—the geometric mean for all hypocenters (Supplementary Figure 3.15). Second, the algorithm calculates the absolute location of the hypocentroid and updates the absolute hypocenter locations of every event in the cluster using all the arrival times at close range. In our case, more than 4,500 arrival time readings at distances of less than 0.7° contributed to the absolute relocation step (Supplementary Figures 3.16, 3.17). The high density of local recordings allowed us to solve for focal depth as a free parameter, though for some events we manually adjusted depths to better fit near-source or local-distance data. We utilized a bespoke regional velocity model for the crust and upper mantle and the ak135 global model for below 120 km (Kennett et al., 1995) (Supplementary Table 3.5). Our relocated hypocentral data set is tabulated in Supplementary Long table 3.8 and travel time residuals are plotted in Supplementary Figure 3.17.

Regional Moment Tensors

Among the 197 relocated events, we also calculated regional moment tensor (RMT) solutions for the mainshock and 89 best-recorded aftershocks. We modeled regional waveforms collected from the Incorporated Research Institutions for Seismology (IRIS) and the Nevada Seismological Laboratory at the University of Nevada, Reno (UNR) at distances of 0–500 km (see Data and Resources Section). For events M_w 5.0 or smaller, we used the whole seismograms, bandpass filtered at ∼10–100 s. For events larger than M_w 5.0, we used W-phase waveforms filtered in the passband ∼50–2000 s. We solved for the RMTs by using the inversion methods, Green's functions, and central U.S. velocity model of Herrmann et al. (2011). To determine the best fit between observed and modeled waveforms, we assumed a point source and the moment tensor components were grid searched at 1 km depth intervals. The dense regional station coverage provided well-constrained centroid depths. Further sensitivity testing revealed the other RMT parameters to be insensitive to perturbations of a few kilometers in centroid depth.

3.7 Results

3.7.1 Mainshock Surface Ruptures

Field observations include variably-oriented surface ruptures with discernible slip and measurable offset, and smaller cracks without clear kinematic indicators (Dee et al., 2021; Koehler et al., 2021). Surface ruptures have lengths of ∼100–200 m to ∼1–2 km but are heavily segmented with gaps and stepovers. Individual segments are mostly a few meters to tens of meters long, though a few reach lengths of >100 m. The surface cracks are mostly a few meters to tens of meters long, are distributed away from the main fault trace (up to ∼500 m), and have larger variations in orientation than the surface ruptures (Figure 3.3). In the eastern part of the rupture area, field observations of surface deformation are sparse, and mostly located off the main eastern fault as revealed by InSAR. This is consistent with our eastern InSAR-GNSS model fault, which shows a pronounced shallow slip deficit (Section 3.7.2). The longest alignment of surface ruptures is immediately south of and conjugate to the eastern model fault (Figure 3.3a), and involves up to ∼10 cm of right-lateral motion over a distance of ∼1.2 km (Dee et al., 2021; Koehler et al., 2021).

Most of the observed surface ruptures and cracks lie within the western part of the mainshock fault zone and are the main focus of this section. There are two main alignments, both trending approximately northeast (Figure 3.3a). The first, narrower alignment (referred to herein after as the 'western fault zone') approximates the trace of the western InSAR-GNSS model fault over a distance of ∼10 km, and accommodates up to ∼10 cm of left-lateral and ∼7 cm of vertical motion (Figure 3.3b,c). These motions are roughly consistent with our InSAR analysis, which supports up to ∼10 cm of surficial, oblique (left-lateral–normal) slip along the SE-dipping, western model fault (Section 3.7.2). However, the vertical slip observed in the field exhibits a mix of down-to-the-southeast (DTSE) and down-to-the-northwest (DTNW) throw, indicating that the shallow faulting is more complex than our InSAR-GNSS model can resolve.

The second main alignment of fractures (referred to herein after as the 'northern fault zone') lies ∼1–3 km to the northwest of and sub-parallel to the western fault zone, and contains the largest discrete offset observed anywhere in the field (Figure 3.3b,c). It comprises several discrete arrays of faults and cracks, distributed even more diffusely than in other areas, with thousands of individual fractures across a ∼6 km by ∼1 km zone. Though the overall trend is northeastwards, individual fracture sets exhibit a wide variety of orientations. Where fault slip can be resolved, the kinematics are predominantly left-

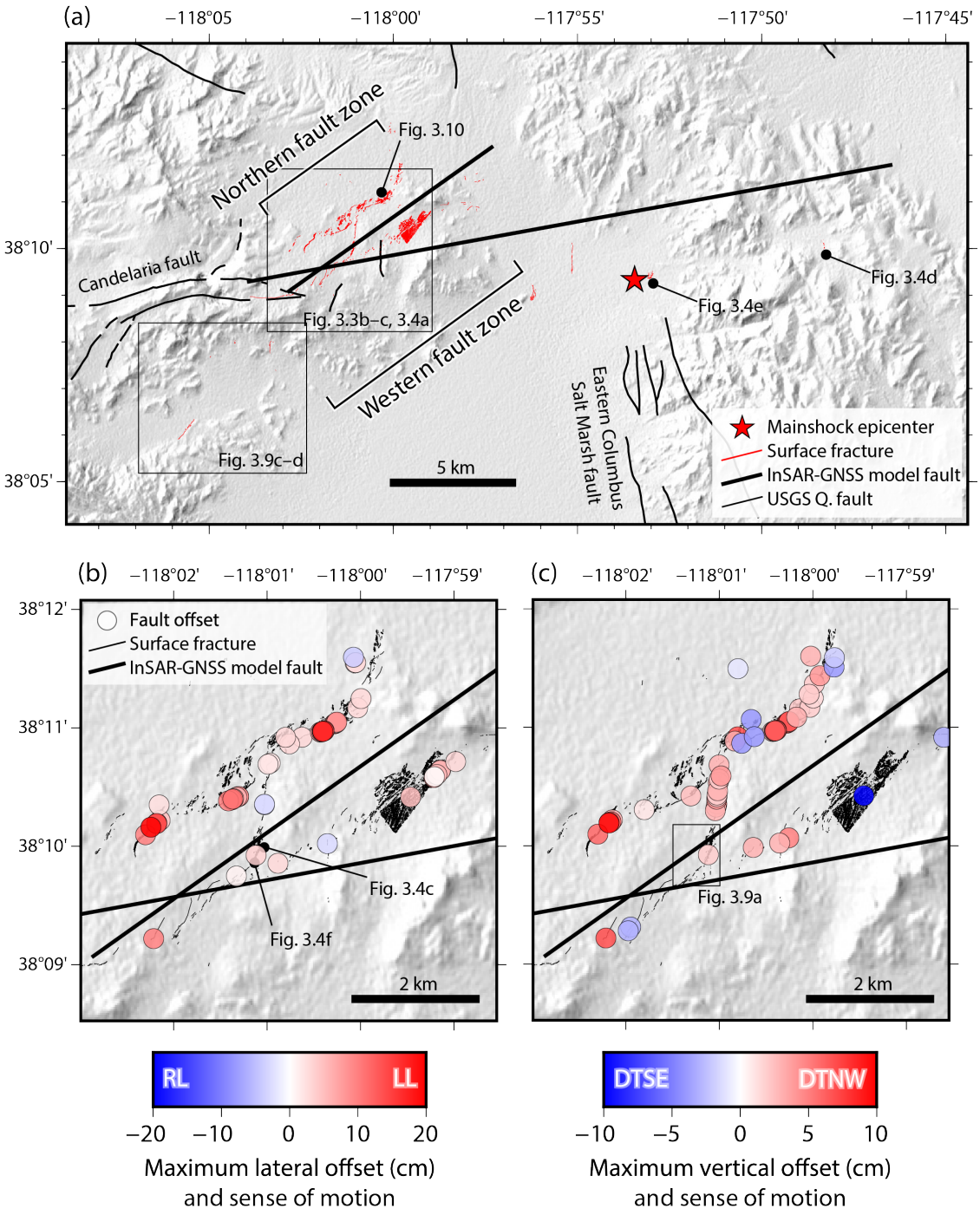


Figure 3.3: (a) Multi-directional hillshade map showing our calibrated relocated MCRE mainshock epicenter (red star), MCRE surface faulting and cracks mapped in the field (Dee et al., 2021; Koehler et al., 2021) (thin red lines), surface projections of our InSAR-GNSS model faults (thick black lines), and regional active faults as in previous figures (thin black lines). Sub-panels show (b) lateral and (c) vertical fault offsets measured in the field. Where several measurements were collected from the same locality, we take the maximum. The red- and blue-shaded circles represent the sense of motion, with the color gradient reflecting the amount of fault offset in centimeters. Positive values are assigned to left-lateral offsets in (b) and down-to-the-NW (DTNW) offsets in (c). Thin black lines are the near-field fractures, and thick black lines are InSAR model fault surface projections.

lateral (with offsets of up to ∼20 cm) and vertical, DTNW (with throw of up to ∼10 cm). Though this fault zone does not align with our InSAR-GNSS model faults, it is consistent with a minor discontinuity visible in the unwrapped interferograms (Figure 3.4a,b). The sense of the LOS displacement discontinuity in the ascending interferogram supports that the left-lateral motion dominates over the vertical component across this northern fault zone.

Within the western and northern fault zones, many of the fractures also exhibit a clearing of loose pebbles or gravel from only one side of each crack (Figure 3.4c–f). This phenomenon is particularly evident where fractures break desert pavement surfaces, and is generally absent from sandy surfaces. The width of the cleared zone is typically a few centimeters, large enough that the cleared side could be mapped from fine-resolution UAS imagery (Dee et al., 2021; Koehler et al., 2021) (Figure 3.4c). The side that is cleared is consistent within each fracture set but can vary between sets, illustrated by the tip of white triangles in Figure 3.4a. For example, fractures along the northern fault zone are predominantly cleared of pebbles to the southeast (upthrown) side. Only a few are bilaterally cleared. We interpret that the predominance of unilateral clearing may represent significantly higher ground acceleration on one side of each fracture during the rupture process, perhaps related to local rupture dynamics. We further discuss the importance of these fractures in Section 3.8.1.

3.7.2 Mainshock Source Model and Mechanisms

Both ascending and descending interferograms contain clear coseismic fringe patterns, with a maximum LOS displacement of ∼31 cm (away from the satellite) observed in the ascending data (Figure 3.2, left column). The E-W orientation of the two largest, northern and southern fringe lobes—with differing sense of LOS displacement in the ascending and descending data—is consistent with predominantly E-W, left-lateral faulting. However, the presence of a third, more condensed southwestern lobe in the descending interferogram hints at some variation in the faulting mechanism. In this area, LOS of displacements are away from the satellite in both ascending and descending interferograms, consistent with localized subsidence (unwrapped interferograms are provided in Supplementary Figure 3.18).

Our modeling results further illuminate the complexity in fault geometry and mechanism. Our preferred two-fault inverse modeling reproduces the InSAR-GNSS data well (Figures 3.2, 3.14, with root mean square residual displacements of 0.6 cm and 0.8 cm in the

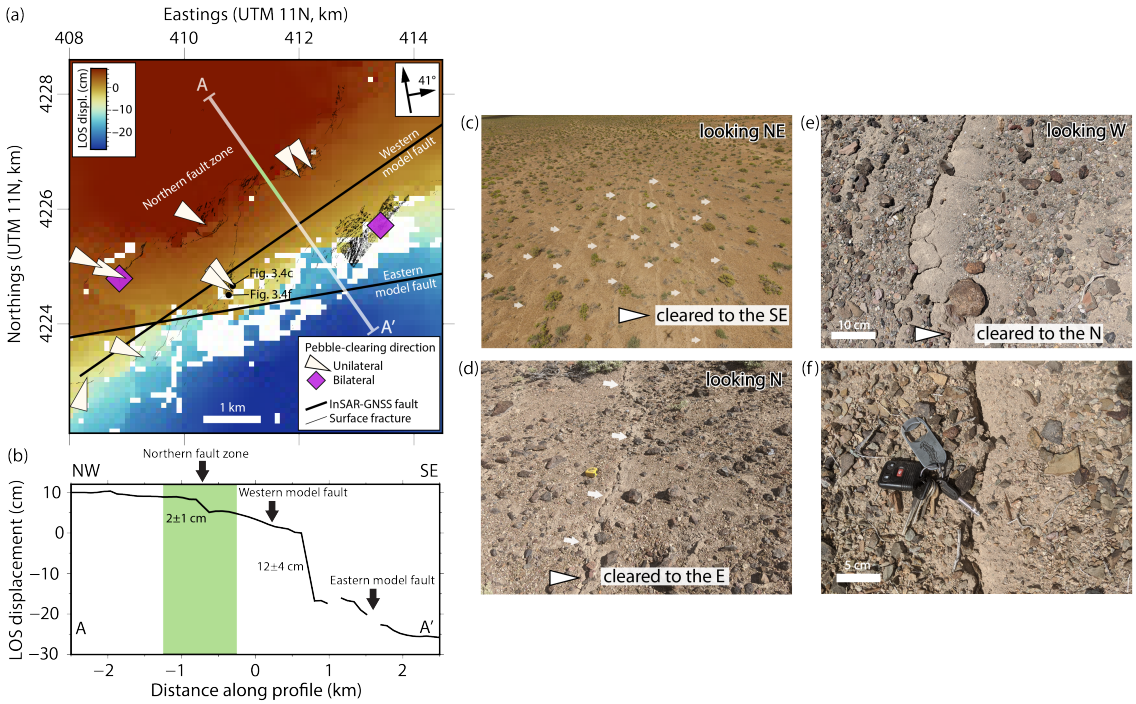


Figure 3.4: Photos of pebble clearing phenomena from cracks and its direction of clearing. (a) Unwrapped ascending interferogram of the western MCRE rupture area showing the MCRE fault offsets and cracks mapped in the field (Dee et al., 2021; Koehler et al., 2021) (thin black lines), model faults (thick black lines), and pebble clearing orientation (symbols). The direction to which the sediments are cleared are represented by white triangles (unilateral—cleared on only one side) and magenta diamonds (bilateral—cleared on both sides); triangle tips point to the cleared side or upthrown direction of the cracks. (b) Transect of unwrapped line-of-sight (LOS) displacements along A–A' in panel (a). The shaded area illustrates the subtle LOS displacement discontinuity which co-locates with the northern fault zone. (c) Oblique uncrewed aerial system view looking northeast of a crack field with clearings on the southeast side of each crack indicated by white arrows. (d) Photo looking north, with a crack cleared to the east (tape measure for scale). (e) Close-up photo looking west, with a crack cleared to the north. (f) Close-up of crack showing clearing of loose materials on one side of the crack. Geographic coordinates of c–f are as follows: (38.1657°N, 118.0184°W), (38.1658°N, 117.8060°W), (38.1562°N, 117.8840°W), (38.1641°N, 118.0190°W).

uniform and distributed slip cases, respectively. In the uniform slip inversion where the fault parameters are solved freely, the western and eastern model faults are 8.4 km and 23.5 km long, respectively (Table 3.2). The eastern model fault strikes 80°, dips steeply southwards at 88°, is predominantly left-lateral with rake −4°, and crosses the entire rupture zone. The shorter western model fault crosses the eastern fault with strike 55°, dips more gently at 49° SE, and exhibits oblique left-lateral–normal motion with rake −54°, explaining the subsidence inferred from the InSAR data. The western model fault terminates along strike from the eastern end of the Candelaria fault (Figure 3.3a), but neither of the model faults align with previously mapped structures. Our model slip distribution shows that of the total geodetic moment of 6.1×10^{18} Nm, ∼70% occurs on the eastern model fault and ∼30% on the western one. Maximum slip of 1.0 m occurs on the eastern fault at 8–10 km depth, but peak slip on the western fault of 0.7 m is much shallower at ∼3–4.5 km (Table 3.2). Both model faults exhibit a clear shallow slip deficit, where only up to 0.1 m of model slip reaches the shallowest sub-faults (discussed further in Section 3.8.3).

We estimate model uncertainties and trade-offs by assessing the 500 Monte Carlo outputs from the uniform slip inversion (Supplementary Figures 3.19, 3.20). Dip and rake are the two most inter-dependent parameters, whereas other parameters are generally clustered and do not strongly trade-off with each other. Inversion solutions with root mean square residual displacements of less than 0.9 cm (i.e. within ∼10% of the global minimum misfit) are used to estimate standard deviations for each parameter. These indicate that western and eastern model fault strike varies by ±8° and ±1° (one standard deviation), respectively, dip by ±2° and ±3°, rake by ±7° and ±1°, easting by ±1 km and ±2 km, northing both by ±0.3 km; fault length by ±0.3 km and ±2 km; top depth by ±0.1 km and ±0.2 km; and bottom depth both by ±2 km.

We conducted some additional tests in order to scrutinize further two of the more interesting aspects of our modeling results. The first of these is that the two model faults cross each other, an unusual attribute if real. To test whether this crossing pattern is robust, we repeated the uniform slip inversion but with the geometry of the eastern model fault fixed in order to force its termination against the western fault (Supplementary Figure 3.21). Uniform slip inversion of this configuration leaves large residual displacements at the fault intersection and the outer ends, showing that two non-intersecting faults cannot explain the InSAR data and suggesting that this unusual geometry is real.

The second interesting aspect of our modeling results is that the data are reproduced well without the need for a model fault along the northern fault zone. However, we ex-

Table 3.2: Parameters of our preferred, two fault InSAR-GNSS uniform and distributed slip models. Easting and Northing refer to the center of the model fault surface projection in the Universal Transverse Mercator (UTM) zone 11N coordinates. The peak slip depth refers to the central depth of the peak slip sub-fault patch. The full slip distribution is tabulated in Supplementary Long table 3.7.

Model fault	Easting (km)	Northing (km)	Strike (°)	Dip (°)	Rake (°)	Length (km)	Width (km)	Top depth (km)	Bottom depth (km)	Moment ($\times 10^{18}$ Nm)	Peak slip (m)	Peak slip depth (km)
Western	412.292	4225.944	55	49	-54	8.4, 10*	15.8, 18.0*	1.3, 0*	13.2, 13.5*	2.1, 1.9*	0.5, 0.7*	3.8*
Eastern	419.401	4225.717	80	88	-4	23.5, 26*	9.0, 14.0*	2.0, 0*	11.0, 14.0*	3.4, 4.1*	0.5, 1.0*	9.0*

*The distributed slip model parameters that changed from the uniform slip.

plored whether a three fault model may explain the InSAR data better still, in particular the subtle LOS displacement discontinuity observed across the northern fault zone which our two fault model cannot emulate (Figure 3.4a,b). To do so, we first fixed all parameters of the western and eastern model faults with their best uniform slip solutions from Table 3.2 (except the dip, rake, and bottom depth of the western segment). We then added a third, northern model fault to account for the northern fault zone, fixing several of its own parameters: its strike of 54° or 234°, center points and length of 6 km are chosen to approximate the mapped fractures, and its top depth of 0 km accounts for surface rupturing (Supplementary Table 3.4). Finally, we solved for the northern fault dip, rake, bottom depth, and slip, with each given broad parameter bounds for the algorithm to search for the lowest misfit. The inversion results match but do not improve upon the 0.8 cm misfit of the simpler two fault model (Figure 3.5, second column). We obtain a similar moment of 5.6×10^{18} Nm, but with 7 cm of right-lateral–normal slip (rake = $-138°$) on the northern fault (Supplementary Table 3.6), opposite in sense to the left-lateral field offsets. We further experimented with adjusted inversion configurations but none yielded stable results that agreed with field or seismological observations. This difficulty might arise because a rectangular fault plane poorly fits the sinusoidal trace of the northern fault zone (Figure 3.3a), or because the near-field InSAR data along the northern fault zone exhibit a relatively gradual phase gradient resulting in fewer downsampled InSAR data points for the inversion. We overcame this challenge by generating a suite of uniform slip forward models with varying geometries for the northern model fault: NW-dipping left-lateral–normal, SE-dipping left-lateral–reverse, and a vertical fault with left-lateral–dip-slip motion (Supplementary Table 3.6). Slip was fixed to 10 cm, the median offset measured in the field. Results suggest that a vertical northern fault with left-lateral oblique motion

best reproduces the InSAR data, though it does not fully match the observation (Figure 3.5, last three columns). We discuss this geometry further in Section 3.8.1.

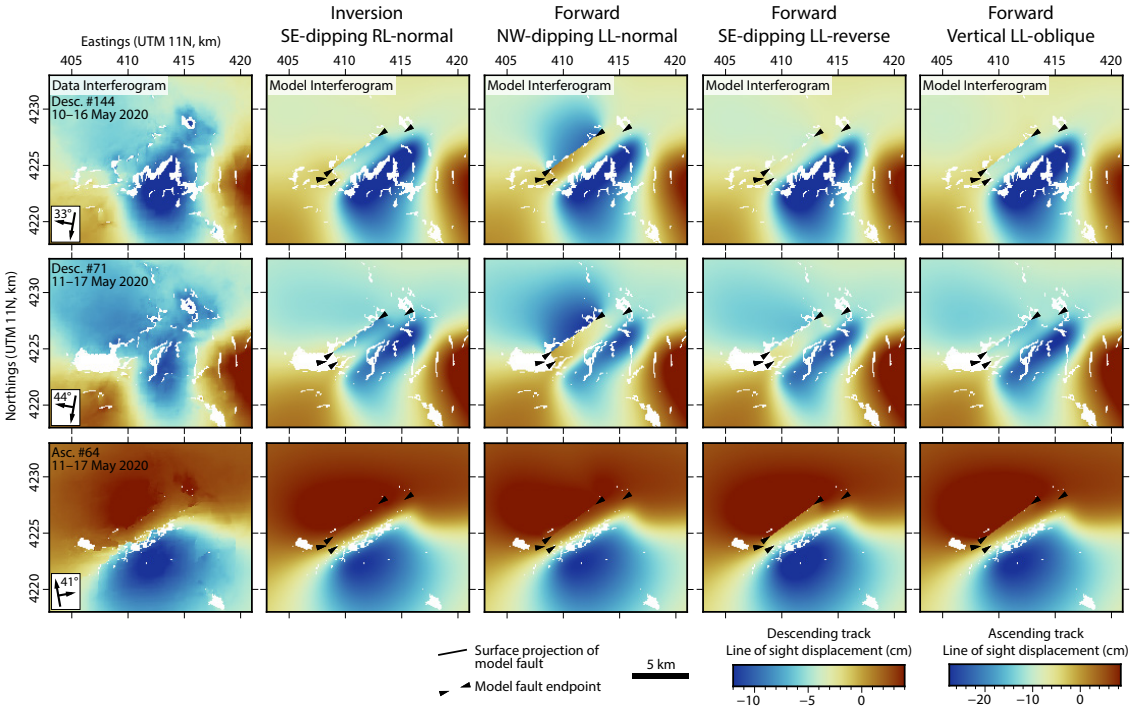


Figure 3.5: Observed and model interferograms in the western MCRE rupture zone, showing the addition of a third, northern model fault along the northern fault zone. The left-hand column shows unwrapped data interferograms for the descending (upper and middle rows) and ascending (bottom row) tracks. Each remaining column shows an inverse or forward model interferogram for a particular northern model fault dip direction and slip sense (LL—left-lateral; RL—right-lateral). Black triangles mark the model fault end points so as to not obscure subtle phase discontinuities or the comparison with the data interferogram.

Our seismological analyses reveal additional characteristics of the mainshock rupture. The relocated, calibrated mainshock hypocenter is at 9 km depth on the eastern model fault plane (Figure 3.6a), indicating that the earthquake ruptured bilaterally and mostly up dip. The W-phase moment tensor is predominantly strike-slip but exhibits a significant non-double couple component, broadly consistent with the orientation and kinematics of our InSAR fault model (Figure 3.7). The W-phase centroid depth of 11 km is a little below the peak slip depth in our InSAR-GNSS model of 8–10 km (Supplementary Figure 3.22, Long table 3.9), and the W-phase moment of 6.8 $\times$ 10^{18} Nm is $\sim$10% larger than (and likely within error of) our geodetic moment.

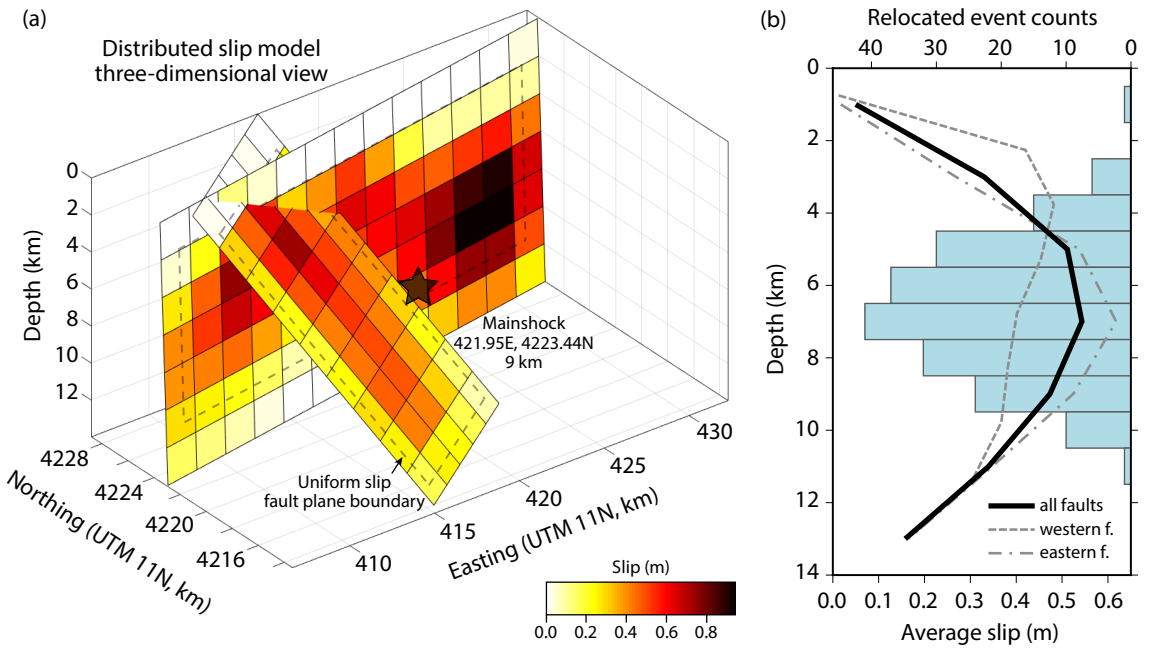


Figure 3.6: (a) Three-dimensional view of our preferred InSAR-GNSS distributed slip inverse model. Each sub-fault patch is 2 km×2 km and the star shows our relocated mainshock hypocenter. Full parameters of each sub-fault patch are tabulated in Supplementary Long table 3.7. Dashed lines show the fault plane boundary from our uniform slip inversion. (b) Model slip and aftershock depth profiles. Dashed and dashed-dotted gray lines show the average slip for each of the two model faults, plotted against the central depth of each row of sub-faults. The thick black line shows the weighted average for all model faults, calculated by averaging all sub-fault patches within 2 km depth increments and plotting against the central depth of the bin range. The histogram shows the number of calibrated relocated earthquakes at each 1 km increment in focal depth.

3.7.3 Aftershock Distribution and Mechanisms

Relocated aftershock hypocenters are scattered along a ∼34 km-long, ∼ENE trend, and span a focal depth range of 1–11 km with the greatest concentration at ∼4–9 km (Figure 3.7). Individual hypocenters have typical, formal uncertainties of ∼0.4–0.6 km in epicentral coordinates (the average lengths of the short and long semi-axes of the 90% confidence ellipse) and estimated uncertainties of ±1–4 km in focal depth. RMT centroid depths are generally in close agreement (Supplementary Figure 3.22), but extend slightly deeper, to 15 km. We conservatively estimated centroid depth uncertainties to be ∼5 km, so we do not view the differences with focal depths to be significant. However, we consider the focal depths most reliable on the basis of their smaller uncertainties and overall narrower range.

The relocated aftershocks approximate the trend of the InSAR-GNSS model faults, but are concentrated mostly to the south of the model fault surface projections. This is especially evident for the western model fault, with aftershocks reaching as far as 4–5 km southeast of its surface trace, consistent with the southeastward dip inferred from InSAR modeling. However, the aftershock map (Figure 3.7a) and cross-sections (Figure 3.7b,c) both reveal numerous events up to several kilometers from the mainshock model faulting. Two clusters of off-fault aftershocks are located at both ends of the mainshock rupture. Other clusters are distributed along ∼NW-SE trends, conjugate to the mainshock faulting.

The aftershocks exhibit a mix of strike-slip and normal RMT mechanisms, many of them with ENE-trending nodal planes (Figures 3.7a, 3.23). In the eastern rupture area, most aftershock mechanisms are predominantly strike-slip with ENE-trending left-lateral nodal planes, and therefore roughly consistent with our InSAR-GNSS model. However, based on the presence of conjugate trends in relocated epicenters and field observations of scattered right-lateral offsets in this region, we interpret that some of these aftershocks involve NNW-striking right-lateral faults. We also observe many aftershocks with pronounced non-double couple components. Like the mainshock, these smaller aftershocks may have involved multiple faults of differing kinematics that sum to a non-double couple mechanism.

In the western rupture area, there is a wider mix of aftershock mechanisms including pure normal, oblique-normal, and strike-slip faulting. The normal mechanisms are concentrated near the western end of the rupture, are relatively shallow, and mostly involve NE-trending nodal planes slightly oblique to the western model fault. The strike-slip mechanisms are concentrated near the eastern half of the western model fault, are relatively deep, and have ENE-trending, left-lateral nodal planes. This hints that the real faulting at depth involves distinct strike-slip and normal faults which are in close proximity but slightly oblique to one another. The crossing of our InSAR-GNSS eastern and western model faults supports this interpretation.

3.7.4 Comparisons with other Geodetic Slip Models and Seismological Observations

We now compare our mainshock slip model with four previously published ones: Cui et al. (2021) and Li et al. (2021b) who like us inverted InSAR and GNSS displacements to solve for the fault geometry and slip distribution, and Zheng et al. (2020) and Liu et al. (2021a) who also incorporated a range of seismological data to solve for the kinematic

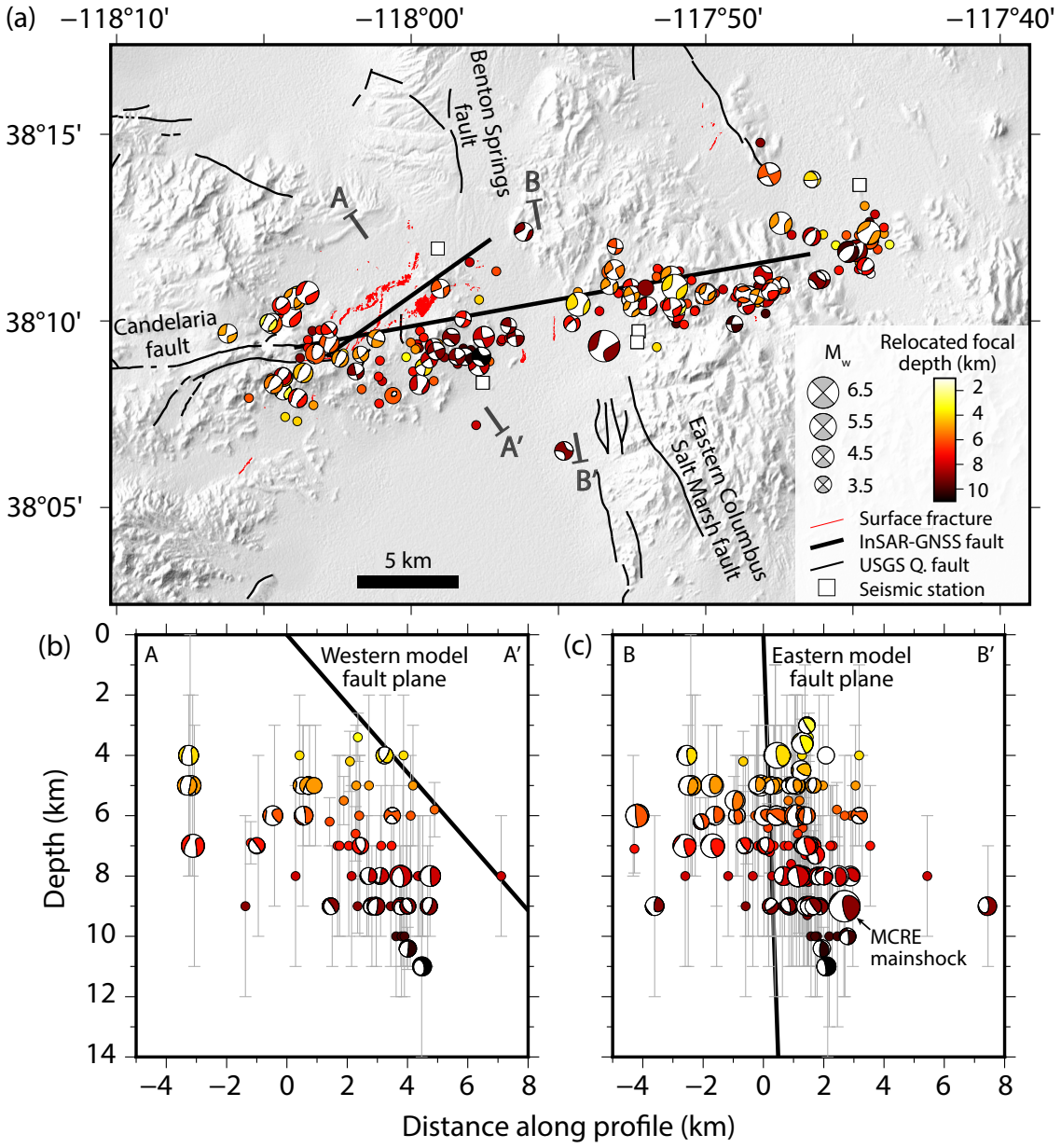


Figure 3.7: (a) Multi-directional hillshade map showing the relocated hypocenters and their focal mechanisms where available, plotted and colored by calibrated focal depth. Focal mechanisms are lower hemisphere projections scaled by moment magnitude. Smaller circles are events that are too small for waveform modeling (M_w<3.5) plotted without any magnitude scaling. The thick black lines indicate the surface projection of the two model faults, thin black lines are the US Quaternary faults, and thin red lines are the MCRE surface ruptures (Dee et al., 2021; Koehler et al., 2021). The black T-shape lines denote the cross-section transects and squares indicate close-in seismic stations. (b–c) Cross-sectional views of the relocated hypocenters and focal mechanisms, plotted by calibrated focal depth with its uncertainties (Supplementary Long table 3.8). Earthquakes are included where they lie within 5 km (b) or 13 km (c) of the cross-section lines on (a). Focal mechanisms are back-hemisphere projections scaled by moment magnitude and, similar to (a), smaller circles are the remaining relocated hypocenters without mechanisms. Thick black lines are cross sections of the (b) western and (c) eastern model faults.

rupture process. While we also acknowledge the GNSS-derived uniform slip model of Hammond et al. (2021), this lacks the spatial resolution of the InSAR-based models and is excluded from our comparison.

Though the source geometries vary in detail between the five studies, all models including ours exhibit comparable kinematics: almost pure left-lateral slip on steep SSE-dipping faulting in the east and oblique left-lateral–normal slip on a more gently SE-dipping structure in the west. Our eastern model fault dip of 88° is comparable to three of the other studies (78–83°) but steeper than the dip obtained by Cui et al. (2021) of 65°. Our eastern fault length of 26 km is also consistent with three of the other models (26–28 km) but longer than Li et al. (2021b)'s solution of 18 km. However, ours is the only model in which the eastern fault extends across the entire MCRE rupture zone and crosses the western model fault. This is slightly different from Zheng et al. (2020) and Cui et al. (2021) whose eastern model faults extend to approximately the center of the western segment, but more markedly different from Liu et al. (2021a) and Li et al. (2021b) whose model faults align end-to-end and form a right step, respectively.

In the western rupture area, our western model fault is similar to that of Zheng et al. (2020), Cui et al. (2021), and Li et al. (2021b), and only Liu et al. (2021a) subdivide this into two sub-faults, one dipping steeply below ∼5 km and one dipping gently above. Our western model fault dip of 49° is intermediate between the other models (40–64°). However, our aftershock relocations and mechanisms support overlapping NE-striking normal faulting and ENE-striking left-lateral faulting in this area, where the other geodetic models have only a single, western model fault. Ours is therefore the only model in which the continuation of the eastern model fault across the western fault explains the aftershock distribution and its mixed kinematics. This highlights the importance of incorporating complementary aftershock data sets to illuminate the mainshock rupture in greater detail. Similarly, none of the InSAR-GNSS inverse models capture the ∼6 km-long northern fault zone, highlighting an important limitation in the spatial resolution of geodetic source inversions. It is only through forward modeling that we are able to characterize this structure, supporting left-lateral–normal slip on a vertical fault (Figure 3.5).

Another significant difference between our model and the others is in the depth extents of coseismic slip. Whereas the bottom depths of our model fault planes are fixed to 14 km on the basis of the deepest, calibrated focal depths (11 km ± 4 km, Section 3.7.3), the other models have no such constraint with their model fault planes reaching depths of 21–24 km (Zheng et al., 2020; Cui et al., 2021; Li et al., 2021b; Liu et al., 2021a). In some cases, several centimeters of slip occur at the bottom of these planes (Figure 3.8), well be-

low the base of the seismogenic layer and despite slip below ∼10 km being poorly resolved by available geodetic data (as acknowledged by Liu et al. (2021a) in their checkerboard resolution test). Our shallower bottom depth likely explains why our model moment of 6.1×10^{18} Nm is 10–20% smaller than that of Zheng et al. (2020) and Liu et al. (2021a). This provides another example of how carefully calibrated aftershock data are useful in constraining mainshock properties.

There are also some more subtle differences in the model slip distributions. All of them show slip concentrated in two areas—a deeper (>5 km) patch on the eastern, left-lateral fault and a shallower (<5 km) patch on the western, oblique fault—and our peak slip of 1 m lies within the range of 0.6–1.7 m of the other four models. However, Zheng et al. (2020), Cui et al. (2021), and Li et al. (2021b) place the greatest slip on the western fault at ∼3–5 km depth, whereas we and Liu et al. (2021a) place it on the eastern fault at ∼6–10 km depth (Figure 3.6b, 3.8a). All five models display a pronounced shallow slip deficit (Figure 3.8b). Most of our shallowest row of sub-fault patches contain no model slip (Figure 3.6a), consistent with Zheng et al. (2020) and Li et al. (2021b) but in contrast to Liu et al. (2021a) and Cui et al. (2021) who each model has surface slip of up to ∼0.4 m, greater than observed field offsets. We return to the shallow slip deficit in Section 3.8.3.

Lastly, we compare our seismological results with those from Ruhl et al. (2021) which also incorporated eight temporary seismic stations deployed soon after the mainshock (Bormann et al., 2021). They located and then relocated (with waveform-based double-differencing) ∼18,000 events from January 1 to August 31, 2020, and used regional waveform modeling to estimate 128 moment tensors including for the mainshock. For the mainshock, their double-difference based depth is 3.7 km but their waveform model is 8.0 km, consistent with our InSAR peak slip at 8–10 km and within error of our own W-phase centroid depth of 11 km. Their best double-couple approximation of the fault plane shares the same strike and agrees to within 7° in dip and rake with ours. However, their mechanism has a higher double-couple percentage (>95% versus ∼68%). Their relocated aftershocks are distributed almost exclusively above 12 km, in close agreement with our arrival time-based calibrated focal depth range (up to 11 km) and a little shallower than our RMT centroid depth range (up to 15 km). Their aftershock moment tensors include a wide variety of strike-slip and normal mechanisms, similar to ours. In cross-sectional view, their denser, double-difference relocated aftershock clouds exhibit clear alignments that are not apparent in our own sparser data. These include structures that appear to align with our InSAR-GNSS model faults. For example, a transect across the central rupture zone reveals distinct shallow, ∼60°-dipping and deep, sub-vertical structures (Figure

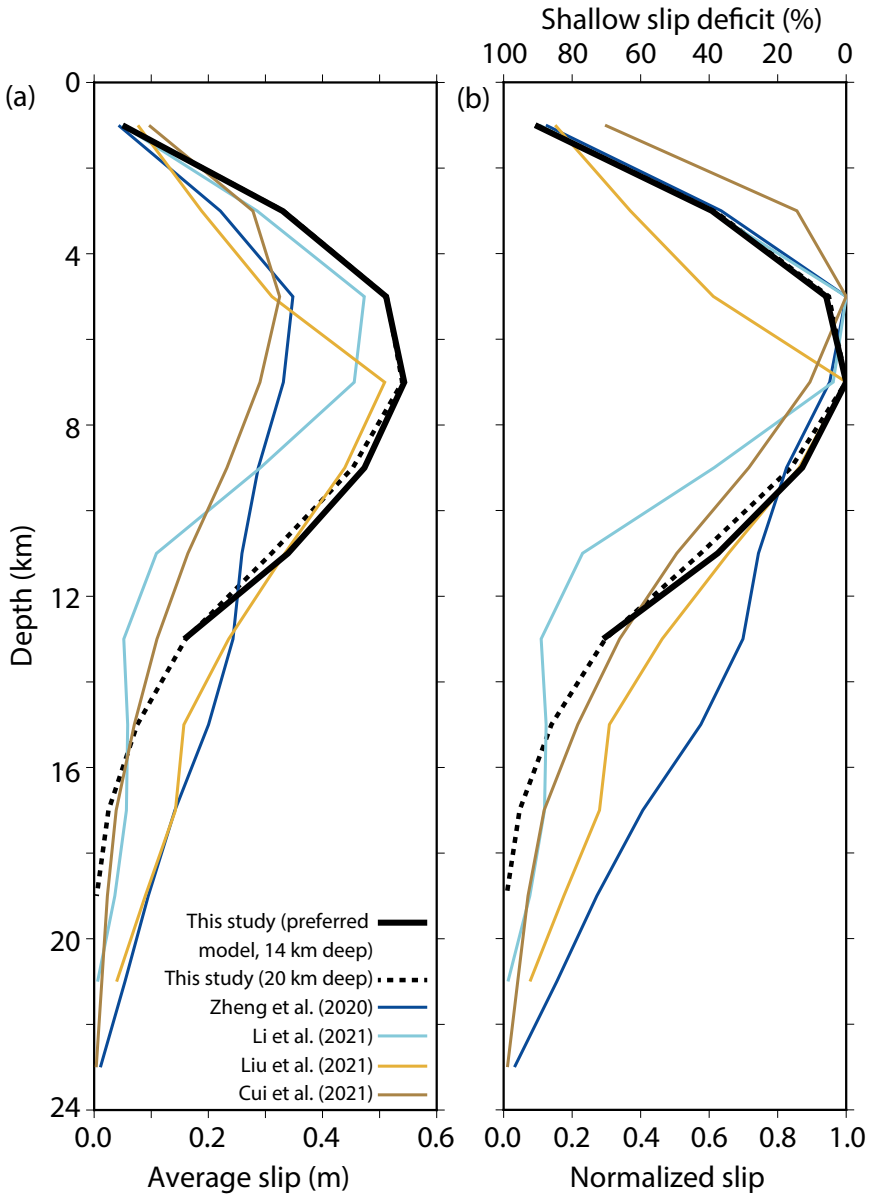


Figure 3.8: Comparison of MCRE geodetic model slip profiles from our paper and other studies. (a) Average and (b) normalized slip in 2 km depth increments, demonstrating the pronounced shallow slip deficit. The deficit amount annotated along the top of panel (b) refers to the the shallowest data point of the profile, and is equal to one minus the normalized slip of the surficial row of model sub-fault patches (0–2 km) expressed as a percentage. See Section 3.8.3 for details of the slip profile calculations and further discussion.

5e in Ruhl et al., 2021), consistent with the geometry of mainshock slip where our western and eastern model faults cross one another (Figure 3.6a).

3.7.5 Evidence of Previous Ruptures and Cumulative Offset

Although our InSAR-GNSS model faults do not align with previously mapped faults, we found some field evidence for prior faulting along the MCRE surface ruptures and along the surface projection of the model faults. At several locations within the western fault zone, we observed NE-trending calcite-filled cracks of a few to tens of centimeters in length (Figure 3.9a,b). One of these is well exposed along a flat, scraped road surface. We interpret that the cracks formed in one or more previous earthquakes and were subsequently cemented. Southwest of our western model fault, mapped MCRE surface ruptures with left-lateral and vertical DTNW offsets of 1–3 cm (Dee et al., 2021; Koehler et al., 2021) align at the foot of and thus appear to have reactivated a $\sim$1 km-long, NW-facing fault scarp—an opposite vertical slip sense to our western model fault (Figure 3.9c–e). Our topographic profiles reveal vertical separations of 7 m $\pm$2 m, indicative of several prior earthquakes along this structure. Otherwise, there is in general a limited expression of clear, neotectonic landforms such as scarps, channel offsets, or shutter ridges along the surface projections of our model faults.

Along the northern fault zone, our exploratory paleoseismic trench was sited where 8–9 cm left-lateral and 6–7 cm vertical DTNW surface offsets of the MCRE were measured (Dee et al., 2021; Koehler et al., 2021). The trenching reveals a sequence of sub-horizontal fluvial and alluvial sands and gravels that are offset by faults and fissures (Figure 3.10a,b). The three main stratigraphic units, from the lowest (oldest) to highest (youngest), include alluvial gravels from the trench floor to $\sim$0.4 m-–0.5 m depth, bedded fluvial and alluvial sand and gravels from 0.4–0.2 m, and loose alluvium and silt capping the exposure (units A1, A2, and A3, respectively in Figure 3.10c,d). We observe at least five distinct vertical to sub-vertical fissures with openings up to $\sim$17 cm wide, and one filled with gravels. Each fissure is marked by a white carbonate zone and alignments of pebbles that taper towards the trench floor. Three fissures disrupt unit A1 and are capped by A2, while the remaining two fissures extend to the surface. The surface-breaking fissures also contain white carbonate, but in these two fissures, the carbonate is disrupted. We interpret the capped and carbonate lined fissures to be evidence of prior surface rupturing earthquakes, and that the surface-breaking fissures result from both the 2020 MCRE and at least one prior earthquake. On the southern surface-breaking fissure, unit A2–A3 alluvium contact

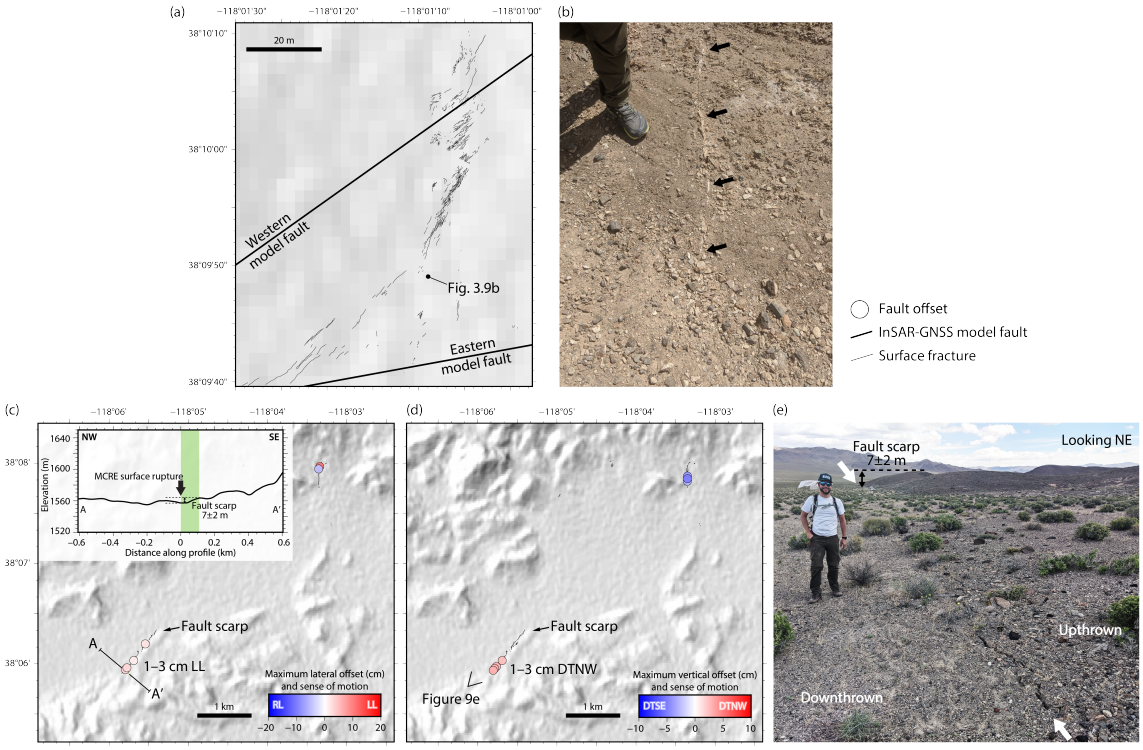


Figure 3.9: Hillshade topography maps and field photos showing evidence of previous ruptures. (a) Hillshade topography of the western rupture zone illustrating the MCRE surface ruptures (thin black line), surface projection of the InSAR-GNSS model faults (thick black lines), and the (b) calcite-filled cracks denoted by the black arrows (38.1636°N, 118.0192°W). (c–d) Hillshade topography map southwest of the western model fault (see panel boundary in Figure 3.3a) showing the MCRE surface ruptures along the foot of a NW-facing fault scarp (38.0989°N, 118.0967°W), with their (c) lateral and (d) vertical fault offsets measured in the field (Dee et al., 2021; Koehler et al., 2021). The inset cross-section A–A' in panel (c) illustrates the fault scarp vertical separation. The open arrow in panel (d) shows the approximate NE viewing angle of (e) the field photo viewing along strike of the surface fractures next to the scarp.

has a 6–7 cm down to the north offset—consistent with the 2020 MCRE surface fault offset adjacent to the trench (Figure 3.10a,d). This vertical offset is also observed at the unit A1–A2 boundary, but the contact irregularity there prevents an accurate quantification. The co-location of older and recent fissures demonstrates that the MCRE ruptured at least one preexisting fault structure.

The main fault trace of the MCRE trends approximately along strike from the Candelaria fault (Figure 3.1, 3.3a), which exhibits net, left-lateral–normal slip of ∼900 m since ∼3 Ma (Wesnousky, 2005). However, despite a rich and varied surface geology, our examination of digital topography and multi-spectral imagery (see Section 3.6.1) yielded only two potential indicators of cumulative offset along the MCRE fault trace. Along the western model fault, outcrops of sedimentary rocks of the Candelaria (Triassic) and Palmetto (Ordovician) formations (Ferguson et al., 1954) yield an apparent left-lateral offset of 600–700 m, using the interpreted geologic boundaries as piercing points (Figure 3.11a–e). Along the eastern model fault, a ridge of Pliocene andesite (Ferguson et al., 1953) exhibits 170 $\pm$ 40 m of apparent left-lateral offset, using projections of the ridgelines on either side of the fault to the inferred fault trace (Figure 3.11f–j). However, both estimates are tentative given that thick alluvium obscures much of the geology in the west and the low relief of the ridge in the east.

3.8 Discussion

3.8.1 Fault Kinematics and Complexity Revealed by Combining Geodesy, Seismology, and Field Observations

Overall, the MCRE and its aftershock sequence are consistent with previous interpretations of active faulting in the Mina deflection and its role in regional tectonics. The mix of left-lateral and left-lateral–normal faulting mimics the slip sense of other neighbouring faults (Figures 3.3, 3.7), in particular the well-studied Candelaria fault which exhibits both vertical scarps and left-lateral geomorphic offsets (Wesnousky, 2005). While oblique (left-lateral–normal) slip on the western, NE-striking mainshock fault supports transtensional regional kinematic models (e.g., Oldow et al., 2008), pure left-lateral slip on the eastern, E-striking mainshock fault is more consistent with the clockwise vertical-axis block rotation model for right-lateral shear transfer through the Mina deflection (Wesnousky, 2005). Normal faulting aftershock focal mechanisms located at the ends of the mainshock faulting also support the paired basins produced as a result of block rotation

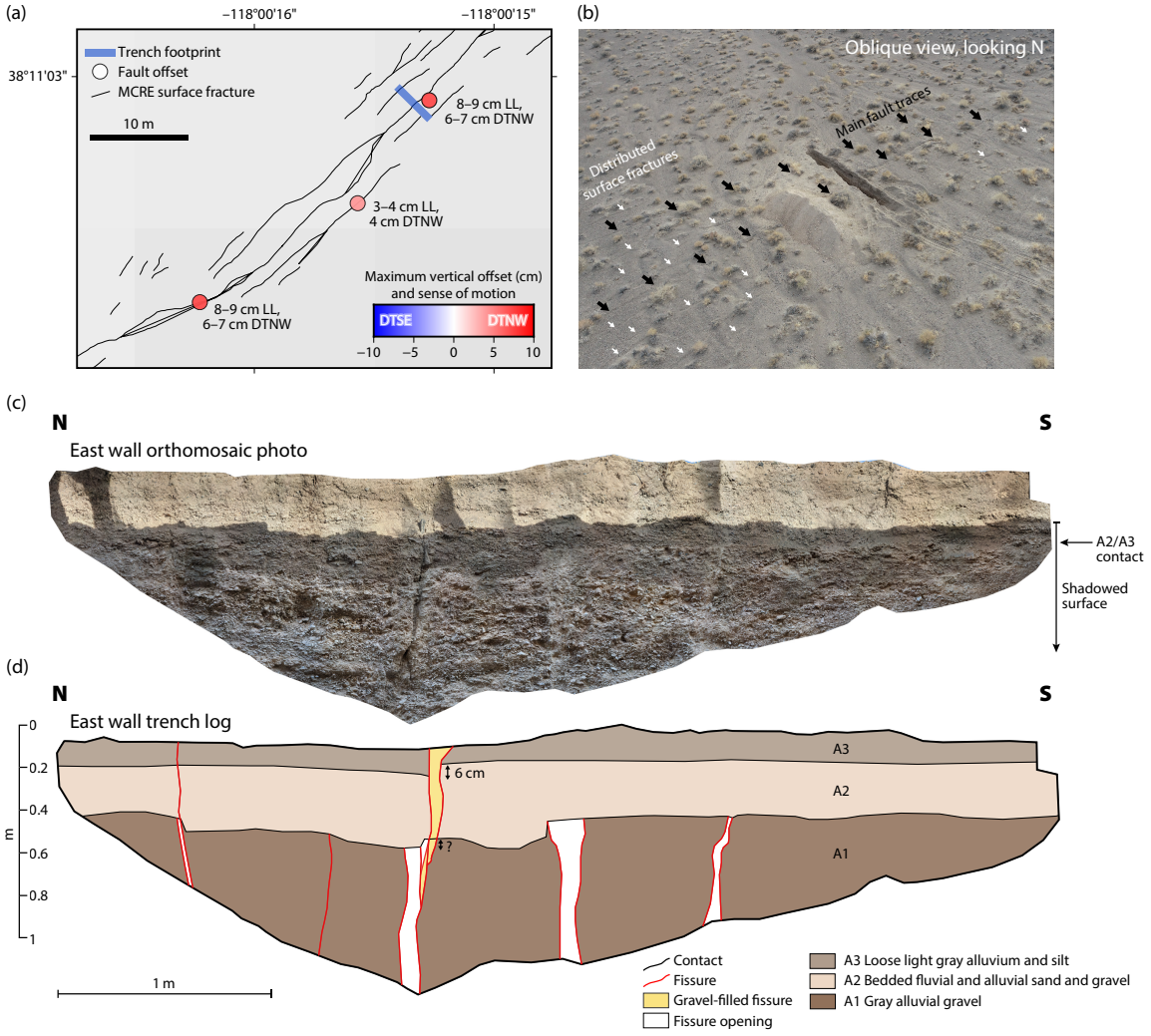


Figure 3.10: Paleoseismic trench across the northern fault zone of the MCRE surface rupture (38.1841° N, 118.0043° W). (a) Map view of the trench footprint, with the MCRE rupture trace and vertical fault offset measurements from Dee et al. (2021) and Koehler et al. (2021). (b) Uncrewed aerial system oblique view of the trench looking north. The larger black arrows indicate the main continuous fault traces that cross the trench, and the smaller white arrows highlight the surface cracks concentrated at the southwest side of the trench. (c) Orthomosaic photo of the eastern trench wall. Note that the darker brown shading is the shadowed surface, not to be confused with a unit contact. (d) Eastern wall trench log showing the three stratigraphic alluvium units, fissures, and offset measurements.

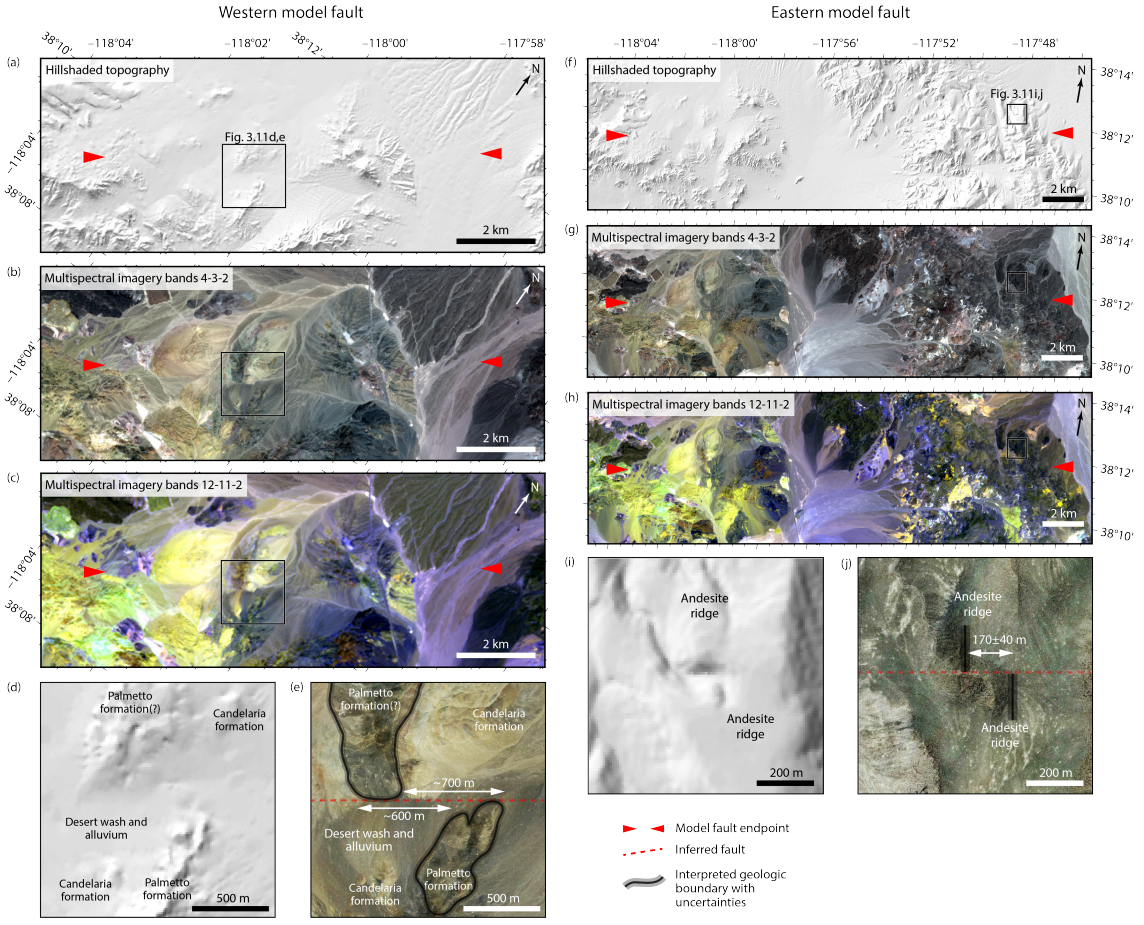


Figure 3.11: Hillshaded topography, multispectral imagery natural color bands 4-3-2, and geology composition bands 12-11-2 along the western (a–c) and eastern (f–h) InSAR-GNSS model faults, respectively (see Sections 3.6.1, 3.7.5, Data and Resources). The red triangles indicate the model fault endpoints. The boxes denote boundaries of panels (d), (e), (i), and (j) showing potential geologic or geomorphic offset markers used to estimate the cumulative fault offset along the surface projection of the two model faults. The satellite photo in panels (e) and (j) is the 2016 Google Earth imagery with our own contrast enhancement.

(Wesnousky, 2005) (Supplementary Figure 3.23). In the long-term, these block rotations may divert fault orientations away from those favorable to slip, promoting the formation of new faults and preventing older ones from becoming structurally mature (discussed further in Section 3.8.2). The off-fault aftershock cluster at the western end of our model faults might be associated with energy radiated at the western rupture termination, reactivating the Candelaria and other local faults. We interpret that NW-trending right-lateral strike-slip faults are also involved in the MCRE sequence; focal mechanisms conjugate to the eastern model faults project along strike with the major right-lateral Benton Springs and Petrified Springs faults, which help accommodate dextral shear transferred through the Mina deflection (Figure 3.1, 3.7) (Wesnousky, 2005; DeLano et al., 2019).

One of the most unique attributes of the MCRE is that the western and eastern mainshock faults cross one another, according to both our InSAR-GNSS modeling and aftershock hypocenters and focal mechanisms (Figures 3.2, 3.7). In most seismic sequences with intersecting faults, the structures rupture sequentially in separate earthquakes—for example, the 1987 M_S 6.2 and M_S 6.6 Superstition Hills earthquakes and the 2019 M_w 6.4 and M_w 7.1 Ridgecrest earthquakes in California (Barnhart et al., 2019a; Hudnut et al., 1989). In contrast, the MCRE ruptured two oblique cross faults in a single event. Examples of continental earthquakes in which conjugate faults ruptured together include the 1927 M 7.0 Kita Tango, Japan and the 1992 M_w 6.5 Big Bear, California earthquakes (Jones et al., 1993; Matsu'ura, 1977). Dynamic simulations suggest that orthogonal faults are most likely to rupture together when both have high shear stress and when the initial slip direction towards the second fault is favorable for failure, leading to larger dynamic stress drops that promote rupture propagation across geometric complexities (Lozos, 2022; Thatcher and Hill, 1991). Our work motivates similar studies of obliquely crossing faults.

Our combination of near- and far-field surface deformation observations further reveals the complexity of the western MCRE kinematics. Our western InSAR-GNSS model fault dips southeastwards with left-lateral–normal slip, and the unwrapped data interferogram shows a clear LOS displacement jump of 12 $\pm$4 cm (Figure 3.4a,b). Approximately 1 km to the northwest, the northern fault zone displays a more subtle change in LOS displacement of 2 $\pm$1 cm across a 100–150 m distance, aligning with field observations of dominant left-lateral and vertical DTNW fault offsets (Figure 3.3b,c), and surface cracks with preferential pebble-clearing to the southeast, also consistent with DTNW motion (Figure 3.4a). The western and northern fault zones therefore have opposing vertical slip sense, with an upthrown block in between. Three competing structural configurations could potentially explain these observations. In the first configuration, the northern fault

dips to the NW and away from the western fault, accommodates left-lateral–normal slip, and forms a horst structure (Figure 3.12a). However, the absence of normal-faulting aftershocks to the NW or along strike of the northern fault zone implies that this may only be a very shallow structure (Figure 3.7a). In the second configuration, the northern fault dips to the SE, sub-parallel to the main fault, and slips in a left-lateral–reverse sense (Figure 3.12b). However, we do not observe any reverse-sense aftershock focal mechanisms (Figure 3.7b). In the third configuration, the northern fault is vertical and has left-lateral–oblique motion (Figure 3.12c). This third scenario is supported by the focal mechanism cluster in the west—although located ∼2 km northwest of the northern fault zone its steeply-dipping geometry and kinematics match our proposed model (Figure 3.7a,b)—and by our vertical InSAR-GNSS forward model fault (Figure 3.5, last column).

Along the secondary, northern fault, our geodetic, field, and seismological observations are only in partial agreement, reflecting each method's strengths and resolution in light of the geological complexity of the area. The poor depth resolvability of the shallowest aftershocks (∼<4 km) a function of the lack of close-in seismic stations and the relocation method, illustrates the limitations of using regional seismograms to characterize the shallowest structures. However, aftershock relocations and mechanisms offer unique constraints on fault complexity within the deeper seismogenic layer. The shallower structures are likely best represented by field observations, while InSAR best captures the mainshock rupture at larger length- and depth-scales. Furthermore, the geodetic and field data are, at first glance, contradictory: the major InSAR displacement discontinuity does not fully correspond to the largest fault offsets measured in the field. This likely reflects further complexity in the shallow fault zone as well as an abundance of off-fault deformation. Overall, our study demonstrates the importance of integrating geodesy, seismology, and field geology, perhaps along with other methods, in order to resolve the complexity of an earthquake sequence along and across strike and down dip, where a single method on its own could easily lead to misinterpretation.

3.8.2 Characteristics of Structural Immaturity in the MCRE and Implications for Seismic Hazard Assessment

The MCRE ruptured faults that we interpret as being structurally immature, with few long-term geomorphic or geologic offsets discernible in the field or resolvable from satellite imagery and tentative cumulative offsets of only ∼600–700 m (Section 3.7.5). Where known, other E-trending left-lateral strike-slip faults in the Mina deflection have slow slip

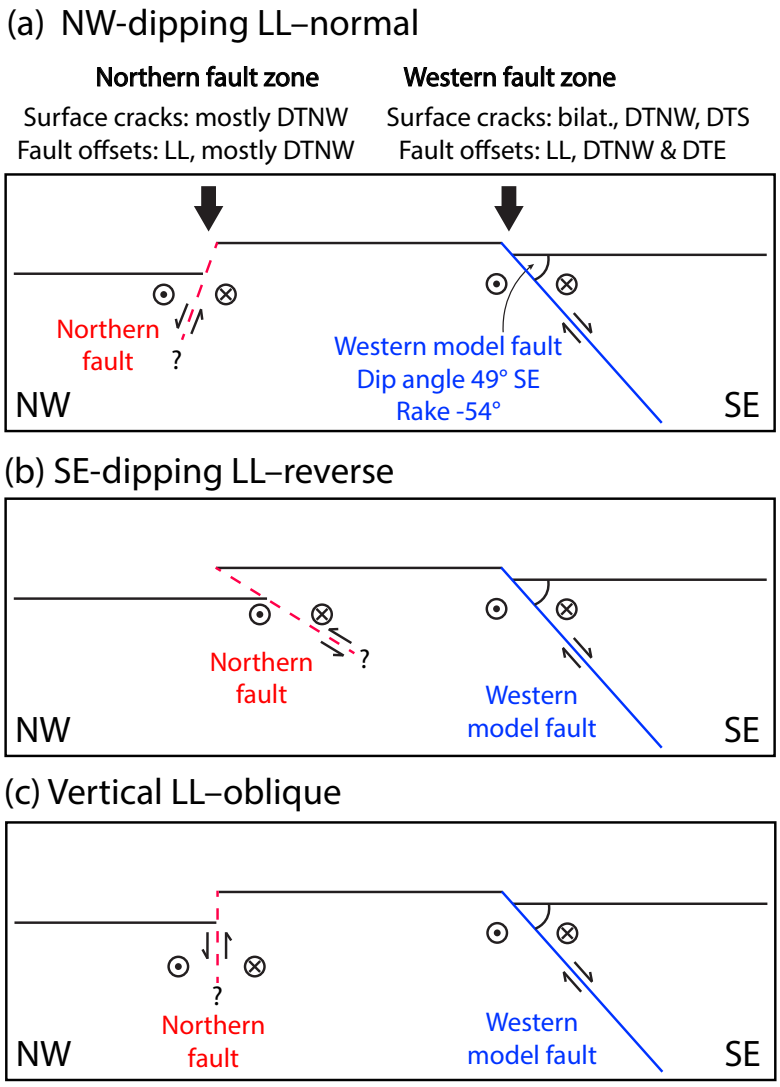


Figure 3.12: Three, competing, interpreted cross-sections of the fault structure and kinematics in the western MCRE rupture area, inferred from near- and far-field observations. The SE-dipping solid blue line is the InSAR-derived western model fault and the dashed red line is the secondary, northern fault beneath the northern fault zone with its DTNW sense of throw. The secondary fault is interpreted as (a) a NW-dipping left-lateral–normal, (b) a SE-dipping left-lateral–reverse, and (c) a vertical left-lateral oblique fault. Abbreviations: bilat—bilateral; DTE—down-to-the-east; DTNW—down-to-the-northwest; DTS—down-to-the-south; LL—left-lateral.

rates of ∼0.3–0.4 mm/yr (Speed and Cogbill, 1979; Lee et al., 2006), another hallmark of structural immaturity. The weak manifestation of geomorphic offsets and slow individual fault slip rates likely reflect that vertical axis crustal block rotations produce diffuse, highly-segmented faulting rather than a long, through-going fault.

The MCRE sequence therefore provides an example of rupture on a fault system of pronounced structural immaturity, and many of the rupture attributes may be characteristic of this. As described above, the mainshock geometry is complex for an earthquake of this magnitude, involving crossing faults with two distinct kinematic styles: sub-vertical left-lateral faulting in the east and inclined, left-lateral–normal faulting in the west. Moreover, broadly-distributed fractures around the main fault traces reflect non-localized deformation commonly observed in immature fault zones (e.g., Zinke et al., 2015). The off-fault distribution of aftershocks, their non-double couple focal mechanisms, and their wide variety of kinematics and orientations (Figure 3.7) are further indications of a lack of a dominant through-going structure in the area. In addition, Liu et al. (2021a) reported an average mainshock rupture velocity of ∼1.5 km/s, a relatively slow speed that is in agreement with other earthquakes along immature faults (e.g., Perrin et al., 2016; Chounet et al., 2018).

Our study also highlights the care needed for seismic hazard assessment in highly-distributed, immature fault systems. For example, paleoseismic trenching would likely be required across a very large number faults for the full history of major earthquakes in this region to be captured, but could still miss large events that did not rupture fully to the surface. Furthermore, simple fault length-magnitude scaling relations would not have anticipated an earthquake of the magnitude of the MCRE, and the characteristic earthquake model is probably inapplicable in regions of such diffuse faulting. Our work thus encourages seismic hazard calculations to consider that short segments may rupture together to generate large magnitudes, including unusual crossing fault configurations.

3.8.3 Shallow Slip Deficit in the MCRE

Averaged over several earthquake cycles, the offset accommodated across a fault zone may be expected to be constant with depth. However, geodetic slip inversions of large earthquakes commonly exhibit peak model slip at depths of ∼3–6 km with a reduction closer to the surface, termed the shallow slip deficit (SSD) (e.g., Simons et al., 2002; Fialko et al., 2005). The effect is often illustrated with a normalized slip profile (a plot of average slip against depth normalized against peak average slip) and parameterized as one minus the

normalized slip of the surficial row of model slip patches (usually expressed as a percentage). While absolute values depend in part upon whether or not near-field geodetic data are incorporated (Vallage et al., 2015; Xu et al., 2016; Marchandon et al., 2018; Scott et al., 2019), upon the assumed elastic structure (Amoruso et al., 2004; Hearn and Bürgmann, 2005; Barbot et al., 2008; Marchandon et al., 2021), and upon other choices made in the modeling (Huang et al., 2017; Ragon et al., 2018; Li et al., 2020b), the general inference of SSDs in many large earthquakes is considered robust. Moreover, SSDs are also manifest in field measurements of surface slip along the primary fault trace (Dolan and Haravitch, 2014).

Several possible mechanisms causing SSD have been invoked, each with important implications for fault mechanics and earthquake physics. A switch to velocity-strengthening fault friction at shallow depths would naturally favour aseismic over seismic slip (Marone et al., 1991; Marone, 1998). Damaged zones above a strike-slip fault may have a locally reduced seismic velocity, promoting inelastic off-fault deformation (Zhang et al., 2009). Regions surrounding the shallow fault might undergo distributed deformation predominantly during the interseismic period, thereby accumulating little elastic strain (Fialko et al., 2005; Lindsey et al., 2014). Coseismic rupture might dissipate in the near surface through plastic yielding, particularly when near-surface materials are poorly-consolidated (Kaneko and Fialko, 2011; Brooks et al., 2017; Roten et al., 2017). Alternatively, SSDs might simply reflect random differences in the depth extents of individual ruptures within the seismogenic zone (Berberian et al., 2001; Yang and Yao, 2021; Yao and Yang, 2022). This would help explain why the largest events (M_w>7.5), which are those most likely to fill the entire seismogenic layer and drive slip in any velocity strengthening region, generally have reduced or absent SSDs (Tong et al., 2010; Lauer et al., 2020). Finally, SSDs might arise due to assumptions made in geodetic slip models, such as simplification of the Earth's elastic structure (Marchandon et al., 2021), or due to near-fault image decorrelation leading to insufficient surface displacement data points to solve for shallow slip (Xu et al., 2016).

Understanding what causes SSDs and how they might be compensated is vital for seismic hazard assessment, for a number of reasons. Firstly, active fault mapping, slip rate estimations, and paleoseismic trenching all rely upon surface offsets; a pronounced SSD acts to obscure the link with earthquake faulting at depth (Dolan and Haravitch, 2014; Brooks et al., 2017). Secondly, the suppression of near surface slip can affect strong ground motions near the fault trace (Kaneko et al., 2008; Pitarka et al., 2009). Thirdly, there is the possibility that the slip deficit is removed by subsequent earthquakes centered at

shallower depths (Berberian et al., 2001; Jackson et al., 2006; Elliott et al., 2011; Mackenzie et al., 2016). Alternatively, shortfalls in coseismic surface slip could be compensated through distributed coseismic deformation away from the main fault trace (Rockwell et al., 2002; Simons et al., 2002; Dolan and Haravitch, 2014; Zinke et al., 2014; Milliner et al., 2015; Scott et al., 2018), as postseismic afterslip (Fielding et al., 2009), or as interseismic creep (Fialko et al., 2005; Floyd et al., 2016; Brooks et al., 2017).

We now consider shallow slip deficit in the MCRE in this context, using our own and other published InSAR models (Zheng et al., 2020; Cui et al., 2021; Li et al., 2021b; Liu et al., 2021a) and derived normalized slip profiles calculated using a common 2 km depth increment. Our own model has average surface slip of 0.05 m compared to peak average values of 0.54 m at 6–8 km depth (Figure 3.8a), resulting in an SSD of 91% (Figure 3.8b). SSDs of the other published models calculated in the same way span between 82–89% except for a lower value of 70% obtained for Cui et al. (2021)'s model. This general agreement implies that the large SSD inferred for the MCRE is robust.

The biggest difference between our normalized slip profiles and those of the other models is our shallower bottom depth, fixed to 14 km on the basis of relocated seismicity. We were therefore interested in the extent to which this could influence the calculated SSD. We test this effect by producing an alternative InSAR-GNSS model in which the fault planes are extended to ∼20 km depth, but with an otherwise identical setup to our preferred model. The 20 km-deep model yields average surficial slip of 0.05 m and peak average slip of 0.54 m at 6–8 km depth for a 91% SSD, values that are identical to our preferred 14 km-deep model (Figure 3.8). This suggests that varying the bottom depth does not influence the SSD. Rather, the main effect of increasing the bottom depth is to redistribute the deeper model slip: below 14 km, slip averages less than 0.08 m and tapers towards zero at 20 km (Figure 3.8a). However, the overall moment is only ∼3% larger than our 14 km-deep model.

The SSD in the MCRE may be compensated through several mechanisms. Shallow slip on the western fault might transfer in part to the nearby, sub-parallel northern fault zone, which is not represented in our InSAR-GNSS inverse model but where field offsets of up to ∼20 cm were recorded (Dee et al., 2021; Koehler et al., 2021) (Figure 3.3). The northern fault zone might therefore account for up to around one quarter of SSD along our western model fault. Along the eastern fault, conjugate surface fractures with up to ∼10 cm of slip can likewise only make up a small proportion of the SSD. However, given the broad deformation field, we expect that additional, unmapped fractures, folding or volumetric strain could account for more of the absent shallow deformation. In addition,

some amount of the SSD may have been removed by postseismic afterslip, of which only 1–2 days are captured in our interferograms. Hammond et al. (2021) compared coseismic and postseismic surface displacements across the MAGNET GNSS Network within 70 km of the MCRE epicenter over a period of several months. They found that postseismic displacements mimicked coseismic displacement patterns at ∼9–51% of their values, but the long wavelength of this deformation suggests deep rather than shallow afterslip. Li et al. (2021b) modeled a 6-month InSAR time series and showed that rapid afterslip also occurred at shallow depths of 0–3 km with a peak slip of ∼0.3 m. This likely recovered around another one third of the missing slip, though later afterslip after the study period could potentially raise this contribution further. Any remaining shallow deformation is unlikely to be recovered by aftershocks or future earthquakes since they would need to be centered at unusually shallow depths. Our calibrated relocated aftershocks mostly occur at depths greater than 4 km, exhibit small magnitudes, and are located off the main fault model (Figure 3.7).

3.8.4 Are Shallow Slip Deficits Governed by Fault Structural Maturity?

We have demonstrated that the MCRE occurred along a highly immature fault system and involved a pronounced SSD. In this final section, we consider whether these two characteristics are linked by assessing SSDs calculated from InSAR slip models of other continental, strike-slip earthquakes. This extends the work of Dolan and Haravitch (2014), who associated SSD with structural maturity by comparing published subsurface model slip distributions with field offsets of six large (M_w 7.1–7.9) continental strike-slip earthquakes. They found that for earthquake ruptures that occur on structurally mature faults (cumulative displacement ≥85 km), ∼85–95% of slip at depth reaches the surface (equivalent to a 5–15% SSD), whereas for ruptures on immature faults (cumulative displacement ≤25 km) only ∼50–60% does (a 40–50% SSD). This pattern holds regardless of their geometrical complexity; straight and continuous sections of immature faults still exhibit a pronounced SSD. Dolan and Haravitch (2014) interpret that for ruptures on immature faults, the larger SSDs reflect more off-fault deformation at shallow depths, and that for ruptures on mature faults, the smaller SSDs reflect more localized slip on a principle surface trace.

We investigate this further by comparing our normalized slip profile with those of twenty-seven other continental strike-slip earthquakes modeled with InSAR (Figure 3.13a,

Table 3.3). We only consider earthquakes larger than M_w 6.4 since smaller events are less likely to rupture the full seismogenic layer. Many of the events have multiple published InSAR models, but we simplify our analysis by choosing one with a publicly available slip distribution (Figure 3.8b would suggest that differences in profile shape are anyway likely to be modest). The normalized slip profiles are plotted according to the cumulative offset of the host fault, a common proxy for structural maturity, and separately by moment magnitude (Figures 3.13b,c). We further extract the SSD for each earthquake from the shallowest data point of the slip profile, and compare the value with cumulative offset of the host fault and with moment magnitude (Figures 3.13d,e).

Our results suggest that SSD does not consistently correlate with cumulative offset (Figure 3.13d). For instance, the 2020 Elazığ earthquake ruptured the relatively mature East Anatolian fault (9–26 km net slip, Duman and Emre (2013)) but exhibits a modeled SSD of 85% (Pousse-Beltran et al., 2020), while the 2019 Ridgecrest earthquakes ruptured very immature faults (<100 m, Gold et al. (2021)) with only ∼30 % SSD (Xu et al., 2020). In contrast, moment magnitude does seem to correlate with SSD, with an R^2 value of 0.55 (Figure 3.13e). Earthquakes of M_w ≥7.2 produce small SSDs, mostly <10% and up to a maximum of 30% (in the 2021 Maduo earthquake). Earthquakes of M_w <7.2 generally produce much larger SSDs, with half of them exceeding 80%, but also encompass a much broader range of values, from negligible deficits (e.g., 1999 Hector Mine, 2017 Ormoc) to nearly complete ones (e.g., 2016 Muji, 2017 Ormoc, 2018 Kaktovik). In this context, the 91% SSD of the MCRE is more a function of its magnitude than its structural immaturity. This pattern can be explained in terms of the earthquake slip budget—moderate sized earthquakes will break to the surface most easily when the hypocenter is shallow but will otherwise leave large SSDs, whereas large earthquakes will rupture more fully to the surface whatever the nucleation depth (Lauer et al., 2020; Yang and Yao, 2021; Yao and Yang, 2022).

3.9 Conclusions

Our geodetic, seismological, and field observations and modeling suggest that the MCRE ruptured two main structures, an eastern left-lateral fault and a western left-lateral–normal fault, that cross each other at an oblique angle, while also generating abundant off-fault deformation. Peak geodetic model slip of 1 m is buried at 8–10 km depth, and only up to 0.1 m of slip reaches the top 2 km of the crust (yielding a shallow slip deficit of 91%), consistent with at most ∼20 cm of fault offset mapped in the field. A third, northern fault is

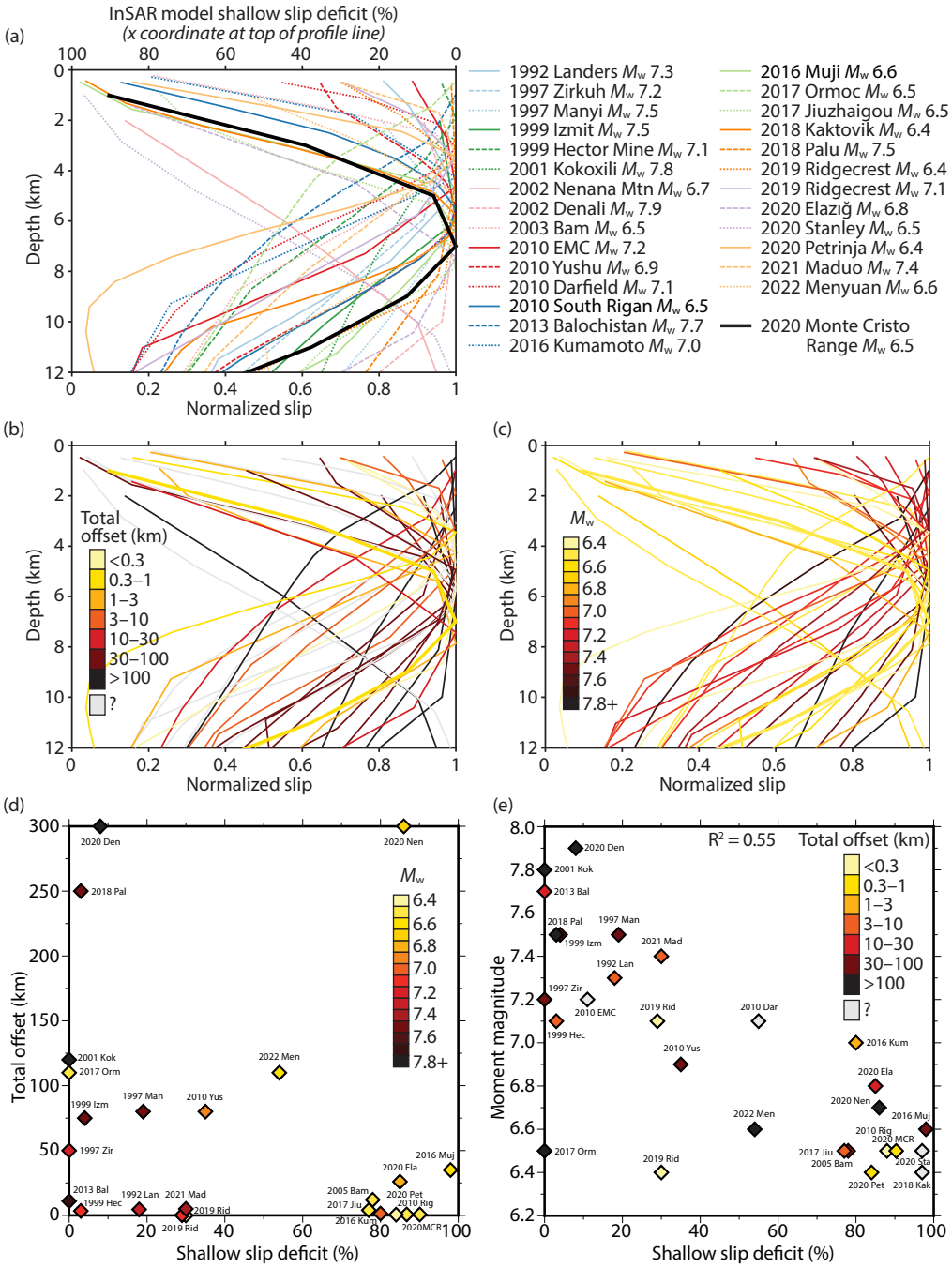


Figure 3.13: (a) Normalized slip profiles from InSAR-derived coseismic slip models of twenty-eight large (M_w 6.4–7.9), predominantly strike-slip, continental earthquakes. Average slip in each layer of the model is normalized against whichever layer has greatest average slip. The shallow slip deficit annotated along the top of the panel refers to the the shallowest data point of the profile, and is equal to one minus the normalized slip of the surficial row of model sub-fault patches expressed as a percentage (e.g., Fialko et al., 2005). InSAR model references are given in Table 3.3. (b) Normalized slip profiles colored by the total geological offset accumulated by the host fault (see Table 3.3 for offset values and references). (c) Normalized slip profiles colored by moment magnitude. (d, e) Scatter plots between shallow slip deficit in percentage versus (d) total offset in kilometers (colored by moment magnitude), and (e) moment magnitude (colored by total offset). Earthquakes with unknown cumulative offsets on the host fault are excluded from panel (d). Data points are labeled with the event year and the first three letters of the event name, unless noted in Table 3.3.

Table 3.3: List of earthquakes, InSAR model shallow slip deficits, and cumulative, geological offsets for the earthquakes profiled in Figure 3.13. For each InSAR model, the shallow slip deficit is equal to one minus the normalized slip of the surficial row of model sub-fault patches (the shallowest data point of the profile in Figure 3.13), expressed as a percentage (e.g., Fialko et al., 2005). Abbreviations: EMC—El Mayor-Cucapah; MCR—Monte Cristo Range; pers. comm.—personal communication.

Earthquake	M_w	**InSAR model shallow slip deficit**		**Total geological offset**	
		Value	Source	Value	Source
1992 Landers	7.3	18%	Xu et al. (2016)*	3.1–4.6 km	Jachens (2002)
1997 Manyi	7.5	19%	Funning et al. (2007)	∼20–80 km	Zhikun Ren, pers. comm.
1997 Zirkuh	7.2	0%	Marchandon et al. (2018)*	∼10–50 km	Richard Walker, pers. comm.
1999 Izmit	7.5	4%	Çakir et al. (2003)	∼4–75 km	Šengör et al. (2005)
1999 Hector Mine	7.1	3%	Xu et al. (2016)*	3.4 km	Jachens (2002)
2001 Kokoxili	7.8	0%	Lasserre et al. (2005)	100 ±20 km	Fu and Awata (2007)
2002 Nenana Mtn†	6.7	86%	Wright et al. (2003)	∼300 km	Eisbacher (1976)
2002 Denali	7.9	8%	Wright et al. (2004)	∼300 km	Eisbacher (1976)
2003 Bam	6.5	78%	Fialko et al. (2005)	≪12 km	Jackson et al. (2006)
2010 EMC	7.2	11%	Xu et al. (2016)*	Mixed/unknown	Fletcher et al. (2014)
2010 Yushu	6.9	35%	Li et al. (2011)	39–80 km	Wang et al. (2008)
2010 Rigan	6.5	87%	Walker et al. (2013)	Probably small	Walker et al. (2013)
2010 Darfield	7.1	55%	Elliott et al. (2012)	Unknown	Jongens et al. (2012)
2013 Balochistan	7.7	0%	Lauer et al. (2020)*	∼11 km	Zinke et al. (2014)
2016 Kumamoto	7.0	80%	Scott et al. (2019)*	800–1400 m	Scott et al. (2018)
2016 Muji	6.6	98%	Feng et al. (2017)	∼30–35 km	Li Tao, pers. comm.
2017 Ormoc	6.5	0%	Yang et al. (2018)	∼110 km	Cole et al. (1989)
2017 Jiuzhaigou	6.5	77%	Li et al. (2020b)	1–4 km	Li et al. (2019)
2018 Kaktovik	6.4	97%	Gaudreau et al. (2019)	Unknown	–
2018 Palu	7.5	3%	Socquet et al. (2019)*	150–250 km	Silver et al. (1983)
2019 Ridgecrest	6.4	30%	Xu et al. (2020)*	<20 m	Gold et al. (2021)
2019 Ridgecrest	7.1	29%	Xu et al. (2020)*	<100 m	Gold et al. (2021)
2020 Elazığ	6.8	85%	Pousse-Beltran et al. (2020)	9–26 km	Duman and Emre (2013)
2020 Stanley†	6.5	97%	Yang et al. (2021)	Unknown	–
2020 MCR	6.5	91%	This study	∼600–700 m	This study
2020 Petrinja	6.4	84%	Xiong et al. (2022)	∼560 m	Baize et al. (2022)
2021 Maduo	7.4	30%	Jin and Fialko (2021)	∼2.5–5 km	Li Tao/Jinrui Liu, pers. comm.
2022 Menyuan	6.6	54%	Yang et al. (2022a)	95 ±15 km	Gaudemer et al. (1995)

*Slip models that also incorporate near-field displacement fields from optical image correlation or differential lidar.

†InSAR model slip in the 2002 Nenana Mountain and the 2020 Stanley earthquakes peaks at 14 km and 12.5 km depth, respectively (Wright et al., 2003; Yang et al., 2021).

required in order to account for mapped surface fractures with distinctive pebble-clearing patterns, but is at the resolution limit of the InSAR-GNSS modeling. The intersecting fault geometry and distributed surface ruptures of the mainshock, the off-fault aftershocks with varying orientations and kinematics, and the limited expression of clear geomorphic features indicative of active faulting are indications that the MCRE ruptured an emergent

zone of highly-distributed faulting with only ∼600–700 m of cumulative offset. However, comparisons with InSAR slip models of twenty-seven other continental, strike-slip earthquakes suggest that the pronounced shallow slip deficit of the MCRE is controlled more by its moderate magnitude than by the structural immaturity of its host faults.

3.10 Data and Resources

Supplemental Material for this article includes Figures 3.14–3.23, Tables 3.4–3.6, and Long tables 3.7–3.9 showing the full results and supporting material of the InSAR-GNSS inversion and forward models, and the seismological modeling. All data used in this study are freely available through the following platforms. SAR and multispectral images from Sentinel-1 and -2 satellites were accessed from the Alaska Satellite Facility (`https://search.asf.alaska.edu`, last accessed September 2020) and the Copernicus Open Access Hub (`https://scihub.copernicus.eu`, last accessed May 2022). We used the 3 arc-second Shuttle Radar Topography Mission DEM obtained from OpenTopography (`https://opentopography.org`, last accessed May 2020), and the 1/3 arc-second USGS 3DEP DEM (`https://apps.nationalmap.gov/downloader`, last accessed May 2022). Earthquake arrival times were collected from the ISC Bulletin (`https://doi.org/10.31905/D808B830`) and the ANSS ComCat system (`https://doi.org/10.5066/P95R8K8G`). Regional waveform data were obtained from IRIS (`http://ds.iris.edu/ds/nodes/dmc/data`, last accessed December 2020) and the Nevada Seismological Laboratory, UNR (`http://seismo.unr.edu`, last accessed December 2020). The GNSS coseismic offsets (19 June 2020 data set) were obtained from NGL (`http://geodesy.unr.edu/news_items/20200619/nn00725272_24hr_19-Jun-2020.txt`, last accessed November 2020). UAS survey data are in preparation for public release on OpenTopography by Pierce et al. Figures were plotted using the Generic Mapping Tools version 6 (Wessel et al., 2019). Fault lines in figures were acquired from the USGS Quaternary fault and fold database (`https://usgs.gov/natural-hazards/earthquake-hazards/faults`, last accessed July 2021). Historic earthquake epicenters in figures were obtained from the USGS NEIC (`https://earthquake.usgs.gov/earthquakes/search`, last accessed May 2022). Sentinel-2 false color maps were generated using the open-source QGIS software. The paleoseismic trench orthomosaic was produced in Agisoft Metashape (`https://agisoft.com`).

3.11 Acknowledgments

We are grateful to Harley Benz for kindly helping us with the regional moment tensor solutions and for his support and encouragement of our work, to Austin Elliott and two anonymous reviewers, and to the associate editor Richard Briggs for suggestions that improved the paper. This study is funded through grants from the Natural Sciences and Engineering Research Council of Canada (NSERC), the Canada Foundation for Innovation (CFI), and the BC Knowledge Development Fund (BCKDF), as well as a University of Victoria Graduate Award, a James A. & Laurette Agnew Memorial Award, and an Anand-UVic Fund Graduate Scholarship to I.S., a Tier 2 Canada Research Chair to E.N., and a Leverhulme Trust project 'EROICA' to I.P.

3.12 Supplemental Material

Description of Supplemental Material

The supplemental material includes ten figures (Figures 3.14–3.23), three tables (Tables 3.4–3.6), and three long tables (Long tables 3.7–3.9). The figures show additional and supporting results from the InSAR-GNSS inversion and seismological modeling. Tables in the supplementary information include the velocity model used in the earthquake relocation, fault parameters and their search bounds for the InSAR-GNSS inverse and forward models, the full distributed slip model, and our relocated hypocenters and focal mechanisms. Descriptions of each data field (column) in the data files are included in this document.

List of Supplemental Tables

1. Table 3.4: Uniform slip inversion parameter bounds
2. Table 3.5: Velocity model used in the *mloc* relocation
3. Table 3.6: Configurations for the secondary, northern fault uniform slip model and model results

List of Supplemental Figures

1. Figure 3.14: Observed versus modeled surface displacements
2. Figure 3.15: Relative and absolute location results from *mloc*
3. Figure 3.16: Theoretical and observed arrival time data

4. Figure 3.17: Arrival times from various scales of epicentral distances
5. Figure 3.18: Unwrapped interferograms of our preferred two-fault model
6. Figure 3.19: Western model fault parameter uncertainties
7. Figure 3.20: Eastern model fault parameter uncertainties
8. Figure 3.21: Wrapped interferograms of the non-crossing fault geometry test
9. Figure 3.22: Comparison of the centroid and focal depths
10. Figure 3.23: Relocated focal mechanisms displayed by their kinematics

List of Supplemental Long Tables

1. Long table 3.7: Parameters of the distributed slip model sub-fault patches
2. Long table 3.8: *mloc* calibrated hypocenters
3. Long table 3.9: Regional moment tensor solutions

Table 3.4: Fault parameter search bounds used in the uniform slip modeling. We inverted the InSAR and GNSS data 500 times with starting parameters picked at random from within the search bounds, using the downhill simplex algorithm to obtain 500 local misfit minima, from which the global minimum misfit was obtained. Our preferred inverse model comprises a western and eastern model fault. Later, a northern model fault was added to account for the northern fault zone mapped in the field and visible as a minor InSAR displacement discontinuity (see the Mainshock Source Model and Mechanisms Section in the main paper). Easting and northing refer to the center point of the model fault surface projection and are in the Universal Transverse Mercator (UTM) zone 11N coordinates.

Model fault	Easting (km)	Northing (km)	Strike (°)	Dip (°)	Rake (°)	Length (km)	Top depth (km)	Bottom depth (km)	Slip (m)
Western	412 ±4	4225 ±4	55 ±10	50 ±20	−50 ±20	10 ±4	2 ±2	10 ±5	0.5*
Eastern	419 ±4	4226 ±4	80 ±10	70 ±20	0 ±20	20 ±5	2 ±2	10 ±5	0.5*
Northern	410.905*	4226.140*	54*/234*	50 ±30	−90 ±60	6*	0*	6 ±6	0.1 ±0.1

*Parameters that were fixed in the inversion.

Table 3.5: One-dimensional velocity model used in the *mloc* relocation, with customized phase velocities for the crust and upper mantle (<120 km) and the ak135 global model used below 120 km (Kennett et al., 1995). The Moho depth is at 30 km.

Depth range (km)	P (km/s)	S (km/s)
0.00–10.00	5.90	3.30
10.00–30.00	6.35	3.65
30.00–77.50	7.950	4.48–4.49
77.50–120.00	7.95–8.05	4.49–4.50

Table 3.6: Uniform slip parameter configurations and results for the northern fault in the three-fault modeling scenario. The inversion results (first row) are based on the parameter space provided in Supplementary Table 3.4 (third row, northern model fault). The forward modeling results (second to fourth rows) reflect possible structural configurations discussed in the Mainshock Source Model and Mechanisms Section of the main paper. Forward model interferograms for each row are shown in Figure 3.5 of the main paper.

Model type	Easting (km)	Northing (km)	Strike (°)	Dip (°)	Rake (°)	Length (km)	Top depth (km)	Bottom depth (km)	Slip (cm)
Inversion	410.905	4226.140	54	56	−138	6	0	2	7
Forward (NW-dipping LL-normal)	410.905	4226.140	234	45	−45	6	0	5	10
Forward (SE-dipping LL-reverse)	410.905	4226.140	54	45	45	6	0	5	10
Forward (Vertical LL-oblique)	410.905	4226.140	234	89.99	−45	6	0	5	10

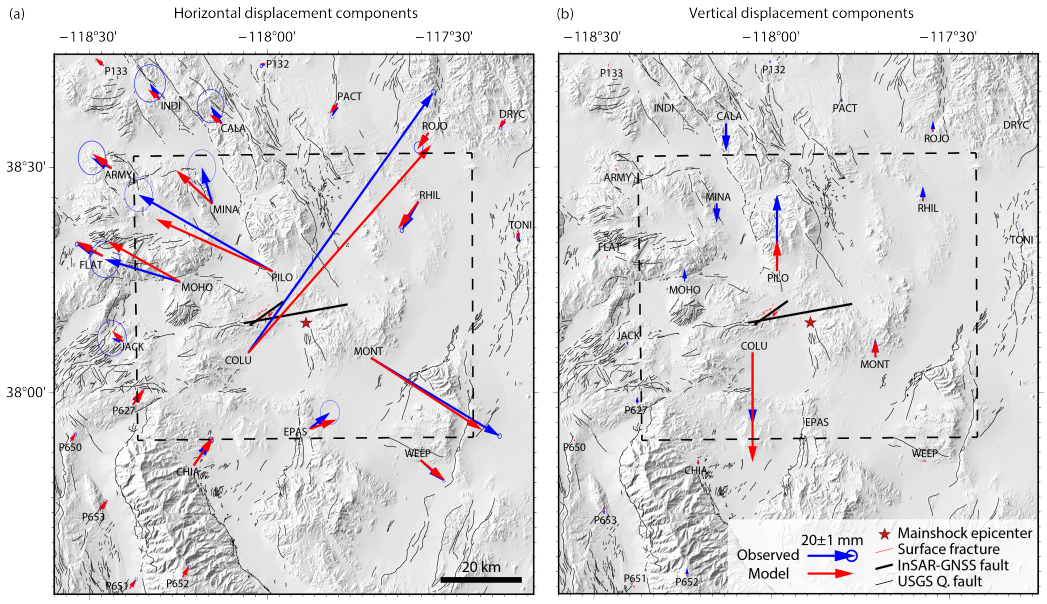


Figure 3.14: (a) Horizontal and (b) vertical GNSS coseismic surface displacements in the MCRE. Blue vectors are observed displacements processed by the Nevada Geodetic Laboratory as of 19 June 2020 (Blewitt et al., 2018), labeled with station names. Red vectors are our InSAR-GNSS distributed slip model surface displacements at the same locations. Thick black lines show the surface projections of our two model faults. The dashed box indicates the boundary of Figure 2 of the main paper. See the Geodetic Slip Modeling Section of the main paper for further details. Station locations and coseismic offsets can be found at `http://geodesy.unr.edu/news_items/20200619/nn00725272_24hr_19-Jun-2020.txt`.

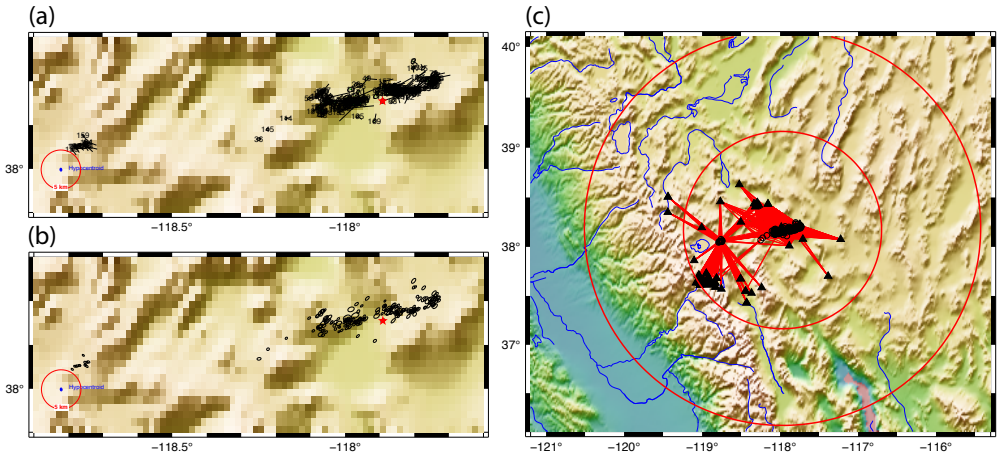


Figure 3.15: (a) Relocated epicenters (event numbers) and cluster vectors (black lines) showing the shift from starting locations to final, relative relocations. The red circle is a 5 km radius scale. (b) Similar to panel (a) but with 90% confidence ellipses. (c) Raypaths used for the direct calibration (absolute locations). Open circles are calibrated epicenters, black triangles are seismic stations, and red vectors are raypaths used for direct calibration. The two red circles show 1.0° and 2.0° radii centered upon the cluster hypocentroid. See https://seismo.com/mloc/summary-plots/ for more details.

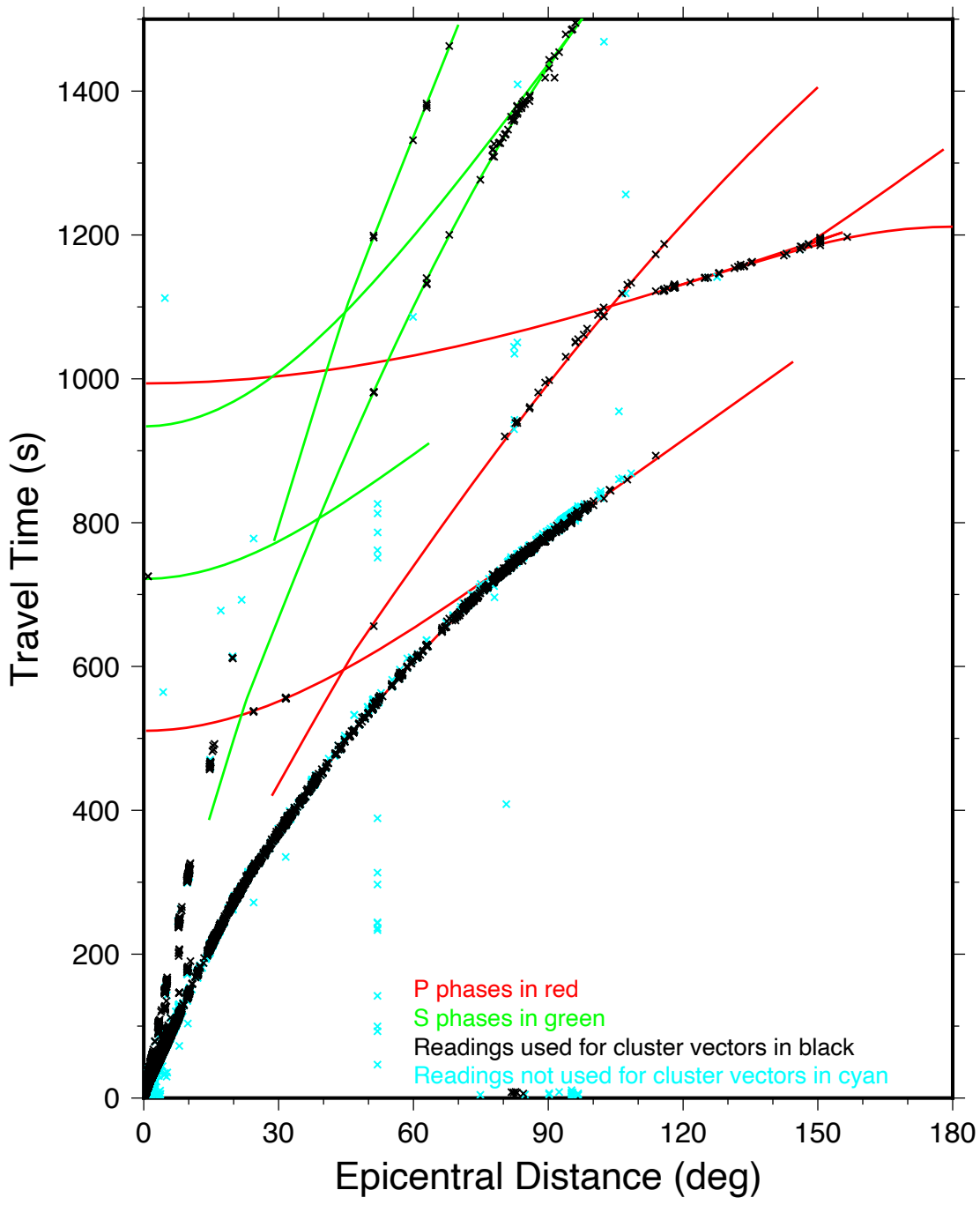


Figure 3.16: Theoretical and observed arrival times. Theoretical curves are from the customized velocity model in Table 3.5, which incorporates the ak135 global model (Kennett et al., 1995) below 120 km. Cross symbols are individual arrival time data, colored by their usage in the relocation: black—travel times used for cluster vectors but not for hypocentroid; cyan—travel times neither used for cluster vectors nor hypocentroid.

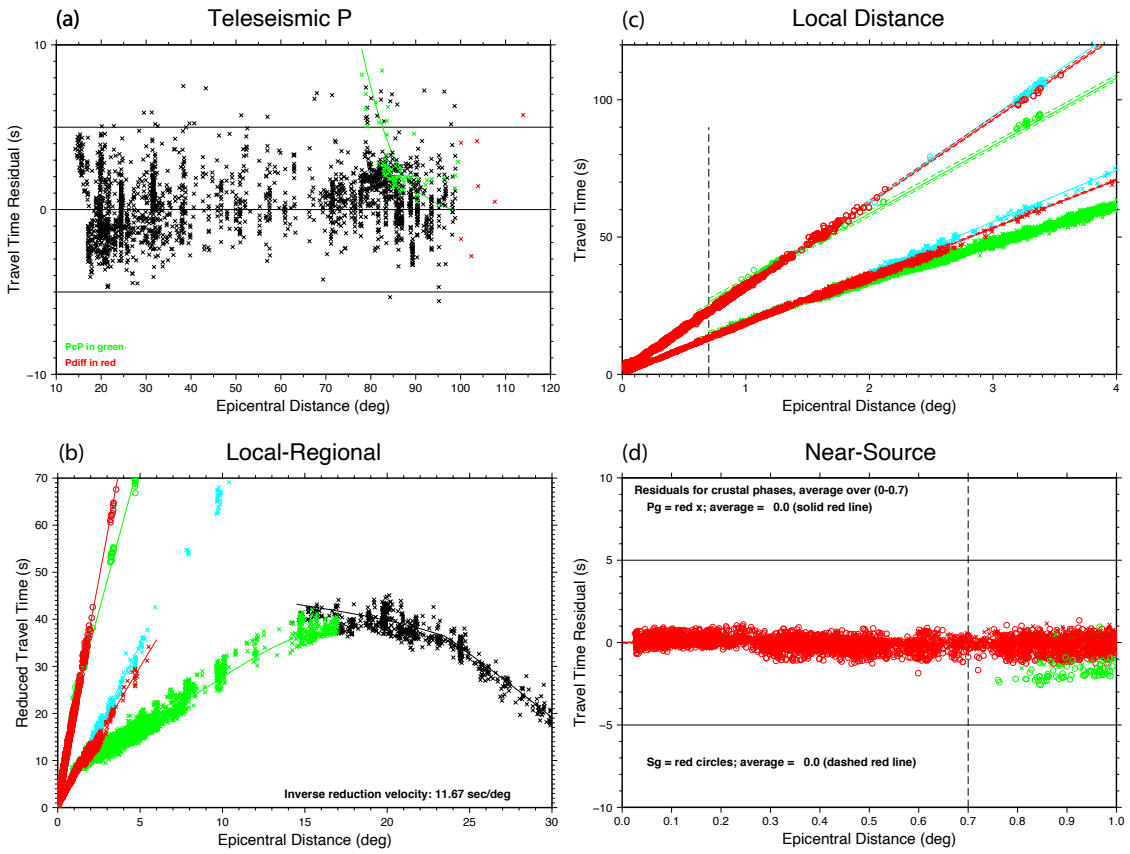


Figure 3.17: Arrival times at various epicentral distance ranges. (a) P phase arrivals (black crosses) from 10°–120°, reduced to the theoretical time (ak135, (Kennett et al., 1995)). The green line denotes the theoretical arrival time of phase PcP. (b) Travel times up to an epicentral distance of 30°, and reduced for visual readability (11.67 seconds/degree in inverse form, or 350 seconds at 30°). The phases include: red crosses—Pg and Sg; blue crosses—Pb and Sb; green crosses—Pn and Sn; black crosses—P; cyan circles—any other phases. (c) Travel times over 0°–4° epicentral distances. The theoretical travel times are based on the customized velocity model in Supplementary Table B1. The phases include: red crosses—Pg; blue crosses—Pb; green crosses—Pn; red circles—Sg; blue circles—Sb; green circles—Sn; cyan circles—any other phases. The vertical dashed line denotes the distance limit used to calculate the hypocentroid. (d) The residual for each arrival time within the epicentral distance used for estimating the hypocentroid, illustrated by the vertical dashed line at 0.7°. The solid and dashed red lines represent the average travel time residual for each phase. The green circles beyond the 0.7° mark is phase Sn.

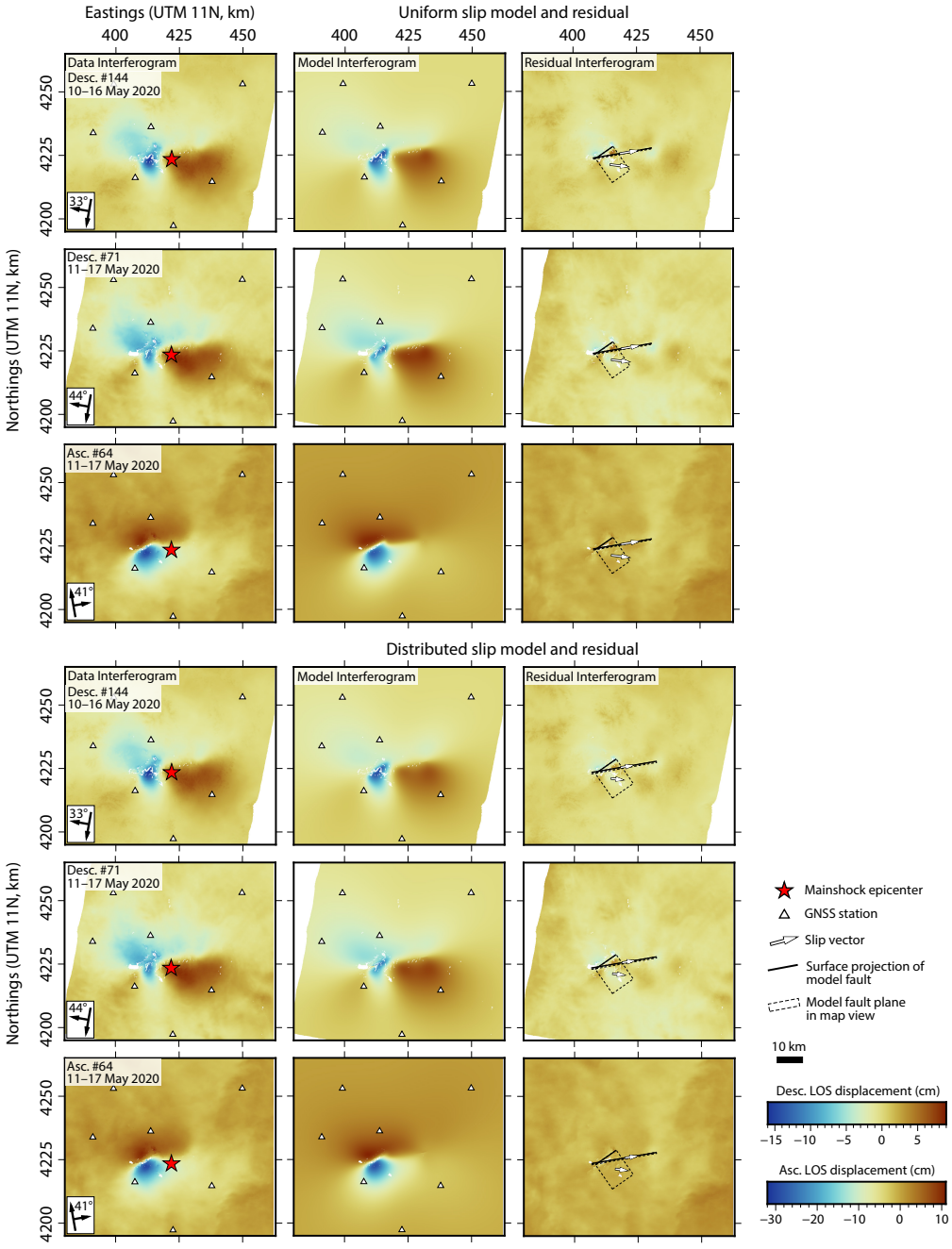


Figure 3.18: Observed (left column), uniform slip model (center), and residual (right) unwrapped interferograms of our preferred two-fault model (see the Mainshock Source Model and Mechanisms Section). The satellite orbital tracks (desc.—descending, asc.—ascending) are followed by the track number and the interferogram date range. Satellite track and line-of-sight (LOS) azimuths are given as long and short vectors in the corner of the data interferograms, along with the incidence angle. The thick black lines indicate the surface projection of the model fault, the red star is our relocated mainshock epicenter, and the white triangles are nearby GNSS stations.

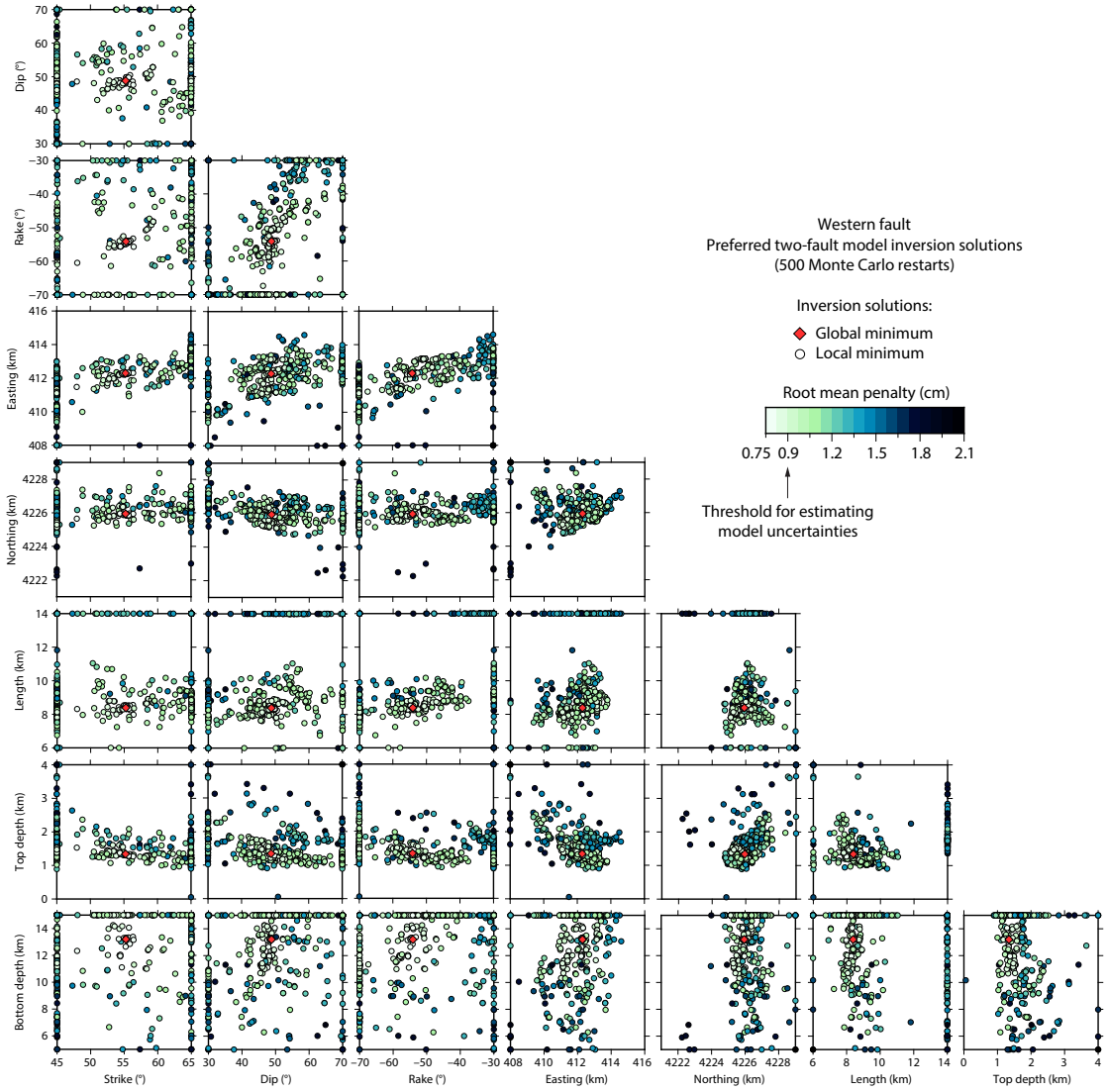


Figure 3.19: Western model fault plane parameters yielded by the 500 Monte Carlo restarts of the two fault, uniform slip inversion. Solutions for 499 local misfit minima are colored by the root mean square residual displacement between the InSAR-GNSS data and model. The global minimum misfit solution is indicated by the red diamond. Model runs with root mean square residuals of lesser than 0.9 cm are used to estimate parameter uncertainties. See the Mainshock Source Model and Mechanisms Section of the main paper for more details.

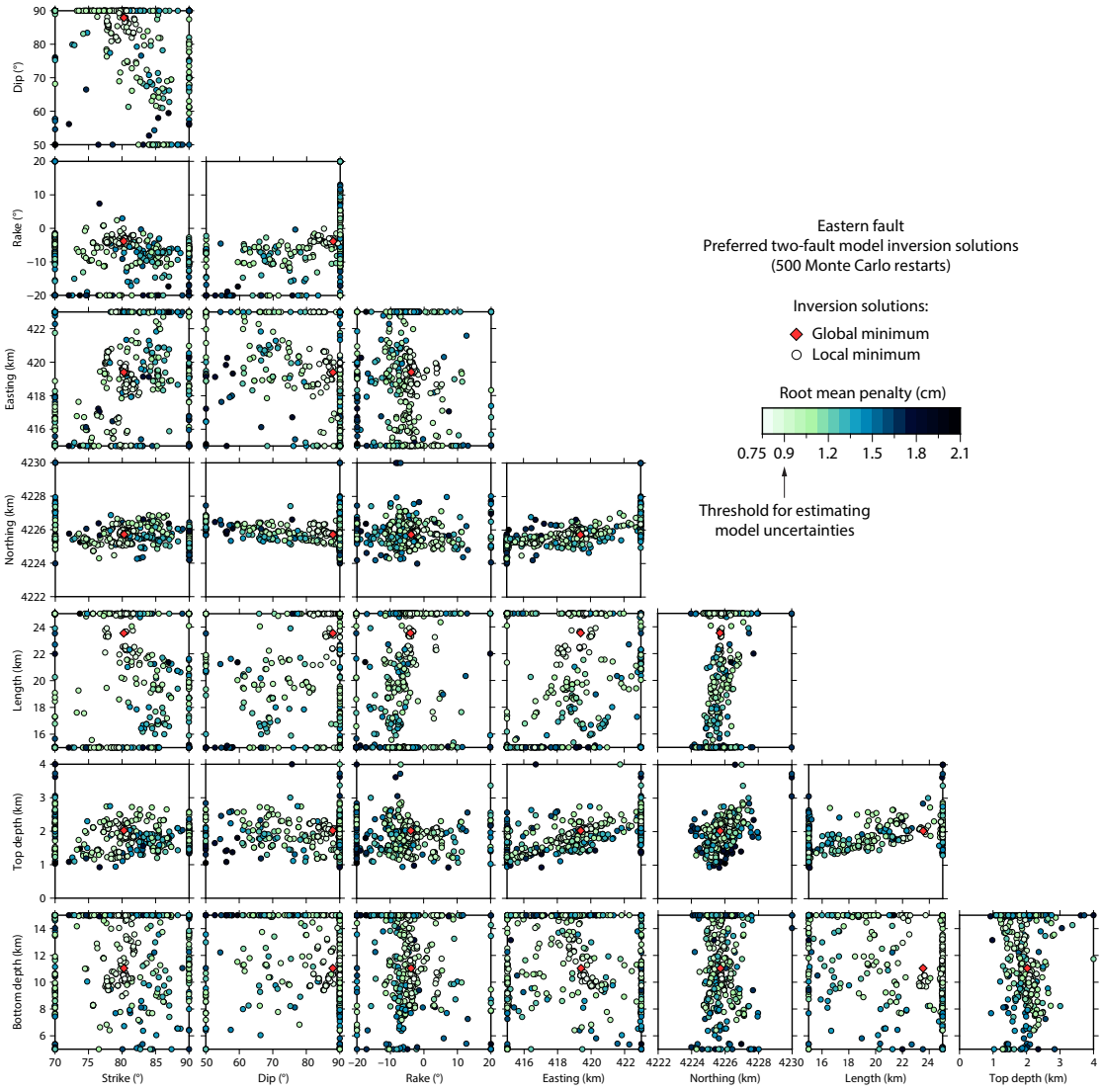


Figure 3.20: Eastern model fault plane parameters yielded by the 500 Monte Carlo restarts of the two fault, uniform slip inversion. Details are as in Supplementary Figure 3.19.

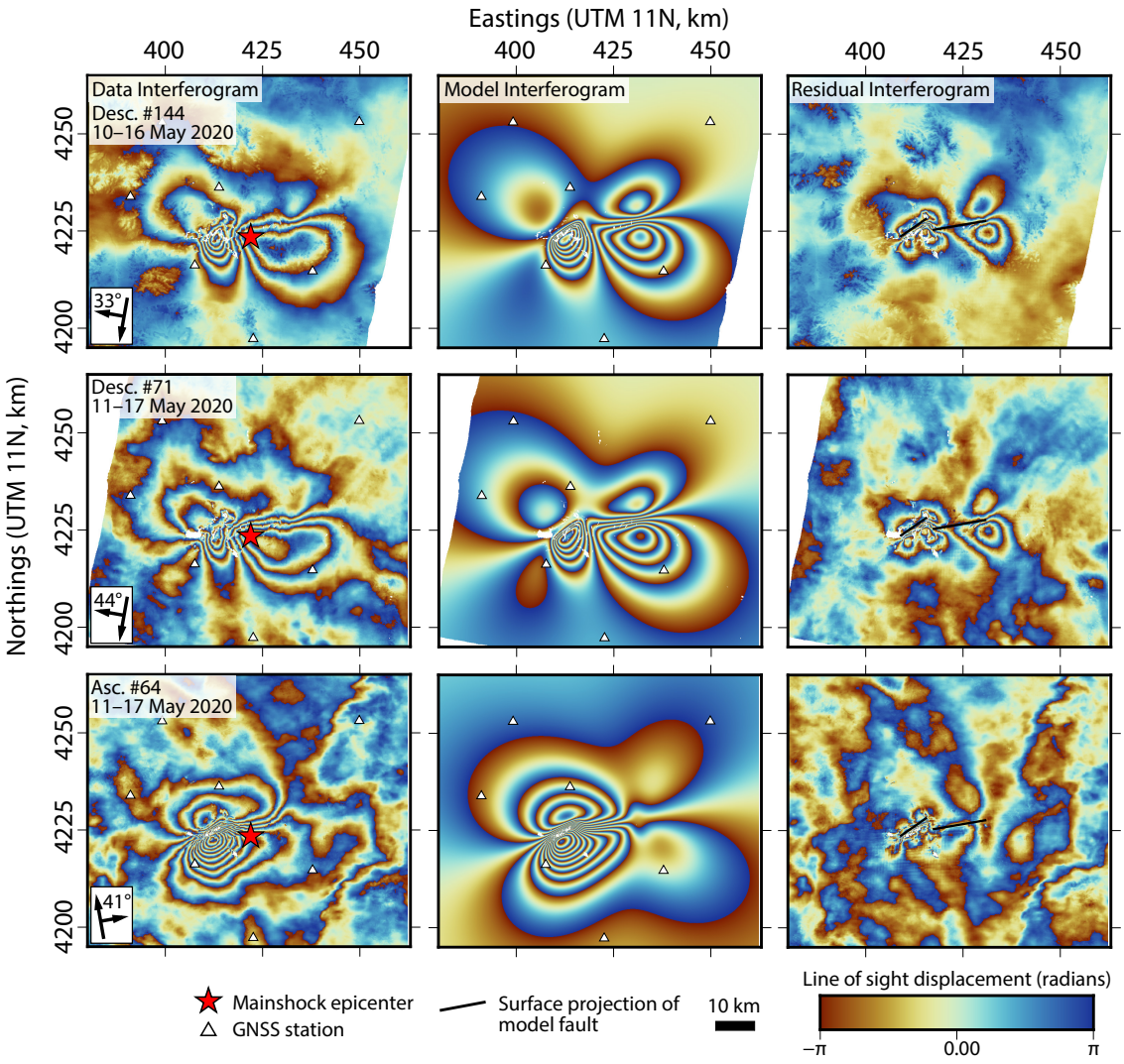


Figure 3.21: Observed (left column), model (center), and residual (right) wrapped interferograms of the uniform slip inversion in which we tested a non-crossing fault configuration. The satellite orbital tracks (desc.—descending, asc.—ascending) are followed by the track number and the interferogram date range. Satellite track and line-of-sight azimuths are given as long and short vectors in the corner of the data interferograms, along with the incidence angle. The thick black lines in the residual column indicate the surface projection of the model fault, the red star is our relocated mainshock epicenter, and the white triangles are nearby GNSS stations.

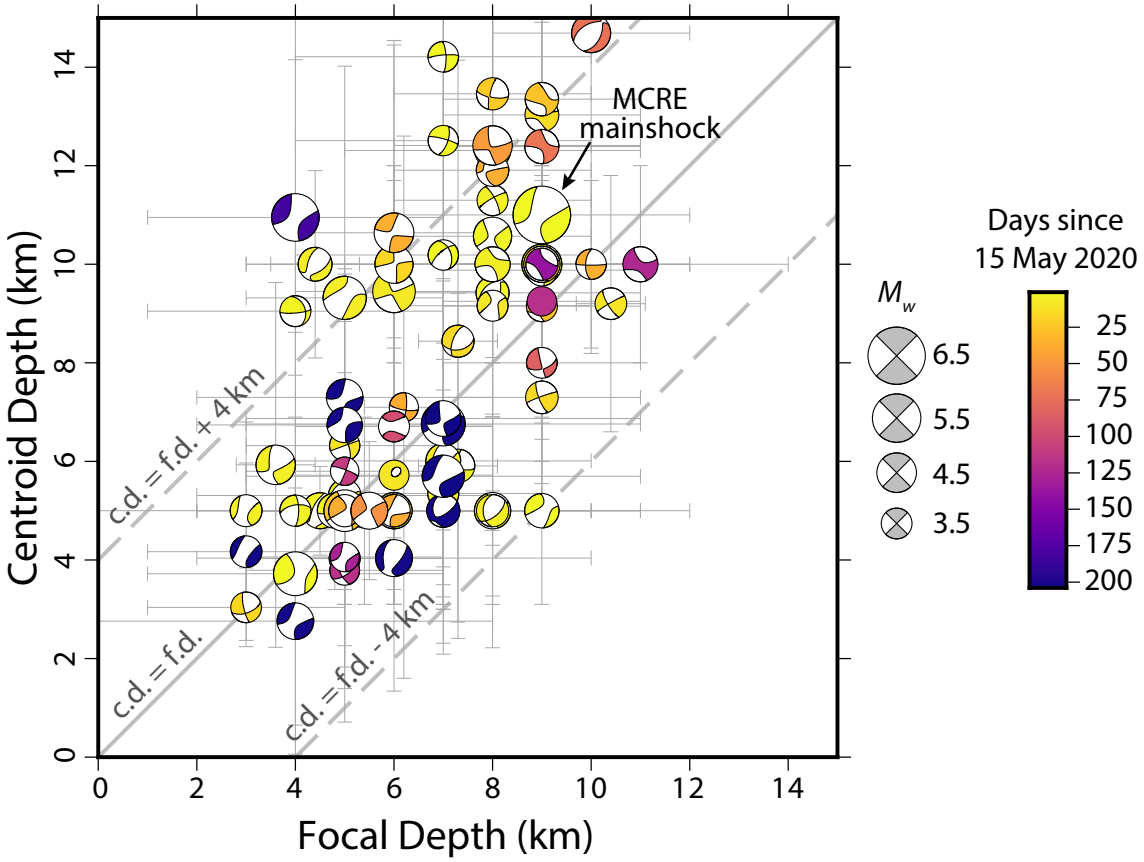


Figure 3.22: Comparison of centroid and focal depths of the 90 best-recorded events of the MCRE sequence (including the mainshock), calculated from regional waveform modeling and calibrated multi-event relocations, respectively (see the Seismological Analysis Section of the main paper for further details). The focal mechanisms are shaded by the number of days since 15 May 2020 (the mainshock) and scaled by moment magnitude, with estimated uncertainty ranges as thin gray bars. The thicker gray line represents equality of centroid depths (c.d.) and focal depths (f.d.), and dashed gray lines denote 4 km offsets between the two.

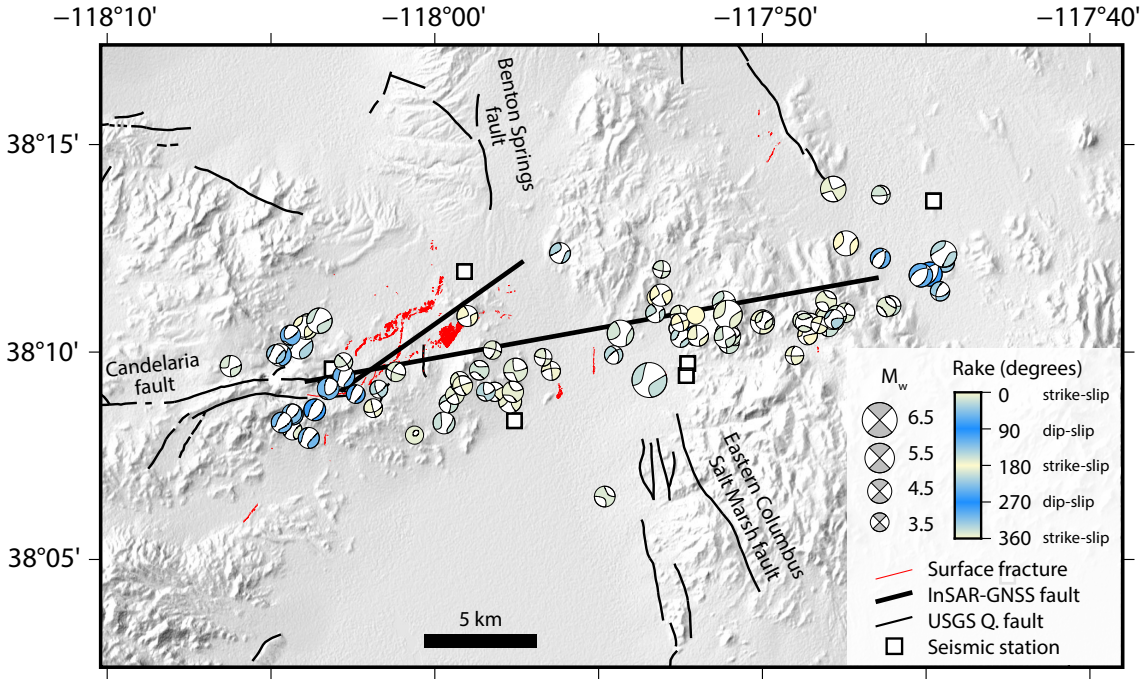


Figure 3.23: Hillshade map showing the focal mechanisms, plotted by their relocated epicenters and colored by rake values in degrees. We used the 'rake 2' values from our moment tensor solutions (Supplementary Long table 3.9, and added 360° to the negative values. Rake values of 0°, 180°, and 360° indicate strike-slip focal mechanisms; 90° and 270° are dip-slip; and values in between are oblique-slip. The thick black lines indicate the surface projection of the two model faults, thin black lines are the US Quaternary faults, thin red lines are the MCRE surface ruptures (Dee et al., 2021; Koehler et al., 2021), and white squares indicate nearby seismic stations.

Table 3.7: Parameters of the InSAR-GNSS distributed slip model sub-fault patches. Eastings and Northings are in UTM zone 11N, referring to the central coordinates of each sub-fault patch's surface projection. Each patch is 2 km × 2 km. The sub-fault patches of the western and eastern model faults span rows 1–45 and 46–136, respectively. See Table 3.2 in the main text for strike, dip, and rake values for each model fault.

Easting (m)	Northing (m)	Model slip (m)	Top depth (km)	Bottom depth (km)
409006	4223663	0.023	0.00	1.50
409006	4223663	0.306	1.50	3.01
409006	4223663	0.281	3.01	4.51
409006	4223663	0.222	4.51	6.02
409006	4223663	0.204	6.02	7.52
409006	4223663	0.244	7.52	9.03
409006	4223663	0.283	9.03	10.53
409006	4223663	0.265	10.53	12.04
409006	4223663	0.166	12.04	13.54
410649	4224804	0.001	0.00	1.50
410649	4224804	0.472	1.50	3.01
410649	4224804	0.554	3.01	4.51
410649	4224804	0.477	4.51	6.02
410649	4224804	0.418	6.02	7.52
410649	4224804	0.439	7.52	9.03
410649	4224804	0.467	9.03	10.53
410649	4224804	0.419	10.53	12.04
410649	4224804	0.257	12.04	13.54
412292	4225944	0.013	0.00	1.50
412292	4225944	0.650	1.50	3.01
412292	4225944	0.726	3.01	4.51
412292	4225944	0.632	4.51	6.02
412292	4225944	0.531	6.02	7.52
412292	4225944	0.499	7.52	9.03
412292	4225944	0.487	9.03	10.53
412292	4225944	0.417	10.53	12.04
412292	4225944	0.250	12.04	13.54
413935	4227084	0.018	0.00	1.50
413935	4227084	0.433	1.50	3.01
413935	4227084	0.489	3.01	4.51
413935	4227084	0.514	4.51	6.02
413935	4227084	0.469	6.02	7.52
413935	4227084	0.417	7.52	9.03
413935	4227084	0.371	9.03	10.53

Continued on next page

Table 3.7 – *Continued from previous page*

Easting (m)	Northing (m)	Model slip (m)	Top depth (km)	Bottom depth (km)
413935	4227084	0.296	10.53	12.04
413935	4227084	0.173	12.04	13.54
415578	4228225	0.009	0.00	1.50
415578	4228225	0.239	1.50	3.01
415578	4228225	0.361	3.01	4.51
415578	4228225	0.423	4.51	6.02
415578	4228225	0.388	6.02	7.52
415578	4228225	0.309	7.52	9.03
415578	4228225	0.229	9.03	10.53
415578	4228225	0.144	10.53	12.04
415578	4228225	0.078	12.04	13.54
407573	4223691	0.000	0.00	2.00
407573	4223691	0.048	2.00	4.00
407573	4223691	0.281	4.00	6.00
407573	4223691	0.412	6.00	7.99
407573	4223691	0.388	7.99	9.99
407573	4223691	0.283	9.99	11.99
407573	4223691	0.157	11.99	13.99
409545	4224029	0.000	0.00	2.00
409545	4224029	0.235	2.00	4.00
409545	4224029	0.473	4.00	6.00
409545	4224029	0.530	6.00	7.99
409545	4224029	0.426	7.99	9.99
409545	4224029	0.264	9.99	11.99
409545	4224029	0.119	11.99	13.99
411516	4224366	0.132	0.00	2.00
411516	4224366	0.548	2.00	4.00
411516	4224366	0.742	4.00	6.00
411516	4224366	0.666	6.00	7.99
411516	4224366	0.450	7.99	9.99
411516	4224366	0.230	9.99	11.99
411516	4224366	0.081	11.99	13.99
413487	4224704	0.049	0.00	2.00
413487	4224704	0.516	2.00	4.00
413487	4224704	0.720	4.00	6.00
413487	4224704	0.618	6.00	7.99
413487	4224704	0.379	7.99	9.99
413487	4224704	0.159	9.99	11.99
413487	4224704	0.036	11.99	13.99

Continued on next page

Table 3.7 – *Continued from previous page*

Easting (m)	Northing (m)	Model slip (m)	Top depth (km)	Bottom depth (km)
415458	4225042	0.000	0.00	2.00
415458	4225042	0.297	2.00	4.00
415458	4225042	0.499	4.00	6.00
415458	4225042	0.447	6.00	7.99
415458	4225042	0.259	7.99	9.99
415458	4225042	0.083	9.99	11.99
415458	4225042	0.000	11.99	13.99
417430	4225379	0.002	0.00	2.00
417430	4225379	0.391	2.00	4.00
417430	4225379	0.512	4.00	6.00
417430	4225379	0.417	6.00	7.99
417430	4225379	0.232	7.99	9.99
417430	4225379	0.071	9.99	11.99
417430	4225379	0.000	11.99	13.99
419401	4225717	0.000	0.00	2.00
419401	4225717	0.520	2.00	4.00
419401	4225717	0.645	4.00	6.00
419401	4225717	0.524	6.00	7.99
419401	4225717	0.322	7.99	9.99
419401	4225717	0.143	9.99	11.99
419401	4225717	0.038	11.99	13.99
421372	4226055	0.000	0.00	2.00
421372	4226055	0.379	2.00	4.00
421372	4226055	0.612	4.00	6.00
421372	4226055	0.602	6.00	7.99
421372	4226055	0.457	7.99	9.99
421372	4226055	0.273	9.99	11.99
421372	4226055	0.115	11.99	13.99
423344	4226392	0.000	0.00	2.00
423344	4226392	0.178	2.00	4.00
423344	4226392	0.492	4.00	6.00
423344	4226392	0.646	6.00	7.99
423344	4226392	0.603	7.99	9.99
423344	4226392	0.433	9.99	11.99
423344	4226392	0.216	11.99	13.99
425315	4226730	0.000	0.00	2.00
425315	4226730	0.091	2.00	4.00
425315	4226730	0.460	4.00	6.00
425315	4226730	0.737	6.00	7.99

Continued on next page

Table 3.7 – *Continued from previous page*

Easting (m)	Northing (m)	Model slip (m)	Top depth (km)	Bottom depth (km)
425315	4226730	0.775	7.99	9.99
425315	4226730	0.606	9.99	11.99
425315	4226730	0.322	11.99	13.99
427286	4227068	0.000	0.00	2.00
427286	4227068	0.090	2.00	4.00
427286	4227068	0.529	4.00	6.00
427286	4227068	0.872	6.00	7.99
427286	4227068	0.933	7.99	9.99
427286	4227068	0.743	9.99	11.99
427286	4227068	0.402	11.99	13.99
429257	4227405	0.011	0.00	2.00
429257	4227405	0.099	2.00	4.00
429257	4227405	0.577	4.00	6.00
429257	4227405	0.911	6.00	7.99
429257	4227405	0.947	7.99	9.99
429257	4227405	0.743	9.99	11.99
429257	4227405	0.401	11.99	13.99
431229	4227743	0.031	0.00	2.00
431229	4227743	0.093	2.00	4.00
431229	4227743	0.443	4.00	6.00
431229	4227743	0.651	6.00	7.99
431229	4227743	0.648	7.99	9.99
431229	4227743	0.496	9.99	11.99
431229	4227743	0.265	11.99	13.99

Table 3.8: *mloc* calibrated hypocenters of the mainshock and 196 aftershocks. The relocated hypocentral values include the origin date, origin time, latitude and longitude, and focal depth. The earthquake magnitude and magnitude type (columns 5–6) are gathered from the ISC Bulletin and the USGS ANSS ComCat. *mloc* depth code (column 8) refers to the methods and/or data source of the focal depth estimation (m—mloc free parameter solution, n—near-source readings, l—local-distance readings). For focal depth uncertainties (column 9), in free depth solutions, the uncertainties are calculated from the covariance matrix of the relocation. For manually fixed depths, the errors are estimated from observations and trials to be ±2 km and ±3 km for the depth codes n and l, respectively. The 90% confidence ellipse semi-axis azimuth and its length (columns 10–12) reflects the uncertainties in the epicenter location. The short semi-axis azimuth is implied (perpendicular to the long semi-axis). Further information of *mloc* direct calibration output and depth constraints can be found at `https://seismo.com/mloc/hdf-files/` and `https://seismo.com/mloc/depth-constraint/`.

Origin date (yyyy-mm-dd)	Origin time (UTC)	Latitude (°)	Longitude (°)	Magnitude	Magnitude type	Focal depth (km)	Depth code	Depth uncertainty (± km)	Ellipse long semi-axis azim-uth (°)	Ellipse long semi-axis length (km)	Ellipse short semi-axis length (km)	Area of 90% confidence ellipse (km^2)
2020-05-08	14:55:08.88	38.0596	-118.7524	3.7	Mw	5.0	l	3.0	159	0.47	0.39	0.6
2020-05-15	11:03:27.74	38.1555	-117.8908	6.5	Mw	9.0	l	3.0	35	0.66	0.45	0.9
2020-05-15	11:18:13.48	38.1622	-117.9950	4.8	mb	7.0	l	3.0	59	0.99	0.68	2.1
2020-05-15	11:26:02.64	38.1742	-117.9055	5.0	Mw	4.0	l	3.0	36	0.70	0.43	0.9
2020-05-15	11:30:17.11	38.1490	-118.0177	4.1	ML	7.0	l	3.0	50	0.79	0.56	1.4
2020-05-15	11:52:07.34	38.1566	-117.9845	4.2	mb	5.0	l	3.0	28	0.60	0.43	0.8
2020-05-15	12:00:41.73	38.1749	-117.8038	4.0	mb	5.0	l	3.0	33	0.68	0.46	1.0
2020-05-15	13:02:12.65	38.1771	-117.8058	3.8	ML	8.0	l	3.0	39	0.76	0.48	1.1
2020-05-15	13:35:25.42	38.2462	-117.8024	3.6	ML	9.0	l	3.0	32	0.80	0.48	1.2
2020-05-15	13:51:37.86	38.1812	-117.9834	3.9	Mw	6.0	l	3.0	64	0.88	0.67	1.8
2020-05-15	15:07:26.13	38.1656	-117.9090	3.9	ML	7.0	l	3.0	50	0.84	0.60	1.6
2020-05-15	15:23:24.91	38.1813	-117.8008	4.3	mb	8.0	l	3.0	34	0.71	0.44	1.0
2020-05-15	17:08:07.98	38.1895	-117.8599	3.4	ML	7.0	l	3.0	39	0.84	0.49	1.3
2020-05-15	17:18:30.11	38.1928	-117.7462	3.1	ML	5.0	l	3.0	34	0.63	0.46	0.9
2020-05-15	17:25:21.46	38.1538	-118.0525	3.4	ML	9.0	l	3.0	44	0.75	0.56	1.3
2020-05-15	17:38:17.79	38.1622	-118.0559	3.5	ML	9.0	l	3.0	49	0.78	0.48	1.2
2020-05-15	17:42:26.17	38.1501	-118.0629	3.2	ML	9.0	l	3.0	53	0.93	0.54	1.6
2020-05-15	17:50:17.33	38.1865	-117.8529	4.3	Mw	5.0	l	3.0	32	0.56	0.41	0.7
2020-05-15	18:10:32.84	38.1733	-117.8678	3.7	Mw	5.0	l	3.0	28	0.59	0.40	0.7

Continued on next page

Table 3.8 – *Continued from previous page*

Origin date (yyyy-mm-dd)	Origin time (UTC)	Latitude (°)	Longitude (°)	Magnitude	Magnitude type	Focal depth (km)	Depth code	Depth uncertainty (± km)	Ellipse long semi-axis azim-uth (°)	Ellipse long semi-axis length (km)	Ellipse short semi-axis length (km)	Area of 90% confidence ellipse (km^2)
2020-05-15	18:38:14.13	38.2109	-117.7406	3.2	ML	10.0	l	3.0	35	0.79	0.44	1.1
2020-05-15	18:52:42.20	38.1763	-117.8761	3.5	Mw	6.0	l	3.0	54	1.04	0.73	2.4
2020-05-15	19:05:10.05	38.2043	-117.7733	3.7	Mw	8.0	l	3.0	36	0.84	0.49	1.3
2020-05-15	19:59:36.80	38.1655	-117.8500	3.1	ML	10.0	l	3.0	40	0.70	0.43	0.9
2020-05-15	20:03:47.37	38.1725	-117.8750	3.7	Mw	5.0	l	3.0	41	0.76	0.46	1.1
2020-05-15	20:54:12.14	38.1563	-117.9964	3.3	ML	8.0	l	3.0	44	0.72	0.46	1.0
2020-05-15	21:29:43.90	38.1929	-117.9669	3.2	ML	8.0	l	3.0	41	0.63	0.44	0.9
2020-05-15	21:59:43.55	38.1789	-117.7982	4.2	ML	7.0	l	3.0	40	0.72	0.43	1.0
2020-05-15	22:15:50.51	38.1569	-118.0463	4.1	Mw	6.0	l	3.0	36	0.53	0.40	0.7
2020-05-15	22:25:09.10	38.2026	-117.7404	3.8	ML	6.0	l	3.0	41	0.83	0.48	1.3
2020-05-15	22:46:30.73	38.1733	-117.8661	3.9	Mw	8.0	l	3.0	37	0.62	0.41	0.8
2020-05-15	22:50:24.13	38.1818	-117.8755	3.5	ML	7.0	l	3.0	42	0.98	0.51	1.6
2020-05-16	2:50:46.45	38.1628	-118.0464	3.5	ML	7.0	l	3.0	48	0.82	0.50	1.3
2020-05-16	4:12:21.82	38.1382	-117.9953	4.1	Mw	8.0	l	3.0	43	0.63	0.41	0.8
2020-05-16	4:32:17.05	38.1889	-117.8482	3.4	ML	8.0	l	3.0	35	0.66	0.41	0.8
2020-05-16	5:01:09.39	38.1675	-117.9707	3.8	ML	7.0	l	3.0	57	1.07	0.69	2.3
2020-05-16	6:06:17.64	38.0684	-118.2492	3.5	Mw	7.0	l	3.0	79	0.57	0.49	0.9
2020-05-16	6:40:45.72	38.2143	-117.7375	3.3	ML	8.0	l	3.0	35	0.84	0.46	1.2
2020-05-16	6:59:34.03	38.2049	-117.7467	3.3	ML	6.0	l	3.0	39	0.88	0.47	1.3
2020-05-16	9:08:40.11	38.1971	-117.7547	3.3	ML	10.0	l	3.0	35	0.70	0.41	0.9
2020-05-16	10:28:41.35	38.2065	-117.9363	3.9	Mw	9.0	l	3.0	38	0.70	0.43	1.0
2020-05-16	11:50:54.75	38.1980	-117.7480	4.5	Mw	9.0	l	3.0	36	0.76	0.44	1.0
2020-05-16	17:50:00.57	38.1582	-118.0584	3.3	ML	7.0	l	3.0	50	0.69	0.44	1.0
2020-05-16	18:06:43.15	38.2053	-117.7668	2.9	ML	4.0	l	3.0	43	0.76	0.48	1.2
2020-05-16	18:49:43.66	38.2056	-117.7325	2.7	ML	5.0	l	3.0	42	0.85	0.49	1.3
2020-05-16	20:17:44.98	38.2299	-117.7731	3.8	ML	4.0	l	3.0	35	0.70	0.43	1.0
2020-05-16	20:58:19.06	38.1889	-117.9518	3.2	ML	6.2	m	0.8	30	0.51	0.37	0.6
2020-05-16	21:15:59.23	38.1546	-117.9955	2.9	ML	9.0	m	0.9	37	0.56	0.43	0.8
2020-05-16	22:45:38.66	38.1219	-118.0644	3.0	ML	4.2	m	0.9	38	0.54	0.45	0.8
2020-05-16	23:27:14.99	38.1520	-118.0542	4.1	Mw	6.0	l	3.0	42	0.56	0.41	0.7
2020-05-17	6:42:03.00	38.1794	-117.8130	3.5	Mw	7.0	n	2.0	46	0.93	0.59	1.7
2020-05-17	8:28:48.76	38.1703	-117.8503	3.8	Mw	7.3	m	0.8	30	0.57	0.38	0.7

Continued on next page

Table 3.8 – *Continued from previous page*

Origin date (yyyy-mm-dd)	Origin time (UTC)	Latitude (°)	Longitude (°)	Magnitude	Magnitude type	Focal depth (km)	Depth code	Depth uncertainty (± km)	Ellipse long semi-axis azim-uth (°)	Ellipse long semi-axis length (km)	Ellipse short semi-axis length (km)	Area of 90% confidence ellipse (km^2)
2020-05-17	9:42:21.50	38.1441	-117.9989	3.1	ML	7.0	n	2.0	38	0.58	0.43	0.8
2020-05-17	11:22:50.48	38.2051	-117.7847	3.4	ML	8.0	n	2.0	35	0.72	0.42	1.0
2020-05-17	11:53:53.46	38.1469	-117.9617	4.3	Mw	8.0	n	2.0	37	0.58	0.41	0.8
2020-05-17	19:08:23.84	38.1592	-117.9409	3.9	ML	9.0	n	2.0	42	0.78	0.46	1.1
2020-05-17	21:17:02.63	38.1801	-117.8006	4.0	Mw	9.0	n	2.0	34	0.67	0.41	0.9
2020-05-17	21:47:44.87	38.1435	-118.0611	4.1	Mw	4.5	m	0.9	44	0.63	0.43	0.9
2020-05-17	23:19:54.94	38.1460	-117.9929	3.9	ML	4.0	n	2.0	40	0.57	0.41	0.7
2020-05-18	2:19:08.87	38.1611	-118.1038	4.0	Mw	4.8	m	0.8	38	0.52	0.41	0.7
2020-05-18	7:53:58.07	38.1901	-117.8606	2.9	ML	7.0	n	2.0	36	0.70	0.41	0.9
2020-05-18	8:05:15.47	38.1893	-117.7579	2.8	ML	7.0	n	2.0	33	0.75	0.43	1.0
2020-05-18	9:45:55.61	38.1494	-117.9898	3.5	ML	8.0	n	2.0	43	0.88	0.52	1.5
2020-05-18	23:23:34.72	38.1550	-117.8610	3.1	ML	4.0	l	3.0	38	0.80	0.42	1.1
2020-05-19	7:02:02.06	38.0609	-118.7421	3.2	ML	7.0	l	3.0	145	0.50	0.38	0.6
2020-05-19	9:08:34.07	38.1872	-117.8008	3.9	Mw	8.0	n	2.0	29	0.56	0.38	0.7
2020-05-19	9:48:50.46	38.1353	-118.0724	3.6	Mw	3.0	l	3.0	27	0.49	0.38	0.6
2020-05-19	10:58:43.32	38.1825	-117.7913	3.6	Mw	6.0	l	3.0	33	0.62	0.40	0.8
2020-05-19	18:01:59.36	38.1796	-117.9057	2.8	ML	5.0	n	2.0	40	0.74	0.45	1.1
2020-05-19	22:12:45.94	38.1741	-117.8512	4.4	Mw	3.6	m	0.8	30	0.58	0.42	0.8
2020-05-20	1:44:34.69	38.1864	-117.8612	3.2	ML	6.0	n	2.0	34	0.65	0.40	0.8
2020-05-20	3:13:49.42	38.1416	-118.0722	3.8	Mw	4.4	m	0.9	44	0.70	0.46	1.0
2020-05-20	3:49:21.60	38.1420	-118.0727	2.9	ML	8.0	l	3.0	57	0.84	0.53	1.4
2020-05-20	3:49:58.03	38.1238	-118.0713	3.9	ML	4.0	l	3.0	46	0.75	0.55	1.3
2020-05-20	9:46:16.92	38.1384	-118.0779	3.9	Mw	5.4	m	0.8	35	0.51	0.41	0.7
2020-05-20	12:36:53.76	38.2061	-117.7411	4.9	Mw	5.0	n	2.0	34	0.76	0.46	1.1
2020-05-20	13:34:55.54	38.2049	-117.7537	3.0	ML	6.0	l	3.0	35	0.74	0.42	1.0
2020-05-20	13:57:22.27	38.2005	-117.7597	3.2	ML	3.3	m	1.4	39	1.03	0.62	2.0
2020-05-20	14:44:29.72	38.2181	-117.7434	3.0	ML	5.0	l	3.0	37	0.80	0.46	1.2
2020-05-20	15:19:17.00	38.1810	-117.7880	3.1	ML	8.0	l	2.0	35	0.67	0.41	0.9
2020-05-20	20:19:14.82	38.1878	-117.7400	3.1	ML	1.0	l	3.0	41	0.79	0.50	1.2
2020-05-20	21:07:00.81	38.2008	-117.7293	3.2	ML	3.0	l	3.0	34	0.57	0.42	0.7
2020-05-21	16:33:10.74	38.1593	-117.9929	2.8	ML	7.0	l	3.0	41	0.66	0.44	0.9
2020-05-22	0:22:01.11	38.2321	-117.7972	4.8	Mw	6.0	n	2.0	21	0.51	0.36	0.6

Continued on next page

Table 3.8 – *Continued from previous page*

Origin date (yyyy-mm-dd)	Origin time (UTC)	Latitude (°)	Longitude (°)	Magnitude	Magnitude type	Focal depth (km)	Depth code	Depth uncertainty (± km)	Ellipse long semi-axis azim-uth (°)	Ellipse long semi-axis length (km)	Ellipse short semi-axis length (km)	Area of 90% confidence ellipse (km^2)
2020-05-22	10:29:26.75	38.1399	-117.9872	2.8	ML	6.0	n	2.0	40	0.62	0.41	0.8
2020-05-22	13:01:06.67	38.1322	-118.0641	4.3	mb	7.0	l	3.0	42	0.69	0.46	1.0
2020-05-22	17:50:45.80	38.1516	-117.9644	2.8	ML	5.0	n	2.0	46	0.64	0.51	1.0
2020-05-23	9:19:18.28	38.1333	-118.0103	3.6	ML	6.0	n	2.0	33	0.55	0.39	0.7
2020-05-23	13:07:09.31	38.1551	-117.9873	3.5	Mw	8.0	n	2.0	26	0.57	0.40	0.7
2020-05-23	18:53:49.83	38.1715	-117.8393	2.7	ML	7.0	n	2.0	26	0.58	0.42	0.8
2020-05-24	5:53:30.82	38.1589	-117.9574	2.9	ML	4.0	n	2.0	26	0.60	0.41	0.8
2020-05-24	9:57:52.66	38.1507	-117.9695	3.9	ML	10.4	m	0.7	9	0.59	0.45	0.8
2020-05-24	15:02:54.59	38.1786	-117.8752	3.3	ML	5.0	n	2.0	31	0.59	0.41	0.8
2020-05-24	22:32:00.93	38.1887	-117.8873	3.6	ML	6.0	n	2.0	37	0.63	0.43	0.9
2020-05-25	0:41:27.16	38.1986	-117.7360	3.2	ML	6.3	m	0.9	32	0.65	0.42	0.9
2020-05-25	2:54:53.07	38.1504	-117.9812	3.1	ML	9.0	n	2.0	29	0.59	0.42	0.8
2020-05-25	2:55:50.65	38.1594	-117.9774	3.7	Mw	9.0	n	2.0	25	0.55	0.40	0.7
2020-05-25	3:01:08.87	38.1544	-117.9705	2.9	ML	10.0	n	2.0	20	0.50	0.37	0.6
2020-05-25	4:03:16.88	38.1525	-117.9703	3.1	ML	10.0	n	2.0	21	0.51	0.38	0.6
2020-05-25	4:32:21.25	38.1578	-117.9573	2.8	ML	8.0	n	2.0	20	0.50	0.36	0.6
2020-05-25	4:44:25.54	38.1505	-118.0028	3.0	ML	3.4	m	0.8	15	0.49	0.37	0.6
2020-05-25	21:40:52.62	38.1782	-117.8475	3.3	ML	7.0	n	2.0	23	0.63	0.46	0.9
2020-05-25	22:52:30.44	38.1898	-117.7467	2.9	ML	7.6	m	0.9	27	0.57	0.41	0.7
2020-05-26	0:47:52.60	38.2084	-117.7325	2.8	ML	7.0	n	2.0	26	0.58	0.42	0.8
2020-05-26	6:40:47.10	38.1411	-118.0793	3.0	ML	6.0	n	2.0	20	0.50	0.38	0.6
2020-05-26	9:30:42.52	38.1202	-117.9632	3.1	ML	8.0	n	2.0	32	0.57	0.40	0.7
2020-05-26	22:14:30.77	38.1774	-117.8166	3.3	ML	7.3	m	0.8	21	0.52	0.37	0.6
2020-05-27	0:57:03.09	38.1498	-118.0402	3.5	Mw	5.0	n	2.0	22	0.52	0.39	0.6
2020-05-27	3:16:10.51	38.1651	-117.8456	3.2	ML	7.0	n	2.0	20	0.51	0.37	0.6
2020-05-27	16:03:24.30	38.1793	-117.7969	3.8	Mw	9.0	n	2.0	21	0.51	0.37	0.6
2020-05-27	17:43:12.43	38.1744	-117.8439	3.0	ML	6.4	m	0.8	27	0.60	0.39	0.7
2020-05-27	21:45:03.92	38.1320	-118.0651	3.1	ML	4.7	m	0.8	19	0.49	0.37	0.6
2020-05-28	4:18:09.62	38.0511	-118.7775	3.2	ML	5.0	l	3.0	147	0.48	0.37	0.6
2020-05-28	4:19:10.21	38.0516	-118.7739	3.3	ML	6.0	l	3.0	150	0.47	0.36	0.5
2020-05-28	6:28:47.07	38.1154	-118.1703	2.9	ML	6.0	n	2.0	11	0.48	0.38	0.6
2020-05-28	8:29:46.86	38.1588	-118.0198	3.8	ML	5.0	n	2.0	26	0.54	0.38	0.6

Continued on next page

Table 3.8 – *Continued from previous page*

Origin date (yyyy-mm-dd)	Origin time (UTC)	Latitude (°)	Longitude (°)	Magnitude	Magnitude type	Focal depth (km)	Depth code	Depth uncertainty (± km)	Ellipse long semi-axis azim-uth (°)	Ellipse long semi-axis length (km)	Ellipse short semi-axis length (km)	Area of 90% confidence ellipse (km^2)
2020-05-28	18:45:35.86	38.1849	-117.8413	3.0	ML	7.0	n	2.0	17	0.49	0.35	0.5
2020-05-29	6:26:36.68	38.2312	-117.8016	2.9	ML	7.1	m	0.8	21	0.56	0.39	0.7
2020-05-29	19:22:23.38	38.1547	-117.9966	2.7	ML	6.6	m	0.9	27	0.55	0.40	0.7
2020-05-29	19:36:28.83	38.1571	-118.0002	2.9	ML	5.5	m	0.8	26	0.59	0.41	0.8
2020-05-29	20:45:39.91	38.1911	-117.7429	3.9	ML	7.3	m	0.8	24	0.56	0.39	0.7
2020-05-29	23:43:43.54	38.1532	-117.9858	4.0	ML	9.0	n	2.0	10	0.56	0.40	0.7
2020-05-30	9:07:32.75	38.0526	-118.7684	3.4	ML	7.0	l	3.0	154	0.46	0.35	0.5
2020-05-30	9:22:57.83	38.0530	-118.7668	3.6	Mw	7.0	l	3.0	157	0.45	0.34	0.5
2020-05-30	15:55:02.93	38.1730	-117.8490	3.7	ML	3.0	n	2.0	18	0.54	0.39	0.7
2020-05-31	1:07:16.08	38.0510	-118.7820	4.3	Mw	6.0	l	3.0	159	0.45	0.34	0.5
2020-05-31	5:03:15.78	38.1547	-118.0584	3.2	ML	7.2	m	0.7	24	0.52	0.38	0.6
2020-06-01	0:54:25.05	38.1711	-117.8395	3.4	ML	7.1	m	0.8	29	0.60	0.43	0.8
2020-06-01	9:38:49.75	38.1810	-117.8728	3.2	ML	6.4	m	0.8	21	0.54	0.38	0.6
2020-06-02	0:47:34.61	38.1790	-117.8280	2.8	ML	8.0	n	2.0	21	0.51	0.36	0.6
2020-06-04	0:49:06.17	38.1398	-118.0164	3.4	ML	8.0	n	2.0	13	0.46	0.34	0.5
2020-06-05	17:48:04.52	38.1323	-118.0918	3.1	ML	6.0	n	2.0	19	0.50	0.39	0.6
2020-06-06	2:28:15.34	38.1769	-117.7995	3.6	Mw	8.0	n	2.0	15	0.50	0.38	0.6
2020-06-06	5:41:20.07	38.1537	-117.9662	3.4	ML	10.0	n	2.0	28	0.59	0.40	0.7
2020-06-06	10:13:04.59	38.1785	-117.8019	3.5	ML	8.2	m	0.7	23	0.55	0.39	0.7
2020-06-07	9:23:26.02	38.1298	-118.0181	3.2	ML	7.0	n	2.0	12	0.45	0.34	0.5
2020-06-07	13:13:24.90	38.0442	-118.7887	3.3	ML	6.0	l	3.0	152	0.47	0.35	0.5
2020-06-08	3:24:06.35	38.2103	-117.7908	4.7	Mw	5.0	n	2.0	20	0.53	0.40	0.7
2020-06-08	8:22:50.50	38.1508	-117.9740	3.5	Mw	9.0	n	2.0	23	0.52	0.37	0.6
2020-06-09	13:38:55.02	38.1853	-117.7680	3.8	Mw	9.0	n	2.0	25	0.56	0.39	0.7
2020-06-09	22:40:14.33	38.1885	-117.8844	3.3	ML	6.0	n	2.0	23	0.54	0.39	0.7
2020-06-10	22:09:06.22	38.1806	-117.8663	3.1	ML	8.0	n	2.0	25	0.57	0.40	0.7
2020-06-10	23:03:18.73	38.1791	-117.8827	3.2	ML	7.2	m	0.7	17	0.49	0.35	0.5
2020-06-11	0:04:12.51	38.1576	-117.9491	3.3	ML	8.0	n	2.0	18	0.48	0.35	0.5
2020-06-11	6:06:38.48	38.1711	-117.8934	2.9	ML	7.6	m	0.7	19	0.51	0.36	0.6
2020-06-13	11:33:20.43	38.0898	-118.2230	3.3	ML	8.0	n	2.0	8	0.50	0.43	0.7
2020-06-15	0:27:57.50	38.1486	-117.9556	3.0	ML	5.8	m	0.9	31	0.58	0.43	0.8
2020-06-15	1:32:36.20	38.1475	-117.9737	2.9	ML	9.0	n	2.0	28	0.59	0.42	0.8

Continued on next page

Table 3.8 – *Continued from previous page*

Origin date (yyyy-mm-dd)	Origin time (UTC)	Latitude (°)	Longitude (°)	Magnitude	Magnitude type	Focal depth (km)	Depth code	Depth uncertainty (± km)	Ellipse long semi-axis azim-uth (°)	Ellipse long semi-axis length (km)	Ellipse short semi-axis length (km)	Area of 90% confidence ellipse (km^2)
2020-06-15	9:12:37.44	38.1290	-118.0553	3.3	ML	5.0	n	2.0	23	0.53	0.40	0.7
2020-06-19	10:26:44.25	38.1779	-117.8090	4.1	Mw	9.0	n	2.0	32	0.58	0.39	0.7
2020-06-19	10:43:39.41	38.1776	-117.8103	3.0	ML	9.3	m	0.7	20	0.51	0.37	0.6
2020-06-19	20:42:21.89	38.1788	-117.8332	4.5	Mw	6.0	n	2.0	5	0.61	0.49	0.9
2020-06-19	23:25:07.88	38.1653	-117.8170	4.0	ML	10.0	n	2.0	31	0.70	0.44	1.0
2020-06-20	3:49:56.37	38.1735	-117.8103	3.7	Mw	8.0	n	2.0	22	0.57	0.38	0.7
2020-06-20	11:24:27.97	38.1815	-117.7955	3.7	Mw	6.0	m	0.8	17	0.50	0.36	0.6
2020-06-21	2:01:22.25	38.1824	-117.8878	3.6	Mw	5.0	n	2.0	24	0.58	0.40	0.7
2020-06-22	4:04:28.55	38.1362	-118.0280	2.7	ML	6.0	n	2.0	14	0.50	0.39	0.6
2020-06-22	9:18:58.80	38.1999	-117.8846	3.6	ML	6.2	m	0.8	14	0.47	0.34	0.5
2020-06-22	19:30:38.43	38.1585	-117.9486	2.9	ML	8.0	n	2.0	29	0.59	0.40	0.7
2020-06-23	4:46:33.65	38.0760	-118.7568	3.2	ML	4.0	l	3.0	153	0.46	0.34	0.5
2020-06-30	9:24:23.61	38.1595	-117.9589	4.5	Mw	8.0	n	2.0	37	0.69	0.42	0.9
2020-07-04	20:09:38.25	38.0602	-118.7461	3.2	ML	6.0	l	3.0	149	0.48	0.35	0.5
2020-07-06	6:12:55.35	38.1896	-117.8849	4.2	Mw	5.5	m	0.8	17	0.50	0.36	0.6
2020-07-06	8:22:18.08	38.1418	-118.0184	2.7	ML	7.0	n	2.0	20	0.51	0.37	0.6
2020-07-12	18:10:15.09	38.1522	-118.0383	3.1	ML	4.0	n	2.0	17	0.53	0.38	0.6
2020-07-13	1:33:17.03	38.1808	-117.8235	3.2	ML	8.0	n	2.0	19	0.54	0.39	0.7
2020-07-14	5:59:29.13	38.0533	-118.7521	3.6	Mw	6.0	l	3.0	153	0.48	0.35	0.5
2020-07-19	8:03:32.50	38.1764	-117.8365	3.1	ML	5.5	m	0.8	11	0.49	0.36	0.6
2020-07-19	10:07:44.85	38.0550	-118.7513	3.4	ML	5.0	l	3.0	155	0.46	0.34	0.5
2020-07-23	17:10:35.72	38.1086	-117.9135	3.9	Mw	9.0	n	2.0	28	0.56	0.44	0.8
2020-07-25	18:32:16.73	38.1761	-117.9615	2.7	ML	4.2	m	1.0	25	0.60	0.42	0.8
2020-07-26	2:06:29.08	38.1975	-117.7527	4.4	Mw	10.0	n	2.0	20	0.65	0.48	1.0
2020-07-28	18:18:13.98	38.1626	-118.0516	2.9	ML	6.9	m	0.7	23	0.52	0.38	0.6
2020-08-01	19:32:30.54	38.0515	-118.7474	3.2	ML	6.0	l	3.0	147	0.52	0.37	0.6
2020-08-06	13:01:58.24	38.1442	-118.0313	3.5	Mw	9.0	n	2.0	19	0.58	0.43	0.8
2020-08-07	14:13:02.75	38.1540	-117.9975	2.6	ML	5.0	n	2.0	14	0.53	0.39	0.7
2020-08-08	19:38:47.84	38.1739	-117.8565	2.9	ML	7.0	n	2.0	19	0.53	0.39	0.7
2020-08-14	10:32:37.21	38.1589	-117.9446	3.1	ML	8.0	n	2.0	24	0.56	0.40	0.7
2020-08-19	4:31:05.16	38.1785	-117.8118	3.5	Mw	6.0	n	2.0	20	0.54	0.40	0.7
2020-09-01	0:30:52.82	38.1776	-117.8042	3.5	ML	5.0	n	2.0	21	0.56	0.43	0.8

Continued on next page

Table 3.8 – *Continued from previous page*

Origin date (yyyy-mm-dd)	Origin time (UTC)	Latitude (°)	Longitude (°)	Magnitude	Magnitude type	Focal depth (km)	Depth code	Depth uncertainty (± km)	Ellipse long semi-axis azim-uth (°)	Ellipse long semi-axis length (km)	Ellipse short semi-axis length (km)	Area of 90% confidence ellipse (km^2)
2020-09-07	0:47:07.40	38.1646	-117.9449	3.5	ML	9.0	n	2.0	23	0.54	0.37	0.6
2020-09-08	12:35:18.05	38.1518	-118.0285	3.5	ML	5.0	n	2.0	25	0.60	0.44	0.8
2020-09-09	10:07:28.88	38.1814	-117.8673	3.6	ML	9.0	n	2.0	18	0.52	0.37	0.6
2020-09-15	16:33:36.91	38.1507	-117.9603	4.0	Mw	11.0	n	3.0	21	0.57	0.39	0.7
2020-09-18	14:00:01.30	38.1794	-117.8324	3.3	Mw	5.0	n	2.0	24	0.58	0.42	0.8
2020-09-29	11:36:12.32	38.1848	-117.7702	3.6	Mw	9.0	n	2.0	19	0.53	0.39	0.6
2020-11-13	9:13:52.23	38.1817	-117.8508	5.4	Mw	4.0	n	3.0	25	0.61	0.48	0.9
2020-11-13	9:29:24.87	38.1700	-117.7994	4.0	ML	10.0	n	3.0	21	0.65	0.49	1.0
2020-11-20	10:10:06.43	38.1799	-117.7969	3.6	Mw	7.0	n	2.0	20	0.51	0.36	0.6
2020-12-01	23:32:56.98	38.1692	-118.0687	4.9	Mw	7.0	l	4.0	26	0.56	0.40	0.7
2020-12-01	23:43:08.95	38.1777	-118.0643	3.9	mb	4.0	l	4.0	30	0.58	0.45	0.8
2020-12-01	23:47:06.08	38.1656	-118.0787	4.2	ML	6.0	l	4.0	37	0.68	0.45	1.0
2020-12-02	2:23:45.53	38.1762	-118.0654	4.2	mb	5.0	n	3.0	32	0.71	0.51	1.1
2020-12-02	4:49:29.33	38.1769	-118.0666	4.1	ML	5.0	n	3.0	38	0.65	0.47	1.0
2020-12-02	10:41:02.25	38.1659	-118.0807	3.6	Mw	3.0	n	2.0	29	0.58	0.40	0.7
2020-12-02	16:08:29.55	38.1735	-118.0734	3.7	Mw	7.0	l	4.0	29	0.60	0.41	0.8
2020-12-03	3:18:10.89	38.1727	-117.8523	4.0	Mw	7.0	l	4.0	32	0.78	0.51	1.3
2020-12-03	5:15:30.48	38.1793	-118.0587	4.8	Mw	7.0	l	4.0	27	0.56	0.37	0.7

Table 3.9: Regional moment tensor solutions for the 90 best-recorded events, involving waveform modelling and inversion for: moment magnitude (column 5), centroid depths (C.D., km) and uncertainties (Unc., ± km) (columns 6–7), six moment tensor components (mrr, mtt, mpp, mrt, mrp, and mtp) in N·m (columns 8–13), and two nodal planes (s,d,r for strike, dip, rake in degrees) (columns 14–19). Additional details include origin date (yyyy-mm-dd), origin time (UTC), epicentral latitude (Lat., °), and longitude (Lon., °) sourced from the USGS NEIC (columns 1–4). The last column indicates the data source for focal mechanisms (us—NEIC and nn—UNR) and phase type used in the inversion (Mwr—whole seismogram and Mww—W-phase). Refer to the Seismological Analysis subsection for full details of the waveform modelling.

Origin date	Origin time	Lat.	Lon.	M_w	C.D.	Unc.	mrr	mtt	mpp	mrt	mrp	mtp	s1	d1	r1	s2	d2	r2	Source
2020-05-15	11:03:27.18	38.169	-117.850	6.5	11.0	1.8	-1.897E+18	-1.882E+18	3.779E+18	-2.274E+18	-2.540E+16	5.478E+18	168	67	-167	73	78	-24	us_Mww
2020-05-15	11:26:01.75	38.181	-117.871	5.0	3.7	4.9	-2.241E+15	-2.321E+16	2.546E+16	3.154E+15	1.380E+16	1.825E+16	65	74	12	332	78	163	us_Mww
2020-05-15	13:51:37.15	38.169	-117.942	3.9	5.0	1.9	-7.700E+12	-5.181E+14	5.258E+14	2.298E+14	1.229E+14	6.356E+14	71	88	17	340	73	178	us_Mwr
2020-05-15	15:07:25.70	38.156	-117.898	3.4	10.2	8.1	-7.720E+13	-6.580E+13	1.430E+14	9.690E+13	2.770E+13	5.760E+13	230	70	-45	339	48	-153	nn_Mwr
2020-05-15	15:23:24.68	38.167	-117.801	4.1	12.3	7.3	0.000E+00	2.690E+14	-2.690E+14	-4.130E+14	3.600E+13	1.530E+15	95	90	-15	185	75	-180	us_Mwr
2020-05-15	17:50:16.94	38.173	-117.830	4.3	5.0	1.9	-1.067E+15	-8.559E+14	1.923E+15	9.715E+14	-1.218E+14	3.206E+15	350	71	-168	256	78	-19	us_Mwr
2020-05-15	18:10:32.48	38.186	-117.844	3.7	5.3	4.6	-2.083E+14	1.310E+14	7.726E+13	-2.324E+14	-1.523E+14	2.085E+14	215	23	-110	57	69	-82	us_Mwr
2020-05-15	18:52:41.35	38.172	-117.859	3.5	5.0	1.9	-4.826E+13	1.036E+14	-5.530E+13	-1.290E+13	-1.373E+14	1.174E+14	281	47	-15	21	79	-136	nn_Mwr
2020-05-15	19:05:09.20	38.215	-117.723	3.7	9.4	7.2	-4.301E+14	8.416E+13	3.460E+14	1.032E+14	-1.306E+14	2.516E+14	12	52	-116	230	45	-61	nn_Mwr
2020-05-15	20:03:46.75	38.170	-117.838	3.7	5.0	1.9	-1.613E+14	6.510E+12	1.548E+14	-4.458E+13	8.791E+13	3.294E+14	80	65	-20	179	72	-154	nn_Mwr
2020-05-15	21:59:43.29	38.166	-117.798	3.7	5.0	1.9	-2.750E+13	-4.790E+13	7.540E+13	-1.580E+14	2.420E+13	4.290E+14	85	85	-20	177	70	-175	us_Mwr
2020-05-15	22:15:49.95	38.152	-118.014	4.1	5.0	1.9	-1.283E+15	-1.302E+14	1.413E+15	-3.078E+14	3.558E+14	9.414E+14	49	47	-55	183	53	-122	us_Mwr
2020-05-15	22:25:08.74	38.180	-117.729	3.5	5.0	1.9	-1.630E+14	1.350E+14	2.740E+13	-3.960E+13	1.240E+14	1.630E+14	203	61	-132	85	50	-40	nn_Mwr
2020-05-15	22:46:30.27	38.169	-117.842	3.9	10.0	2.0	-1.255E+14	-3.179E+14	4.434E+14	-1.003E+14	4.320E+14	8.068E+14	169	86	-153	77	63	-5	us_Mwr
2020-05-15	22:50:24.03	38.183	-117.919	3.4	14.2	7.2	-1.610E+13	-1.410E+13	3.020E+13	4.670E+13	-2.650E+13	1.720E+14	265	80	-15	358	75	-170	nn_Mwr
2020-05-16	2:50:45.56	38.162	-118.009	3.4	5.0	1.9	3.850E+13	-1.380E+14	9.900E+13	-3.180E+13	8.310E+13	4.600E+13	321	78	144	60	55	15	nn_Mwr
2020-05-16	4:12:21.43	38.131	-117.976	4.1	5.0	1.9	-7.025E+14	-6.987E+14	1.401E+15	-3.426E+14	8.347E+14	8.624E+14	164	74	-138	60	50	-21	us_Mwr
2020-05-16	5:01:09.09	38.175	-117.935	3.4	12.5	7.9	-2.450E+13	9.870E+13	-7.410E+13	5.820E+13	-4.330E+13	1.250E+14	285	80	-25	20	65	-169	nn_Mwr
2020-05-16	6:06:17.32	38.058	-118.236	3.5	5.0	1.9	5.736E+13	-2.318E+14	1.745E+14	4.275E+13	2.291E+13	1.478E+14	64	86	12	333	78	176	nn_Mwr
2020-05-16	10:28:40.65	38.192	-117.901	3.9	5.0	1.9	-2.592E+14	-1.237E+14	3.829E+14	3.526E+14	6.637E+13	6.792E+14	352	60	-167	255	79	-31	nn_Mwr
2020-05-16	11:50:54.31	38.212	-117.735	4.5	10.0	1.8	-7.306E+15	2.529E+15	4.777E+15	1.071E+15	5.480E+13	3.842E+15	223	48	-81	30	43	-100	us_Mwr
2020-05-16	20:17:44.62	38.220	-117.763	3.5	9.1	8.4	5.850E+13	-7.860E+13	2.000E+13	1.580E+14	3.470E+13	1.110E+14	85	80	55	341	36	163	nn_Mwr
2020-05-16	23:27:14.58	38.143	-118.033	4.1	5.0	1.9	-1.031E+15	1.640E+13	1.015E+15	-4.637E+14	7.338E+14	7.306E+14	56	43	-42	179	63	-125	us_Mwr
2020-05-17	6:42:02.52	38.177	-117.786	3.5	5.4	2.1	-7.370E+13	-1.710E+14	2.447E+14	5.473E+13	-4.573E+13	9.500E+11	318	79	-156	223	67	-12	nn_Mwr
2020-05-17	8:28:48.51	38.162	-117.844	3.8	5.9	3.5	-2.628E+13	2.135E+14	-1.872E+14	-7.079E+13	2.042E+14	5.283E+14	99	72	-10	192	81	-162	us_Mwr

Continued on next page

Table 3.9 – *Continued from previous page*

Origin date	Origin time	Lat.	Lon.	M_w	C.D.	Unc.	mrr	mtt	mpp	mrt	mrp	mtp	s1	d1	r1	s2	d2	r2	Source
2020-05-17	11:53:53.34	38.150	-117.955	4.3	10.6	7.3	-2.998E+14	-3.105E+15	3.404E+15	-4.503E+14	-1.632E+14	1.681E+15	149	82	-178	58	88	-8	us_Mwr
2020-05-17	19:08:23.51	38.157	-117.935	3.6	9.9	3.1	-1.600E+13	-7.580E+13	9.180E+13	3.560E+13	-9.240E+13	2.540E+14	352	85	-160	260	70	-5	nn_Mwr
2020-05-17	21:17:02.47	38.175	-117.803	4.0	10.0	2.0	-8.400E+13	8.260E+13	1.400E+12	2.410E+14	-3.183E+14	1.215E+15	2	79	-166	270	76	-11	us_Mwr
2020-05-17	21:47:44.65	38.145	-118.046	4.1	5.0	0.9	-1.407E+15	3.194E+14	1.087E+15	3.540E+13	5.272E+14	8.123E+14	43	37	-73	202	54	-103	us_Mwr
2020-05-17	23:19:54.77	38.144	-117.993	3.5	5.0	1.9	-7.110E+13	2.100E+12	6.890E+13	6.000E+13	-1.040E+14	1.960E+14	0	73	-148	260	60	-20	nn_Mwr
2020-05-18	2:19:08.41	38.165	-118.100	4.0	5.0	1.6	-1.661E+14	-9.720E+13	2.633E+14	-1.853E+14	2.284E+14	1.013E+15	84	75	-11	176	79	-165	us_Mwr
2020-05-18	9:45:55.13	38.138	-117.979	3.5	11.3	7.0	-1.850E+13	-1.580E+14	1.770E+14	6.150E+13	-4.900E+12	1.070E+14	240	80	-15	333	75	-170	nn_Mwr
2020-05-19	9:08:33.88	38.178	-117.802	3.9	10.0	2.0	1.532E+14	-5.442E+14	3.910E+14	1.998E+14	-1.067E+14	8.489E+14	346	82	-173	255	83	-8	us_Mwr
2020-05-19	9:48:50.24	38.137	-118.063	3.6	5.0	1.8	-1.019E+14	-1.649E+14	2.668E+14	-8.822E+13	-8.073E+13	1.525E+14	59	82	-29	153	62	-170	nn_Mwr
2020-05-19	10:58:43.11	38.178	-117.792	3.6	10.0	2.0	-2.339E+13	1.816E+14	-1.582E+14	-1.006E+14	1.122E+14	2.768E+14	104	78	-21	198	70	-167	nn_Mwr
2020-05-19	22:12:45.64	38.176	-117.854	4.4	5.9	3.7	-1.712E+15	-1.465E+15	3.177E+15	-2.257E+15	8.862E+14	4.323E+15	71	70	-26	170	65	-158	us_Mwr
2020-05-20	3:13:49.19	38.137	-118.067	3.8	10.0	1.9	-5.188E+14	1.535E+14	3.652E+14	-1.805E+14	2.053E+14	4.369E+14	64	50	-50	192	54	-127	nn_Mwr
2020-05-20	3:49:57.90	38.126	-118.063	3.6	5.0	0.4	-2.720E+14	5.000E+12	2.670E+14	-1.790E+14	-3.150E+13	1.610E+14	50	60	-60	181	41	-131	nn_Mwr
2020-05-20	9:46:16.71	38.135	-118.068	3.9	5.0	1.9	-6.305E+14	2.363E+14	3.942E+14	-1.770E+14	2.465E+14	5.550E+14	67	49	-51	196	54	-126	us_Mwr
2020-05-20	12:36:53.45	38.201	-117.745	4.9	9.3	4.7	-1.176E+16	5.833E+15	5.922E+15	3.044E+15	-6.882E+15	2.324E+16	265	63	-23	6	69	-152	us_Mww
2020-05-22	0:22:00.59	38.231	-117.794	4.8	9.5	5.0	-5.200E+13	-1.263E+16	1.268E+16	-3.030E+15	2.230E+14	1.338E+16	159	82	-176	68	86	-8	us_Mww
2020-05-22	13:01:06.44	38.129	-118.062	3.9	6.0	3.7	-5.549E+14	-1.296E+14	6.845E+14	-4.408E+14	-2.491E+14	5.587E+14	174	40	-142	54	67	-56	us_Mwr
2020-05-23	9:19:17.81	38.136	-118.009	3.4	5.7	1.0	-1.330E+13	1.280E+14	1.410E+14	-4.120E+13	1.880E+13	5.610E+13	148	80	-165	55	75	-10	nn_Mwr
2020-05-23	13:07:08.77	38.147	-117.991	3.5	9.2	2.2	-4.582E+13	-1.441E+14	1.899E+14	6.028E+13	9.180E+12	1.116E+14	240	80	-19	333	72	-170	nn_Mwr
2020-05-24	9:57:52.26	38.138	-117.978	3.6	9.2	2.6	1.330E+13	-2.560E+14	2.430E+14	-5.270E+13	-5.910E+13	1.360E+14	240	85	15	149	75	175	nn_Mwr
2020-05-24	15:02:54.03	38.174	-117.879	3.4	6.3	1.0	0.000E+00	-9.910E+13	9.910E+13	5.270E+13	1.920E+13	1.180E+14	250	90	-20	340	70	-180	nn_Mwr
2020-05-24	22:32:00.76	38.185	-117.884	3.4	10.0	1.7	0.000E+00	-1.670E+14	1.670E+14	-3.490E+13	-2.920E+13	2.950E+13	50	90	-15	140	75	-180	nn_Mwr
2020-05-25	2:55:49.94	38.144	-117.989	3.7	12.4	2.5	1.280E+14	-3.530E+14	2.250E+14	-2.825E+13	-1.017E+14	2.218E+14	151	73	161	247	72	18	nn_Mwr
2020-05-27	0:57:02.39	38.139	-118.049	3.5	4.0	2.2	-1.795E+14	1.708E+13	1.624E+14	-2.797E+13	4.120E+13	1.166E+14	46	44	-66	193	50	-112	nn_Mwr
2020-05-27	16:03:23.89	38.175	-117.802	3.8	13.0	2.9	1.212E+14	-3.921E+14	2.709E+14	-1.512E+14	-3.435E+13	5.177E+14	163	75	177	254	87	15	us_Mwr
2020-05-28	8:29:46.17	38.152	-118.026	3.7	5.0	1.5	-6.890E+13	2.820E+14	-2.130E+14	-1.570E+14	1.220E+14	2.410E+14	110	80	-30	206	61	-168	nn_Mwr
2020-05-29	20:45:39.48	38.188	-117.743	3.6	8.4	5.7	-2.180E+14	1.480E+14	6.930E+13	-3.190E+13	1.810E+14	2.100E+14	201	63	-127	80	45	-40	nn_Mwr
2020-05-29	23:43:43.15	38.151	-117.993	3.7	7.3	2.2	1.870E+13	-2.740E+14	2.560E+14	-8.780E+13	-6.930E+13	3.010E+14	250	85	15	159	75	175	nn_Mwr
2020-05-30	15:55:02.40	38.168	-117.849	3.5	3.0	0.8	-4.220E+13	-6.400E+13	1.060E+14	-5.400E+13	7.710E+13	1.340E+14	168	77	-149	70	60	-15	nn_Mwr
2020-05-31	1:07:15.78	38.045	-118.762	4.3	10.0	2.0	-1.762E+14	-9.145E+14	1.091E+15	4.248E+14	-1.640E+14	3.501E+15	352	84	-176	262	86	-6	us_Mwr
2020-06-06	2:28:14.90	38.168	-117.801	3.6	13.5	3.1	-4.755E+13	1.517E+14	-1.041E+14	-4.416E+13	1.214E+14	2.900E+14	100	71	-13	194	77	-160	us_Mwr
2020-06-08	3:24:05.88	38.206	-117.791	4.7	5.0	1.6	-3.034E+15	-8.283E+15	1.132E+16	1.134E+15	1.193E+15	7.842E+15	64	90	7	334	83	180	us_Mwr
2020-06-08	8:22:49.99	38.146	-117.978	3.5	9.2	3.6	-5.845E+13	-5.490E+13	1.133E+14	-7.711E+13	7.533E+13	1.622E+14	71	63	-21	171	72	-151	nn_Mwr
2020-06-09	13:38:54.52	38.178	-117.773	3.8	13.4	4.0	2.095E+14	-2.026E+14	-6.910E+12	1.700E+14	1.003E+14	4.768E+14	89	71	28	350	64	159	us_Mwr
2020-06-19	10:26:43.70	38.172	-117.818	4.1	10.0	2.0	4.838E+14	-9.878E+14	5.040E+14	-7.875E+14	-4.659E+14	1.141E+15	159	55	163	259	76	36	us_Mwr

Continued on next page

Table 3.9 – *Continued from previous page*

Origin date	Origin time	Lat.	Lon.	M_w	C.D.	Unc.	mrr	mtt	mpp	mrt	mrp	mtp	s1	d1	r1	s2	d2	r2	Source
2020-06-19	20:42:21.45	38.170	-117.835	4.5	10.6	3.9	-5.132E+14	2.982E+15	-2.469E+15	-6.696E+14	7.662E+14	5.884E+15	102	84	-8	193	82	-174	us_Mwr
2020-06-19	23:25:07.38	38.173	-117.813	3.4	10.0	1.7	-1.530E+13	1.530E+13	0.000E+00	-8.660E+13	1.330E+13	1.520E+14	90	85	-30	183	60	-174	nn_Mwr
2020-06-20	3:49:55.96	38.175	-117.817	3.7	11.9	5.0	-6.200E+11	-1.068E+14	1.074E+14	-2.585E+14	-6.286E+13	2.798E+14	259	90	42	169	48	179	us_Mwr
2020-06-20	11:24:27.45	38.178	-117.797	3.7	5.0	1.6	-8.317E+13	1.448E+14	-6.160E+13	-7.693E+13	8.924E+13	3.474E+14	96	75	-17	190	74	-165	us_Mwr
2020-06-21	2:01:21.67	38.174	-117.886	3.6	5.0	1.9	-1.618E+13	-2.391E+14	2.552E+14	1.157E+14	7.073E+13	1.911E+14	334	67	180	64	90	23	nn_Mwr
2020-06-22	9:18:58.19	38.194	-117.885	3.3	7.1	5.5	1.400E+13	2.100E+13	-3.500E+13	2.860E+13	2.250E+13	9.740E+13	6	76	164	100	75	15	nn_Mwr
2020-06-30	9:24:23.55	38.154	-117.958	4.5	12.4	4.3	-2.799E+14	-2.158E+15	2.438E+15	-1.489E+15	7.141E+14	5.395E+15	170	78	-170	77	81	-13	us_Mww
2020-07-06	6:12:54.85	38.186	-117.891	4.2	5.0	1.4	-8.980E+13	-1.741E+15	1.831E+15	1.459E+14	-1.978E+14	1.105E+15	331	89	-173	241	83	-1	us_Mwr
2020-07-23	17:10:35.22	38.105	-117.922	3.9	12.4	4.3	1.419E+14	-1.081E+14	-3.379E+13	1.732E+14	-1.857E+13	7.431E+14	359	76	178	89	88	14	us_Mwr
2020-07-26	2:06:28.54	38.184	-117.755	4.4	14.7	6.5	-4.304E+15	1.991E+15	2.313E+15	1.319E+15	-1.023E+15	2.832E+15	23	48	-119	243	50	-62	us_Mwr
2020-08-06	13:01:57.70	38.135	-118.039	3.5	8.0	2.0	-1.629E+13	-8.122E+13	9.750E+13	-3.823E+13	1.009E+14	1.409E+14	165	86	-147	73	57	-5	nn_Mwr
2020-08-19	4:31:05.00	38.176	-117.811	3.5	6.7	1.8	-6.498E+13	2.276E+14	-1.626E+14	-5.280E+12	3.834E+13	4.600E+12	133	77	-14	226	76	-167	nn_Mwr
2020-09-01	0:30:52.23	38.177	-117.802	3.2	5.8	2.0	-2.370E+12	5.220E+13	-4.980E+13	1.410E+12	-1.510E+13	5.890E+13	21	85	-170	290	80	-5	nn_Mwr
2020-09-07	0:47:06.88	38.154	-117.948	3.3	10.0	1.7	1.620E+13	1.850E+13	-3.470E+13	4.690E+13	9.700E+12	9.690E+13	100	80	25	5	65	169	nn_Mwr
2020-09-08	12:35:17.38	38.150	-118.038	3.4	3.8	2.4	-5.110E+13	-6.410E+13	1.150E+14	-6.310E+13	1.540E+13	5.980E+13	55	65	-30	159	63	-152	nn_Mwr
2020-09-09	10:07:28.39	38.177	-117.872	3.3	9.3	2.8	0.000E+00	5.920E+13	-5.920E+13	-3.890E+13	-8.350E+13	4.970E+13	25	90	-130	295	40	0	nn_Mwr
2020-09-15	16:33:36.49	38.160	-117.962	4.0	10.0	2.0	1.803E+14	-7.613E+14	5.811E+14	-1.952E+14	1.409E+14	8.223E+14	70	81	-5	161	85	-171	us_Mwr
2020-09-18	14:00:00.69	38.171	-117.832	3.3	4.1	1.8	-3.688E+13	-2.682E+13	6.370E+13	-1.727E+13	8.400E+12	1.101E+14	170	79	-170	78	80	-12	nn_Mwr
2020-09-29	11:36:11.89	38.185	-117.777	3.6	10.0	2.0	1.418E+14	-6.402E+13	-7.776E+13	-3.938E+13	-1.165E+13	3.196E+14	272	79	14	180	76	169	nn_Mwr
2020-11-13	9:13:51.86	38.169	-117.853	5.4	11.0	3.2	-3.392E+16	-4.325E+16	7.717E+16	-1.270E+16	1.194E+16	1.211E+17	76	81	-7	167	83	-171	us_Mww
2020-11-20	10:10:05.97	38.175	-117.802	3.6	5.0	1.5	8.840E+12	-2.261E+13	1.377E+13	-1.642E+14	-7.243E+13	2.490E+14	174	58	172	269	83	33	nn_Mwr
2020-12-01	23:32:56.57	38.164	-118.084	4.9	6.8	2.9	-1.358E+16	-7.703E+15	2.128E+16	-1.172E+16	-2.347E+15	2.429E+16	169	59	-161	68	73	-32	us_Mww
2020-12-01	23:43:08.52	38.173	-118.070	4.1	2.8	2.7	-5.654E+14	-4.640E+13	6.119E+14	-4.433E+14	9.370E+13	1.870E+15	83	80	-17	176	74	-170	us_Mwr
2020-12-01	23:47:05.59	38.168	-118.081	4.2	4.0	2.7	-1.515E+15	-3.747E+14	1.889E+15	-1.007E+15	-4.303E+14	8.101E+14	170	42	-135	44	62	-58	us_Mwr
2020-12-02	2:23:45.03	38.175	-118.073	4.1	7.3	2.5	-3.852E+14	1.564E+14	2.288E+14	-1.390E+14	3.218E+14	1.882E+15	180	83	-168	89	78	-7	us_Mwr
2020-12-02	4:49:28.77	38.169	-118.071	4.0	6.7	2.1	-1.986E+14	-1.826E+14	3.812E+14	-7.770E+13	-2.235E+14	1.087E+15	173	88	170	263	80	2	us_Mwr
2020-12-02	10:41:01.74	38.172	-118.080	3.6	4.2	1.8	-1.552E+14	-3.390E+13	1.891E+14	-7.774E+13	-5.282E+13	1.847E+14	57	63	-52	177	45	-141	nn_Mwr
2020-12-02	16:08:29.01	38.165	-118.083	3.7	5.0	2.0	-2.708E+14	-5.481E+13	3.256E+14	-3.457E+14	-1.026E+14	2.104E+14	173	37	-147	56	71	-57	nn_Mwr
2020-12-03	3:18:10.46	38.165	-117.858	4.0	6.9	1.2	-2.011E+14	-5.760E+14	7.771E+14	-3.019E+14	3.007E+14	1.167E+15	73	74	-11	167	79	-163	nn_Mwr
2020-12-03	5:15:29.99	38.175	-118.065	4.8	5.7	2.7	-6.166E+15	-1.460E+14	6.311E+15	-7.133E+15	5.130E+14	1.383E+16	77	74	-33	178	58	-161	us_Mwr

Chapter 4

Recent earthquakes on unmapped faults highlight hidden seismic hazards within the Golden Triangle region of Laos, Thailand, and Myanmar

4.1 Author Names, Affiliation, and Roles

I. Sethanant[1], E. Nissen[1], E. Bergman[2], S. J. Oliva[1,6], L. Pousse-Beltran[3], E. Karasözen[4], P. Pananont[5]

[1]School of Earth and Ocean Sciences, University of Victoria, British Columbia, Canada

[2]Global Seismological Services, Golden, Colorado, USA

[3]Université Grenoble Alpes, Université Savoie Mont Blanc, CNRS, IRD, Université Gustave Eiffel, ISTerre, 38000 Grenoble, France

[4]Alaska Earthquake Center, University of Alaska Fairbanks, Fairbanks, Alaska, USA

[5]Department of Earth Sciences, Faculty of Science, Kasetsart University, Bangkok, Thailand

[6]Department of Geophysics, Universidad de Chile, Santiago, Chile

This chapter is based on a manuscript submitted to the Geophysical Journal International. I undertook InSAR modelling and analysis, data curation and formal analysis, generated and illustrated figures, wrote and edited the text. Dr. Edwin Nissen supervised

this work and provided manuscript edits. Dr. Eric Bergman and Dr. Ezgi Karasözen conducted the earthquake relocation and provided minor manuscript edits. Dr. Sarah Jaye Oliva conducted regional waveform modelling and contributed minor manuscript edits. Dr. Léa Pousse-Beltran supervised InSAR corrections and provided minor manuscript edits.

4.2 Abstract

In the past decade, six $M_w \geq 5.5$ earthquakes struck the mountainous Golden Triangle region (Laos, Thailand, Myanmar) of the southeast India-Eurasia collision zone. The largest of them, the 2019 M_w 6.2 Sainyabuli earthquake in western Laos, shook river communities, dams, and a UNESCO World Heritage Site, prompting a need to understand regional earthquake potential. We used Interferometric Synthetic Aperture Radar (InSAR) data and modelling to solve for the 2019 mainshock source parameters, revealing right-lateral strike-slip along a 24 km-long NNW-trending fault which has limited topographic expression and was previously unmapped. InSAR modelling of its largest (M_w 5.5) aftershock in 2021 revealed a 7 km-long splay fault, also previously unrecognized. The 2022 M_w 5.9 Keng Tung earthquake in the northern Golden Triangle also ruptured a previously unidentified, NW-trending right-lateral fault conjugate to longer, NE-trending faults nearby. Collectively, this shows that the region contains faults which are little evident in the topography but long enough to generate sizeable earthquakes that should be accounted for in seismic hazard assessments. We relocated well-recorded aftershocks and other background events (1978–2023) from across the Golden Triangle using the *mloc* software. Calibrated hypocenters span focal depths of 5–24 km and are distributed away from the main InSAR fault traces, another indication of fault structural immaturity. For the three 2019–2022 InSAR-imaged events, we also obtained moment tensor solutions from regional seismic waveform inversion. Peak slip depths inferred from InSAR and seismological centroid depths are mostly shallow (3–5 km), while focal depths are generally located in areas of low coseismic slip near the bottom of InSAR model faults. More broadly, we estimate a regional seismogenic thickness of $\sim$17 km (the 90$\%$ seismicity cut-off depth), a crucial parameter for seismic hazard calculations and building codes. Our integration of remote-sensing, seismologic, and topographic analyses could be a blueprint for assessing earthquake potential of other regions with sparse instrumentation and limited topographic fault expression.

4.3 Introduction

The mountainous Shan Plateau is a region of complex faulting in the northwestern corner of the Indochina (or Sunda/Sundaland) Block within the "Golden Triangle" border region of Laos, Thailand, Myanmar, and China (Figure 4.1). The plateau is bordered to the West by the N-S, right-lateral (∼20 mm/yr) Sagaing fault, which accommodates northward and obliquely subducting motion of the Indian Plate beneath the Myanmar Plate along the Indo-Burma subduction zone, and to the North-East by the NW–SE, right-lateral (∼2 mm/yr) Red River fault, which accommodates eastward motion of the South China block with respect to Sibumasu-Indochina (Vigny et al., 2003; Shen et al., 2005; Simons et al., 2007; Wang et al., 2014b; Shi et al., 2018). The plateau is crisscrossed by an array of long (up to ∼400 km), NE-trending, arcuate (concave northwestwards), left-lateral faults together with a few, shorter (up to ∼200 km), conjugate right-lateral faults (Figure 4.2; Lacassin et al. (1998); Wang et al. (2014b)). Global Navigation Satellite systems (GNSS) velocities show that these faults together accommodate ∼12 mm/yr of SW-oriented, left-lateral shear between stable Indochina and the northern Shan Plateau (Kreemer et al., 2014; Shi et al., 2018). This shear is driven in turn either by clockwise rotation of material around the eastern Himalayan syntaxis (Shen et al., 2005; Simons et al., 2007), or by N–S dextral shear between the Sagaing and Red River faults inducing 'bookshelf' faulting with vertical axis rotations (Lacassin et al., 1998; Copley, 2008; Ji et al., 2017) (for further discussion of regional geodynamic models, see Shi et al. (2018)). Though there are few firm estimates of long-term slip rates on individual NE-trending faults, sinistral river offsets of ∼10–20 km (summing to ∼110–130 km) yield average fault slip rates of ∼1 mm/yr if it is assumed that slip initiated at ∼10 Ma (Shi et al., 2018), an age supported by magnetostratigraphic and thermochronologic data (Cao et al., 2011; Li et al., 2013). The resultant cumulative slip rate matches the GNSS rate of ∼12 mm/yr. Superposition of these sinistral offsets on older dextral offsets explains the distinctive 'hair-pin' loops of the Mekong and Salween rivers and their tributaries, attesting to a switch in slip sense, likely in the early Miocene (Lacassin et al., 1998).

At least twenty magnitude >6 earthquakes have been recorded across the Shan Plateau since the early twentieth century (Figure 4.2), but only a few of these are attributed to known faults with any confidence (Wang et al., 2014b), and precise epicentral locations and focal depths are mostly lacking. This reflects both the lack of dense seismic instrumentation and the difficulty of imaging surface deformation with satellite radar or optical imagery beneath the dense forest cover. Counter-intuitively, the largest pair of

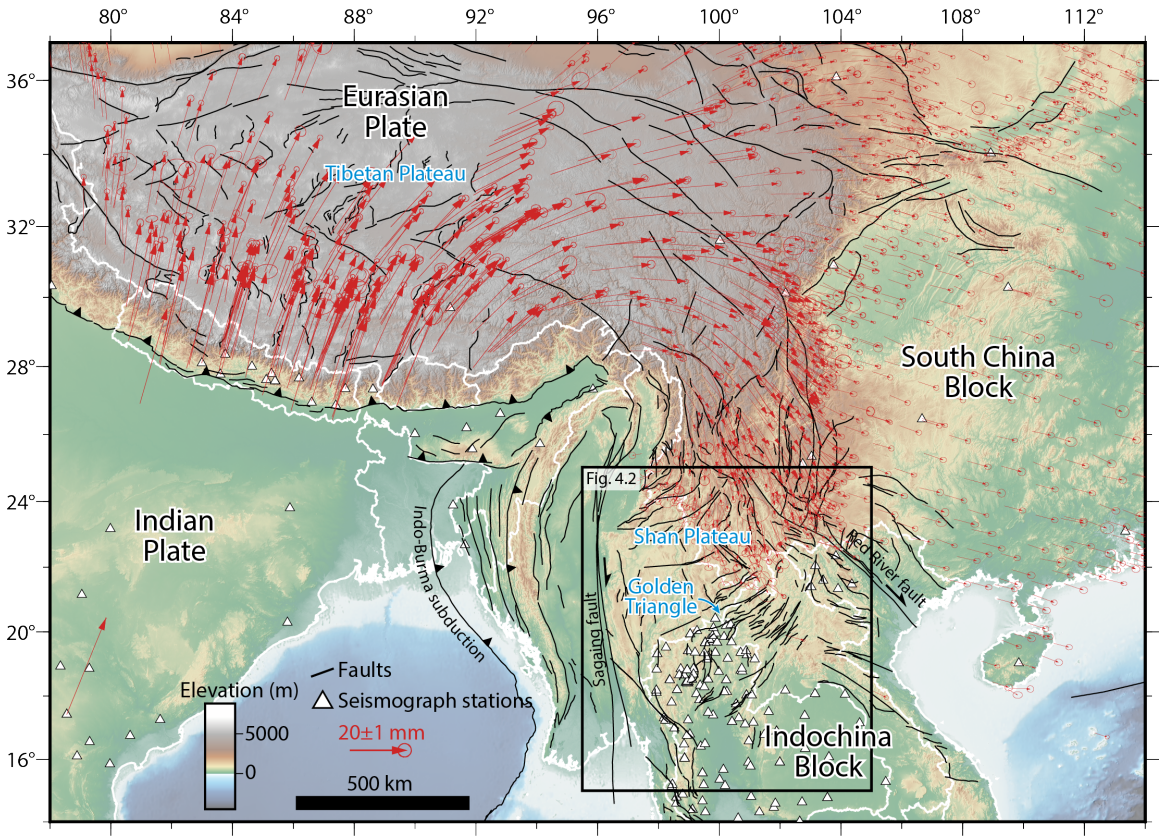


Figure 4.1: Tectonic setting of the Shan Plateau within the broader India-Eurasia collision zone. Red arrows are GNSS velocities with respect to stable Eurasia from Wang and Shen (2020), showing clockwise rotation around the southeastern Himalayan syntaxis and NE–SW-oriented sinistral shear across the Shan Plateau. Black lines are active faults from Thailand's Department of Mineral Resources, Earth Observatory Singapore, and Global Earthquake Model Foundation. White triangles are seismograph stations used in this study from the International Seismological Centre, National Earthquake Information Center (NEIC, U.S. Geological Survey), and local networks (data available in GCCEL, see Data and resources). Underlying hillshaded topography and bathymetry is the U.S. Geological Survey GTOPO30 Digital Elevation Model (see Data and resources).

events each ruptured NW-trending dextral faults: the May 23, 1912 M_w 7.7 earthquake on the Northern Kyaukkyan fault in the western Shan Plateau (Wang et al., 2014b) and the November 6, 1988 M_S 7.6 and 7.3 doublet on the Lancang fault in the central plateau (Chen and Wu, 1989; Wang et al., 1991). These are the two most prominent NW-trending faults in the study area, both around ∼200 km long (Wang et al., 2014b). The July 11, 1995 M_w 6.8 Myanmar-China border earthquake, the first in the region to be mapped using Interfermetric Synthetic Aperture Radar (InSAR), also ruptured a NW-trending dextral fault, though in this case the fault was previously unrecognized (Ji et al., 2017). Of the

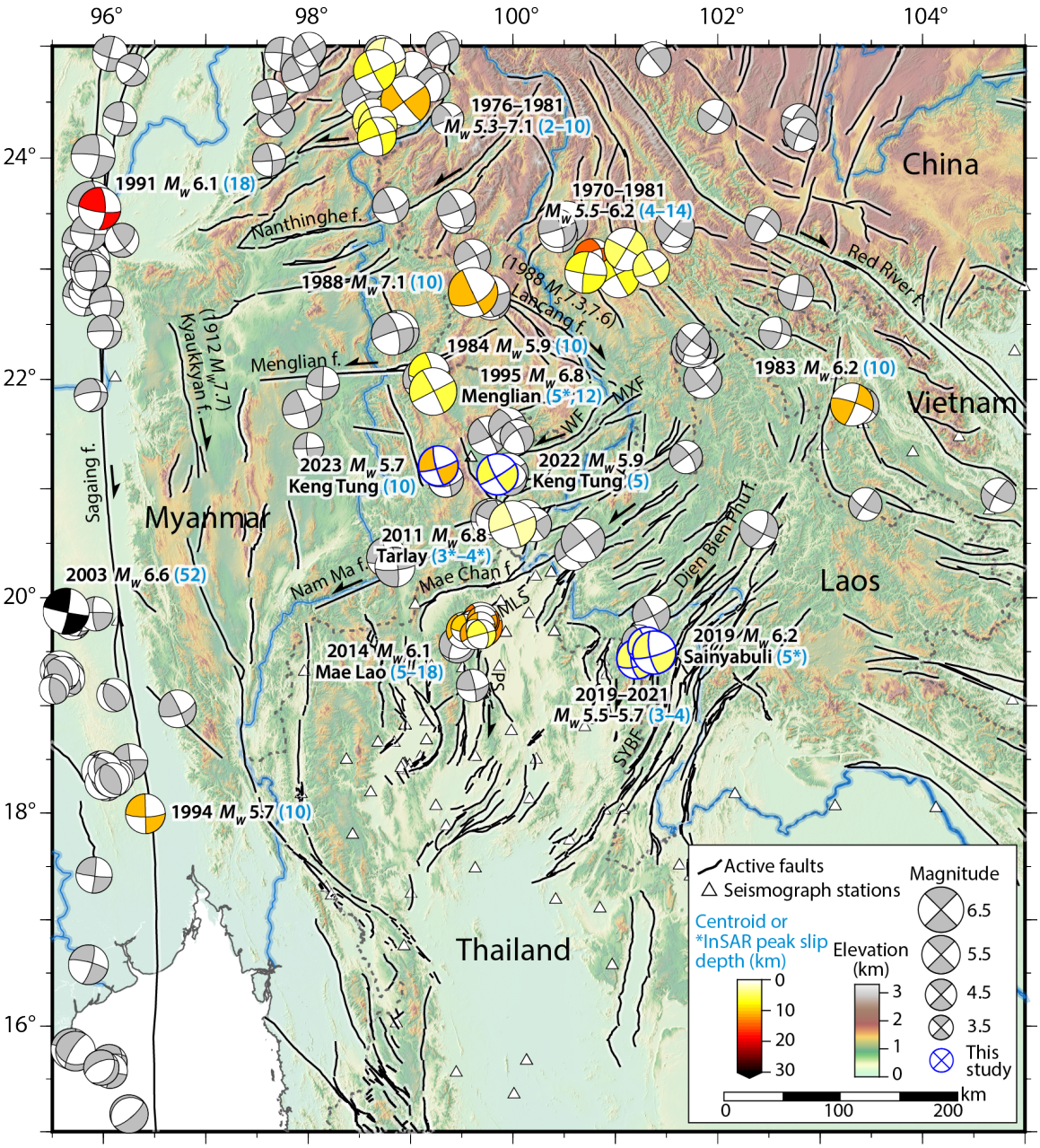


Figure 4.2: Mapped active faults and earthquake focal mechanisms from across the Shan Plateau. Gray beach balls are earthquakes without independent waveform modelling or InSAR analysis, gathered from the automated GCMT catalog (Dziewonski et al., 1981; Ekström et al., 2012) and the ANSS ComCat (U.S. Geological Survey, Earthquake Hazards Program, 2017) and spanning the years 1976–2019. They are scaled by magnitude and plotted at ISC-EHB catalog epicenters (Engdahl et al., 1998, 2020; International Seismological Centre, 2023; Weston et al., 2018). Other mechanisms are coloured by centroid depths from published waveform modelling studies (Chen and Molnar, 1990; Holt et al., 1991; Kumar et al., 2015; Le Dain et al., 1984; Ma and Hao, 1997; Pananont et al., 2017) or peak slip depths from InSAR slip models (Feng et al. (2013); Ji et al. (2017); Wang et al. (2014a), and this paper); these depths are also labelled in blue (in units of kilometers), with InSAR depths asterisked. Topography is from the Shuttle Radar Topography Mission 3 arc second DEM (see Data and resources). Dotted lines are national boundaries, blue lines show major rivers, and white triangles are regional seismograph stations used in this study. Abbreviations: f.—fault; MXF—Mengxing fault, SYBF—Sainyabuli fault, WF—Wan Ha fault, and the MLS—Mae Lao segment and PS—Pan segment of the Phayao fault zone.

more prominent, NE-trending sinistral faults, the Nam Ma fault broke in the March 24, 2011 M_w 6.8 Tarlay, Myanmar earthquake, generating both clear surface ruptures and clear InSAR fringes (Feng et al., 2013; Tun et al., 2014; Wang et al., 2014a), while the Mae Chan fault may have hosted the May 16, 2007 M_w 6.3 Bokeo, Laos earthquake, though in this case a definitive InSAR signal is lacking (e.g., Lee and Shyu, 2015). A dense, temporary network deployed after the May 5, 2014 M_w 6.2 Mae Lao earthquake in Chiang Rai, Thailand supported coeval rupture of the conjugate Mae Lao and Pan segments of the Phayao fault zone (Pananont et al., 2017; Boonchaisuk et al., 2017; Pananont et al., 2014). All of these earthquakes are at crustal depths. Intraslab seismicity within the subducting Indian Plate is limited to well to the West of the Sagaing fault (Fadil et al., 2023). Locally-recorded focal and centroid depths in the Mae Lao (Chiang Rai) sequence are up to ∼14 km and ∼18 km, respectively (Pananont et al., 2017), consistent with regional centroid depths of ∼2–14 km from teleseismic waveform inversions of a handful of other moderate to large earthquakes from across the Shan Plateau (Le Dain et al., 1984; Chen and Molnar, 1990; Holt et al., 1991; Ma and Hao, 1997; Kumar et al., 2015; Pananont et al., 2017). Dislocation modelling of the M_w 6.8 1995 Myanmar–China and 2011 Tarlay earthquakes revealed peak slip at ∼3–5 km depth and deepest slip at ∼12–20 km (Feng et al., 2013; Wang et al., 2014a; Ji et al., 2017). Collectively, therefore, the limited available data support a regional seismogenic layer thickness somewhere in the range of ∼10–20 km, but additional constraints on this important parameter are clearly a high priority.

The purpose of this paper is to reevaluate the seismic potential of the Golden Triangle by investigating several new earthquakes from the past five years. We draw upon improvements in mapping subtle surface deformation signals in dense forest cover through use of the European Space Agency Sentinel-1A/1B satellites, whose shorter (6 or 12 day) revisit times provide better interferometric coherence than earlier C-band SAR platforms (Funning and Garcia, 2019). We also build upon gradual improvements in regional seismic station coverage in two ways. First, we are able to estimate moment tensors of moderate (M_w 5–6) earthquakes using waveforms recorded by regional seismic networks (Pananont et al., 2017; Fadil et al., 2023), where previous modelling studies relied upon teleseismic signals (Le Dain et al., 1984; Chen and Molnar, 1990; Holt et al., 1991; Ma and Hao, 1997). Second, we are able to determine more precise hypocentral parameters, not only for the best-recorded modern earthquakes but also any earlier events (going back decades) that share common seismic station picks (e.g. Walker et al., 2011; Karasözen et al., 2016, 2019).

An initial focus of ours is the M_w 6.2 earthquake that struck Sainyabuli (also spelled Xayaburi or Xaignabuli) province of western Laos on November 20, 2019 at 23:50 UTC,

or November 21 at 06:50 Indochina Time (Figure 4.2). This was widely felt in Laos, Thailand (as distant as Bangkok, population >10 million), Myanmar, Vietnam, and southern China. The 2019 earthquake lies south or east of those studied previously and thus provides vital information about the seismic potential of the southeastern Golden Triangle, a region containing potentially vulnerable populations, infrastructure, and cultural sites. The earthquake risk is exemplified by the proximity of the 2019 earthquake to the Sainyabuli hydroelectric dam on the Mekong River (∼40 km away) and to Luang Prabang UNESCO World Heritage Site (∼90 km away). The United States Geological Survey (USGS) Advanced National Seismic System Comprehensive Earthquake Catalog (ANSS ComCat) places the earthquake near the ∼140 km-long, ∼N–S-trending Sainyabuli dextral fault system—which hosted at least three earthquakes in the past ∼3,000 years according to paleoseismic trenching (horizontal slip rate of 0.8 mm/yr, Nualkhao et al., 2016)—and along strike southwestwards from the ∼370 km-long Dien Bien Phu fault zone, the southeasternmost of the pronounced, NE-trending sinistral faults of the Shan Plateau (Wang et al., 2014b; Zuchiewicz et al., 2004). Other new earthquakes of interest to us include a M_w 5.7 foreshock that preceded the November 20 2019 M_w 6.2 Sainyabuli earthquake by three hours; a M_w 5.5 earthquake on December 19, 2021, also in the Sainyabuli region; and a pair of M_w 5.9 and 5.7 earthquakes on July 21, 2022 and November 17, 2023 near Keng Tung, Myanmar (Figure 4.2). These latter events lie near the ∼140 km and ∼180 km-long, NE-trending Wan Ha and Mengxing sinistral faults in the central Shan Plateau (Lacassin et al., 1998; Wang et al., 2014b).

We investigate these five earthquakes using Sentinel-1 InSAR and seismological observations and modelling. For the 2019 M_w 6.2 Sainyabuli mainshock, we also invert the InSAR data to find the best-fit source parameters and slip distribution. Independently, we perform a calibrated multi-event relocation in order to assess hypocentral distributions of the 2019–2021 Sainyabuli and 2022–2023 Keng Tung sequences and other notable well-recorded earthquakes in the region. We also model regional waveforms to estimate moment tensors with centroid depths for the Sainyabuli and Keng Tung earthquakes. Together, the new constraints from InSAR modelling, hypocentral relocations, and regional moment tensors help us estimate the regional seismogenic layer thickness, which sets the lower depth limit for slip in large earthquakes and is thus an important parameter for seismic hazard assessment. Finally, we analyze the topographic expression of the faults responsible for the Sainyabuli and Keng Tung earthquakes, which is also important for understanding regional earthquake potential. Overall, our work on the Golden Triangle provides a blueprint for studying moderate-to-large strike-slip earthquakes and seismic

hazards in other regions with sparse instrumentation.

4.4 Data and Methods

4.4.1 InSAR Data Processing and Source Modelling

We mapped surface deformation in the 2019 and 2021 Sainyabuli and 2022 and 2023 Keng Tung earthquakes using C-band (wavelength 5.55 cm) Synthetic Aperture Radar (SAR) data, acquired by the European Space Agency's Sentinel-1A/1B satellites and processed using GAMMA software (Wegmüller et al., 2016). For each earthquake, we used scenes from one ascending track (a99 for Sainyabuli and a172 for Keng Tung) and one descending track (d62 and d135) to produce two, 12-day interferograms (Table 4.1). For the November 20, 2019 Sainyabuli earthquakes, we also generated a third, 6-day ascending interferogram covering the southern epicentral area; all three interferograms capture both the M_w 5.7 foreshock (21:03 UTC) and the M_w 6.2 mainshock (23:50 UTC). InSAR topographic phase contributions were removed using the 3 arc-second (90-m) Shuttle Radar Topography Mission (SRTM) digital elevation model (Farr and Kobrick, 2000; Farr et al., 2007; Kobrick, 2006; Rosen et al., 2000) and the interferograms were filtered using a power spectrum algorithm (Goldstein and Werner, 1998) to remove phase noise and improve the visibility of fringes. Interferograms were unwrapped using the minimum cost flow algorithm, which we found through experimentation to be most effective in this highly-vegetated region, and then georectified to the Universal Transverse Mercator coordinate system (UTM zone 47N) with a 90 m pixel resolution. Lastly, we removed residual atmospheric and orbital noise using the Generic Atmospheric Correction Online Service (GACOS) (Yu et al., 2017, 2018b,a). Correction of signals from tropospheric delay did not visually improve the interferograms, likely due to the sparse geodetic instruments in this region, and so the final interferograms post-processed in GACOS only included planar trend corrections.

Of the earthquakes investigated with InSAR, only the November 20, 2019 Sainyabuli M_w 6.2mainshock (captured with its M_w 5.7 foreshock) produced a sufficient deformation signal-to-noise for inverse modelling. Neither the observed deformation nor our fault model are indicative of multiple ruptures, and so we interpret both as representing only the larger mainshock. We followed a common two-step inversion strategy, solving first for uniform slip on a planar, rectangular fault and thereafter for the slip distribution. To prepare the data for modelling, we first identified phase unwrapping errors as isolated patches of coherent data bordered by spurious phase jumps, and manually added or sub-

Table 4.1: Details of the InSAR imagery used to study the M_w 6.2 November 20, 2019 Sainyabuli earthquake (2019SYB), the M_w 5.5 December 19, 2021 Sainyabuli earthquake (2021SYB), the M_w 5.9 July 21, 2022 Keng Tung earthquake (2022KT), and the M_w 5.7 November 17, 2023 Keng Tung earthquake (2023KT). *i* is the line-of-sight (LOS) incidence angle measured from the vertical and *Az.* is the azimuth measured from north, both determined at the ANSS ComCat event epicenter. Abbreviations: a—ascending track, d—descending track.

Interferogram	Track	Date 1	Date 2	*i* (°)	Az. (°)
2019SYB-01	a99	Nov 15, 2019	Nov 27, 2019	38	349
2019SYB-02	d62	Nov 11, 2019	Nov 24, 2019	40	191
2019SYB-03	a62	Nov 18, 2019	Nov 24, 2019	40	191
2021SYB-01	a99	Dec 10 2021	Dec 22, 2021	38	349
2021SYB-02	d62	Dec 7, 2021	Dec 19, 2021	40	191
2022KT-01	a172	Jul 19, 2022	Jul 31, 2022	44	350
2022KT-02	d135	Jul 16, 2022	Jul 28, 2022	38	191
2023KT-01	a172	Nov 11, 2023	Nov 23, 2023	44	350
2023KT-02	d135	Nov 8, 2023	Nov 20, 2023	38	191

tracted 2π (or multiples of 2π) radians to these patches in order to align with surrounding, coherent data. Then, we downsampled the data using the Quadtree algorithm (Jónsson et al., 2002; Wright et al., 2003), adjusting the sampling block size and phase variance and coherence thresholds in order to densify sampling of areas with steep, coherent phase gradients while avoiding sampling of mostly decorrelated areas. The final downsampled data sets had between ∼300 and ∼600 points each, with very few of these lying within the patchy, decorrelated center of the InSAR deformation pattern. Later tests in which isolated data patches were removed altogether prior to downsampling yielded no significant difference in model results.

To estimate the geometry of the 2019 Sainyabuli mainshock, we solved the Okada (1985) equations to invert for the strike, dip, rake, location, length, top and bottom depths, and uniform slip of a rectangular fault plane embedded in an elastic half-space with Lamé parameters λ and μ, both 3.2×10^{10} Pa. Each parameter is solved non-linearly except for slip. We also jointly inverted for three nuisance parameters for each interferogram: a wholesale translation in line-of-sight (LOS) displacement to account for the unknown displacement at the unwrapping reference point, and east-west and north-south linear ramps to account for residual orbital ramps. The two descending interferograms were weighed half of that of the ascending interferogram in the inversion to balance the LOS displacements from both satellite viewing geometries. We used the downhill simplex algorithm

(Press et al., 1992) to minimize misfits between observed and modelled surface displacements. We provided generous search bounds for each fault plane parameter (Table 4.2) with median values taken either directly from the InSAR data (fault position, strike, and length), from the ANSS ComCat automated mainshock focal mechanism (dip, rake), or using the Visible Earthquake synthetic interferogram tool (top depth, bottom depth, slip) (Funning and Cockett, 2012) (see Data and resources). To ensure that the global minimum misfit solution was obtained, we used a Monte Carlo procedure to restart the inversion 100 times using starting parameters selected randomly from within these bounds (Wright et al., 1999; Funning et al., 2005; Elliott et al., 2012). Finally, we repeated the inversion using narrower search bounds centered upon the converging source parameters from the first iteration. Theses narrower bounds confirmed that we found a global minimum. We also considered a more complex fault geometry by adding a second model fault and solving for both geometries simultaneously. However, this did not improve the fit visually or quantitatively compared to the preferred, one fault model.

Next, we inverted for the slip distribution of the 2019 Sainyabuli mainshock. To allow for tapered slip, we first extended the uniform slip model fault plane by a few kilometers along strike (to 24 km), up dip (to the surface), and down dip (to 13 km). The latter value is based on depth resolution tests in which we repeated the uniform slip inversion with bottom depths fixed at increments either side of the minimum misfit value (9 km); resulting forward model interferograms are visually indifferent over the range 6–12 km. In addition, our independent calibrated relocation (described later) shows that within two hours of the mainshock, aftershock focal depths range from 7 to 13 km. The extended fault plane was subdivided into 2 km $\times$ 2 km patches and the slip distribution calculated using a Laplacian smoothing operator (Wright et al., 2004; Funning et al., 2005) and a slip positivity constraint (Bro and De Jong, 1997). We manually chose the smoothing parameter that best balances our desire for a realistically smooth slip distribution with the model misfit.

The 2021 M_w 5.5 Sainyabuli and 2022 M_w 5.9 Keng Tung earthquakes generated smaller InSAR fringe patterns with insufficient deformation signal-to-noise for slip inversion. Instead, we produced uniform slip forward models using fixed parameters estimated either directly from the InSAR data (fault strike, length), from the ANSS ComCat automated focal mechanism (dip, rake), or from the Visible Earthquake synthetic interferogram tool (top depth, bottom depth, slip) (Funning and Cockett, 2012). Through iteration, we then adjusted these parameters until we achieved a satisfying fit to the data. We also generated forward models using the alternate nodal plane, in order to verify our distinction of fault

Table 4.2: Earthquake source parameters of the five earthquakes studied here, from our study (regional seismic waveform modelling, and where available, InSAR modelling solutions) and from other automated catalogs. For the 2019 Sainyabuli mainshock InSAR model, we also provide parameter search bounds (see text). Easting and northing refer to the center point of the InSAR model fault surface projection in UTM zone 47N coordinates. For the deviatoric moment tensor solutions, the best solutions are reported, and the mean and one standard deviation are listed in the brackets (see Tables 4.5 and 4.6 for the inversion reference points and moment tensor solution components). For other automated focal mechanisms, easting and northing are instead listed in degrees longitude and latitude, respectively.

Model type	Easting (km)	Northing (km)	Strike (°)	Dip (°)	Rake (°)	Length (km)	Top (km)	Bottom (km)	Centroid (km)	Slip (m)	M_0 (N·m)	M_w
2019 Sainyabuli foreshock												
This study: Regional waveform modelling												
Deviatoric	745	2143	175	56	−158	–	–	–	3.6	–	2.78×10^{17}	5.6
			(198 ± 63)	(66 ± 11)	(−129 ± 75)				(4.2 ± 1.2)			
Other mechanisms:												
GCMT	101.41	19.44	345	88	−152	–	–	–	12	–	4.05×10^{17}	5.7
USGS Mww	101.25	19.45	161	75	−177	–	–	–	20	–	3.97×10^{17}	5.7
USGS Mwb	101.25	19.45	160	79	−177	–	–	–	14	–	3.26×10^{17}	5.7
2019 Sainyabuli mainshock												
This study: InSAR inverse modelling												
Search bounds	756 ± 6	2152 ± 6	170 ± 20	70 ± 20	−160 ± 40	20 ± 10	5 ± 5	10 ± 10	–	1.0*	–	–
Uniform slip	754	2151	166	76	−167	16	2	8	5†	0.7	2.48×10^{18}	6.2
Distributed slip	754	2151	166	76	−167	24	0	14	5‡	1.0‡	2.48×10^{18}	6.2
This study: Regional waveform modelling												
Deviatoric	749	2141	174	67	−141	–	–	–	4.2	–	1.35×10^{18}	6.1
			(177 ± 31)	(70 ± 7)	(−136 ± 42)				(4.0 ± 0.7)			
Other mechanisms:												
GCMT	101.44	19.36	163	84	−153	–	–	–	12	–	1.88×10^{18}	6.1
USGS Mww	101.36	19.45	169	65	−155	–	–	–	18	–	2.28×10^{18}	6.2
USGS Mwb	101.36	19.45	164	55	−167	–	–	–	4	–	1.49×10^{18}	6.1
2021 Sainyabuli aftershock												
This study: InSAR forward modelling												
Uniform slip	750	2160	330	77	−179	7	1	5	3†	0.3	2.76×10^{17}	5.6
This study: Regional waveform modelling												
Deviatoric	747	2157	339	86	140	–	–	–	3.1	–	1.93×10^{17}	5.5
			(254 ± 88)	(84 ± 6)	(10 ± 150)				(3.1 ± 0.5)			
Other mechanisms:												
GCMT	101.41	19.48	337	83	162	–	–	–	12	–	2.32×10^{17}	5.5
USGS Mww	101.31	19.56	336	77	−179	–	–	–	12	–	2.09×10^{17}	5.5
USGS Mwb	101.31	19.56	154	86	−176	–	–	–	9	–	1.32×10^{17}	5.3
2022 Keng Tung mainshock												
This study: InSAR forward modelling												
Uniform slip	594	2337	148	66	−174	11	2	6	4†	0.4	6.16×10^{17}	5.8
This study: Regional waveform modelling												
Deviatoric	591	2329	151	77	−172	–	–	–	4.9	–	5.94×10^{17}	5.8
			(176 ± 73)	(80 ± 6)	(−69 ± 98)				(5.0 ± 0.7)			
Other mechanisms:												
GCMT	99.95	21.14	329	72	179	–	–	–	12	–	9.6×10^{17}	5.9
USGS Mww	99.88	21.15	151	66	−176	–	–	–	16	–	1.03×10^{18}	5.9
USGS Mwb	99.88	21.15	152	85	−175	–	–	–	10	–	6.52×10^{17}	5.8
2023 Keng Tung mainshock												
This study: Regional waveform modelling												
Deviatoric	531	2323	166	76	−168	–	–	–	10.1	–	3.15×10^{17}	5.6
			(173 ± 26)	(79 ± 4)	(−158 ± 49)				(9.0 ± 1.5)			
Other mechanisms:												
GCMT	99.37	21.16	346	86	162	–	–	–	12	–	5.43×10^{17}	5.8
USGS Mww	99.33	21.22	339	76	−179	–	–	–	20	–	3.92×10^{17}	5.7
USGS Mwb	99.33	21.22	169	77	180	–	–	–	6	–	3.72×10^{17}	5.6

*Parameters that are linearly inverted without search bounds
†Uniform slip model: central depth of fault plane
‡Distributed slip model: peak slip and peak slip depth

and auxiliary plane. Interferograms capturing the 2023 M_w 5.7 Keng Tung earthquake do not exhibit a clear InSAR deformation signal. However, to be confident of our interpretation, we assessed the expected earthquake signal using forward models, similar to above.

4.4.2 Earthquake Relocation

To reduce the ∼10 km epicentral and focal depth uncertainties typical of routine, automated global catalogs (e.g. Weston et al., 2011), we relocated hypocenters of the 2019–2021 Sainyabuli and 2022–2023 Keng Tung earthquakes and their largest aftershocks. These were incorporated within a larger relocation cluster spanning the southern and central Shan Plateau and going as far back as 1978, with other major events including the May 16, 2007 M_w 6.3 Bokeo, Laos, March 24, 2011 M_w 6.8 Tarlay, Myanmar, and May 5, 2014 M_w 6.1 Mae Lao, Thailand earthquakes. We used the *mloc* program (e.g., Bergman et al., 2023), which is based on the Hypocentroidal Decomposition method in Jordan and Sverdrup (1981). *mloc* utilizes reported seismic phase arrival times for events recorded at common seismograph stations to minimize the earthquake location bias due to unknown Earth structure ('calibration'). This involves an iteration of two inversion steps. First, the program uses all available arrival times from local (within ∼1°), regional (∼1–15°), and teleseismic (>15°) distances to solve for relative locations in space and time (so-called cluster vectors) of all events to the geometric mean of the entire cluster (the hypocentroid). Second, in a direction calibration, only nearby and local distance arrival time data are inverted for the absolute position and time of the hypocentroid. We used arrival times reported by the International Seismological Centre (ISC), augmented with regional and local data (crucial for direct calibration) from the Thai Meteorological Department (TMD), Department of Mineral Resources Thailand (DMR), and temporary stations deployed by Pananont et al. (2017) (see Data and resources).

The ∼200 km dimensions our relocation cluster, double those typical for *mloc* studies (Bergman et al., 2023), posing a variety of challenges. Firstly, since the cluster spans multiple countries, a huge communication effort was needed to acquire all of the necessary regional data. Secondly, the large dimensions raise the likelihood of significant lateral heterogeneity in Earth structure, a major cause of earthquake location bias. While acknowledging this limitation, we minimize this bias by exploiting *mloc*'s capability to customize the local velocity model; we started with the global ak135 model (Kennett et al., 1995) but adjusted crustal velocities above an estimated Moho at 37 km by fitting theoretical and

observed arrival time curves (Table 4.3). The final challenge is that the sparse instrumentation results in weak azimuthal control for each localized grouping of events ('sub-cluster') within the overall cluster. We initially considered relocating each sub-cluster on its own, the typical procedure for >100 km-scale *mloc* studies (Aziz Zanjani et al., 2013; Gaudreau et al., 2019; Karasözen et al., 2019; Pousse-Beltran et al., 2020; Nissen et al., 2022). However, in our case the local and regional seismogragh stations required for this were either absent or poorly distributed, introducing azimuthal gaps exceeding ∼180°, non-optimal for *mloc* (Figures 4.3). For example, the 2014 Mae Lao earthquakes lacked stations to the northwest, the 2019 Sainyabuli earthquakes required stations to the north, east, and south, and the 2022 Keng Tung event needed stations to the north and east. To overcome this challenge, we relocated the several sub-clusters together, exploiting their connection through common regional and teleseismic stations and thus improving overall azimuthal control.

Table 4.3: One-dimensional velocity model used in the *mloc* relocation. The crust and upper mantle velocities are customized based on fitting arrival time data while below 120 km depth are velocities from the global ak135 model (Kennett et al., 1995).

Depth (km)	P (km/s)	S (km/s)
0.0–10.0	5.40	3.35
10.0–25.0	5.65	3.45
25.0– 37.0*	6.70	3.85
37.0*–77.5	7.85	4.40
77.5–120.0	7.85–8.05	4.40–4.50

*Depth estimate of Moho

We found it necessary to relocate the 2014 Mae Lao sub-cluster independently first, since its rich TMD dataset and the well-distributed temporary stations from Pananont et al. (2017) helped stabilize the relocation prior to adding the remaining sub-clusters. Arrival time data from Pananont et al. (2017) comprised 227 events recorded from 24 permanent stations from TMD and DMR at regional distances, and from 11 temporary stations deployed within 24 hours of and 30 km from the mainshock rupture. We included other available data of the 2014 Mae Lao sequence from ISC, TMD, and DMR at all distances. We manually assessed data quality, re-picked arrival time data for multiply reported phases, and dropped events with spurious phase picks, large arrival time scatter, or open azimuths of >200°, thus ensuring sufficient azimuthal coverage for constraining cluster vectors. The calibrated events of the 2014 Mae Lao sub-cluster are published in the

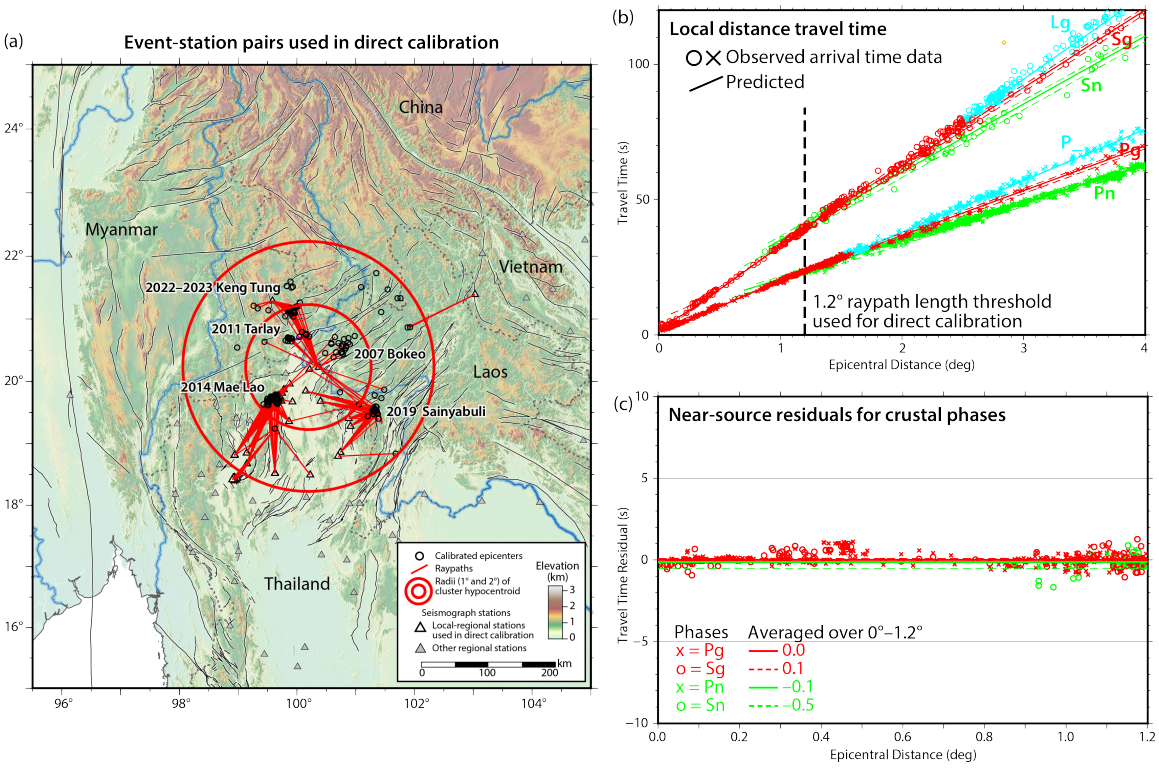


Figure 4.3: (a) Map of event-station raypaths (red vectors) and local-regional stations used in the direct calibration for calculating the absolute locations (white triangles) and those that are not involved (gray triangles). Open circles are calibrated epicenters. The two red circles show 1.0° and 2.0° radii centered upon the cluster hypocentroid (the average location of all events in the cluster). (b) Observed and modelled arrival times at local distances out to 4°. Modelled curves are from the customized velocity model in Table 4.3. The vertical dashed line indicates the raypath length limit of 1.2° used in the direct calibration step. The phases include: red crosses—Pg; cyan crosses—$P_$; green crosses—Pn; red circles—Sg; cyan circles—Lg; green circles—Sn. (c) The arrival time residuals within 1.2° epicentral distance. The solid and dashed red lines represent the average travel time residual for each phase; the values annotated at each line.

Global Catalog of Calibration Earthquake Locations (See Data and resources).

The remaining sub-clusters were then incorporated into the relocation, adopting similar data quality assessments. Initial runs of the inversion provided unstable solutions for the 2014 Mae Lao, 2019 Sainyabuli, and 2022 Keng Tung mainshocks. We found that dominant teleseismic data of the 2014 Mae Lao event in the western epicentral hemisphere (mostly in Europe) produced longitudinal bias, shifting locations eastward. We fixed this by incrementally adding data into the cluster and using data only out to 15° epicentral distance for the cluster vectors. Then we added to the data set only the highest quality

arrival time readings from greater distances, first up to 30° then up to 45°. Lastly, in the direct calibration inversion, we calculated the asbolute locations using a relatively large threshold of 1.2° for the event-station raypath lengths. This higher epicentral distance limit ensured sufficient close-in and well-distributed arrival time data for azimuthal control and cluster stability. InSAR fault models of the Sainyabuli and Keng Tung earthquakes (from our study) and of the 2011 Tarlay earthquake (Feng et al., 2013; Wang et al., 2014a), which are well distributed across the region, helped verify the relocated epicenters.

4.4.3 Waveform Modelling

Finally, we estimated moment tensors for the 2019 M_w 5.7 and M_w 6.2 Sainyabuli foreshock and mainshock, the 2021 M_w 5.5 Sainyabuli earthquake, and the 2022 M_w 5.9 and 2023 M_w 5.7 Keng Tung earthquakes, by inverting long-period waveforms filtered to 0.02–0.05 Hz from stations within ∼10° epicentral distance. The resulting source parameters and centroid depths provide independent checks of our InSAR modelling results. Green's functions were computed for a 1D velocity model derived via the frequency-wave number integrator method (Saikia, 1994). We performed the probabilistic inversion and optimization with the open-source Pyrocko software (Heimann et al., 2018), and used Bayesian bootstrapping (with n = 100) to produce uncertainty estimates for various model parameters. The inversion allowed N–S and E–W source shifts of up to 30 km from our *mloc* relocated epicenters or the surface projection of InSAR centroid slip (Table 4.5), and source depths of 1–30 km. Since isotropic source components are not expected in this strike-slip-dominated, non-volcanic study area, we solved for the deviatoric moment tensor.

4.5 The 2019–2021 Sainyabuli, Laos Earthquakes

4.5.1 The 2019 Sainyabuli Mainshock Kinematics

All three interferograms show far-field deformation fringes hinging around a ∼25 km-long, ∼N–S-trending, largely incoherent region (Figure 4.4, Figure 4.13, left hand column). Decorrelation in this area is likely caused by a combination of steep deformation gradients and strong ground shaking near the earthquake source, exacerbated by mountainous topography. The ascending interferogram displays four lobes with more fringes visible west of the partially decorrelated zone than east of it (Figure 4.4a); unwrapped LOS displace-

ments peak at ∼13 cm away from the satellite in the southwest lobe and ∼9 cm towards the satellite in the northwest lobe (Figure 4.4d). The two descending interferograms show asymmetric double lobes, with more fringes east of the decorrelated zone than west of it (Figure 4.4g, Figure 4.13) and peak LOS displacements of ∼11 cm towards and ∼11 cm away from the satellite (Figure 4.4j). The contrast in the location of the dominant fringes between the ascending and descending interferograms is characteristic of roughly N–S trending strike slip faults (Funning et al., 2005), with the sense of displacement indicating right-lateral motion.

Our uniform slip InSAR inverse modelling supports rupture of a 16 km-long, steeply WSW-dipping right-lateral strike-slip fault that strikes SSE across the partially decorrelated zone, with a small component of normal slip (strike, dip, and rake are 166°, 76°, and −167°, respectively; Table 4.2). This geometry is therefore consistent with our first order observations of the data interferograms. The model fault has 0.7 m of slip and top and bottom depths of 1.8 km and 8.3 km, respectively. Distributed slip inversion on an extended fault plane (see Data and Methods) yielded peak slip of 1.0 m at ∼5 km depth and only up to 0.3 m of model slip at the surface (Figure 4.5a). Slip is concentrated at the center of the model fault plane between 3–7 km depth. To quantify this shallow slip deficit (SSD), we averaged the slip values across all sub-fault patches in each row, and normalized the mean against the peak average slip. SSD is then calculated as one minus the normalized slip of the surficial model fault patches, expressed as a percentage. The averaged and normalized slip across the surficial row of our model fault are 0.11 m and 0.20, respectively yielding a SSD of 80% (Figure 4.5b).

The model interferograms match the data well, with root mean square error in LOS displacement of 0.8 cm (Figure 4.4, middle column) and far-field, long wavelength residual fringes not necessarily greater than atmospheric noise (Figure 4.4, right column). However, unwrapped descending interferograms display shorter-wavelength residual deformation parallelling the model fault within the region of partial decorrelaton (Figure 4.4l, Figure 4.13). These residuals may reflect undersampling of InSAR data points and/or phase unwrapping errors in this area. However, we tested the effect of near-fault data sampling on model results and found that including more data points from isolated InSAR data patches near the fault center neither impacted the model fault geometry nor reduced the residuals. Another possibility is that these residuals arise from our model assumptions of a planar fault. We tested this by inverting the InSAR data with two model fault segments, end-to-end with a change in strike, but the solution did not improve the quantitative or visual fits. We therefore prefer the simpler one fault geometry.

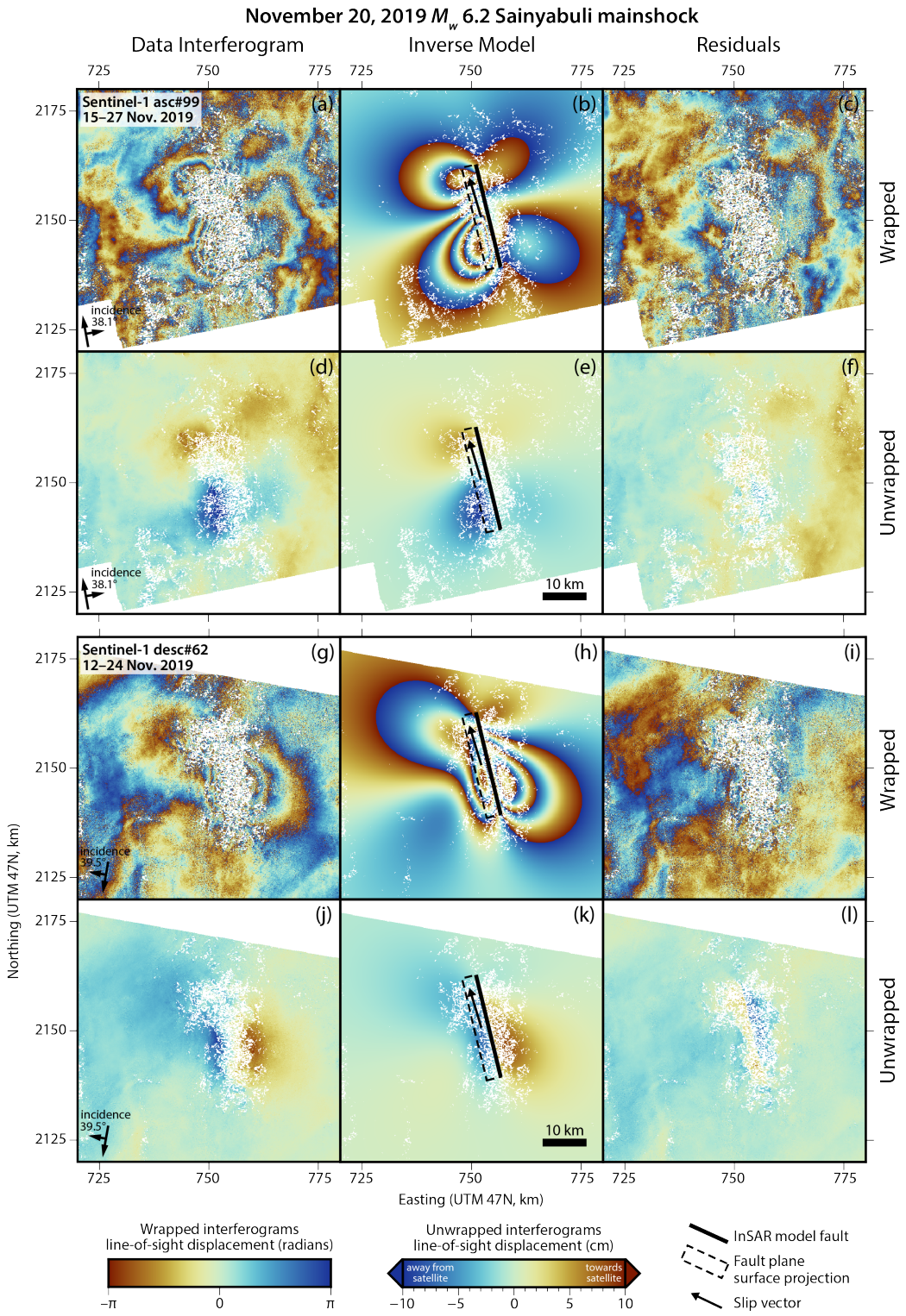


Figure 4.4: Observed (left column), distributed slip inverse model (middle column), and residual (right column) interferograms of the 2019 M_w 6.2 Sainyabuli mainshock. (a–f) show the ascending interferogram and (g–l) the descending one; (a–c, g–i) are wrapped and (d–f, j–l) unwrapped with red indicating motion towards the satellite. In the middle column, the thick black line and dashed rectangle indicate the InSAR model fault surface projection and corner coordinates, respectively, and the arrow shows the slip vector azimuth. The third InSAR data set only partially captured the rupture area and is shown in Figure 4.13.

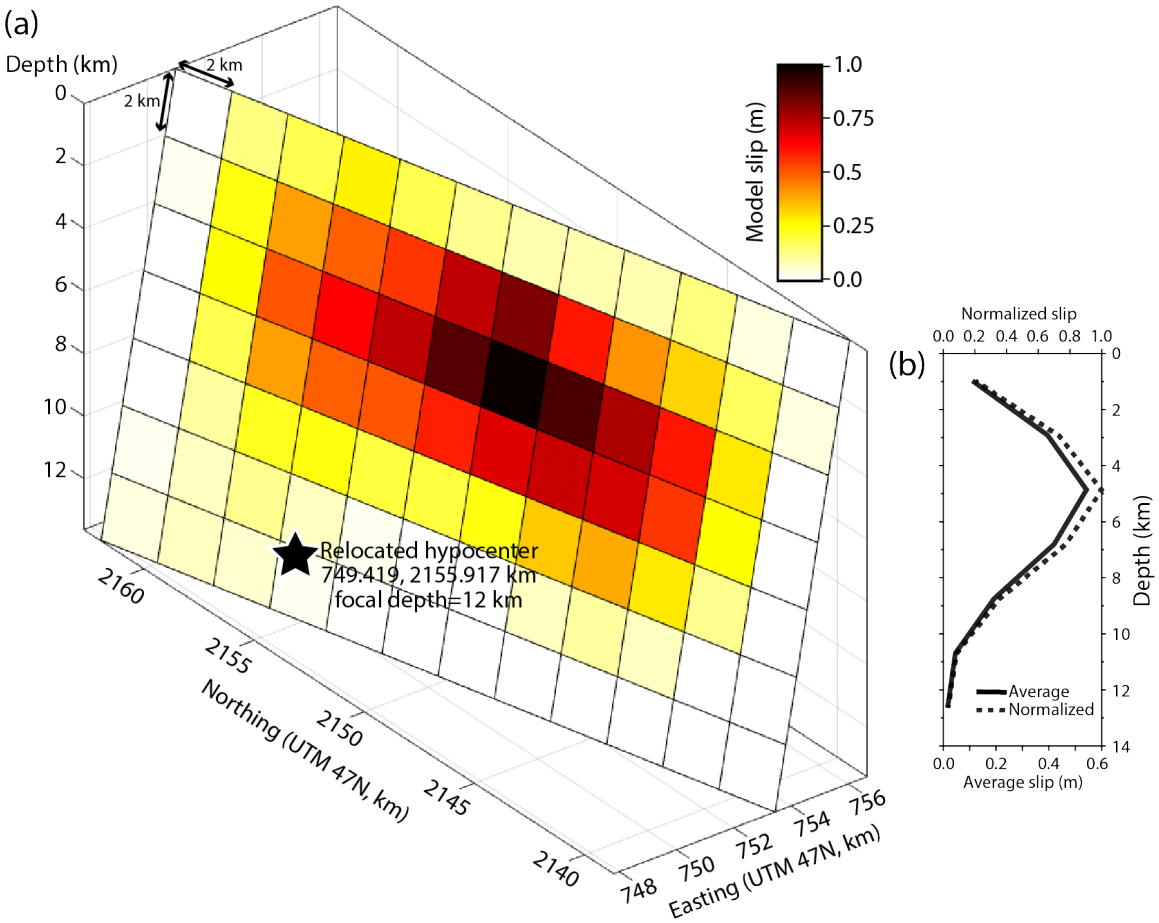


Figure 4.5: (a) Three-dimensional view of our InSAR distributed slip model for the 2019 M_w 6.2 Sainyabuli mainshock. Each sub-fault patch is 2 km by 2 km. (b) Depth profiles of average (solid line) and normalized slip (dashed line), plotted against the central depth of each sub-fault patch.

Our multi-event relocation places the mainshock hypocenter along the northern half of the InSAR model fault, and at 12 km $\pm$ 4 km depth (Figures 4.6, 4.7g, h, and Table 4.4). Together, this suggests an upward and partially bilateral rupture. Our centroid depth from waveform modelling is shallower with a minimum misfit value of 4.2 km and a mean and standard deviation of 4.0 km $\pm$ 0.7 km (Table 4.2, Figure 4.10b). The centroid depth is therefore in close agreement with the InSAR peak slip depth at $\sim$5 km. Our waveform model moment tensor solution has a SSE-trending nodal plane with strike, dip, and rake values of 174° (mean 177° $\pm$ 31°), 70° (70° $\pm$ 7°), and $-141°$ ($-136°$ $\pm$ 42°), respectively (Table 4.2, Figure 4.10b). Our InSAR model fault strike and dip lie within a few degrees of these values, and while there is a greater discrepancy in rake, the InSAR value of $-166°$

still lies within the seismological uncertainties.

Table 4.4: Relocated hypocenters of the five largest events studied here, and three other events discussed. Area of confidence ellipse refers to the epicentral uncertainties. For full calibrated locations of the whole cluster, see Supplemental Long table 4.8.

Event	Yr/mo/day	hr:min:sec (UTC)	Longitude (°)	Latitude (°)	Confidence ellipse (km^2)	Focal depth (km)
2007 Bokeo mainshock	2007/05/16	08:56:12.28	100.76472	20.56756	3.6	13 (+6, −2)
2011 Tarlay mainshock	2011/03/24	13:55:10.66	99.90313	20.69534	2.6	15 ± 4
2014 Mae Lao mainshock	2014/05/05	11:08:42.11	99.70969	19.69162	4.1	11 ± 4
2019 SYB foreshock	2019/11/20	21:03:56.23	101.20787	19.44473	3.3	13 ± 4
2019 SYB mainshock	2019/11/20	23:50:41.50	101.37618	19.48227	2.3	12 ± 4
2021 SYB aftershock	2021/12/19	21:06:12.20	101.30785	19.56231	3.7	8 ± 4
2022 KT mainshock	2022/07/21	17:07:25.71	99.84235	21.13601	3.0	20 ± 4
2023 KT mainshock	2023/11/17	01:37:08.88	99.27014	21.21042	4.1	14 ± 4

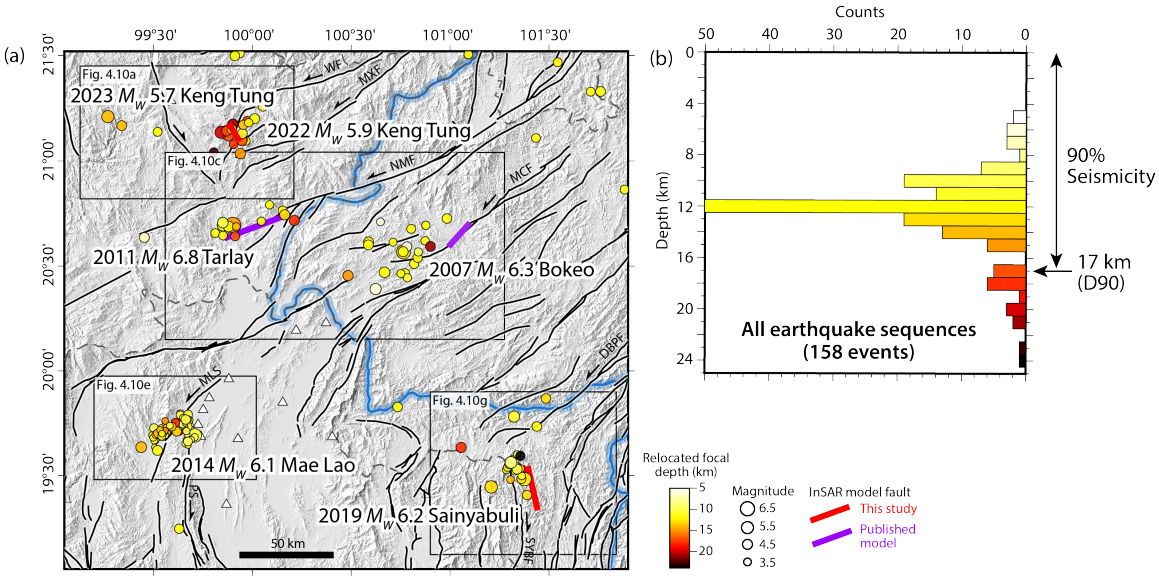


Figure 4.6: (a) Calibrated epicenters of all 158 events in our relocation cluster coloured by focal depth and (b) a histogram of the overall focal depth distribution illustrating our interpreted seismogenic thickness of 17 km (D90). The map also displays all available InSAR model faults as thick lines, in solid red (this study) or purple (Feng et al., 2013; Wang et al., 2014a; Lee and Shyu, 2015). Faults include: DBPF—Dien Bien Phu fault, MCF—Mae Chan fault, MXF—Mengxing fault, NMF—Nam Ma fault, SYBF—Sainyabuli fault, WF—Wan Ha fault, and the MLS—Mae Lao segment and PS—Pan segment of the Phayao fault zone.

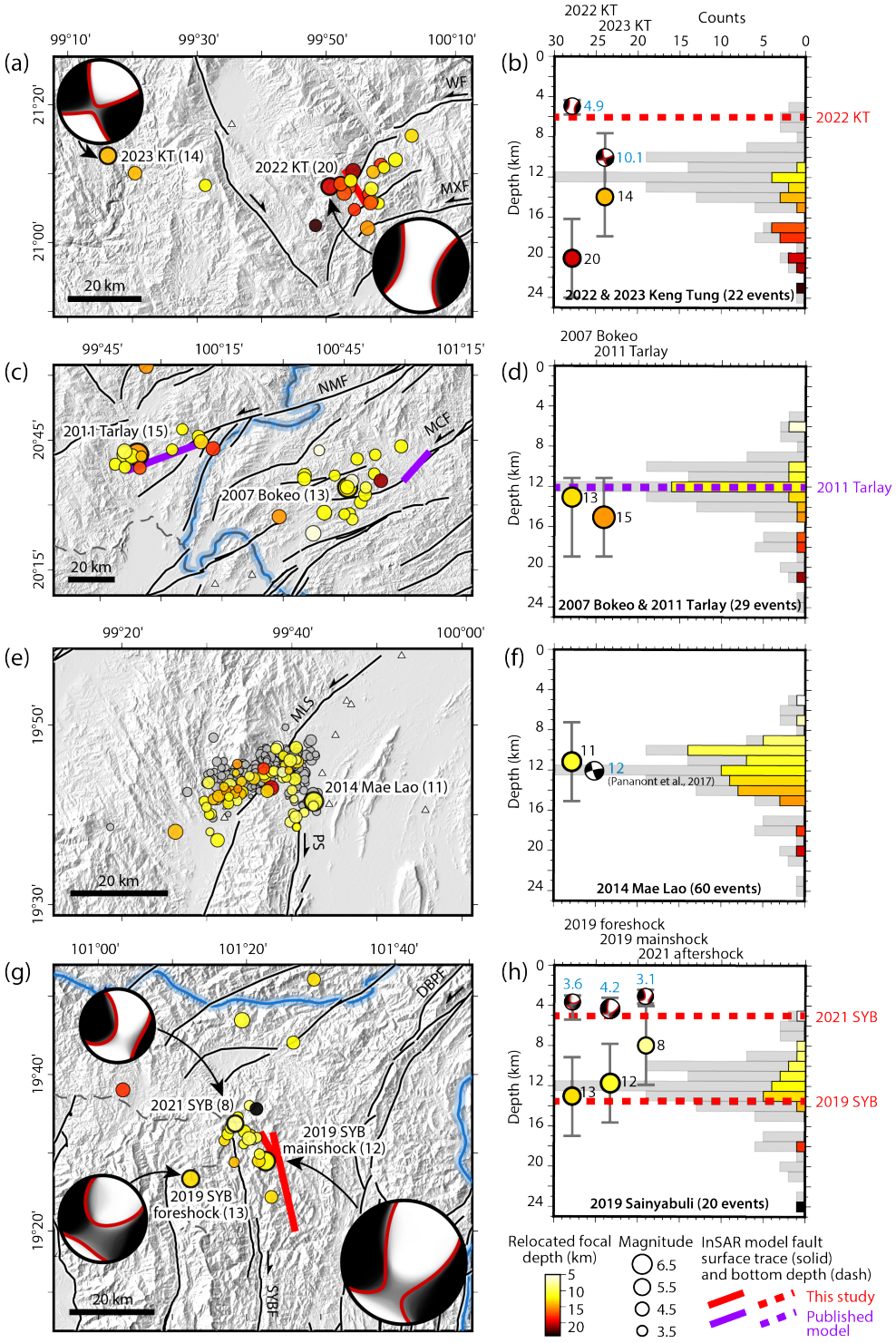


Figure 4.7: Zoomed in maps and histograms for each distinct earthquake sequence within the cluster: (a–b) 2022–2023 Keng Tung, (c–d) 2007 Bokeo and 2011 Tarlay; (e–f) 2014 Mae Lao; and (g–h) 2019–2021 Sainyabuli, with focal depths of the largest events (thick outlined circles) labelled in parentheses on the maps and in black text on the histograms. Maps also show all available InSAR model faults as thick lines, in solid red (this study) or purple (Feng et al., 2013; Wang et al., 2014a), and those of the (a) Keng Tung and (g) Sainyabuli regions also include deviatoric moment tensors from our regional waveform modelling, with red lines representing the best mechanism and the fuzziness illustrating uncertainty. The histograms include the overall depth distribution (from Figure 4.6b) in gray, best centroid depths with the means and standard deviations in blue (see Table 4.2), and InSAR model bottom depths as dashed red (this study, Table 4.2) and dashed purple (published models) lines. Historic events prior to year 2007 are excluded from the histogram of each earthquake sequence. The gray circles in panel (e) and focal mechanism in panel (f) are from Pananont et al. (2017). Faults include: DBPF—Dien Bien Phu fault, MCF—Mae Chan fault, MXF—Mengxing fault, NMF—Nam Ma fault, SYBF—Sainyabuli fault, WF—Wan Ha fault, and the MLS—Mae Lao segment and PS—Pan segment of the Phayao fault zone.

4.5.2 The 2021 Sainyabuli Earthquake

Ascending and descending interferograms of the 2021 Sainyabuli earthquake both show two deformation lobes, aligned NNW–SSE and ∼5–10 km in diameter (Figure 4.8, left column). These are proximal to the 2019 Sainyabuli earthquake, of which we therefore consider this event to be a late aftershock. A small, central area of decorrelation was presumably caused by strong ground shaking or steep phase gradients, but the interferograms are otherwise mostly coherent. In the wrapped interferograms the lobes contain 1–2 fringes (Figure 4.8a, e), and in the unwrapped interferograms LOS displacements reach ∼9 cm (Figure 4.8c, g). The lobes in the ascending interferogram have an opposite sense of LOS displacement and are positioned on the opposite (western) side of the decorrelated area than those in the descending interferogram, a pattern consistent with approximately NNW-trending right-lateral strike-slip faulting (Funning et al., 2005).

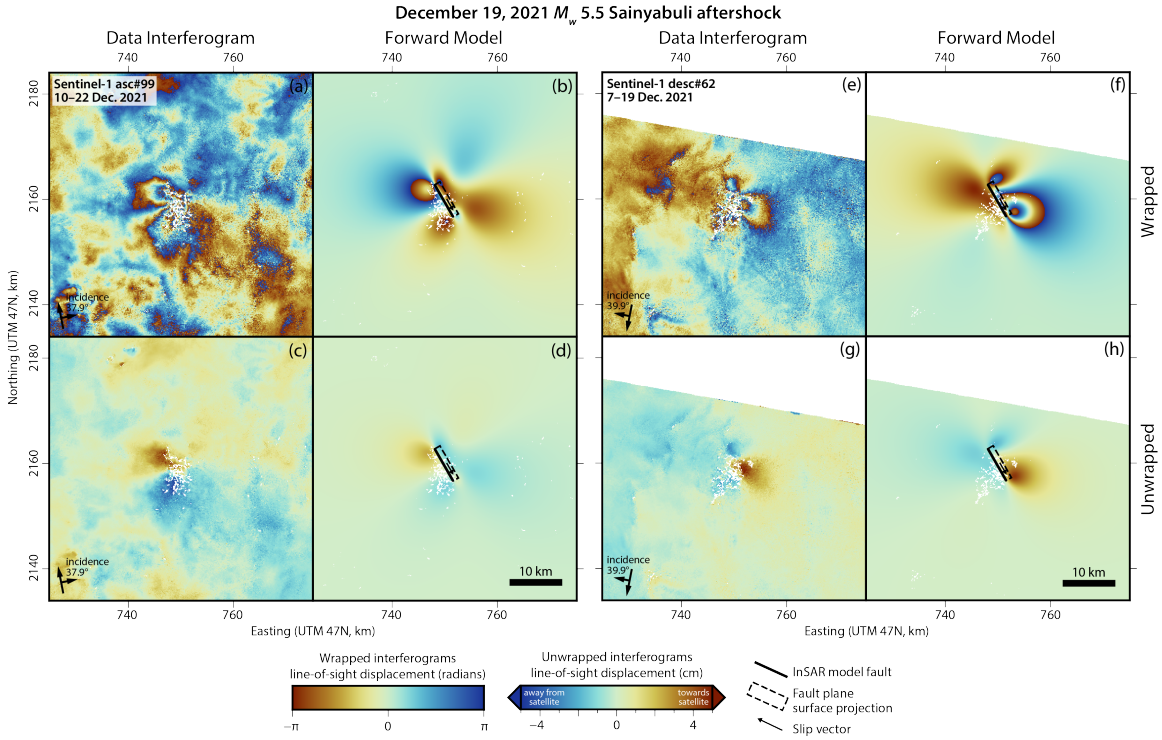


Figure 4.8: Observed (left column) and forward model (right column) interferograms of the 2021 M_w 5.5 Sainyabuli aftershock, shown both wrapped (a–b, e–f) and unwrapped (c–d, g–h), with red indicating motion towards the satellite). The thick black line is our inferred forward model fault, the dashed rectangle marks its corner coordinates, and the arrow indicates the slip vector azimuth. See Figure 4.14 for the forward model testing whether the second nodal plane can explain the InSAR data.

InSAR foward models illustrate that of the two seismological nodal planes, only the

NNW-striking right-lateral fault can reproduce the observed fringe pattern (Figure 4.8, right column, Figure 4.14), consistent with our first order interpretations. This fault is located just west of and oblique to (strike 330°) the northern portion of the 2019 mainshock fault, but dips in the opposite direction, 77° northeastward (Table 4.2). The observed fringes are reproduced reasonably well using uniform slip of 0.3 m at 1–5 km depth, a little shallower on average than the mainshock inverse model slip plane.

According to our hypocentral relocation, the 2021 earthquake initiated at 8 km ± 4 km depth, a little below the InSAR forward model fault plane (Table 4.4, Figures 4.6, 4.7g, h). Our moment tensor inversion yields a best centroid depth of 3.1 km (mean 3.1 km ± 0.5 km), consistent with the center of the InSAR model fault (Table 4.2, Figure 4.10c). The waveform model implies NNW-trending right-lateral strike-slip kinematics similar to the InSAR model, with best strike, dip, and rake values of 339° (mean 254° ± 88°), 86° (84° ± 6°), and 140° (10° ± 150°), respectively.

4.5.3 Other Earthquakes of the Sainyabuli Sequence

The November 20, 2019 M_w 5.7 foreshock is relocated ∼20 km west of the mainshock fault (Figure 4.7g), confirming our initial interpretation that the observed InSAR deformation represents the mainshock only. Its moment tensor has similar nodal planes and centroid depth to the mainshock (Table 4.2, Figure 4.10a), with the absence of a clear InSAR signal despite the shallow (∼4 km) centroid depth perhaps implying that the N–S nodal plane represents the fault. The calibrated hypocenter is deeper at ∼13 km, implying rupture upwards from near the base of the fault (Table 4.4, Figure 4.7h).

Relocated aftershocks of the Sainyabuli sequence are mostly distributed northwest of the mainshock (Figures 4.6a, 4.7g, and Supplemental Long table 4.8). Early aftershocks in 2019 are aligned along a northwesterly trend, along strike from the InSAR model fault, but later ones in 2020–2021 form a ∼15 km-long northeasterly trend, hinting at triggering along a conjugate structure (Figure 4.9). Calibrated aftershock focal depths range from 5–24 km, with uncertainties for each individaul depth estimated at ± 4 km (Figure 4.7h). The deepest is therefore twice the depth of the 2019 mainshock rupture plane.

4.6 The 2022 and 2023 Keng Tung, Myanmar Earthquakes

The July 21, 2022 M_w 5.9 and November 17, 2023 M_w 5.7 earthquakes are relocated to ∼50 km east and ∼80 km west of the Keng Tung town in the central Shan Plateau (Fig-

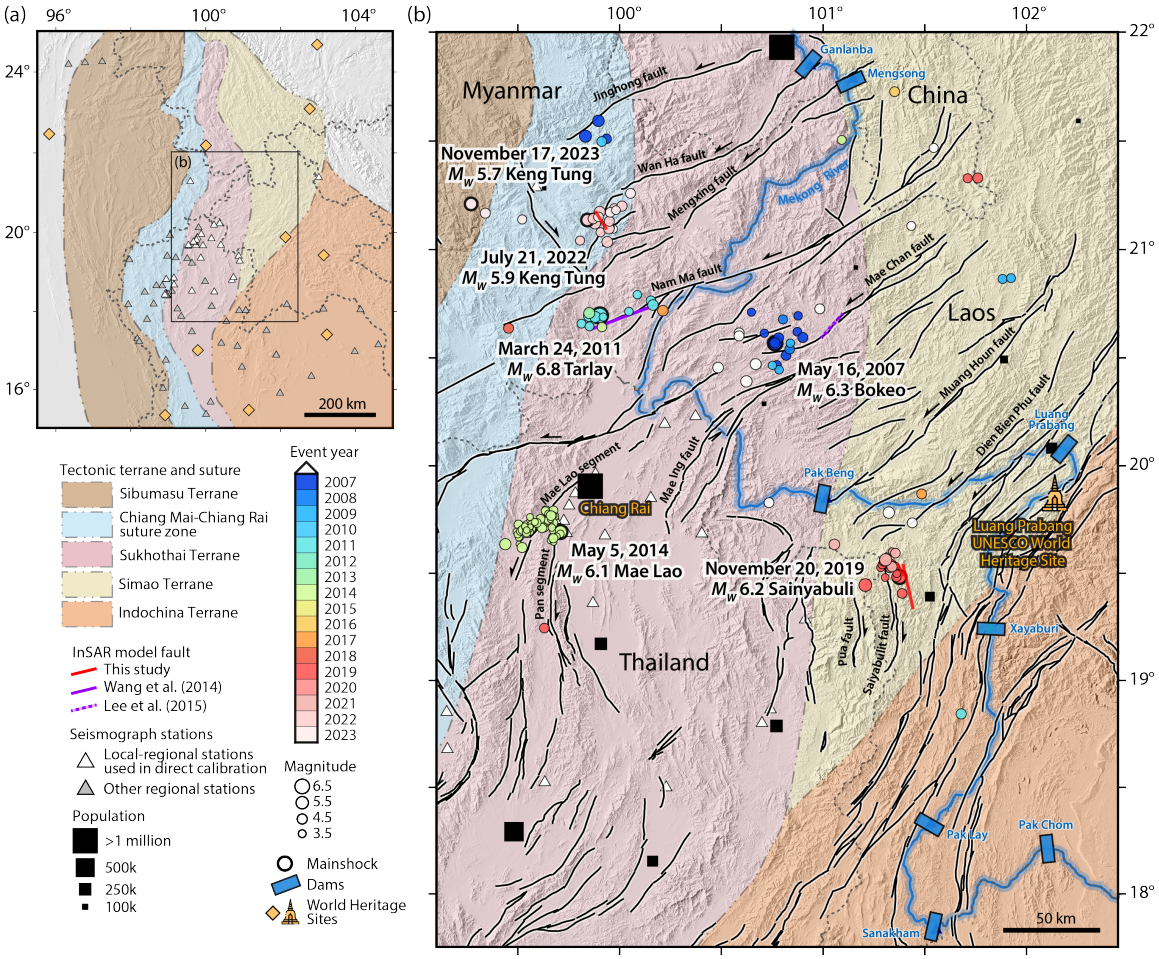


Figure 4.9: (a) Regional index map (at the scaling of Figure 4.2) and (b) close-in map showing the distribution of our relocated epicenters (circles, coloured by year of earthquake and scaled by magnitude) with respect to InSAR model faults (red and purple lines), mapped faults (black lines), tectonic terranes and their suture boundaries (background colours, digitized from Metcalfe (2021)), cities (black squares), World Heritage Sites (yellow diamonds), and major dams along Mekong River (blue rectangles). White triangles are seismograph stations at local and regional distances used to calculate the relocation hypocentroid, while gray triangles represent other stations used to estimate the relative locations in the cluster.

ure 4.2). While they share the same geographic name, the two earthquakes belong to distinct sequences.

The July 21, 2022 M_w 5.9 Keng Tung earthquake interferograms are more decorrelated than those of the Sainyabuli earthquakes, but a pair of small (∼5–10 km diameter) deformation lobes can still be made out in both ascending and descending frames (Figure 4.11a, e). The signal yields at most 6–7 cm of LOS displacement (Figure 4.11c,

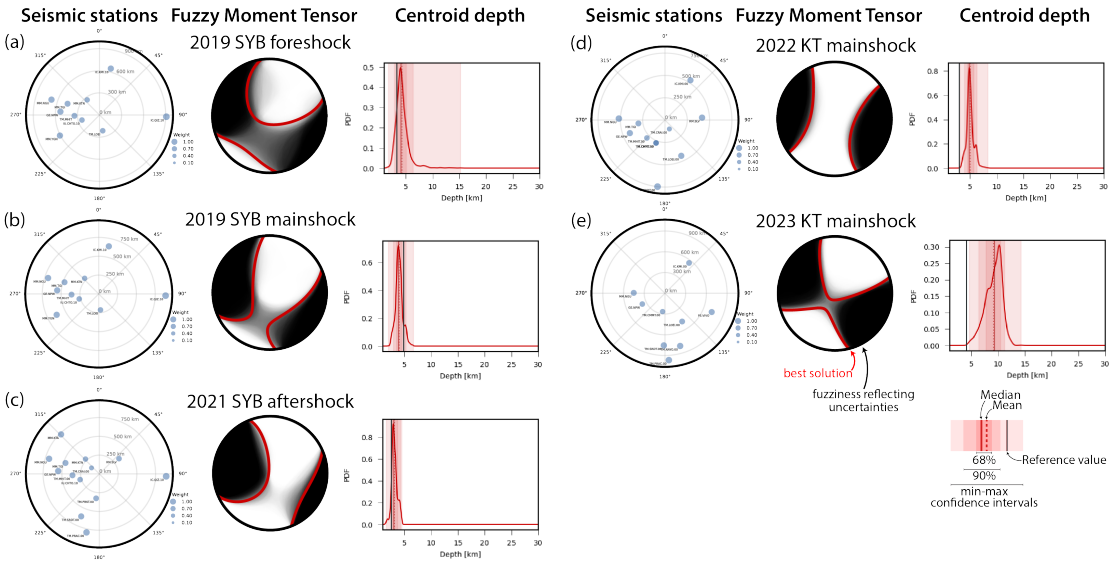


Figure 4.10: (a–e) Moment tensor solutions of the five earthquakes we modelled using regional waveforms. In each panel, the left column shows the station distribution in terms of distance and azimuth. The center of the plot corresponds to the origin of the search space (see Table 4.5). Blue circles are scaled according to the weighting factor of the corresponding station's transverse component in the misfit function. The central column is a fuzzy moment tensor illustration of solution uncertainty, with P wave radiation patterns of every ensemble solution stacked. If the variability of the ensemble solutions is small, the fuzzy plot has clearly separated black and white fields, consistent with the nodal lines of the global best solution (indicated in red). The right column is a histogram showing the distribution of modelled centroid depths displayed as Gaussian kernel densities (curved solid red line) with vertical solid and dashed red lines giving the median and mean values, the pink shaded areas denoting the 68% and 90% confidence intervals and minimum and maximum values (from narrowest to widest), the plot range indicating the searched parameter space, and the vertical grey line indicating the reference values (InSAR centroid slip depth or relocated focal depth, see Table 4.5).

g), with the sense of displacement indicative of either NE-trending left-lateral or NW-trending right-lateral strike-slip kinematics. InSAR forward modelling shows that the NW-trending right-lateral slip plane is the more likely of the two (Figure 4.11, right column, Figure 4.15) (Table 4.2, rake $-174°$). The model fault is $\sim$11 km long, strikes 148°, dips 66° southwestwards, and has uniform slip of 0.4 m across a relatively shallow depth range of 2–6 km (Table 4.2).

Our relocated hypocenter for the 2022 Keng Tung earthquake lies west of the InSAR model fault, consistent with the SW-dipping geometry, but is significantly deeper at 20 km $\pm$ 4 km (Figure 4.7a, b, and Table 4.4). Our waveform model centroid depth of 4.9 km

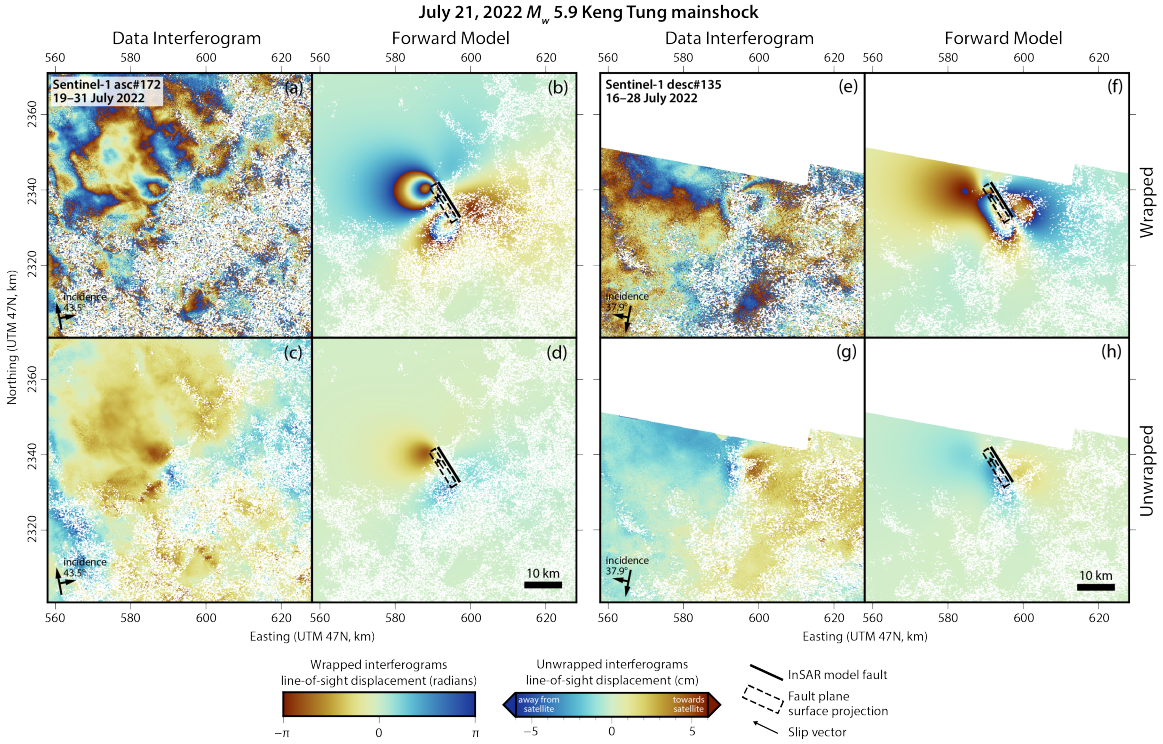


Figure 4.11: Observed (left column) and forward model (right column) interferograms of the 2021 M_w 5.9 Keng Tung earthquake, shown both wrapped (a–b, e–f) and unwrapped (c–d, g–h), with red indicating motion towards the satellite. The thick black line is our inferred forward model fault surface projection, the dashed rectangle marks its corner coordinates, and the arrow is the slip vector azimuth. See Figure 4.15 for the forward model test of the second nodal plane.

(mean 5.0 km $\pm$ 0.7 km) is in close agreement with our InSAR forward model (Table 4.2). Together, these data suggest that the earthquake nucleated in and ruptured upwards from a region of low eventual slip (e.g. Wei et al., 2015; Karasözen et al., 2016). The waveform model has a NW-trending nodal plane with strike, dip, and rake values of 151° (mean 176° $\pm$ 73°), 77 (80° $\pm$ 6°), and -172 ($-69°$ $\pm$ 98°), respectively, consistent with InSAR. Relocated aftershocks of the 2022 Keng Tung earthquake are concentrated around the ends of the InSAR model fault. However, a few events are located east of it along a northeastward trend, conjugate to the InSAR fault but consistent with the strike of the nearby left-lateral Wan Ha fault. Aftershocks exhibit focal depths ranging from 11–23 km, with individual uncertainties of $\pm$ 3–4 km, nucleating at greater depths than the mainshock rupture plane (Figure 4.7b).

InSAR data for the November 17, 2023 M_w 5.7 Keng Tung earthquake do not show clear deformation signals in either the wrapped or unwrapped interferograms, even after

correcting for tropospheric delays (Figure 4.12, left column). In the unwrapped interferograms, however, the slight positive to negative change in LOS displacement, close to our relocated epicenter, may be indicative of the mainshock deformation (Figure 4.12d,j). We conducted forward modelling of NW-trending and NE-trending nodal planes to investigate which could be the causative fault (Figure 4.12, middle and right columns). The fault geometry of the forward model was taken from the ANSS ComCat (dip, rake), estimated from the InSAR data (strike, length), and obtained from independent earthquake relocation analysis (top and bottom depths), and we assumed a slip value of 0.3 m to allow for agreement with the seismic moment. Our results show that neither fault orientation produces a satisfying fit (visually or statistically) with the InSAR data, suggesting that the depth of the earthquake is likely below the limits of InSAR detection.

Our relocated hypocenter places this earthquake on an unmapped fault in mountainous topography west of Keng Tung, nucleating at 14 km $\pm$ 4 km depth (Table 4.4, Figure 4.7a, b). Our waveform modelling reveals a consistent centroid depth of 10 km (mean 9.0 km $\pm$ 1.5 km) (Table 4.2). Although InSAR forward models cannot resolve the fault geometry, the orientation of the two possible nodal planes are in agreement with the focal mechanisms, exhibiting strike, dip, and rake values of 166° (mean 173° $\pm$ 26°), 76 (79° $\pm$ 4°), and -168 ($-158°$ $\pm$ 49°), respectively. Although the mainshock ruptured an unmapped fault, the NW-striking nodal plane parallels a structural fabric evident in the topography (Figure 4.7a). Our catalog also includes one aftershock of this earthquake, $\sim$9 km to the southeast (Figure 4.7a), with a similar focal depth of 14 km $\pm$ 4 km (Supplemental Long table 4.8).

4.7 Other Notable Earthquakes

4.7.1 The 2014 Mae Lao, Thailand Earthquake

The May 5, 2014 M_w 6.1 Mae Lao earthquake in northern Thailand and several of its aftershocks were included in our relocation cluster. We found that the mainshock initiated at 11 km $\pm$ 4 km depth (Table 4.4), and that aftershock focal depths range from 5–20 km, each with uncertainties of 1.4–4 km (Figure 4.7e, f, and Supplemental Long table 4.8). The northeasterly lineament of the distribution of our relocated events is roughly consistent with, but slightly oblique to the ENE-striking pattern resolved by Pananont et al. (2017), shown as gray circles in Figure 4.7e. Regional broadband waveform inversion in Pananont et al. (2017) suggests a mainshock centroid depth of 12 km (Figure 4.7f), similar to our

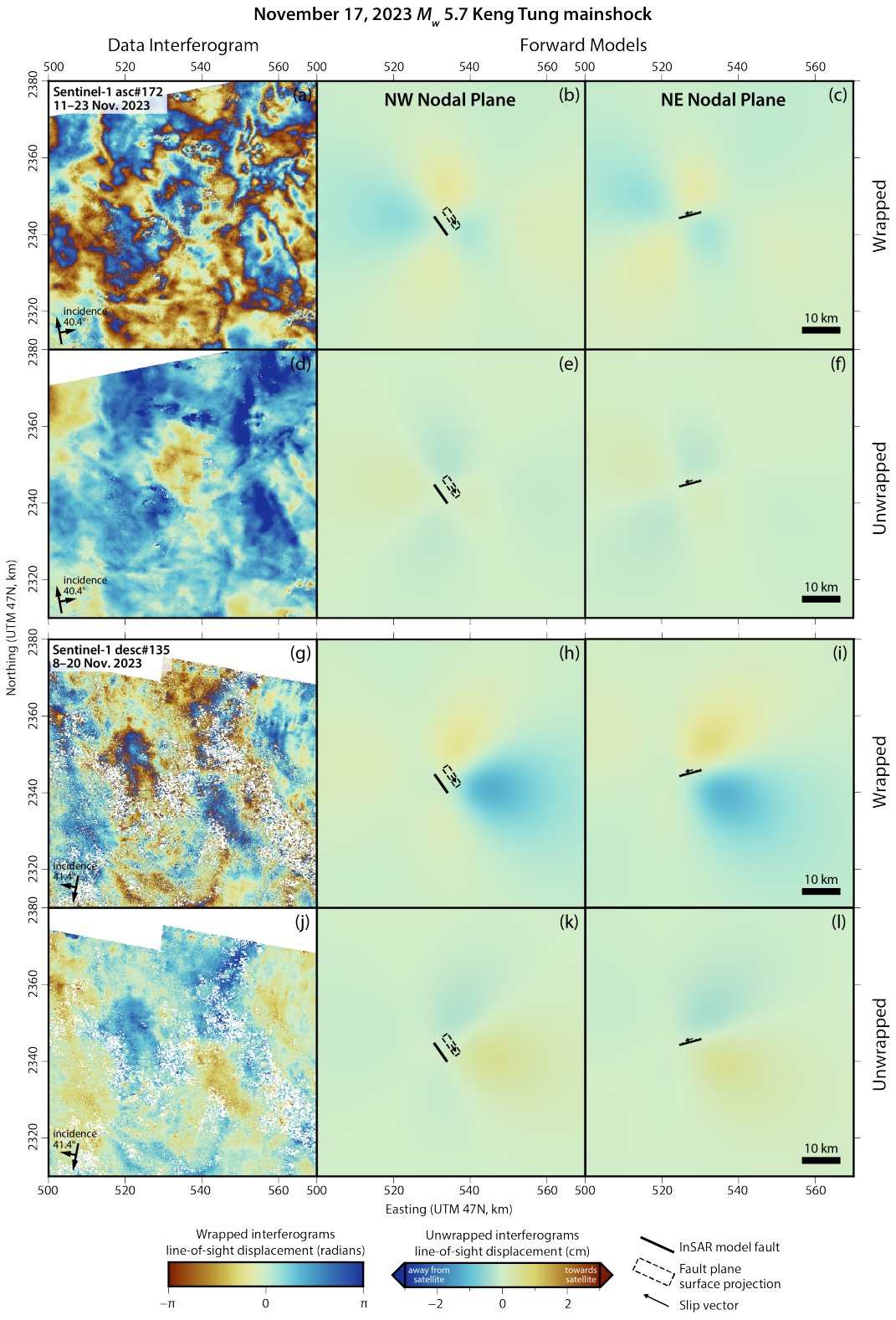


Figure 4.12: Observed (left column) and forward model (middle and right columns) interferograms of the 2023 M_w 5.7 Keng Tung event, shown both wrapped (a–c, g–i) and unwrapped (d–f, j–l), with red indicating motion towards the satellite). Observed interferograms (left column) and forward models of both nodal planes (middle and right columns) show that InSAR cannot distinguish the causative fault in this instance. Dashed rectangles are the model faults in map view, with thick black lines along their surface projections and arrows denoting the slip vector azimuth.

calibrated focal depth (Table 4.4). The regional moment tensor solution from Pananont et al. (2017) also indicates a NNW-striking, right-lateral rupture plane. We were unable to use the Sentinel-1 InSAR data because they were not available until approximately five months after this earthquake.

4.7.2 The 2011 Tarlay, Myanmar Earthquake

The March 24, 2011 M_w 6.8 Tarlay earthquake ruptured the major, NE-trending Nam Ma fault in Myanmar (Figure 4.9). It was a destructive event, killing at least 74 people, damaging or destroying over 700 homes rendering >3,000 people homeless, and impacting at least 18,000 people (United Nations Office for the Coordination of Humanitarian Affairs, 2011, last accessed February 28, 2024). Its left-lateral mechanism and slip distribution were constrained using InSAR and SAR pixel tracking (Feng et al., 2013; Wang et al., 2014a). The earthquake generated a ∼30 km-long surface rupture with shallow offsets of up to ∼2 m, peak slip of at least ∼4 m concentrated at ∼3–5 km depth (implying a ∼50% shallow slip deficit), and major slip down to ∼10 km depth.

Our earthquake relocation reveals that the mainshock initiated at ∼15 km depth (Table 4.4), a few kilometers below the InSAR model fault bottom depth of 12 km in Wang et al. (2014a), and at the western end of the InSAR model fault, suggesting that the earthquake ruptured unilaterally from west to east (Figure 4.7c, d). Large aftershocks are distributed mostly at the fault endpoints and within the surrounding rock volume, consistent with InSAR range offsets which show a ∼1 km wide zone of off-fault deformation Wang et al. (2014a). Aftershock focal depths range from 10–18 km, with individual uncertainties spanning between 3–8 km (Supplemental Long table 4.8). In general, these aftershocks all occur deeper than the main area of concentrated slip revealed by InSAR (Feng et al., 2013; Wang et al., 2014a).

4.7.3 The 2007 Bokeo, Laos Earthquake

The May 16, 2007 M_w 6.3 Bokeo earthquake occurred close to the western section of the Mae Chan fault in western Laos (Figures 4.9). Published focal mechanism (ANSS ComCat) of the mainshock suggested either a NW-striking right-lateral or a NE-striking left-lateral rupture plane, the latter consistent with kinematics of the Mae Chan fault. Additionally, Lee and Shyu (2015) observed an apparent deformation signal in InSAR imagery, and used forward modelling to suggest an ∼18 km-long rupture with 0.7 m of slip distributed between 4 km and 8 km depth.

However, the relocated mainshock epicenter, with its 4 km^2 area of confidence ellipse, occurs at least 20 km west of the InSAR model fault in Lee and Shyu (2015), albeit along on the same Mae Chan fault (Table 4.4). There is no clear surface deformation signal in the InSAR imagery at this location. Our calibrated focal depth reveals that the mainshock initiated at 13 km (+6,−2 km), and aftershock focal depths range from 6–21 km, with individual uncertainties of 3–9 km (Supplemental Long table 4.8). These are distributed away from the mainshock in all directions—some occurring along and off the mapped surface trace of the Mae Chan fault, and others along other, shorter mapped secondary faults (Figure 4.7c, d).

Our relocations therefore suggest that the InSAR signal interpreted by Lee and Shyu (2015) as coseismic is something else. There may be a number of factors at play in this misidentification. Firstly, the noisy and decorrelated InSAR data hinder the ability to identify coseismic signals accurately. Secondly, the mainshock may have ruptured a fault conjugate to the Mae Chan fault, to which the satellite look direction might be insensitive. Thirdly, the mainshock may have ruptured at too great a depth for a strong InSAR signal. The focal depth of the 2007 Bokeo mainshock is strongly constrained by teleseismic depth phases at 13 km (global minimum). A secondary local minimum in the relocation is estimated at approximately 17 km; this deeper focal depth supports the latter scenario.

4.8 Discussion

4.8.1 Seismogenic Layer Thickness and Earthquake Rupture Mechanics

In continental earthquake belts, the seismogenic layer refers to the brittle part of the crust or lithosphere capable of sustaining seismic rupture. Its thickness is a key parameter in seismic hazard analyses, setting the lower limit for slip in major earthquakes and thus partly controlling rupture area and seismic moment. The base of the seismogenic layer can be estimated in a variety of ways: by inverting for coseismic slip distributions in the largest earthquakes, by modelling interseismic locking depths using geodesy, by analyzing seismic tomographic or magnetotelluric datasets, or by determining precise focal or centroid depths for large seismicity datasets. In the last case, it is often parameterized as "D90", defined as the depth above which 90% of earthquakes occur (e.g., Ellis et al., 2023; Seebeck et al., 2023; Zeng et al., 2022).

In our 158 event relocated earthquake catalog, the focal depth at the 90^{th} percentile is

17 km. This estimate of D90 is between InSAR derived estimates for the deepest coseismic slip in the largest modern earthquakes in this region: ∼20 km in the 1995 M_w6.8 Myanmar earthquake (Ji et al., 2017) and ∼12 km in the 2011 M_w6.8 Tarlay earthquakes (Feng et al., 2013; Wang et al., 2014a). Our D90 estimate of 17 km is also consistent with the 10–21 km range of geodetically-derived locking depths along the southern Sagaing fault, west of our study area (e.g., Maurin et al., 2010; Pananont et al., 2017; Tin et al., 2022). It is somewhat deeper than locking depths of 5–15 km along the southern Red River fault, east of our study area (Lu et al., 2021), but magnetotelluric data show a resistive fault zone extending to ∼20 km depth, more consistent with our D90 (Ye et al., 2022). In the 2014 Mae Lao, Thailand sequence—the best locally-recorded seismicity dataset up to this point—the deepest aftershock occurred at 18 km depth according to regional waveform inversion (Pananont et al., 2017), also in close agreement with our interpreted seismogenic thickness.

To place our estimated D90 of 17 km in context, it is at the deeper end of the ∼13–17 km range of values estimated for the eastern California shear zone (Zeng et al., 2022), but slightly shallower than values of ∼20–25 km for eastern Turkey (Turkelli et al., 2003; Duman et al., 2018). The seismogenic layer in the Shan plateau thus appears to be of intermediate thickness amongst comparable continental plate boundary zones.

Our D90 estimate provides additional context for our study of the 2019 M_w 6.2 Sainyabuli and 2022 M_w 5.9 Keng Tung earthquakes, which can now be seen to have ruptured only the upper half of the seismogenic layer (Figure 4.7b, h). This potentially leaves the lower half as an ongoing seismic hazard. Similar inferences were made following the 2003 M_w 6.6 Bam, Iran earthquake, where coseismic slip concentrated above ∼10 km; however, locally-recorded aftershocks illuminated a seismogenic layer of double that thickness (Funning et al., 2005; Jackson et al., 2006). The consequences of this lingering hazard are illustrated by the 2008–2009 Qaidam sequence in north-eastern Tibet: the 2008 M_w 6.3 earthquake ruptured the lower half of the seismogenic layer, and the 2009 M_w 6.3 event broke the upper half directly up dip (Elliott et al., 2011). This further emphasizes that seismic hazard in the immediate vicinity of a recent earthquake should not be assumed to be reduced.

Finally, the largest earthquakes studied here illustrate other aspects of the mechanics of coseismic rupture. In these earthquakes, the peak slip and centroid depths from InSAR and waveform modelling are generally shallower than calibrated focal depths from relocation, implying that seismic slip propagated upwards (Figure 4.7). For example, the 2019 Sainyabuli mainshock nucleated at 12 km ± 4 km near the base of the InSAR model fault

and well below concentrated slip at 3–7 km depth, while the 2022 Keng Tung mainshock initiated at 20 km ± 4 km, much deeper than the uniform slip forward model fault at ∼2–6 km (Figure 4.7b, h). While acknowledging the limited local-distance station coverage near Keng Tung, our calibrated focal depth is still at least several kilometers deeper than the InSAR fault, indicating nucleation within a zone of low eventual slip. Confidence in this interpretation is provided by observations of other, better recorded earthquakes. For instance, the 2014 M_w 6.1 South Napa earthquake in California nucleated at ∼11 km but eventual slip concentrated at just 0–5 km depth (Wei et al., 2015). The 2011 M_w 5.9 Simav earthquake in Turkey similarly nucleated at 18 km depth, much below the InSAR rupture plane at ∼6–11 km (Karasözen et al., 2016). These discrepancies between deep hypocenters and shallow coseismic slip may reflect a tendency for earthquakes to nucleate within a creeping zone near the base of the seismogenic layer (Wei et al., 2015).

4.8.2 Fault Structural Immaturity and Implications for Seismic Hazards

Shallow slip deficit expresses the common discrepancy in InSAR model slip distributions between peak slip (normally inferred at depths of a few kilometers) and surface slip (e.g., Fialko et al., 2005; Dolan and Haravitch, 2014). Dolan and Haravitch (2014) suggested that earthquakes on structurally immature faults are characterized by larger SSDs (in which only ∼50–60% of slip reaches the surface) compared to those on mature faults. Our slip model for the 2019 M_w 6.2 Sainyabuli mainshock has an SSD of 80% which, although not unexpected for an earthquake of this size (Lauer et al., 2020; Sethanant et al., 2023), is at least consistent with a structurally immature fault (e.g., Dolan and Haravitch, 2014). Similarly, the surface projection of our InSAR model fault is inconspicuous in the topography, although it is sub-parallel to and across strike from nearby mapped traces of the Sainyabuli fault zone (Figure 4.7g). A wide zone of aftershock seismicity is another characteristic of a newly-developing fault (Perrin et al., 2021), and our relocated Sainyabuli aftershocks are distributed 1–10 km west and up to 6 km north of the InSAR model fault, with one event located as far as 17 km away (Figure 4.7g). Since our InSAR model fault dips steeply eastwards, it appears that the aftershocks illuminate various secondary fault strands. We conclude that observations of the 2019 Sainyabuli sequence are indeed indicative of young, immature faulting.

While interferograms of the 2022 M_w 5.9 Keng Tung earthquake are noisier than those of the Sainyabuli earthquake, our InSAR uniform slip forward modelling (top depth 2 km)

suggests that it did not rupture to the surface. While the earthquake ruptured an unmapped NW-trending fault, this parallels a distinct, northwesterly structural grain evident in the local topography (Figure 4.7a). The 2023 M_w 5.7 Keng Tung mainshock also co-locates along a subtle, NW-trending topographic lineament, although we were unable to distinguish the fault plane from the auxiliary plane due to the lack of a clear InSAR signal. It is likely that this earthquake ruptured deeper than can be resolved with InSAR. Together, these observations imply that the Keng Tung region, like Sainyabuli, contains unmapped, immature faults capable of hosting significant earthquakes.

Looking more broadly across the Golden Triangle region, while NE-trending sinistral faults are the most pronounced in the landscape, our results demonstrate that several recent M_w 5.5–6.2 events occurred on NW- to NNW-trending right-lateral faults (Figure 4.6a). The July 11, 1995 M_w 6.8 Myanmar earthquake, located ∼90 km NW of Keng Tung (Figure 4.2), shows that even larger earthquakes are possible on NW-striking faults that are little evident in the topography (Ji et al., 2017). Faults in the central and northern Shan Plateau do not seem to align with Tertiary terrane boundaries, such as the NNE-trending suture zones between the Chiang Mai-Chiang Rai suture zone and Sukhothai Terranes (Figure 4.9). This suggests that the largest inherited structures evident in the regional geology do not influence the pattern of earthquakes. However, geological inheritance may play a greater role in the southern Shan Plateau, in northwestern Thailand and north central Laos, where several mapped faults are parallel to the major terrane boundaries (e.g., Chansom et al., 2022; Searle and Morley, 2011).

Our association of at least three newly identified faults with significant recent earthquakes could spur improvements to local seismic hazard estimations. To include these as fault sources in probabilistic seismic hazard analysis (PSHA), detailed fault mapping coupled with paleoseismic investigations and seismic catalogs will be required to obtain fault slip and earthquake rates. However, in the interim until such rates are available, the known presence of the faults in Sainyabuli and Keng Tung is useful information for seismic hazard practitioners working in SE Asia. For instance, the mainshock rupture depth and the seismicity-defined seismogenic thickness (D90) will help define the source geometry (in fault sources or virtual faults in area sources) in PSHA. A relatively deep and thick seismogenic layer implies that the seismic hazard above the rupture initiation may be higher than for sites located further along the fault strike, while a relatively thin layer may suggest higher hazard values beyond the fault endpoints due to a more elongated rupture propagation. Moreover, source geometries and kinematics from this study will guide seismic hazard modellers in selecting the appropriate ground motion models and

characterizing the source-to-site distance in engineering analyses.

4.9 Conclusions

The 2019 M_w 6.2 Sainyabuli mainshock, its 2021 M_w 5.5 aftershock, and the 2022 M_w 5.9 Keng Tung earthquake all ruptured previously unmapped, ∼10–20 km long, NW-trending right-lateral strike-slip faults in the southern and central Shan Plateau, conjugate to the more pronounced NE-trending left-lateral faults in this region. These events exhibited rupture behaviours that may be linked to fault structural immaturity, including limited topographic expression along the model fault surface projections, high shallow slip deficits (80$\%$ in the 2019 Sainyabuli mainshock), and widely distributed aftershocks. In the 2019 Sainyabuli earthquake, peak slip and centroid depths of 4–5 km from InSAR and regional waveform inversion are much shallower than the 12 km calibrated focal depth from relocation, implying nucleation of the earthquake within a low slip zone near the bottom of the InSAR fault. We establish for the first time a seismogenic thickness of ∼17 km, derived from the 90$\%$ seismicity cut-off depth (D90) of our 158 calibrated hypocenters. This also suggests that the deeper half of seismogenic zone beneath the Sainyabuli earthquake remains a potential hazard for future ruptures. Across the Shan Plateau, short, hidden, immature faults, many of them conjugate to the longer, mature faults, are also capable of generating sizeable earthquakes and should not be overlooked in seismic hazard calculations, especially for the designing and retrofitting of nearby hydroelectric dams and cultural sites. Finally, our study provides a blueprint for multi-event earthquake relocation in sparsely instrumented regions. We find that problematic azimuthal gaps can be reduced by incorporating multiple earthquake sequences into a single relocation cluster, with InSAR observations of the largest events an important, independent check on the resulting epicentral distribution.

4.10 Acknowledgement

We kindly thank Santawat Sukrungsri (Thai Meteorological Department) and Dr. Harley Benz (USGS) for their immense support in providing regional arrival time and waveform datasets. The authors are grateful to Dr. Tuna Onur and Ivan Wong for their insights on seismic hazard assessments for emerging faults. We thank Win Shwe Sin Oo and Dr. Wei Shengji (Nanyang Technological University) for their support of this work and

stimulating discussion. This study is partly supported by the Diana and Martin Hocking Graduate Scholarship (University of Victoria) awarded to I.S.

4.11 Data and Resources

Sentinel-1 SAR images were obtained from the Alaska Satellite Facility (https://search.asf.alaska.edu). The Visible Earthquakes InSAR tool was used for preliminary estimates of fault geometries (https://visible-earthquakes.appspot.com, last accessed July 2022). InSAR displacements were corrected for residual linear trends and atmospheric noise using the Generic Atmospheric Correction Online Service (Yu et al., 2017) (http://www.gacos.net). For maps and InSAR topographic phase correction, we used the Shuttle Radar Topography Mission 3 arc second Digital Elevation Model (Farr and Kobrick, 2000; Farr et al., 2007; Kobrick, 2006; Rosen et al., 2000) obtained via https://topex.ucsd.edu/gmtsar/demgen/ and https://opentopography.org, and the USGS Global 30 Arc-Second Elevation Model accessed via https://earthexplorer.usgs.gov. InSAR inversion and forward modelling codes were kindly provided by the Centre for Observation and Modelling of Earthquakes, Volcanoes and Tectonics (COMET). Regional mapped faults were obtained from the Department of Mineral Resources, Thailand (DMR) through Weerachat Wiwegwin (personal communication). Global active faults are from the Global Earthquake Model Foundation's Global Active Faults Database (Stirling et al., 2008). Focal mechanisms were gathered from the automated GCMT catalog (Dziewonski et al., 1981; Ekström et al., 2012) (https://globalcmt.org/CMTsearch.html) and the ANSS ComCat (U.S. Geological Survey, Earthquake Hazards Program, 2017) (https://doi.org/10.5066/F7MS3QZH). Initial earthquake epicenters were obtained from the International Seismological Centre (ISC), Engdahl-van der Hilst-Buland Bulletin (Engdahl et al., 1998, 2020; International Seismological Centre, 2023; Weston et al., 2018) (https://doi.org/10.31905/PY08W6S3). Earthquake arrival times were also gathered from the ISC Bulletin (https://doi.org/10.31905/D808B830), ANSS ComCat (https://doi.org/10.5066/P95R8K8G), Incorporated Research Institutions for Seismology (http://ds.iris.edu/ds/nodes/dmc/data), the Thai Meteorological Department (TMD), the Department of Mineral Resources (DMR) Thailand (Santawat Sukrungsri, personal communication), or picked by ourselves from a waveform catalog provided to us by Passakorn Pananont (Pananont et al., 2017). Station locations are from the International Registry of Seismograph Stations through the ISC (https://doi.org/10.31905/EL3FQQ40), USGS NEIC, TMD, DMR, and the Provincial China Network (Sun Ruomei, personal communi-

cation). Waveforms used in our moment tensor inversion are from the EarthScope Consortium Web Services (`https://service.iris.edu/`), including the following seismic networks: GE, GEOFON Data Centre (1993); IC, Albuquerque Seismological Laboratory (ASL)/USGS (1992); IU, Albuquerque Seismological Laboratory/USGS (2014); MM, Department of Meteorology and Hydrology - National Earthquake Data Center (2016); TM (TMD Seismic Network). Relocated events of the independent 2014 Mae Lao cluster is available at `https://www.sciencebase.gov/catalog/item/6385574dd34ed907bf779994`.

4.12 Supplemental Material

Description of Supplemental Material

The supplemental material includes ten figures (Figures 4.13–4.22), two tables (Tables 4.5–4.6), and two long tables (Long table 4.7–4.8) uploaded separately (descriptions of each data field in the data files are included in this document). These show additional and supporting results for the InSAR inversion and forward models, travel time fits from *mloc* relocation, and waveform fits from our regional waveform modelling.

List of Supplemental Figures

1. Figure 4.13: 2019 Sainyabuli mainshock 6-day descending interferogram
2. Figure 4.14: Second nodal plane InSAR model of the 2021 Sainyabuli event
3. Figure 4.15: Second nodal plane InSAR model of the 2022 Keng Tung event
4. Figure 4.16: Relative location shift
5. Figure 4.17: Travel time fits at different epicentral distances
6. Figure 4.18: Waveform fits for the 2019 M_w 5.7 Sainyabuli foreshock moment tensor solution
7. Figure 4.19: Waveform fits for the 2019 M_w 6.2 Sainyabuli mainshock moment tensor solution
8. Figure 4.20: Waveform fits for the 2021 M_w 5.5 Sainyabuli aftershock moment tensor solution
9. Figure 4.21: Waveform fits for the 2022 M_w 5.9 Keng Tung mainshock moment tensor solution
10. Figure 4.22: Waveform fits for the 2023 M_w 5.7 Keng Tung mainshock moment tensor solution

List of Supplemental Tables

1. Table 4.5: Reference points for moment tensor inversions
2. Table 4.6: Best deviatoric moment tensor solutions

List of Supplemental Long Tables

1. Long table 4.7: 2019 Sainyabuli mainshock distributed slip model sub-fault patch parameters
2. Long table 4.8: Golden Triangle relocated hypocenters from *mloc*

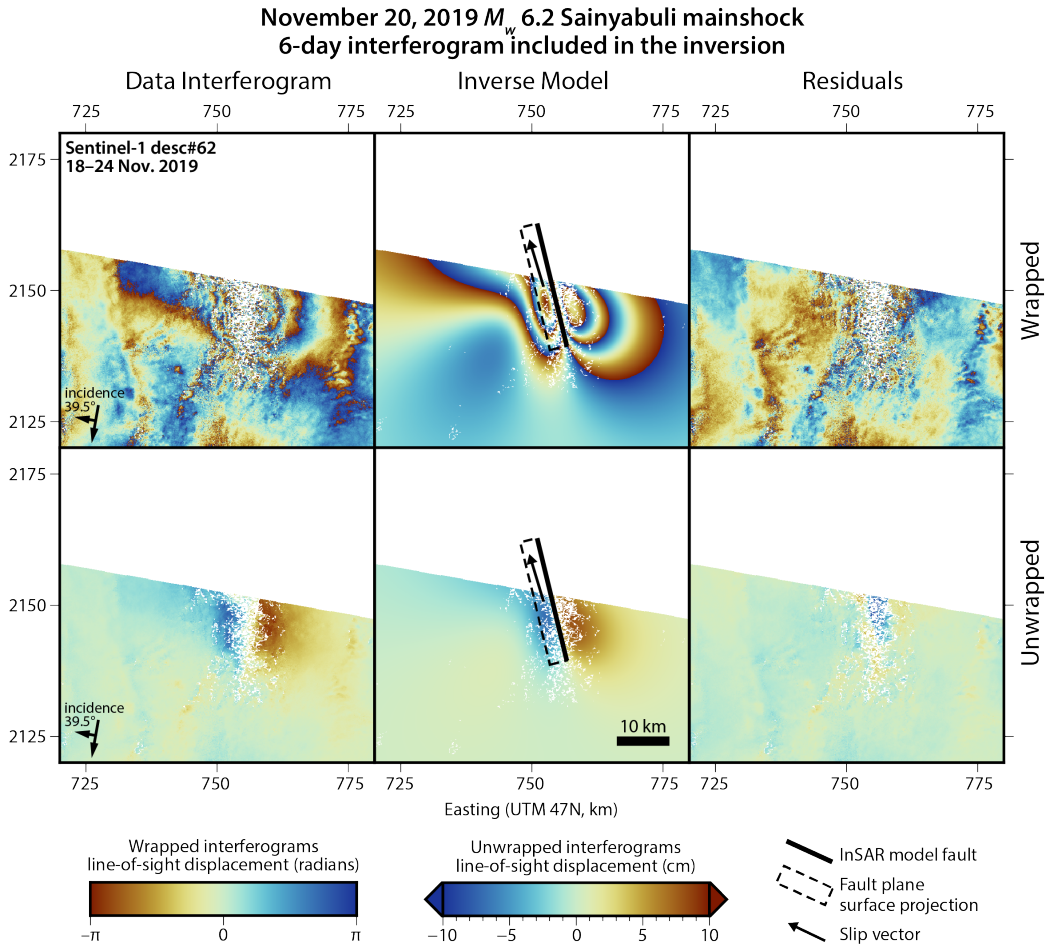


Figure 4.13: Observed (left panel), model (middle), and residual (right) interferograms that partially captured the rupture area of the 2019 M_w 6.2 Sainyabuli mainshock. This 6-day descending Sentinel-1 InSAR data set is included in the model fault inversion with the other two InSAR data sets (Figure 4 in main text) which fully covered the deformation area (see Data and methods section).

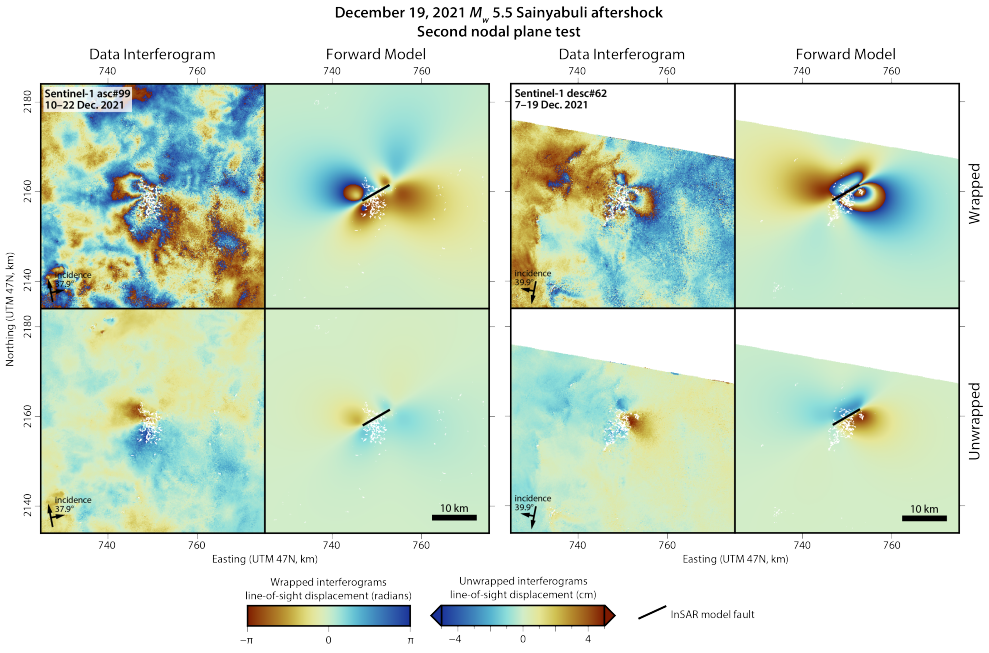


Figure 4.14: Observed and forward model interferograms of the 2021 M_w 5.5 Sainyabuli aftershock, with wrapped and unwrapped InSAR signals in the top and bottom rows, respectively. The forward models of the conjugate NE-trending fault (thick black line) show a mismatch to the data interferograms.

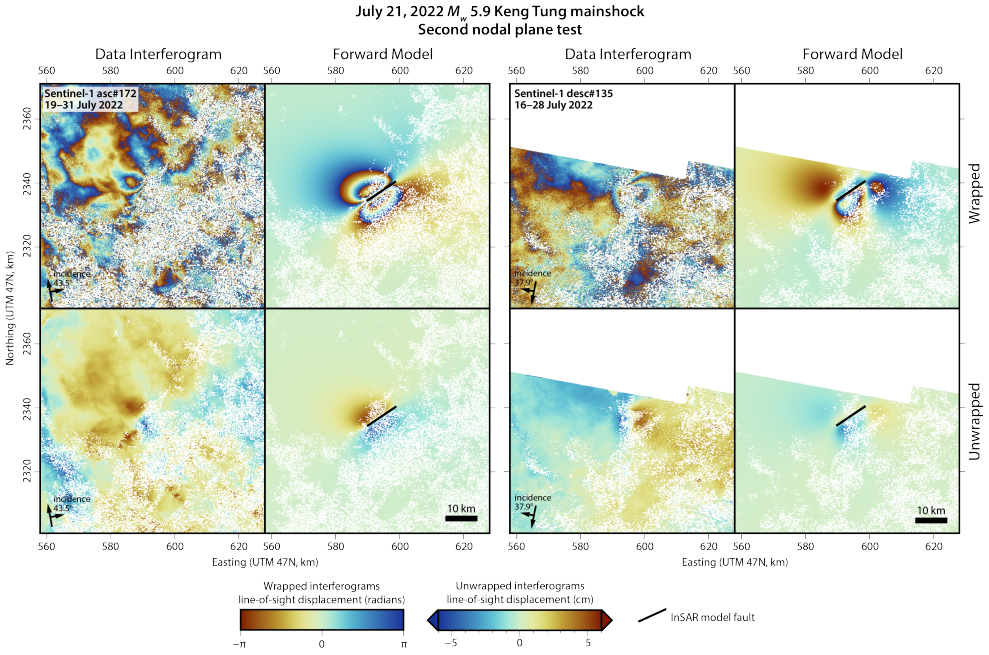


Figure 4.15: Observed and forward model interferograms of the 2022 M_w 5.9 Keng Tung mainshock, with wrapped and unwrapped InSAR signals in the top and bottom rows, respectively. The forward models of the NE-trending fault (thick black line) suggest that the second nodal plane does not explain the InSAR data.

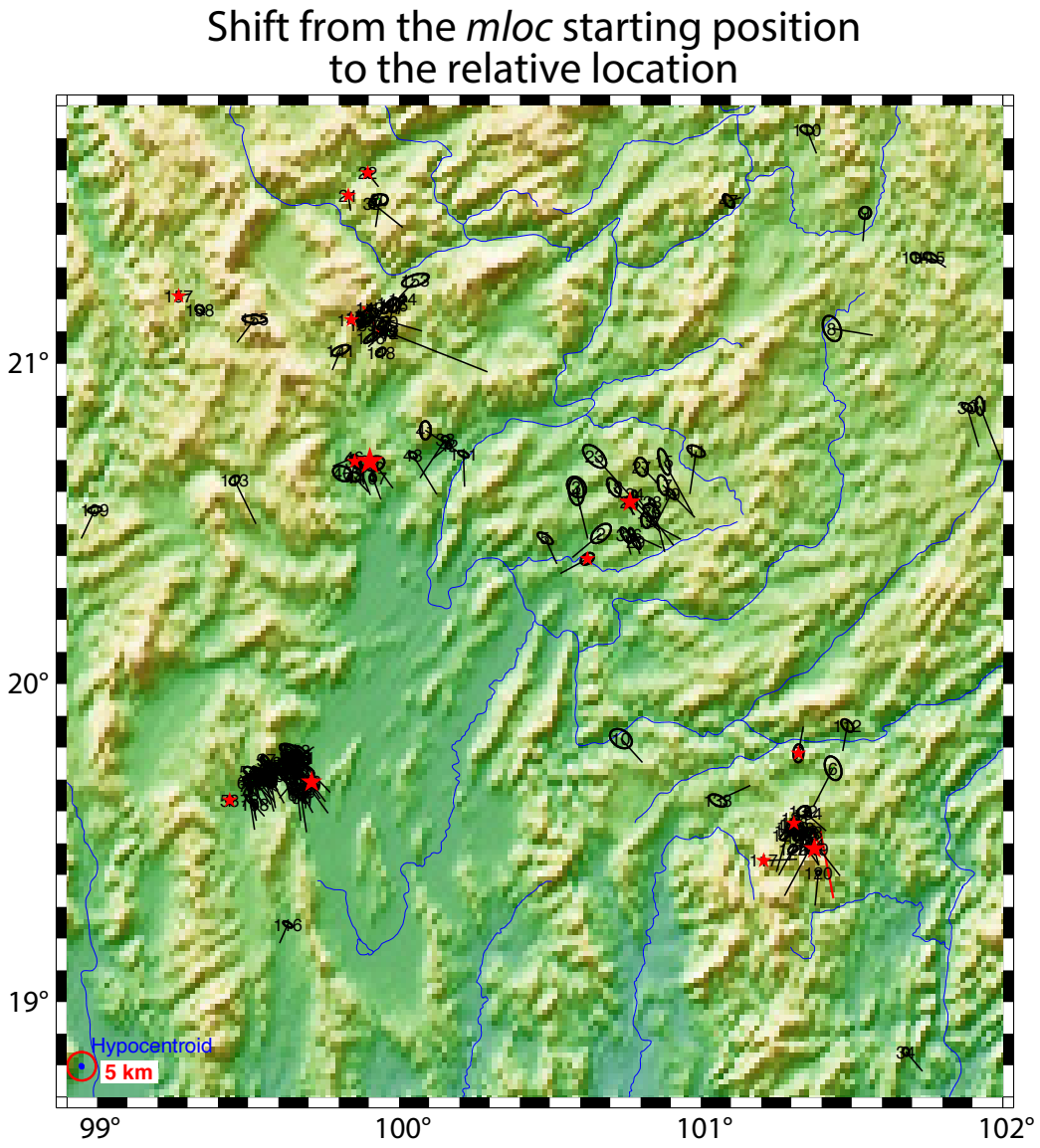


Figure 4.16: Map of epicenters with event numbers showing the shift from the starting position in *mloc* to the relative location. This change is represented by the cluster vector (solid black line), with its 90% confidence ellipse. Red stars are events with magnitudes greater than 5.0. Solid red line indicates our InSAR model faults. Red circle is a 5 km radius scale.

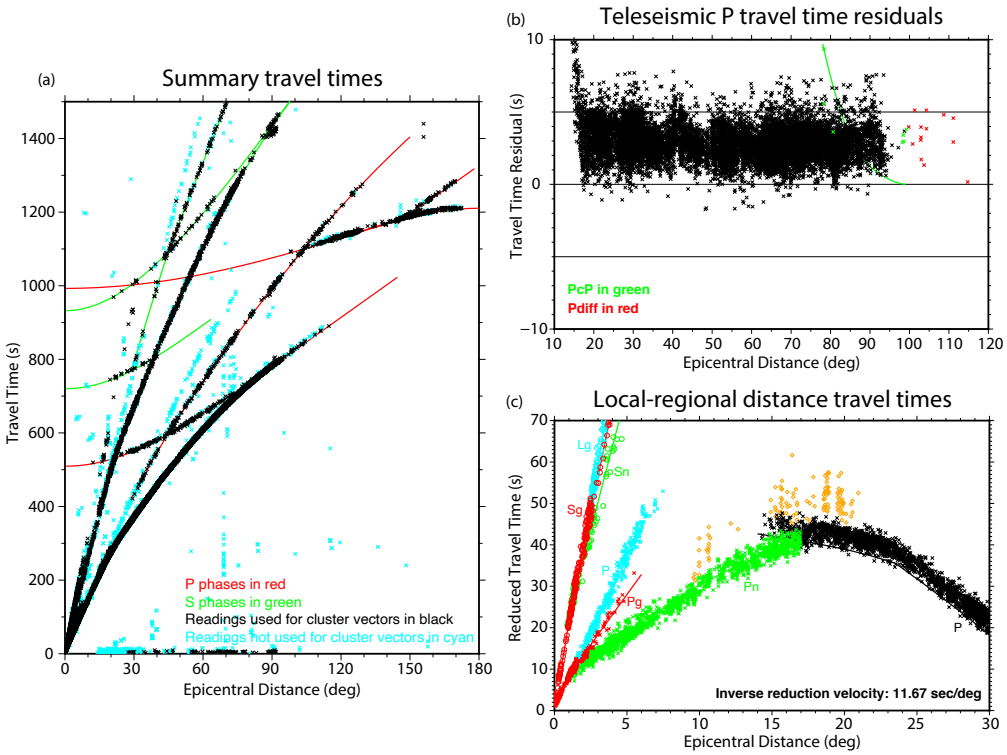


Figure 4.17: Theoretical and observed arrival times at different epicentral distances. (a) Travel times out to 180° distance. Theoretical curves are from the customized velocity model in Table 5 in the main text. Cross symbols are individual observed arrival time data, colored by their usage in the relocation: black—travel times used for cluster vectors but not for hypocentroid; cyan—travel times neither used for cluster vectors nor hypocentroid; red–travel times used both for hypocentroid and cluster vectors; green–travel times used for hypocentroid, but not for cluster vectors in green. Note that because of scale of the plot, the red and green symbols are usually indistinguishable. (b) Teleseismic P phase arrivals (black crosses) from 10°–120°, reduced to the theoretical time (ak135, (Kennett et al., 1995)). The green line denotes the theoretical arrival time of phase PcP. (c) Travel times up to 30° distance, reduced for readability (11.67 seconds/degree in inverse form, or 350 seconds at 30°). The observed phases (crosses and open circles) are annotated in the panel. See https://seismo.com/mloc/summary-plots/ for more details.

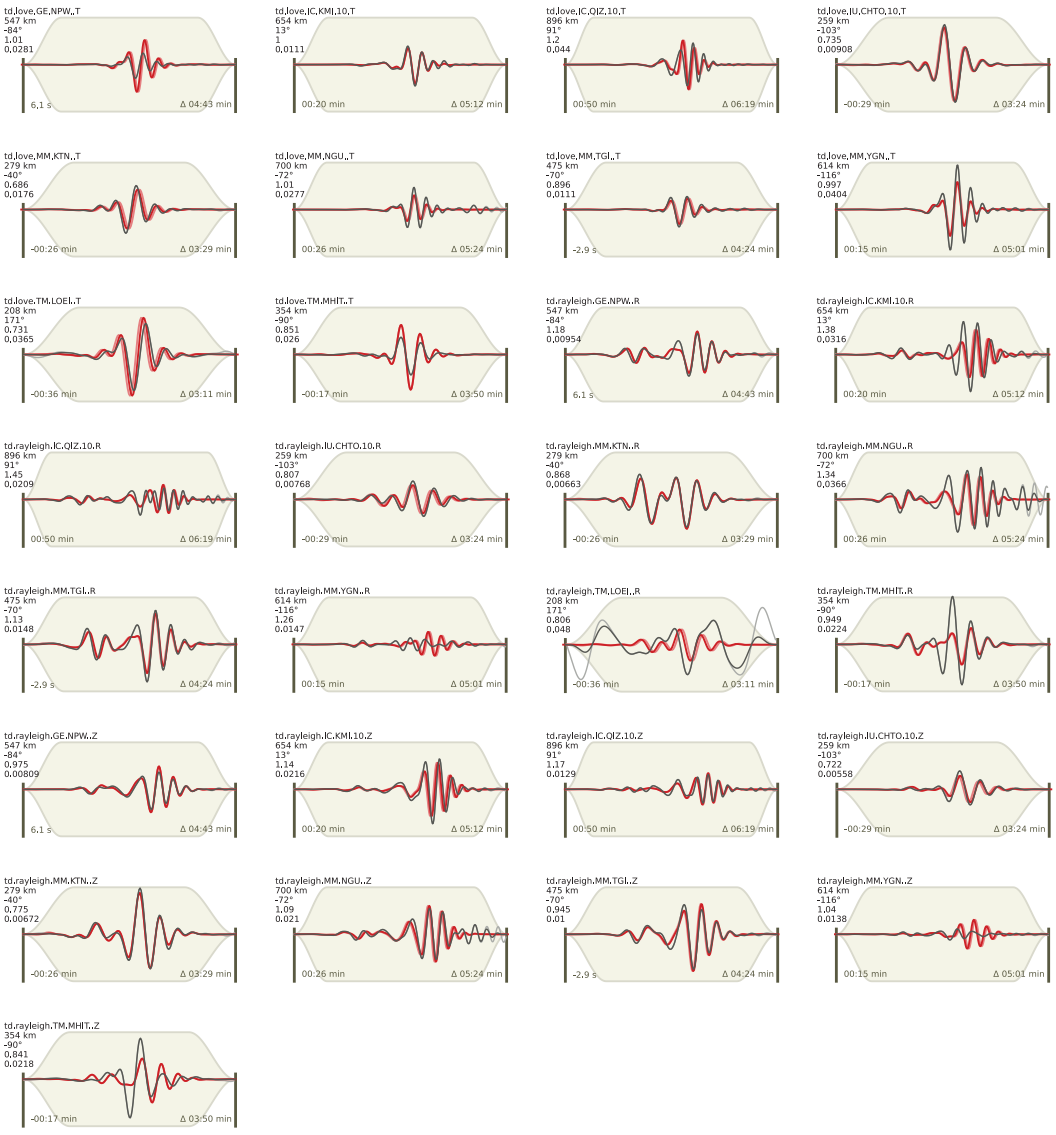


Figure 4.18: Waveform fits for the best deviatoric moment tensor solution for the 2019 M_w 5.7 Sainyabuli foreshock. Top left of each panel lists station name and component, distance to source, and azimuth of station with respect to the source. Starting time of the waveform relative to the origin time and length of the time window are indicated at the bottom left and right, respectively. The background gray area shows the applied taper function. The waveforms shown are: the filtered observed trace without tapering (light grey), the same trace with tapering and processing (dark gray), the synthetic trace (light red) and the filtered, tapered and shifted and processed synthetic target trace (red).

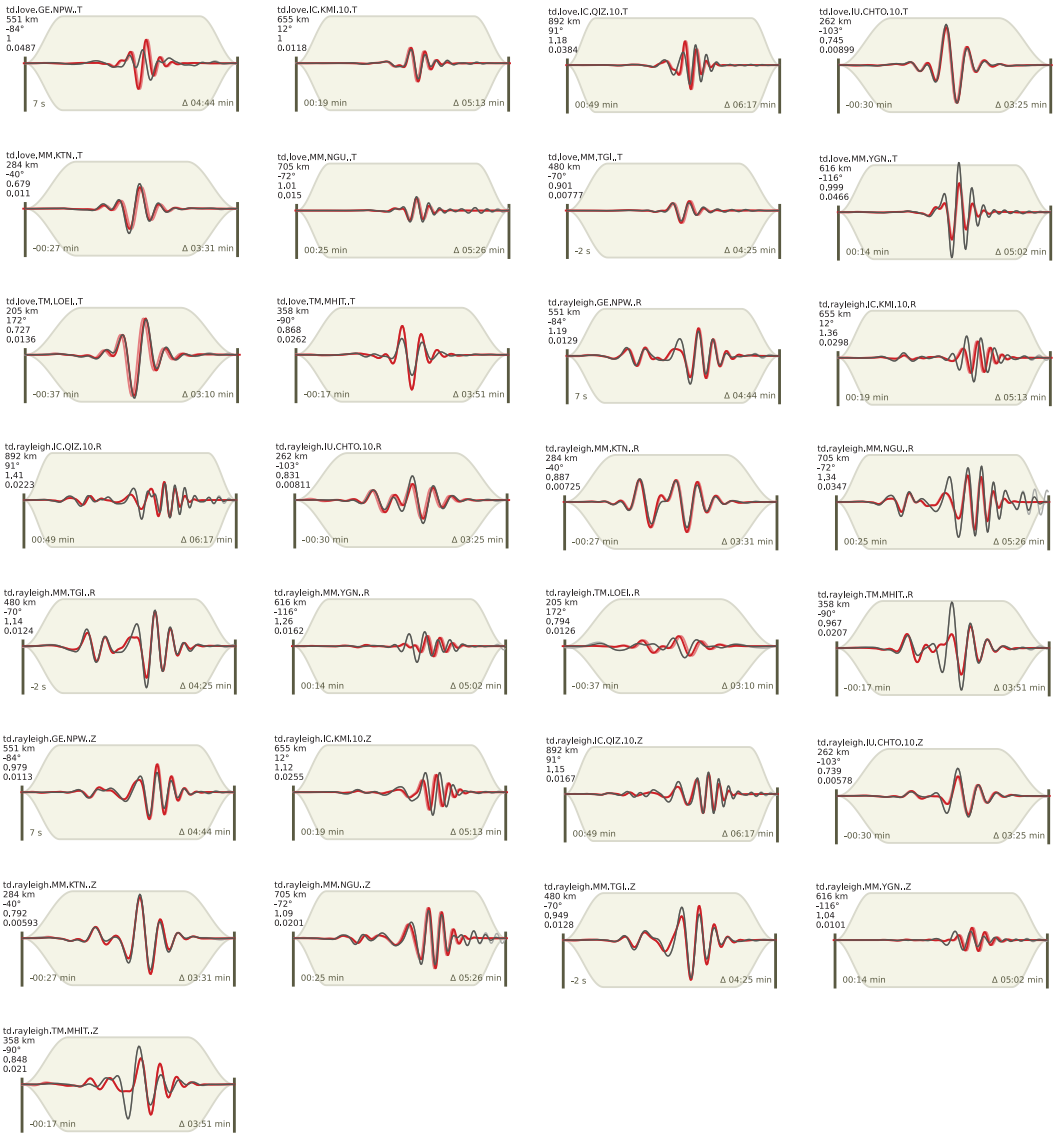


Figure 4.19: Waveform fits for the best deviatoric moment tensor solution for the 2019 M_w 6.2 Sainaybuli mainshock. Top left of each panel lists station name and component, distance to source, and azimuth of station with respect to the source. Starting time of the waveform relative to the origin time and length of the time window are indicated at the bottom left and right, respectively. The background gray area shows the applied taper function. The waveforms shown are: the filtered observed trace without tapering (light grey), the same trace with tapering and processing (dark gray), the synthetic trace (light red) and the filtered, tapered and shifted and processed synthetic target trace (red).

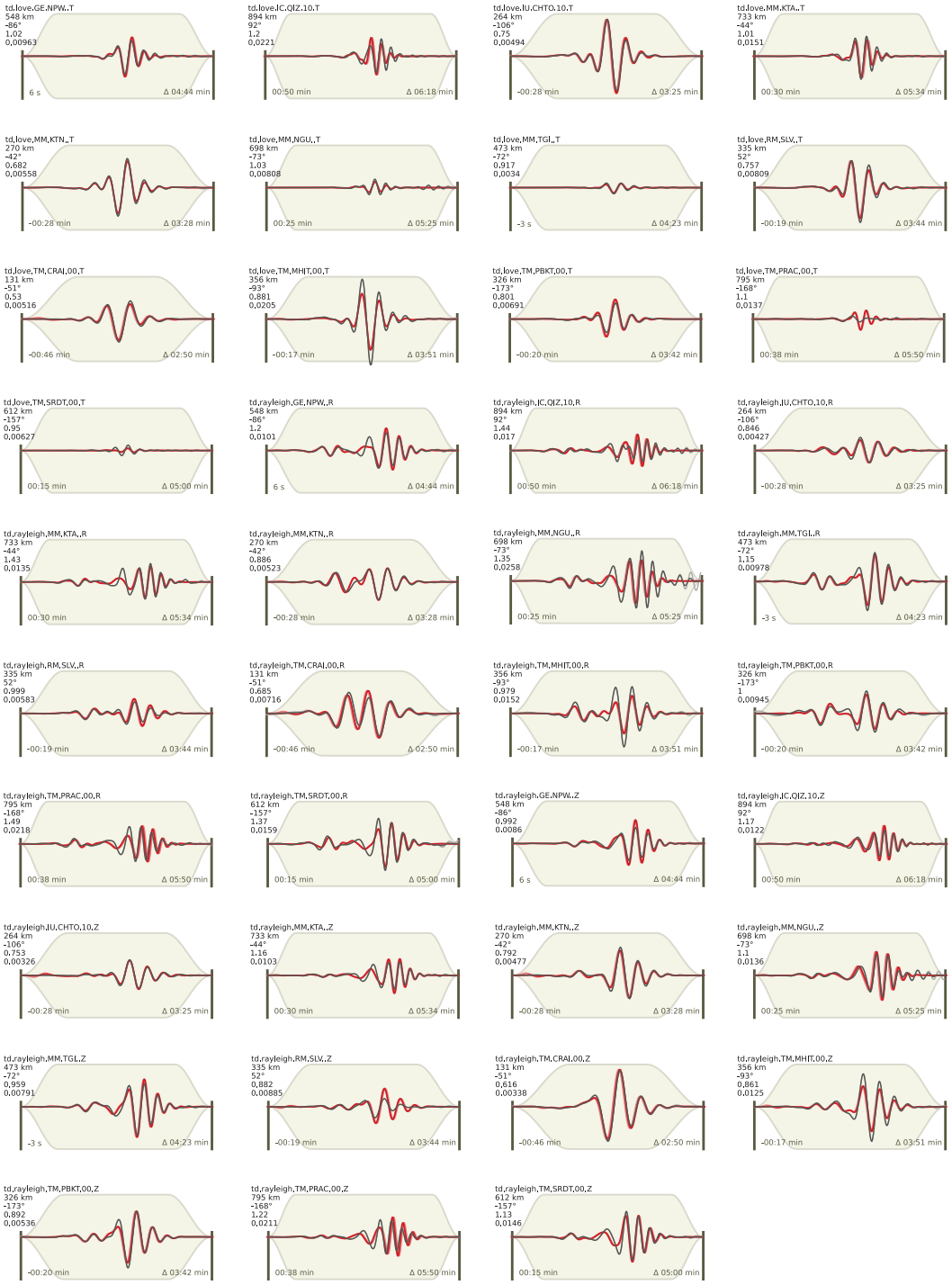


Figure 4.20: Waveform fits for the best deviatoric moment tensor solution for the 2021 M_w 5.5 Sainyabuli aftershock. Top left of each panel lists station name and component, distance to source, and azimuth of station with respect to the source. Starting time of the waveform relative to the origin time and length of the time window are indicated at the bottom left and right, respectively. The background gray area shows the applied taper function. The waveforms shown are: the filtered observed trace without tapering (light grey), the same trace with tapering and processing (dark gray), the synthetic trace (light red) and the filtered, tapered and shifted and processed synthetic target trace (red).

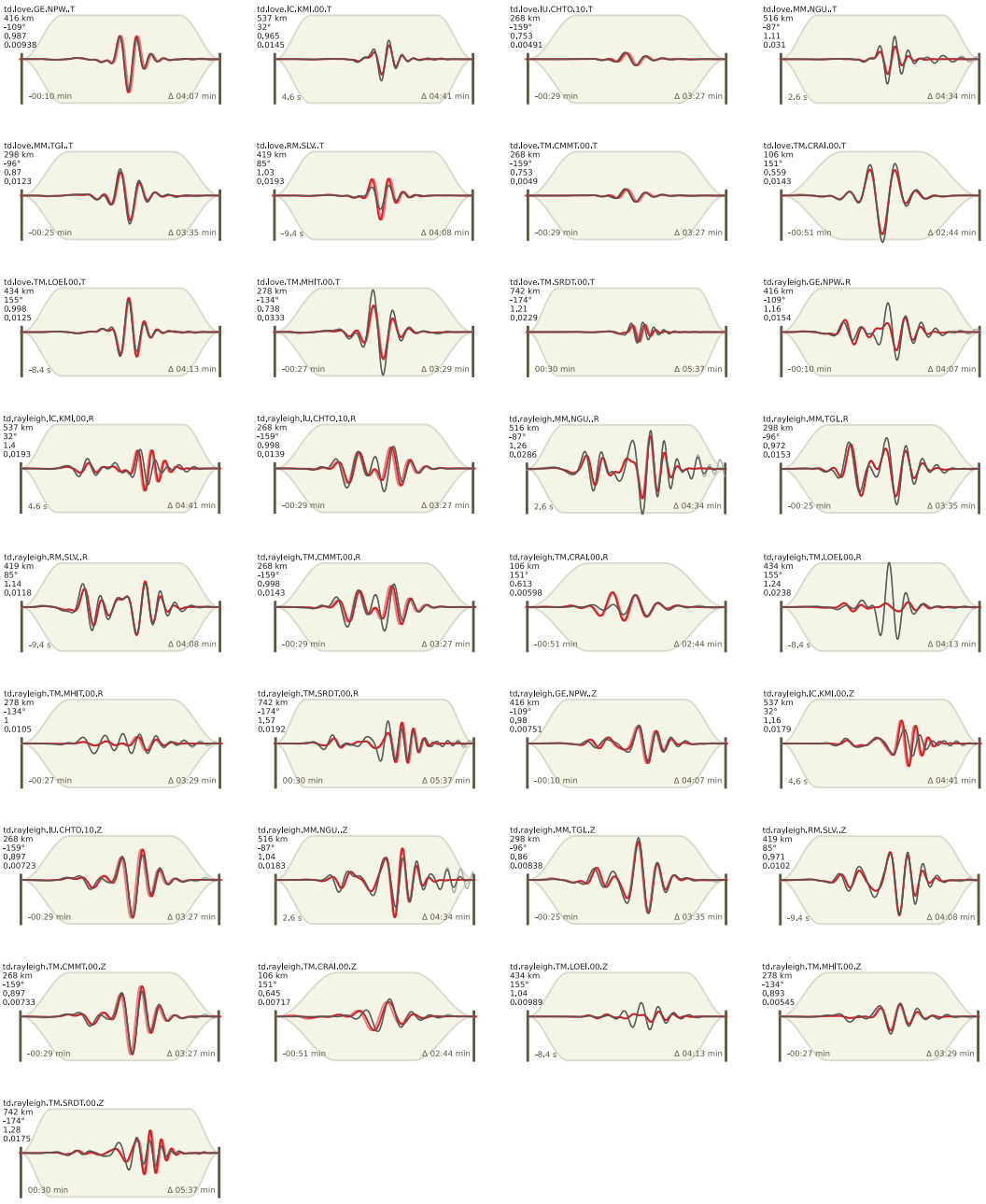


Figure 4.21: Waveform fits for the best deviatoric moment tensor solution for the 2022 M_w 5.9 Keng Tung mainshock. Top left of each panel lists station name and component, distance to source, and azimuth of station with respect to the source. Starting time of the waveform relative to the origin time and length of the time window are indicated at the bottom left and right, respectively. The background gray area shows the applied taper function. The waveforms shown are: the filtered observed trace without tapering (light grey), the same trace with tapering and processing (dark gray), the synthetic trace (light red) and the filtered, tapered and shifted and processed synthetic target trace (red).

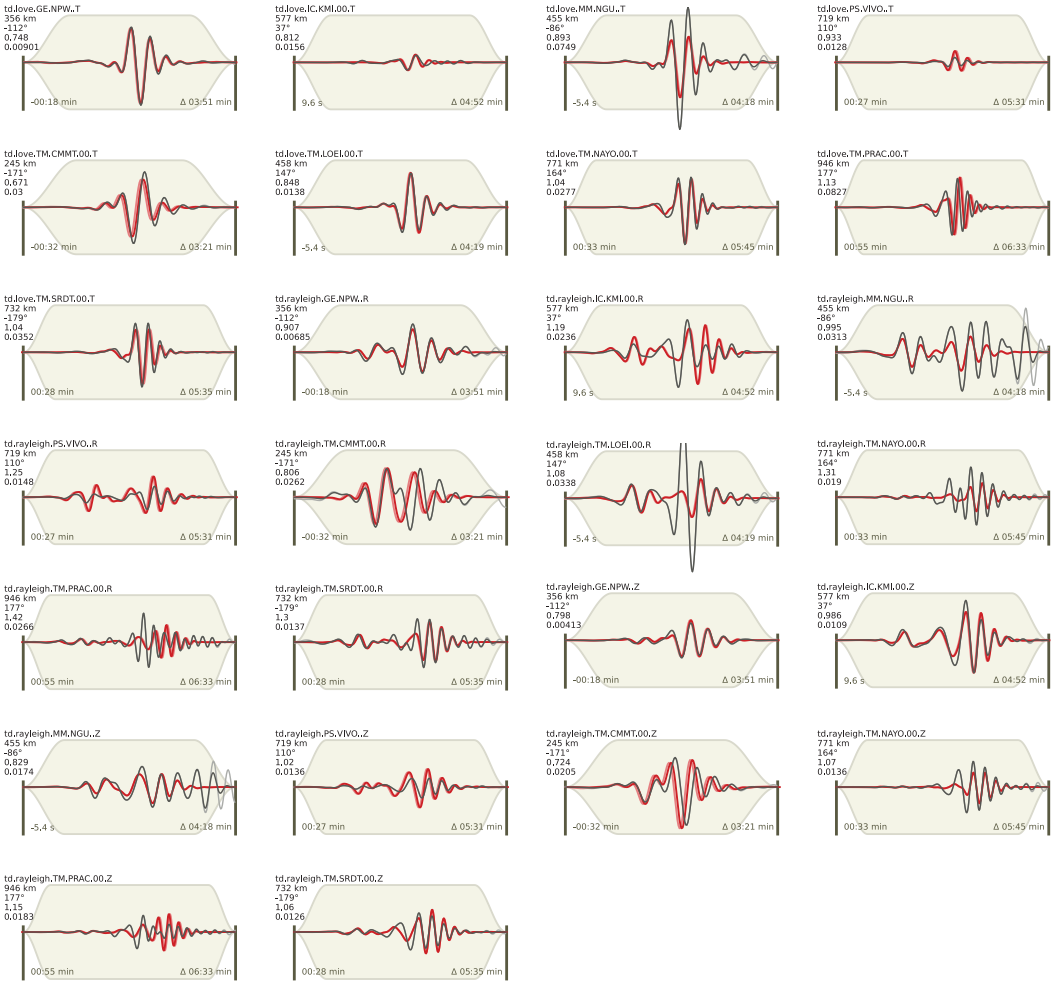


Figure 4.22: Waveform fits for the best deviatoric moment tensor solution for the 2023 M_w 5.7 Keng Tung mainshock. Top left of each panel lists station name and component, distance to source, and azimuth of station with respect to the source. Starting time of the waveform relative to the origin time and length of the time window are indicated at the bottom left and right, respectively. The background gray area shows the applied taper function. The waveforms shown are: the filtered observed trace without tapering (light grey), the same trace with tapering and processing (dark gray), the synthetic trace (light red) and the filtered, tapered and shifted and processed synthetic target trace (red).

Table 4.5: Reference points for the moment tensor inversions. For events with InSAR model faults, Easting and Northing reference locations are the surface projection of the peak slip sub-fault patch (for events with distributed slip inversion), or the surface projection center of the rectangular fault plane (for events with uniform slip). Depth references are either the peak slip depth (for distributed slip) or the fault central depth (for uniform slip). For events without a resolvable InSAR fault, Easting, Northing, and depth references are from our relocated hypocenters (Table 3 in the main text).

Event	**Easting (km)**	**Northing (km)**	**Depth (km)**
Events with InSAR models			
2019 SYB mainshock	752.537	2149.755	4.9 (distributed)
2021 SYB aftershock	749.325	2159.432	2.5 (uniform)
2022 KT mainshock	593.175	2336.684	3 (uniform)
Events without InSAR models			
2019 SYB foreshock	731.799	2151.524	13 (focal)
2023 KT mainshock	528.036	2345.460	14 (focal)

Table 4.6: Best deviatoric moment tensor solutions ($\times 10^{18}$ N·m) for the five largest earthquakes studied here.

Event	M_{nn}	M_{ee}	M_{dd}	M_{ne}	M_{nd}	M_{ed}
2019 SYB foreshock	-0.16	0.57	-0.41	-0.715	-0.36	-0.32
2019 SYB mainshock	-0.144	0.615	-0.472	-0.671	-0.3	-0.38
2021 SYB aftershock	-0.497	0.55	-0.053	-0.522	0.05	-0.67
2022 KT mainshock	-0.562	0.999	-0.436	-0.483	-0.097	0.07
2023 KT mainshock	-0.524	0.493	0.03	-0.814	-0.249	-0.128

Table 4.7: Full parameters of the 2019 Sainyabuli mainshock InSAR distributed slip model. Easting and Northing are in UTM zone 11N, referring to the surface projection of the sub-fault patch central coordinates. Each sub-fault patch is 2 km×2 km.

Easting (m)	Northing (m)	Strike (°)	Dip (°)	Rake (°)	Model slip (m)	Top depth (km)	Bottom depth (km)
751221	2161783	166	76	-167	0.0	0.0	1.9
751221	2161783	166	76	-167	0.0	1.9	3.9
751221	2161783	166	76	-167	0.0	3.9	5.8
751221	2161783	166	76	-167	0.0	5.8	7.8
751221	2161783	166	76	-167	0.0	7.8	9.7
751221	2161783	166	76	-167	0.0	9.7	11.7
751221	2161783	166	76	-167	0.0	11.7	13.6
751692	2159839	166	76	-167	0.1	0.0	1.9
751692	2159839	166	76	-167	0.2	1.9	3.9
751692	2159839	166	76	-167	0.3	3.9	5.8
751692	2159839	166	76	-167	0.2	5.8	7.8
751692	2159839	166	76	-167	0.1	7.8	9.7
751692	2159839	166	76	-167	0.1	9.7	11.7
751692	2159839	166	76	-167	0.1	11.7	13.6
752163	2157896	166	76	-167	0.2	0.0	1.9
752163	2157896	166	76	-167	0.4	1.9	3.9
752163	2157896	166	76	-167	0.5	3.9	5.8
752163	2157896	166	76	-167	0.4	5.8	7.8
752163	2157896	166	76	-167	0.2	7.8	9.7
752163	2157896	166	76	-167	0.1	9.7	11.7
752163	2157896	166	76	-167	0.1	11.7	13.6
752634	2155952	166	76	-167	0.3	0.0	1.9
752634	2155952	166	76	-167	0.5	1.9	3.9
752634	2155952	166	76	-167	0.6	3.9	5.8
752634	2155952	166	76	-167	0.5	5.8	7.8
752634	2155952	166	76	-167	0.2	7.8	9.7
752634	2155952	166	76	-167	0.1	9.7	11.7
752634	2155952	166	76	-167	0.0	11.7	13.6
753105	2154008	166	76	-167	0.2	0.0	1.9
753105	2154008	166	76	-167	0.6	1.9	3.9
753105	2154008	166	76	-167	0.7	3.9	5.8
753105	2154008	166	76	-167	0.5	5.8	7.8
753105	2154008	166	76	-167	0.2	7.8	9.7
753105	2154008	166	76	-167	0.0	9.7	11.7
753105	2154008	166	76	-167	0.0	11.7	13.6
753576	2152064	166	76	-167	0.1	0.0	1.9
753576	2152064	166	76	-167	0.7	1.9	3.9
753576	2152064	166	76	-167	0.9	3.9	5.8
753576	2152064	166	76	-167	0.6	5.8	7.8
753576	2152064	166	76	-167	0.2	7.8	9.7
753576	2152064	166	76	-167	0.0	9.7	11.7
753576	2152064	166	76	-167	0.0	11.7	13.6
754047	2150121	166	76	-167	0.1	0.0	1.9

Continued on next page

Table 4.7 – *Continued from previous page*

Easting (m)	Northing (m)	Strike (°)	Dip (°)	Rake (°)	Model slip (m)	Top depth (km)	Bottom depth (km)
754047	2150121	166	76	-167	0.8	1.9	3.9
754047	2150121	166	76	-167	1.0	3.9	5.8
754047	2150121	166	76	-167	0.7	5.8	7.8
754047	2150121	166	76	-167	0.2	7.8	9.7
754047	2150121	166	76	-167	0.0	9.7	11.7
754047	2150121	166	76	-167	0.0	11.7	13.6
754518	2148177	166	76	-167	0.1	0.0	1.9
754518	2148177	166	76	-167	0.6	1.9	3.9
754518	2148177	166	76	-167	0.9	3.9	5.8
754518	2148177	166	76	-167	0.7	5.8	7.8
754518	2148177	166	76	-167	0.3	7.8	9.7
754518	2148177	166	76	-167	0.1	9.7	11.7
754518	2148177	166	76	-167	0.0	11.7	13.6
754989	2146233	166	76	-167	0.1	0.0	1.9
754989	2146233	166	76	-167	0.4	1.9	3.9
754989	2146233	166	76	-167	0.8	3.9	5.8
754989	2146233	166	76	-167	0.7	5.8	7.8
754989	2146233	166	76	-167	0.4	7.8	9.7
754989	2146233	166	76	-167	0.1	9.7	11.7
754989	2146233	166	76	-167	0.0	11.7	13.6
755460	2144289	166	76	-167	0.1	0.0	1.9
755460	2144289	166	76	-167	0.3	1.9	3.9
755460	2144289	166	76	-167	0.6	3.9	5.8
755460	2144289	166	76	-167	0.6	5.8	7.8
755460	2144289	166	76	-167	0.3	7.8	9.7
755460	2144289	166	76	-167	0.1	9.7	11.7
755460	2144289	166	76	-167	0.0	11.7	13.6
755931	2142346	166	76	-167	0.0	0.0	1.9
755931	2142346	166	76	-167	0.2	1.9	3.9
755931	2142346	166	76	-167	0.3	3.9	5.8
755931	2142346	166	76	-167	0.3	5.8	7.8
755931	2142346	166	76	-167	0.1	7.8	9.7
755931	2142346	166	76	-167	0.0	9.7	11.7
755931	2142346	166	76	-167	0.0	11.7	13.6
756402	2140402	166	76	-167	0.0	0.0	1.9
756402	2140402	166	76	-167	0.0	1.9	3.9
756402	2140402	166	76	-167	0.0	3.9	5.8
756402	2140402	166	76	-167	0.0	5.8	7.8
756402	2140402	166	76	-167	0.0	7.8	9.7
756402	2140402	166	76	-167	0.0	9.7	11.7
756402	2140402	166	76	-167	0.0	11.7	13.6

Table 4.8: Relocated hypocenters of 158 well-recorded events using *mloc* direct calibration include origin date and time in UTC, latitude, longitude, and focal depth. Earthquake magnitude (Mag.) and type (columns 9–10) are from the ISC Bulletin and the USGS ANSS ComCat. The *mloc* depth code (column 12) denotes depth estimation methods: m—mloc free parameter solution, n—near-source readings, l—local-distance readings, c—cluster default depth, d—teleseismic depth phases. Focal depth uncertainties (Unc.) are reported as errors in deeper (column 13) and shallower (column 14) depths in kilometers. For free depth solutions, uncertainties are calculated from the covariance matrix of the relocation; fixed depths have estimated uncertainties. The 90% confidence ellipse (Ell.) semi-axis azimuth (Az.) and length (columns 15–18) indicate epicentral uncertainties. Further descriptions of *mloc* direct calibration output and depth constraints can be found at `https://seismo.com/mloc/hdf-files/` and `https://seismo.com/mloc/depth-constraint/`. Full data files for this relocated cluster, including local-regional stations from local networks, are available in the Global Catalog of Calibrated Earthquake Locations [GCCEL Link].

Origin date and time						Latitude (°)	Longitude (°)	Mag.	Mag. type	Focal depth (km)	Depth code	Unc. (deeper, + km)	Unc. (shallower, − km)	Ell. short semi-axis		Long semi-axis		90% confidence ellipse area (km^2)
yyyy	mm	dd	Hr	Min	Sec									Az. (°)	Length (km)	Az. (°)	Length (km)	
1978	8	2	7	45	46.72	20.3908	100.6236	5.1	mb	6.0	d	5.0	3.0	322	1.88	52	2.65	15.6
1978	9	1	4	55	11.50	20.4705	100.6687	4.9	mb	12.0	c	2.9	2.9	316	2.51	46	4.24	33.4
1989	4	7	21	45	18.48	20.6148	100.5881	4.5	mb	12.0	c	2.9	2.9	55	3.04	145	3.94	37.6
1990	7	14	3	51	53.43	20.6011	100.5870	4.5	mb	12.0	c	2.9	2.9	83	2.66	173	4.75	39.6
1996	12	21	17	51	3.50	20.4550	100.4840	4.7	mb	15.0	d	5.0	8.0	34	1.48	124	3.14	14.6
1999	3	31	3	19	14.68	19.7345	101.4384	4.4	mb	12.0	c	2.9	2.9	69	2.76	159	4.38	38.0
2000	1	19	20	59	24.05	19.7821	101.3231	5.1	mb	11.0	d	7.0	5.0	272	1.89	2	3.24	19.3
2001	2	26	14	21	46.88	21.1091	101.4335	4	mb	12.0	c	2.9	2.9	68	2.96	158	4.65	43.3
2002	1	19	22	14	17.12	21.4678	101.5436	4.1	mb	12.0	c	2.9	2.9	78	2.16	168	2.22	15.1
2002	7	2	3	54	4.60	19.8282	100.7346	4.4	mb	12.0	c	2.9	2.9	35	2.98	125	4.24	39.6
2003	11	23	15	8	10.22	20.7266	100.9841	4.4	mb	12.0	c	2.9	2.9	26	1.77	116	3.33	18.5
2005	8	17	18	37	1.67	21.0948	99.9680	3.9	mb	12.0	c	2.9	2.9	16	1.21	106	2.53	9.6
2007	5	15	14	35	47.79	20.5110	100.8183	4.3	mb	12.0	c	2.9	2.9	79	1.83	169	2.77	15.9
2007	5	16	8	56	12.28	20.5676	100.7647	6.4	MS	13.0	d	6.0	2.0	282	0.98	12	1.16	3.6
2007	5	16	11	16	1.73	20.6941	100.8776	3.8	mb	12.0	c	2.9	2.9	72	1.68	162	4.84	25.5
2007	5	16	13	18	11.34	20.4665	100.7725	4	mb	12.0	c	2.9	2.9	70	1.12	160	2.50	8.8
2007	5	16	17	8	56.88	20.6206	100.8738	3.9	mb	12.0	c	2.9	2.9	74	1.79	164	3.66	20.6
2007	5	17	3	25	44.77	20.6137	100.7112	3.7	mb	12.0	c	2.9	2.9	60	1.84	150	3.68	21.2
2007	6	7	17	21	9.20	20.5937	100.9005	4.5	mb	21.0	d	18.0	4.0	51	1.27	141	2.05	8.2
2007	6	23	6	53	52.07	21.5095	99.9364	4.2	mb	10.0	d	9.0	3.0	356	2.04	86	2.82	18.1
2007	6	23	8	17	15.48	21.5219	99.8324	5.3	mb	9.0	d	4.0	5.0	272	0.85	2	1.10	2.9
2007	6	23	8	27	44.54	21.5923	99.8962	5.2	mb	7.0	d	4.0	3.0	88	1.42	178	1.51	6.8
2007	9	8	7	12	50.82	20.7106	100.6479	3.6	mb	6.0	l	4.0	4.0	45	2.70	135	5.08	43.1
2007	10	16	6	46	54.54	20.5920	100.7814	4.5	mb	6.0	l	4.0	4.0	72	1.04	162	1.64	5.4
2007	11	1	19	5	46.39	20.5689	100.7628	4.6	mb	12.0	c	2.9	2.9	73	1.51	163	2.06	9.7
2008	6	10	21	37	41.05	20.5401	100.8358	4.3	mb	12.0	c	2.9	2.9	36	2.08	126	3.21	21.0
2008	11	29	8	6	24.16	20.6776	100.8031	4.1	mb	12.0	c	2.9	2.9	74	2.20	164	3.39	23.4
2009	5	22	7	58	10.99	20.5674	100.8390	3.8	mb	10.0	d	4.0	4.0	58	0.99	148	1.79	5.6
2009	8	16	17	57	13.75	20.4444	100.7841	3.8	mb	11.0	l	4.0	4.0	60	1.23	150	2.97	11.5

Continued on next page

Table 4.8 – *Continued from previous page*

Origin date and time						Latitude (°)	Longitude (°)	Mag.	Mag. type	Focal depth (km)	Depth code	Unc. (deeper, + km)	Unc. (shallower, − km)	Ell. short semi-axis		Long semi-axis		90% confidence ellipse area (km^2)
yyyy	mm	dd	Hr	Min	Sec									Az. (°)	Length (km)	Az. (°)	Length (km)	
2009	10	14	1	58	36.70	20.8645	101.8824	4.1	mb	12.0	l	4.0	4.0	35	1.28	125	2.19	8.8
2009	11	10	7	36	55.32	20.8682	101.9237	4	mb	19.0	l	4.0	4.0	85	1.55	175	3.30	16.0
2010	3	19	19	53	34.78	21.4976	99.9123	4.4	mb	12.0	c	2.9	2.9	276	1.30	6	1.87	7.7
2010	4	2	18	3	33.61	20.4648	100.7513	3.7	mb	12.0	c	2.9	2.9	60	1.40	150	3.10	13.6
2011	2	23	15	53	14.03	18.8433	101.6788	4.6	mb	12.0	l	4.0	4.0	76	1.28	166	1.66	6.7
2011	3	24	13	55	10.66	20.6953	99.9031	7.2	MS	15.0	l	4.0	4.0	88	0.89	178	0.93	2.6
2011	3	24	14	23	51.07	20.6797	99.8660	4.7	mb	12.0	c	2.9	2.9	1	1.28	91	1.53	6.1
2011	3	24	15	54	33.13	20.6951	99.8525	5.4	mb	11.0	l	4.0	4.0	295	0.93	25	0.94	2.8
2011	3	24	17	20	8.46	20.7642	100.1536	4.2	mb	12.0	c	2.9	2.9	34	1.28	124	1.54	6.2
2011	3	25	0	22	36.75	20.6888	99.8803	4.9	mb	12.0	c	2.9	2.9	354	1.31	84	1.71	7.1
2011	3	25	3	25	58.83	20.6575	99.8127	4	mb	12.0	c	2.9	2.9	27	2.53	117	3.63	28.8
2011	3	25	6	30	37.26	20.7918	100.0875	3.8	mb	12.0	c	2.9	2.9	89	1.97	179	3.27	20.3
2011	3	26	5	57	28.65	20.7441	100.1639	4.7	mb	13.0	d	5.0	8.0	48	1.15	138	1.33	4.8
2011	3	26	20	49	39.74	20.7136	100.0458	3.8	mb	12.0	c	2.9	2.9	41	1.23	131	1.60	6.2
2011	3	27	0	35	46.93	20.6456	99.8524	4	mb	12.0	c	2.9	2.9	13	1.76	103	2.15	11.9
2011	5	28	14	30	46.27	20.6882	99.9196	3.6	mb	14.0	l	4.0	4.0	342	2.58	72	3.43	27.8
2013	5	6	20	17	58.44	20.7070	99.8511	4.9	mb	10.0	l	4.0	4.0	357	1.18	87	1.54	5.7
2014	5	1	18	8	51.50	21.5047	101.0919	4	mb	12.0	c	2.9	2.9	52	1.53	142	2.82	13.6
2014	5	5	11	8	42.11	19.6916	99.7097	6.2	Mw	11.0	l	4.0	4.0	327	1.09	57	1.20	4.1
2014	5	5	11	19	34.68	19.7655	99.6768	4.3	mb	13.0	l	4.0	4.0	27	1.73	117	3.24	17.6
2014	5	5	11	22	17.08	19.7330	99.6726	4.2	mb	11.0	l	4.0	4.0	23	2.07	113	5.06	32.9
2014	5	5	12	20	56.98	19.7925	99.6382	4	mb	5.0	l	4.0	4.0	22	1.96	112	3.81	23.5
2014	5	5	13	34	27.84	19.7376	99.6143	4	mb	13.0	l	4.0	4.0	38	1.49	128	1.87	8.7
2014	5	5	19	12	3.70	19.7914	99.6748	4.1	mb	11.0	l	4.0	4.0	43	0.98	133	1.87	5.8
2014	5	5	20	5	22.30	19.7264	99.5035	4	mb	10.0	l	4.0	4.0	30	1.50	120	2.12	10.0
2014	5	5	21	17	2.09	19.7431	99.6122	4.2	mb	11.0	l	4.0	4.0	19	1.36	109	2.01	8.6
2014	5	5	23	4	54.90	19.6971	99.5198	4.2	mb	14.0	l	4.0	4.0	33	1.28	123	1.58	6.3
2014	5	6	0	50	15.88	19.7166	99.6265	4.9	mb	20.0	l	4.0	4.0	0	0.95	90	1.10	3.3
2014	5	6	0	58	19.43	19.6352	99.4386	5	mb	14.0	d	4.0	7.0	291	1.44	21	1.51	6.8
2014	5	6	12	42	10.53	19.7091	99.5698	3.8	mb	12.0	n	3.0	3.0	54	1.24	144	2.96	11.6
2014	5	6	13	5	14.71	19.6532	99.6628	3.4	ML	9.0	n	3.0	3.0	37	1.08	127	2.27	7.7
2014	5	6	13	47	0.87	19.7467	99.6270	3.8	mb	12.4	m	2.7	2.7	64	1.25	154	3.01	11.8
2014	5	6	14	50	12.01	19.7223	99.5449	4.3	mb	10.0	n	3.0	3.0	72	0.95	162	1.25	3.7
2014	5	6	15	37	41.52	19.6689	99.6693	3.3	ML	10.0	n	3.0	3.0	33	1.49	123	3.18	14.9
2014	5	6	15	57	30.82	19.7109	99.6186	4.3	ML	13.0	n	3.0	3.0	55	1.13	145	3.49	12.4
2014	5	6	16	9	58.19	19.7357	99.6487	3.4	ML	9.0	n	3.0	3.0	58	1.55	148	3.96	19.3
2014	5	6	16	25	37.45	19.7110	99.5467	3.2	ML	14.0	n	3.0	3.0	15	1.41	105	1.79	7.9
2014	5	6	17	21	5.67	19.6437	99.6750	2.6	ML	10.0	n	3.0	3.0	29	1.02	119	1.89	6.0
2014	5	6	18	29	36.95	19.7053	99.5662	3.7	ML	14.0	n	3.0	3.0	52	1.15	142	4.00	14.4
2014	5	6	20	18	26.33	19.6919	99.4952	3.4	ML	12.0	n	3.0	3.0	56	0.94	146	2.12	6.3
2014	5	6	20	52	26.53	19.6969	99.5435	4	mb	10.0	n	3.0	3.0	56	0.87	146	1.18	3.2
2014	5	6	22	7	5.50	19.6682	99.5083	3.6	ML	10.0	n	3.0	3.0	58	0.82	148	1.17	3.0
2014	5	7	11	39	9.89	19.6928	99.5593	3.3	ML	10.0	n	3.0	3.0	50	0.89	140	2.86	8.0
2014	5	7	14	3	11.16	19.6352	99.5061	2.7	ML	10.0	l	4.0	4.0	48	0.97	138	2.38	7.2

Continued on next page

Table 4.8 – *Continued from previous page*

Origin date and time						Latitude (°)	Longitude (°)	Mag.	Mag. type	Focal depth (km)	Depth code	Unc. (deeper, + km)	Unc. (shallower, − km)	Ell. short semi-axis		Long semi-axis		90% confidence ellipse area (km^2)
yyyy	mm	dd	Hr	Min	Sec									Az. (°)	Length (km)	Az. (°)	Length (km)	
2014	5	7	14	27	35.05	19.7446	99.5569	2.4	ML	13.0	n	3.0	3.0	58	1.02	148	3.19	10.2
2014	5	7	15	1	58.79	19.7061	99.5552	3.1	ML	14.0	n	3.0	3.0	54	1.30	144	1.95	8.0
2014	5	7	16	39	52.89	19.6669	99.5048	3.2	ML	12.0	n	3.0	3.0	52	0.79	142	1.59	4.0
2014	5	7	18	41	55.78	19.6809	99.4994	3.2	ML	11.0	n	3.0	3.0	55	0.85	145	1.24	3.3
2014	5	7	19	33	5.13	19.6439	99.6764	2.8	ML	12.0	n	3.0	3.0	22	1.13	112	1.50	5.4
2014	5	7	22	56	58.15	19.7591	99.6524	2.9	ML	13.0	n	3.0	3.0	58	1.25	148	3.38	13.2
2014	5	8	4	22	17.89	19.6960	99.6708	2.7	ML	9.0	n	3.0	3.0	38	1.50	128	2.84	13.4
2014	5	8	4	57	58.49	19.7358	99.6559	3.1	ML	11.0	n	3.0	3.0	53	1.25	143	2.69	10.5
2014	5	8	6	4	52.69	19.7480	99.6314	3.4	ML	10.2	m	3.0	3.0	60	1.38	150	3.88	16.8
2014	5	8	7	10	41.35	19.7286	99.5680	3.3	ML	13.4	m	3.0	3.0	55	0.89	145	2.42	6.7
2014	5	8	10	47	53.49	19.7461	99.6483	3.5	ML	7.0	n	3.0	3.0	61	1.11	151	3.02	10.6
2014	5	8	20	43	36.40	19.7525	99.6112	4	mb	18.0	n	3.0	3.0	53	0.82	143	1.75	4.5
2014	5	9	1	51	30.63	19.6953	99.5132	3.6	ML	13.6	m	1.8	1.8	49	0.98	139	2.58	7.9
2014	5	9	2	48	20.81	19.7895	99.6355	3.7	ML	10.6	m	1.5	1.5	45	1.25	135	2.16	8.5
2014	5	9	3	58	11.68	19.7124	99.6672	3.3	ML	9.8	m	1.6	1.6	34	1.18	124	2.27	8.4
2014	5	9	7	12	29.39	19.7017	99.5234	4	mb	13.9	m	1.7	1.7	49	0.87	139	1.69	4.6
2014	5	9	7	30	17.77	19.7110	99.5380	3.1	ML	15.2	m	2.2	2.2	50	1.02	140	2.83	9.1
2014	5	9	9	53	4.71	19.7703	99.6598	3.5	ML	12.1	m	1.4	1.4	30	1.26	120	2.32	9.2
2014	5	9	10	58	58.52	19.7762	99.6499	3.2	ML	12.3	m	1.4	1.4	78	1.39	168	1.93	8.4
2014	5	9	14	9	27.12	19.7150	99.5608	2.7	ML	15.2	m	2.0	2.0	53	0.92	143	2.62	7.5
2014	5	9	15	30	25.93	19.7584	99.6621	2.6	ML	14.3	m	1.5	1.5	76	1.31	166	1.97	8.1
2014	5	10	5	58	56.25	19.6831	99.7088	3.4	ML	9.6	m	2.2	2.2	20	1.30	110	2.43	9.9
2014	5	10	8	56	0.33	19.6711	99.6908	3.1	ML	9.6	m	2.3	2.3	26	1.11	116	2.04	7.1
2014	5	10	13	14	53.10	19.7611	99.5597	3.1	ML	15.0	m	1.5	1.5	54	0.97	144	2.34	7.2
2014	5	11	9	23	1.70	19.7186	99.5336	3	ML	13.4	m	1.7	1.7	50	1.17	140	3.05	11.2
2014	5	11	10	14	31.46	19.7489	99.6608	2.6	ML	13.3	m	1.5	1.5	40	1.51	130	3.15	15.0
2014	5	12	2	47	24.72	19.6628	99.6745	4.1	ML	9.4	m	1.4	1.4	28	0.88	118	1.38	3.8
2014	5	12	4	44	20.23	19.7688	99.6763	3	ML	9.0	m	1.5	1.5	41	1.22	131	3.03	11.6
2014	5	12	5	46	38.00	19.7340	99.5927	4	ML	13.2	m	1.6	1.6	44	1.01	134	2.13	6.8
2014	5	12	11	5	28.53	19.7677	99.6634	4.3	mb	10.2	m	1.5	1.5	37	0.88	127	1.34	3.7
2014	5	12	14	42	18.09	19.6876	99.5422	3.6	ML	12.4	m	1.7	1.7	14	0.95	104	1.33	4.0
2014	5	12	15	17	22.73	19.7003	99.5435	3	ML	11.9	m	1.8	1.8	33	1.30	123	3.15	12.9
2014	5	12	17	14	23.68	19.7385	99.5833	3.2	ML	10.0	m	1.6	1.6	45	1.11	135	2.17	7.6
2014	6	9	12	59	25.96	20.6426	99.9132	4.2	mb	17.0	l	4.0	4.0	59	1.17	149	1.48	5.4
2014	8	24	22	32	45.49	19.6195	99.5210	4.5	mb	12.0	c	2.9	2.9	44	0.99	134	1.63	5.1
2015	5	24	6	27	31.34	20.5443	98.9920	4.3	mb	12.0	c	2.9	2.9	354	1.36	84	2.49	10.6
2016	3	5	11	20	22.69	21.7264	101.3513	4.4	mb	12.0	c	2.9	2.9	18	1.66	108	2.41	12.5
2017	4	18	9	13	9.07	20.7177	100.2131	4.7	mb	18.0	l	4.0	4.0	27	1.15	117	2.12	7.7
2017	5	5	22	10	0.98	19.8686	101.4846	4.4	mb	13.0	l	4.0	4.0	47	1.69	137	2.75	14.6
2018	2	3	15	29	8.52	20.6365	99.4547	4.5	mb	7.0	l	4.0	4.0	318	1.59	48	2.02	10.1
2019	1	10	12	0	54.05	21.3286	101.7108	4.1	mb	12.0	c	2.9	2.9	53	1.69	143	2.05	10.9
2019	1	14	10	54	48.03	21.3296	101.7605	4.5	mb	12.0	c	2.9	2.9	27	1.56	117	2.70	13.2
2019	2	20	9	5	40.04	19.2443	99.6305	4.3	mb	12.0	l	4.0	4.0	31	1.06	121	1.95	6.5
2019	11	20	21	3	56.23	19.4447	101.2079	5.7	Mw	13.0	l	4.0	4.0	63	0.91	153	1.16	3.3

Continued on next page

Table 4.8 – *Continued from previous page*

Origin date and time						Latitude (°)	Longitude (°)	Mag.	Mag. type	Focal depth (km)	Depth code	Unc. (deeper, + km)	Unc. (shallower, − km)	Ell. short semi-axis		Long semi-axis		90% confidence ellipse area (km^2)
yyyy	mm	dd	Hr	Min	Sec									Az. (°)	Length (km)	Az. (°)	Length (km)	
2019	11	20	21	19	23.70	19.5364	101.3413	4.3	mb	13.0	l	4.0	4.0	333	1.31	63	1.68	6.9
2019	11	20	23	50	41.50	19.4823	101.3762	6.2	Mw	12.0	l	4.0	4.0	61	0.77	151	0.93	2.3
2019	11	21	0	57	13.74	19.4060	101.3889	4.3	mb	13.0	l	4.0	4.0	69	1.03	159	1.16	3.7
2019	11	21	1	14	41.34	19.4826	101.3605	4.2	mb	13.0	l	4.0	4.0	327	1.36	57	1.68	7.2
2019	11	21	2	23	55.52	19.4800	101.3054	3.5	mb	14.0	l	4.0	4.0	329	1.39	59	1.88	8.2
2019	11	21	2	37	31.93	19.5291	101.3472	3.8	M	5.0	l	4.0	4.0	322	1.48	52	2.51	11.7
2019	11	21	12	30	51.88	19.4975	101.3623	3.5	mb	11.0	l	4.0	4.0	337	1.25	67	1.77	6.9
2019	11	21	12	55	28.31	19.5188	101.3270	3.2	mb	11.0	l	4.0	4.0	333	1.18	63	2.16	8.0
2019	11	21	14	9	57.45	19.5262	101.2835	3.6	mb	13.0	l	4.0	4.0	324	1.25	54	2.73	10.7
2019	11	25	6	58	36.24	19.5399	101.2910	3.8	mb	12.0	l	4.0	4.0	346	1.20	76	1.25	4.7
2019	11	27	12	34	17.51	19.5326	101.3561	3.5	mb	10.0	l	4.0	4.0	338	1.30	68	2.31	9.4
2019	11	28	23	50	24.78	19.5453	101.3289	4.2	mb	12.0	l	4.0	4.0	344	1.08	74	1.31	4.4
2019	12	12	9	2	37.27	19.5539	101.2981	4	mb	11.0	l	4.0	4.0	2	1.18	92	1.60	5.9
2020	4	13	21	3	2.49	19.5759	101.3137	3.6	mb	12.0	l	4.0	4.0	324	1.23	54	1.49	5.7
2020	4	13	22	37	2.20	19.6007	101.3394	3.4	mb	9.0	l	4.0	4.0	331	1.66	61	2.49	13.0
2021	7	7	6	43	49.36	19.6339	101.0557	4.7	mb	18.0	l	4.0	4.0	28	1.86	118	3.35	19.6
2021	10	29	19	3	28.34	19.5935	101.3555	4.3	mb	24.0	l	4.0	4.0	60	1.18	150	1.37	5.1
2021	10	31	3	4	52.60	19.5305	101.3388	4.6	mb	10.0	l	4.0	4.0	59	1.15	149	1.34	4.9
2021	12	19	21	6	12.20	19.5623	101.3079	5.4	mb	8.0	l	4.0	4.0	286	1.03	16	1.13	3.7
2022	6	8	3	26	29.32	21.1334	99.8928	4.2	mb	17.0	l	4.0	4.0	320	1.17	50	2.23	8.2
2022	6	29	18	54	42.52	21.1439	99.8703	4.7	mb	20.0	l	4.0	4.0	319	1.17	49	1.52	5.6
2022	7	21	16	40	8.58	21.1203	99.8795	4.9	mb	17.0	l	4.0	4.0	327	1.08	57	1.45	4.9
2022	7	21	17	7	25.71	21.1360	99.8424	5.6	mb	20.0	l	4.0	4.0	336	0.95	66	1.01	3.0
2022	7	21	18	18	53.33	21.0414	99.8057	4.1	mb	23.0	l	4.0	4.0	336	1.61	66	3.35	17.0
2022	7	21	20	0	36.86	21.1884	99.9743	4.4	mb	18.0	l	4.0	4.0	324	1.36	54	2.34	10.0
2022	7	21	22	22	10.89	21.1738	99.9028	4.9	mb	21.0	l	4.0	4.0	321	1.04	51	1.19	3.9
2022	7	24	13	11	12.47	21.2002	100.0118	4.6	mb	12.0	l	4.0	4.0	333	1.27	63	1.43	5.7
2022	7	26	11	51	13.51	21.1180	99.9431	4.2	mb	18.0	l	4.0	4.0	322	1.30	52	1.99	8.1
2022	7	26	12	28	43.46	21.0798	99.9061	4.1	mb	18.0	l	4.0	4.0	323	1.23	53	2.88	11.2
2022	7	26	13	28	56.05	21.1002	99.9512	4.3	mb	13.0	l	4.0	4.0	322	1.10	52	1.78	6.1
2022	7	29	9	58	45.66	21.0351	99.9397	4.8	mb	15.0	l	4.0	4.0	318	1.52	48	2.01	9.6
2022	7	29	10	17	21.83	21.0965	99.9476	4.7	mb	17.0	l	4.0	4.0	328	1.14	58	1.52	5.4
2022	8	1	16	3	49.85	21.1303	99.9497	4.5	mb	11.0	l	4.0	4.0	312	1.33	42	2.27	9.5
2022	10	11	17	32	44.14	21.1420	99.8707	4.6	mb	17.0	l	4.0	4.0	330	1.46	60	1.76	8.0
2023	1	16	21	57	1.02	21.1503	99.8967	4.3	mb	12.0	l	4.0	4.0	334	1.95	64	3.90	23.9
2023	2	16	1	0	0.29	21.2587	100.0537	4.4	mb	13.0	l	4.0	4.0	342	2.06	72	4.82	31.2
2023	6	9	19	35	12.91	21.1714	99.9544	4.3	mb	14.0	l	4.0	4.0	301	1.37	31	1.93	8.3
2023	6	30	16	46	51.69	21.1385	99.5215	4.1	mb	12.0	c	2.9	2.9	2	1.53	92	4.19	20.2
2023	8	2	10	56	57.59	21.1815	99.9822	3.9	mb	12.0	l	4.0	4.0	286	1.94	16	2.66	16.2
2023	11	17	1	37	8.88	21.2104	99.2701	5.6	M	14.0	l	4.0	4.0	83	0.97	173	1.35	4.1
2023	11	17	6	2	19.72	21.1680	99.3400	4.5	mb	14.0	l	4.0	4.0	48	1.50	138	1.84	8.7

Chapter 5

Conclusions

Earthquakes on structurally immature faults do not always rupture fully to the surface. They may be completely buried, or otherwise part of the offset is often accommodated by deformation distributed up to several kilometers from the primary fault trace (e.g., Dolan and Haravitch, 2014; Zinke et al., 2015). This poses challenges to traditional field-based methods for documenting earthquake surface deformation, which could conceivably neglect the off-fault component altogether. In this dissertation, I have demonstrated how satellite-borne Interferometric Synthetic Aperture Radar (InSAR) can reveal new details of these buried ruptures and the faults that host them. In Chapter 2, I showed how coseismic InSAR signals form deformation lobes that are diagnostic of the responsible earthquake, including butterfly patterns for E–W strike-slip earthquakes and four-leaf clover patterns for N–S strike-slip earthquakes. These, respectively, are the patterns characteristic of InSAR signals of my two main case studies: the 2020 M_w 6.5 Monte Cristo Range earthquake in the Mina Deflection Zone of Nevada (the focus of Chapter 3), and the 2019 M_w 6.2 Sainyabuli earthquake in the southern Shan Plateau of Laos (the largest investigated in Chapter 4). Both these earthquakes struck regions distinguished by low levels of background seismicity and, in the latter case, a paucity of prior knowledge about active faulting.

I used Sentinel-1 InSAR imagery to map surface deformation in these two earthquakes, and then inverted these displacements to solve for their geometries and slip distributions. This modelling revealed a particularly complex fault configuration for the Monte Cristo Range earthquake: a longer left-lateral fault that crosses a shorter left-lateral/normal fault at an oblique angle. Relocated aftershocks and their diverse moment tensors appear to confirm this unusual geometry. The Monte Cristo Range earthquake is thus an exceedingly rare case of a pair of crossing faults rupturing together in a single earthquake. In

the Golden Triangle border region of Laos, Thailand, and Myanmar, I was able to exploit Sentinel-1's short revisit times to form coherent interferograms in spite of dense rainforest and mountainous topography. In addition to my InSAR model of the 2019 Sainyabuli earthquake, I detected and partially characterized two smaller earthquakes of M_w 5.5 and 5.9. By tying these to regional earthquake relocations, I made inferences about several earlier earthquakes of note.

Some rupture behaviours common to the Monte Cristo Range and Sainyabuli earthquakes may be more broadly diagnostic of immature faults. Both generated significant off-fault deformation, manifest as aftershock clouds within the rock volume up to 5–10 km from the main fault traces, as well as surface cracks with offsets of up to 20 cm in the Monte Cristo Range earthquake. The shallow slip deficit (SSD) is often considered an indicator of structural immaturity (e.g., Dolan and Haravitch, 2014). Both the Monte Cristo Range and Sainyabuli mainshocks exhibited peak slip of $\sim$1 m at depths of a few kilometers, with only a few tens of centimeters of slip reaching the surface, resulting in SSD values of 80–90%. However, a meta-analysis of published InSAR models of twenty-seven other continental strike-slip earthquakes, presented in Chapter 3, suggests that this behavior is typical for earthquakes smaller than M_w $\sim$7, regardless of the fault structural maturity. Only when magnitudes exceed this threshold do ruptures propagate fully to the surface with any consistency. Perhaps SSD serves as a more meaningful parameter for inferring surface rupture expectations for earthquakes of certain magnitudes. This may be an important consideration for interpreting fault offsets in paleoseismic trenches and for consideration of ground rupture hazards.

The Monte Cristo Range and Sainyabuli earthquakes both occurred on faults with negligible topographic expressions, at least at the spatial resolution of global DEMs. The former earthquake ruptured through low relief desert wash and alluvium that appears absent of geomorphic signatures of active faulting. Upon excavation of a paleoseismic trench across the fresh surface rupture, we did uncover evidence for previous earthquakes, but with offsets of only a few centimeters. The fault surface trace cuts ridges and bedrock boundaries that hint at a cumulative offset of 600–700 m. In contrast, the Golden Triangle region exhibits steep mountainous topography, but the Sainyabuli earthquake fault does not align with any prominent topographic features. One of the smaller earthquakes we detected with InSAR in this region, near Keng Tung, Myanmar, does appear to follow a structural grain evident in the topography, suggesting that not all faults that *could* be mapped in the region *have* been mapped. Both the Mina Deflection Zone and the Shan Plateau are thought to deform via vertical-axis rotations of fault-bound blocks, driven by

distributed shear between the Pacific and North American Plates (Pierce et al., 2021) and by extrusion around the eastern Himalayan syntaxis (Shi et al., 2018), respectively. These rotations may gradually divert currently active faults away from being favorably oriented to slip, preventing a through-going, structurally mature fault system from developing.

Another common thread to Chapters 3 and 4 is that our understanding of earthquake sequences is further enhanced by incorporating state-of-the-art seismological techniques alongside our InSAR slip models. Waveform models provide an independent check on earthquake source geometries and centroid depths, while multi-event hypocentral relocations can illuminate mainshock rupture directivity as well as aftershock distributions. The latter technique is particularly synergistic with the InSAR modelling. In the Monte Cristo Range earthquake—where close in phase arrival time data were available allowing for precise focal depth determination—the relocation results were used to fix the fault bottom depth in the InSAR model, which would otherwise be the most poorly-constrained parameter (e.g., Elliott et al., 2012). In our regional study of the Golden Triangle region—where seismograph stations are much sparser leaving large azimuthal gaps—our InSAR model faults aid in validating epicentral distributions from the relocation. Through the integration of InSAR and seismological models, we were also able to infer the local seismogenic thickness which is vital for seismic hazard assessments. Our calibrated clusters suggested a seismogenic thickness of $\sim$15 km in the Mina Deflection Zone, as inferred from the deepest aftershock. For the Golden Triangle region, we adopted the 90% seismicity cut-off depth to estimate a seismogenic thickness of $\sim$17 km, significantly deeper than the value supported by InSAR slip distributions alone (Feng et al., 2013; Wang et al., 2014a). This is the first study to establish comprehensively the seismogenic thickness of the Golden Triangle region.

Although the Monte Cristo Range earthquake occurred in a remote area and did little damage, studying its characteristics still offers valuable insights into the rupture behaviour of emergent faults. The proximity of the earthquakes studied in the Golden Triangle region to river communities, hydroelectric dams along the Mekong River, and a UNESCO World Heritage Site highlights the urgency of recognizing immature faults in seismic hazard assessments. The geometries of newly-discovered faults responsible for these earthquakes, alongside our regional estimates of seismogenic thickness, could be added to future seismic hazard calculations. However, other important parameters (such as fault slip rates) are much harder to assess for faults with little geomorphic expression.

More broadly, my dissertation highlights how, even in regions containing mature faults that are well-expressed in the topography (such as those along NW trends in the

Eastern California Shear Zone/Walker Lane and those along NE trends across the Shan Plateau), hidden, structurally-immature faults that pose significant ground shaking hazards are also likely to be present. In my view, it is simply not feasible to expect every structurally-immature fault to be identified prior to it rupturing in a large earthquake. However, this dissertation underscores the importance of observational earthquake research, where knowledge of rupture geometries and kinematics provides guidelines for defining seismic sources, their boundaries and rupture directivity, and for selecting appropriate ground motion models in local and regional seismic hazard assessments. In addition to recognizing the possibility of unmapped faults, this broader depiction of potential seismic activity may better encompass off-fault damage. For site-specific seismic hazard assessments, engineers can leverage detailed earthquake investigations, such as ours, to include any additional faults and understand their rupture behaviours beyond those documented by geological survey institutions. They can also use this information as guidance in selecting relevant ground motion time histories (e.g., with the appropriate magnitude, distance, and faulting mechanism) when time-history analyses are needed. Incorporating the possibility of sizeable earthquakes on hidden faults into structural design or retrofitting of critical infrastructure will enhance resilience and mitigate the potential for damage.

Bibliography

Aben, F. M., Doan, M. L., Mitchell, T. M., Toussaint, R., Reuschlé, T., Fondriest, M., Gratier, J. P., and Renard, F. (2016). Dynamic fracturing by successive coseismic loadings leads to pulverization in active fault zones. *Journal of Geophysical Research: Solid Earth*, 121(4):2338–2360.

Aderhold, K. and Abercrombie, R. E. (2015). Seismic Rupture on an Oceanic-Continental Plate Boundary: Strike-Slip Earthquakes along the Queen Charlotte-Fairweather Fault. *Bulletin of the Seismological Society of America*, 105(2B):1129–1142.

Albuquerque Seismological Laboratory (ASL)/USGS (1992). New china digital seismograph network.

Albuquerque Seismological Laboratory/USGS (2014). Global seismograph network (gsn - iris/usgs).

Amoruso, A., Crescentini, L., and Fidani, C. (2004). Effects of crustal layering on source parameter inversion from coseismic geodetic data. *Geophysical Journal International*, 159(1):353–364.

Aziz Zanjani, A., Ghods, A., Sobouti, F., Bergman, E., Mortezanejad, G., Priestley, K., Madanipour, S., and Rezaeian, M. (2013). Seismicity in the western coast of the South Caspian Basin and the Talesh Mountains. *Geophysical Journal International*, 195(2):799–814.

Baize, S., Amoroso, S., Belić, N., Benedetti, L., Boncio, P., Budić, M., Cinti, F. R., Henriquet, M., Jamšek Rupnik, P., Kordić, B., Markušić, S., Minarelli, L., Pantosti, D., Pucci, S., Špelić, M., Testa, A., Valkaniotis, S., Vukovski, M., Atanackov, J., Barbača, J., Bavec, M., Brajkovič, R., Brčić, V., Caciagli, M., Celarc, B., Civico, R., De Martini, P. M., Filjak, R., Iezzi, F., Moulin, A., Kurečić, T., Métois, M., Nappi, R., Novak, A., Novak, M., Pace, B., Palenik, D., and Ricci, T. (2022). Environmental effects and seismogenic source characterization of the December 2020 earthquake sequence near Petrinja, Croatia. *Geophysical Journal International*, 230(2):1394–1418.

Barbot, S., Fialko, Y., and Sandwell, D. (2008). Effect of a compliant fault zone on the inferred earthquake slip distribution. *Journal of Geophysical Research: Solid Earth*, 113(B6):B06404.

Barnhart, W. D., Hayes, G. P., and Gold, R. D. (2019a). The July 2019 Ridgecrest, California, Earthquake Sequence: Kinematics of Slip and Stressing in Cross-Fault Ruptures. *Geophysical Research Letters*, 46(21):11,859–11,867.

Barnhart, W. D., Hayes, G. P., and Wald, D. J. (2019b). Global Earthquake Response with Imaging Geodesy: Recent Examples from the USGS NEIC. *Remote Sensing*, 11(11):1357.

Bennett, R. A., Wernicke, B. P., Niemi, N. A., Friedrich, A. M., and Davis, J. L. (2003). Contemporary strain rates in the northern Basin and Range province from GPS data. *Tectonics*, 22(2):1008.

Benz, H. M. (2021). Global catalog of calibrated earthquake locations. *US Geological Survey Data Release*.

Berberian, M., Jackson, J. A., Fielding, E., Parsons, B. E., Priestley, K., Qorashi, M., Talebian, M., Walker, R., Wright, T. J., and Baker, C. (2001). The 1998 March 14 Fandoqa earthquake (M_w 6.6) in Kerman province, southeast Iran: re-rupture of the 1981 Sirch earthquake fault, triggering of slip on adjacent thrusts and the active tectonics of the Gowk fault zone. *Geophysical Journal International*, 146(2):371–398.

Bergman, E. A., Benz, H. M., Yeck, W. L., Karasözen, E., Engdahl, E. R., Ghods, A., Hayes, G. P., and Earle, P. S. (2023). A Global Catalog of Calibrated Earthquake Locations. *Seismological Research Letters*, 94(1):485–495.

Bergman, E. A. and Solomon, S. C. (1990). Earthquake swarms on the Mid-Atlantic Ridge: Products of magmatism or extensional tectonics? *Journal of Geophysical Research: Solid Earth*, 95(B4):4943–4965.

Berryman, K. R., Cochran, U. A., Clark, K. J., Biasi, G. P., Langridge, R. M., and Villamor, P. (2012). Major Earthquakes Occur Regularly on an Isolated Plate Boundary Fault. *Science*, 336(6089):1690–1693.

Biggs, J., Bergman, E., Emmerson, B., Funning, G. J., Jackson, J., Parsons, B., and Wright, T. J. (2006). Fault identification for buried strike-slip earthquakes using InSAR: The 1994 and 2004 Al Hoceima, Morocco earthquakes. *Geophysical Journal International*, 166(3):1347–1362.

Bilham, R. (2009). The seismic future of cities. *Bulletin of Earthquake Engineering*, 7(4):839–887.

Blewitt, G., Hammond, W. C., and Kreemer, C. (2018). Harnessing the GPS data explosion for interdisciplinary science. *Eos*, 99:485.

Boonchaisuk, S., Noisagool, S., Amatyakul, P., Rung-Arunwan, T., Vachiratienchai, C., and Siripunvaraporn, W. (2017). 3-D magnetotelluric imaging of the Phayao Fault Zone, Northern Thailand: Evidence for saline fluid in the source region of the 2014 Chiang Rai earthquake. *Journal of Asian Earth Sciences*, 147:210–221.

Bormann, J. M., Hammond, W. C., Kreemer, C., and Blewitt, G. (2016). Accommodation of missing shear strain in the Central Walker Lane, western North America: Constraints from dense GPS measurements. *Earth and Planetary Science Letters*, 440:169–177.

Bormann, J. M., Morton, E. A., Smith, K. D., Kent, G. M., Honjas, W. S., Plank, G. L., and Williams, M. C. (2021). Nevada Seismological Laboratory Rapid Seismic Monitoring Deployment and Data Availability for the 2020 M_{ww} 6.5 Monte Cristo Range, Nevada, Earthquake Sequence. *Seismological Research Letters*, 92(2A):810–822.

Bro, R. and De Jong, S. (1997). A fast non-negativity-constrained least squares algorithm. *Journal of Chemometrics*, 11(5):393–401.

Brodsky, E. E., Gilchrist, J. J., Sagy, A., and Collettini, C. (2011). Faults smooth gradually as a function of slip. *Earth and Planetary Science Letters*, 302(1–2):185–193.

Brooks, B. A., Minson, S. E., Glennie, C. L., Nevitt, J. M., Dawson, T., Rubin, R., Ericksen, T. L., Lockner, D., Hudnut, K., Langenheim, V., Lutz, A., Mareschal, M., Murray, J., Schwartz, D., and Zaccone, D. (2017). Buried shallow fault slip from the South Napa earthquake revealed by near-field geodesy. *Science Advances*, 3(7):e1700525.

Bürgmann, R., Rosen, P. A., and Fielding, E. J. (2000). Synthetic Aperture Radar Interferometry to Measure Earth's Surface Topography and Its Deformation. *Annual Review of Earth and Planetary Sciences*, 28:169–209.

Callaghan, E. and Gianella, V. P. (1935). The earthquake of January 30, 1934, at Excelsior Mountains, Nevada. *Bulletin of the Seismological Society of America*, 25(2):161–168.

Cao, S., Neubauer, F., Liu, J., Genser, J., and Leiss, B. (2011). Exhumation of the Diancang Shan metamorphic complex along the Ailao Shan-Red River belt, southwestern Yunnan, China: Evidence from ^{40}Ar/ ^{39}Ar thermochronology. *Journal of Asian Earth Sciences*, 42(3):525–550.

Çakir, Z., de Chabalier, J.-B., Armijo, R., Meyer, B., Barka, A., and Peltzer, G. (2003). Coseismic and early post-seismic slip associated with the 1999 Izmit earthquake (Turkey), from SAR interferometry and tectonic field observations. *Geophysical Journal International*, 155(1):93–110.

Chansom, C., Jitmahantakul, S., Owen, L. A., Wiwegwin, W., and Charusiri, P. (2022). New Insights Into the Paleoseismic History of the Mae Hong Son Fault, Northern Thailand. *Frontiers in Earth Science*, 10:921049.

Cheloni, D., Famiglietti, N. A., Tolomei, C., Caputo, R., and Vicari, A. (2024). The 8 September 2023, M_W 6.8, Morocco Earthquake: A Deep Transpressive Faulting Along the Active High Atlas Mountain Belt. *Geophysical Research Letters*, 51(2):e2023GL106992.

Chen, W.-P. and Molnar, P. (1990). Source parameters of earthquakes and intraplate deformation beneath the Shillong Plateau and the Northern Indoburman Ranges. *Journal of Geophysical Research: Solid Earth*, 95(B8):12,527–12,552.

Chen, Y. and Wu, F. T. (1989). Lancang—Gengma Earthquake: A Preliminary Report on the November 6, 1988, Event and Its Aftershocks. *EOS Transactions*, 70(49):1527–1540.

Childs, C., Manzocchi, T., Walsh, J. J., Bonson, C. G., Nicol, A., and Schöpfer, M. P. J. (2009). A geometric model of fault zone and fault rock thickness variations. *Journal of Structural Geology*, 31(2):117–127.

Childs, C., Watterson, J., and Walsh, J. J. (1995). Fault overlap zones within developing normal fault systems. *Journal of the Geological Society*, 152(3):535–549.

Chounet, A., Vallée, M., Causse, M., and Courboulex, F. (2018). Global catalog of earthquake rupture velocities shows anticorrelation between stress drop and rupture velocity. *Tectonophysics*, 733:148–158.

Choy, G. L. and Kirby, S. H. (2004). Apparent stress, fault maturity and seismic hazard for normal-fault earthquakes at subduction zones. *Geophysical Journal International*, 159(3):991–1012.

Cole, J., McCabe, R., Moriarty, T., Malicse, J. A., Delfin, F. G., Tebar, H., and Ferrer, H. P. (1989). A preliminary Neogene paleomagnetic data set from Leyte and its relation to motion on the Philippine fault. *Tectonophysics*, 168(1):205–220.

Collettini, C. and Sibson, R. H. (2001). Normal faults, normal friction? *Geology*, 29(10):927.

Copley, A. (2008). Kinematics and dynamics of the southeastern margin of the Tibetan Plateau. *Geophysical Journal International*, 174(3):1081–1100.

Cui, Y., Ma, Z., Aoki, Y., Liu, J., Yue, D., Hu, J., Zhou, C., and Li, Z. (2021). Refining slip distribution in moderate earthquakes using Sentinel-1 burst overlap interferometry: a case study over 2020 May 15 M_w 6.5 Monte Cristo Range Earthquake. *Geophysical Journal International*, 229:472–486.

Dee, S., Koehler, R. D., Elliott, A. J., Hatem, A. E., Pickering, A., Pierce, I., Seitz, G. G., Collett, C. M., Dawson, T. E., De Masi, C., Craig, M. D., Hartsorn, E., Madugo, C., Trexler, C. C., Verdugo, D. M., Wesnousky, S. G., and Zachariasen, J. (2021). Surface rupture map of the 2020 M 6.5 Monte Cristo range earthquake, Esmeralda and Mineral counties, Nevada. Technical Report 190, University of Nevada, Reno, Reno, Nevada.

DeLano, K., Lee, J., Roper, R., and Calvert, A. (2019). Dextral, normal, and sinistral faulting across the eastern California shear zone-Mina deflection transition, California-Nevada, USA. *Geosphere*, 15(4):1206–1239.

Department of Meteorology and Hydrology - National Earthquake Data Center (2016). Myanmar national seismic network.

Dohrenwend, J. C. (1982). Surficial geologic map of the Walker Lake 1 degree × 2 degrees quadrangle, Nevada-California. Technical Report Miscellaneous Field Studies Map MF-1382-C, U.S. Geological Survey, Denver, Colorado.

Dokka, R. K. and Travis, C. J. (1990). Role of the Eastern California Shear Zone in accommodating Pacific-North American Plate motion. *Geophysical Research Letters*, 17(9):1323–1326.

Dolan, J. F. and Haravitch, B. D. (2014). How well do surface slip measurements track slip at depth in large strike-slip earthquakes? The importance of fault structural maturity in controlling on-fault slip versus off-fault surface deformation. *Earth and Planetary Science Letters*, 388:38–47.

Duman, T. Y., Çan, T., Emre, Ö., Kadirioğlu, F. T., Başarır Baştürk, N., Kılıç, T., Arslan, S., Özalp, S., Kartal, R. F., Kalafat, D., Karakaya, F., Eroğlu Azak, T., Özel, N. M., Ergintav, S., Akkar, S., Altınok, Y., Tekin, S., Cingöz, A., and Kurt, A. İ. (2018). Seismotectonic database of Turkey. *Bulletin of Earthquake Engineering*, 16(8):3277–3316.

Duman, T. Y. and Emre, O. (2013). The East Anatolian Fault: geometry, segmentation and jog characteristics. *Geological Society of London Special Publications*, 372(1):495–529.

Dziewonski, A. M., Chou, T. A., and Woodhouse, J. H. (1981). Determination of earthquake source parameters from waveform data for studies of global and regional seismicity. *Journal of Geophysical Research: Solid Earth*, 86(B4):2825–2852.

Eisbacher, G. H. (1976). Sedimentology of the Dezadeash flysch and its implications for strike-slip faulting along the Denali Fault, Yukon Territory and Alaska. *Canadian Journal of Earth Sciences*, 13(11):1495–1513.

Ekström, G., Nettles, M., and Dziewoński, A. M. (2012). The global CMT project 2004-2010: Centroid-moment tensors for 13,017 earthquakes. *Physics of the Earth and Planetary Interiors*, 200:1–9.

Elliott, J. R., Biggs, J., Parsons, B., and Wright, T. J. (2008). InSAR slip rate determination on the Altyn Tagh Fault, northern Tibet, in the presence of topographically correlated atmospheric delays. *Geophysical Research Letters*, 35(12):L12309.

Elliott, J. R., Nissen, E. K., England, P. C., Jackson, J. A., Lamb, S., Li, Z., Oehlers, M., and Parsons, B. (2012). Slip in the 2010-2011 Canterbury earthquakes, New Zealand. *Journal of Geophysical Research: Solid Earth*, 117(B3):B03401.

Elliott, J. R., Parsons, B., Jackson, J. A., Shan, X., Sloan, R. A., and Walker, R. T. (2011). Depth segmentation of the seismogenic continental crust: The 2008 and 2009 Qaidam earthquakes. *Geophysical Research Letters*, 38(6):L06305.

Elliott, J. R., Walters, R. J., and Wright, T. J. (2016). The role of space-based observation in understanding and responding to active tectonics and earthquakes. *Nature Communications*, 7:13844.

Ellis, S., Bannister, S., Van Dissen, R., Eberhart-Phillips, D., Boulton, C., Reyners, M., Funnell, R., Mortimer, N., Upton, P., Rollins, C., and Seebeck, H. (2023). New Zealand Fault-Rupture Depth Model v.1.0: A Provisional Estimate of the Maximum Depth of Seismic Rupture on New Zealand's Active Faults. *The Bulletin of the Seismological Society of America*, 114(1):78–94.

Engdahl, E. R., Di Giacomo, D., Sakarya, B., Gkarlaouni, C. G., Harris, J., and Storchak, D. A. (2020). ISC-EHB 1964-2016, an Improved Data Set for Studies of Earth Structure and Global Seismicity. *Earth and Space Science*, 7(1):e00897.

Engdahl, E. R., van der Hilst, R., and Buland, R. (1998). Global teleseismic earthquake relocation with improved travel times and procedures for depth determination. *The Bulletin of the Seismological Society of America*, 88(3):722–743.

England, P. and Jackson, J. (2011). Uncharted seismic risk. *Nature Geoscience*, 4(6):348–349.

European Space Agency (n.d.). European Remote Sensing Satellite (ERS) Radar Course 2. `https://earth.esa.int/eogateway/missions/ers/radar-courses/radar-course-2`. Accessed on May 19, 2024.

European Space Agency (n.d.). S1 Mission, Interferometric Wide Swath. `https://sentiwiki.copernicus.eu/web/s1-mission#S1Mission-InterferometricWideSwathS1-Mission-Interferometric-Wide-Swath`. Accessed on May 15, 2024.

Fadil, W., Wei, S., Bradley, K., Wang, Y., He, Y., Sandvol, E., Huang, B.-S., Hubbard, J., Thant, M., and Htwe, Y. M. M. (2023). Active Faults Revealed and New Constraints on Their Seismogenic Depth from a High-Resolution Regional Focal Mechanism Catalog in Myanmar (2016–2021). *The Bulletin of the Seismological Society of America*, 113(2):613–635.

Fang, J., Houseman, G. A., Wright, T., Evans, L., Craig, T. J., Elliott, J. R., and Hooper, A. (2024). The Dynamics of the India-Eurasia Collision: Faulted Viscous Continuum Models Constrained by High-Resolution Sentinel-1 InSAR and GNSS Velocities. *Journal of Geophysical Research: Solid Earth*, 129(6):e2023JB028571.

Farr, T. G. and Kobrick, M. (2000). Shuttle radar topography mission produces a wealth of data. *EOS Transactions*, 81(48):583–585.

Farr, T. G., Rosen, P. A., Caro, E., Crippen, R., Duren, R., Hensley, S., Kobrick, M., Paller, M., Rodriguez, E., Roth, L., Seal, D., Shaffer, S., Shimada, J., Umland, J., Werner, M., Oskin, M., Burbank, D., and Alsdorf, D. (2007). The Shuttle Radar Topography Mission. *Reviews of Geophysics*, 45(2):RG2004.

Faulkner, D. R., Mitchell, T. M., Jensen, E., and Cembrano, J. (2011). Scaling of fault damage zones with displacement and the implications for fault growth processes. *Journal of Geophysical Research: Solid Earth*, 116(B5):B05403.

Feng, L., Newman, A. V., Farmer, G. T., Psimoulis, P., and Stiros, S. C. (2010). Energetic rupture, coseismic and post-seismic response of the 2008 M_W 6.4 Achaia-Elia Earthquake in northwestern Peloponnese, Greece: an indicator of an immature transform fault zone. *Geophysical Journal International*, 183(1):103–110.

Feng, W., Li, Z., Elliott, J. R., Fukushima, Y., Hoey, T., Singleton, A., Cook, R., and Xu, Z. (2013). The 2011 M_W 6.8 Burma earthquake: fault constraints provided by multiple SAR techniques. *Geophysical Journal International*, 195(1):650–660.

Feng, W., Tian, Y., Zhang, Y., Samsonov, S., Almeida, R., and Liu, P. (2017). A slip gap of the 2016 M_w 6.6 Muji, Xinjiang, China, earthquake inferred from Sentinel-1 TOPS interferometry. *Seismological Research Letters*, 88(4):1054–1064.

Ferguson, H. G., Muller, S. W., and Cathcart, S. H. (1953). Geology of the Coaldale quadrangle, Nevada. Technical Report Geologic Quadrangle Map GQ-23, U.S. Geological Survey, Denver, Colorado.

Ferguson, H. G., Muller, S. W., and Cathcart, S. H. (1954). Geology of the Mina quadrangle, Nevada. Technical Report Geologic Quadrangle Map GQ-45, U.S. Geological Survey, Denver, Colorado.

Fialko, Y., Sandwell, D., Simons, M., and Rosen, P. (2005). Three-dimensional deformation caused by the Bam, Iran, earthquake and the origin of shallow slip deficit. *Nature*, 435(7040):295–299.

Fielding, E. J., Lundgren, P. R., Bürgmann, R., and Funning, G. J. (2009). Shallow fault-zone dilatancy recovery after the 2003 Bam earthquake in Iran. *Nature*, 458(7234):64–68.

Fielding, E. J., Talebian, M., Rosen, P. A., Nazari, H., Jackson, J. A., Ghorashi, M., and Walker, R. (2005). Surface ruptures and building damage of the 2003 Bam, Iran, earthquake mapped by satellite synthetic aperture radar interferometric correlation. *Journal of Geophysical Research: Solid Earth*, 110(B3):B03302.

Finzi, Y., Hearn, E. H., Ben-Zion, Y., and Lyakhovsky, V. (2009). Structural Properties and Deformation Patterns of Evolving Strike-slip Faults: Numerical Simulations Incorporating Damage Rheology. *Pure and Applied Geophysics*, 166(10–11):1537–1573.

Fletcher, J. M., Teran, O. J., Rockwell, T. K., Oskin, M. E., Hudnut, K. W., Mueller, K. J., Spelz, R. M., Akciz, S. O., Masana, E., Faneros, G., Fielding, E. J., Leprince, S., Morelan, A. E., Stock, J., Lynch, D. K., Elliott, A. J., Gold, P., Liu-Zeng, J., González-Ortega, A., Hinojosa-Corona, A., and González-García, J. (2014). Assembly of a large earthquake from a complex fault system: Surface rupture kinematics of the 4 April 2010 El Mayor-Cucapah (Mexico) M_w 7.2 earthquake. *Geosphere*, 10(4):797–827.

Floyd, M. A., Walters, R. J., Elliott, J. R., Funning, G. J., Svarc, J. L., Murray, J. R., Hooper, A. J., Larsen, Y., Marinkovic, P., Bürgmann, R., Johanson, I. A., and Wright, T. J.

(2016). Spatial variations in fault friction related to lithology from rupture and afterslip of the 2014 South Napa, California, earthquake. *Geophysical Research Letters*, 43(13):6808–6816.

Frost, E., Dolan, J., Sammis, C., Hacker, B., Cole, J., and Ratschbacher, L. (2009). Progressive strain localization in a major strike-slip fault exhumed from midseismogenic depths: Structural observations from the Salzach-Ennstal-Mariazell-Puchberg fault system, Austria. *Journal of Geophysical Research: Solid Earth*, 114(B4):B04406.

Fu, B. and Awata, Y. (2007). Displacement and timing of left-lateral faulting in the Kunlun Fault Zone, northern Tibet, inferred from geologic and geomorphic features. *Journal of Asian Earth Sciences*, 29(2–3):253–265.

Funning, G. J. and Cockett, R. (2012). Visible Earthquakes: a web-based tool for visualizing and modeling InSAR earthquake data. In *AGU Fall Meeting Abstracts*, volume 2012, pages ED43E–06.

Funning, G. J. and Garcia, A. (2019). A systematic study of earthquake detectability using Sentinel-1 Interferometric Wide-Swath data. *Geophysical Journal International*, 216(1):332–349.

Funning, G. J., Parsons, B., and Wright, T. J. (2007). Fault slip in the 1997 Manyi, Tibet earthquake from linear elastic modelling of InSAR displacements. *Geophysical Journal International*, 169(3):988–1008.

Funning, G. J., Parsons, B., Wright, T. J., Jackson, J. A., and Fielding, E. J. (2005). Surface displacements and source parameters of the 2003 Bam (Iran) earthquake from Envisat advanced synthetic aperture radar imagery. *Journal of Geophysical Research: Solid Earth*, 110(B9):B09406.

Gao, H., Liao, M., Liang, X., Feng, G., and Wang, G. (2022). Coseismic and Postseismic Fault Kinematics of the July 22, 2020, Nima (Tibet) Ms6.6 Earthquake: Implications of the Forming Mechanism of the Active N-S-Trending Grabens in Qiangtang, Tibet. *Tectonics*, 41(3):e2021TC006949.

Gaudemer, Y., Tapponnier, P., Meyer, B., Peltzer, G., Shunmin, G., Zhitai, C., Huagung, D., and Cifuentes, I. (1995). Partitioning of crustal slip between linked, active faults in the eastern Qilian Shan, and evidence for a major seismic gap, the 'Tianzhu gap', on the western Haiyuan Fault, Gansu (China). *Geophysical Journal International*, 120(3):599–645.

Gaudreau, É., Hollingsworth, J., Nissen, E., and Funning, G. J. (2023). Complex 3-D Surface Deformation in the 1971 San Fernando, California Earthquake Reveals Static and Dynamic Controls on Off-Fault Deformation. *Journal of Geophysical Research: Solid Earth*, 128(3):e2022JB024985.

Gaudreau, É., Nissen, E. K., Bergman, E. A., Benz, H. M., Tan, F., and Karasözen, E. (2019). The August 2018 Kaktovik Earthquakes: Active Tectonics in Northeastern Alaska Revealed With InSAR and Seismology. *Geophysical Research Letters*, 46(24):14,412–14,420.

GEOFON Data Centre (1993). Geofon seismic network.

Gold, R. D., DuRoss, C. B., and Barnhart, W. D. (2021). Coseismic Surface Displacement in the 2019 Ridgecrest Earthquakes: Comparison of Field Measurements and Optical Image Correlation Results. *Geochemistry, Geophysics, Geosystems*, 22(3):e09326.

Goldstein, R. M. and Werner, C. L. (1998). Radar interferogram filtering for geophysical applications. *Geophysical Research Letters*, 25(21):4035–4038.

Golshadi, Z., Famiglietti, N. A., Caputo, R., SoltaniMoghadam, S., Karimzadeh, S., Memmolo, A., Falco, L., and Vicari, A. (2023). Contemporaneous Thick- and Thin-Skinned Seismotectonics in the External Zagros: The Case of the 2021 Fin Doublet, Iran. *Remote Sensing*, 15(12):2981.

Gomberg, J. (1996). Stress/strain changes and triggered seismicity following the M_w 7.3 Landers, California earthquake. *Journal of Geophysical Research: Solid Earth*, 101(B1):751–764.

Grondin, D. P., Petronis, M., Lindline, J., and Romero, B. P. (2016). Vertical axis clockwise rotation of fault blocks in the eastern Mono Basin, California and Nevada. In *Geological Society of America Abstracts with Programs*, volume 48.

Guo, N., Wu, Y., Zhu, S., and Chen, C. (2024). Coseismic deformation and interseismic strain accumulation of the 2024 MS 7.1 Wushi earthquake in Xinjiang, China. *Advances in Space Research*, 74(4):1586–1594.

Hamling, I. J., Hreinsdóttir, S., Clark, K., Elliott, J., Liang, C., Fielding, E., Litchfield, N., Villamor, P., Wallace, L., Wright, T. J., D'Anastasio, E., Bannister, S., Burbidge, D., Denys, P., Gentle, P., Howarth, J., Mueller, C., Palmer, N., Pearson, C., Power, W., Barnes, P., Barrell, D. J. A., Van Dissen, R., Langridge, R., Little, T., Nicol, A., Pettinga, J., Rowland, J., and Stirling, M. (2017). Complex multifault rupture during the 2016 M_w 7.8 Kaikōura earthquake, New Zealand. *Science*, 356(6334).

Hammond, W. C., Blewitt, G., Kreemer, C., Koehler, R. D., and Dee, S. (2021). Geodetic Observation of Seismic Cycles before, during, and after the 2020 Monte Cristo Range, Nevada Earthquake. *Seismological Research Letters*, 92(2A):647–662.

Hatem, A. E., Cooke, M. L., and Toeneboehn, K. (2017). Strain localization and evolving kinematic efficiency of initiating strike-slip faults within wet kaolin experiments. *Journal of Structural Geology*, 101:96–108.

He, Y., Wang, T., and Zhao, L. (2022). The 2021 Mw6.7 Lake Hovsgol (Mongolia) Earthquake: Irregular Normal Faulting with Slip Partitioning Controlled by an Adjacent Strike-Slip Fault. *Remote Sensing*, 14(18):4553.

Hearn, E. H. and Bürgmann, R. (2005). The Effect of Elastic Layering on Inversions of GPS Data for Coseismic Slip and Resulting Stress Changes: Strike-Slip Earthquakes. *Bulletin of the Seismological Society of America*, 95(5):1637–1653.

Hecker, S., Dawson, T. E., and Schwartz, D. P. (2010). Normal-Faulting Slip Maxima and Stress-Drop Variability: A Geological Perspective. *Bulletin of the Seismological Society of America*, 100(6):3130–3147.

Heimann, S., Isken, M., Kühn, D., Sudhaus, H., Steinberg, A., Daout, S., Cesca, S., Bathke, H., and Dahm, T. (2018). Grond: A probabilistic earthquake source inversion framework.

Herrmann, R. B., Benz, H., and Ammon, C. J. (2011). Monitoring the Earthquake Source Process in North America. *Bulletin of the Seismological Society of America*, 101(6):2609–2625.

Hicks, S. P. and Rietbrock, A. (2015). Seismic slip on an upper-plate normal fault during a large subduction megathrust rupture. *Nature Geoscience*, 8(12):955–960.

Hodgkinson, K. M., Stein, R. S., and King, G. C. P. (1996). The 1954 Rainbow Mountain-Fairview Peak-Dixie Valley earthquakes: A triggered normal faulting sequence. *Journal of Geophysical Research: Solid Earth*, 101(B11):25459–25471.

Holt, W. E., Ni, J. F., Wallace, T. C., and Haines, A. J. (1991). The active tectonics of the eastern Himalayan syntaxis and surrounding regions. *Journal of Geophysical Research: Solid Earth*, 96(B9):14,595–14,632.

Huang, M. H., Fielding, E. J., Dickinson, H., Sun, J., Gonzalez-Ortega, J. A., Freed, A. M., and Bürgmann, R. (2017). Fault geometry inversion and slip distribution of the 2010 M_w 7.2 El Mayor-Cucapah earthquake from geodetic data. *Journal of Geophysical Research: Solid Earth*, 122(1):607–621.

Huang, M.-H., Tung, H., Fielding, E. J., Huang, H.-H., Liang, C., Huang, C., and Hu, J.-C. (2016). Multiple fault slip triggered above the 2016 M_w 6.4 MeiNong earthquake in Taiwan. *Geophysical Research Letters*, 43(14):7459–7467.

Hudnut, K. W., Seeber, L., and Pacheco, J. (1989). Cross-fault triggering in the November 1987 Superstition Hills Earthquake Sequence, southern California. *Geophysical Research Letters*, 16(2):199–202.

Hull, J. (1988). Thickness-displacement relationships for deformation zones. *Journal of Structural Geology*, 10(4):431–435.

Hutchison, A. A., Böse, M., and Manighetti, I. (2020). Improving Early Estimates of Large Earthquake's Final Fault Lengths and Magnitudes Leveraging Source Fault Structural Maturity Information. *Geophysical Research Letters*, 47(14):e87539.

International Seismological Centre (2023). ISC-EHB dataset.

Jachens, R. C. (2002). Relationship of the 1999 Hector Mine and 1992 Landers Fault Ruptures to Offsets on Neogene Faults and Distribution of Late Cenozoic Basins in the Eastern California Shear Zone. *Bulletin of the Seismological Society of America*, 92(4):1592–1605.

Jackson, J. (2001). Living with Earthquakes: Know your Faults. *Journal of Earthquake Engineering*, 5:5–123.

Jackson, J., Bouchon, M., Fielding, E., Funning, G., Ghorashi, M., Hatzfeld, D., Nazari, H., Parsons, B., Priestley, K., Talebian, M., Tatar, M., Walker, R., and Wright, T. (2006). Seismotectonic, rupture process, and earthquake-hazard aspects of the 2003 December 26 Bam, Iran, earthquake. *Geophysical Journal International*, 166(3):1270–1292.

Jafari, M., Aflaki, M., Mousavi, Z., Walpersdorf, A., and Motaghi, K. (2023). Coseismic and post-seismic characteristics of the 2021 Ganaveh earthquake along the Zagros foredeep fault based on InSAR data. *Geophysical Journal International*, 234(2):1125–1142.

Jamalreyhani, M., Pousse-Beltran, L., Hassanzadeh, M., Arabi, S. S., Bergman, E. A., Shamszadeh, A., Arvin, S., Fariborzi, N., and Songhori, A. (2023). Co-seismic slip of the 18 April 2021 Mw 5.9 Genaveh earthquake in the South Dezful Embayment of Zagros (Iran) and its aftershock sequence. *Seismica*, 2(1):246.

Ji, L., Wang, Q., Xu, J., and Ji, C. (2017). The July 11, 1995 Myanmar-China earthquake: A representative event in the bookshelf faulting system of southeastern Asia observed from JERS-1 SAR images. *International Journal of Applied Earth Observation and Geoinformation*, 55:43–51.

Jin, Z. and Fialko, Y. (2021). Coseismic and Early Postseismic Deformation Due to the 2021 M7.4 Maduo (China) Earthquake. *Geophysical Research Letters*, 48(21):e95213.

Johanson, I. A., Fielding, E. J., Rolandone, F., and Bürgmann, R. (2006). Coseismic and postseismic slip of the 2004 Parkfield earthquake from space-geodetic data. *Bulletin of the Seismological Society of America*, 96(4B):269–282.

Jones, L. E., Hough, S. E., and Helmberger, D. V. (1993). Rupture process of the June 28, 1992 Big Bear Earthquake. *Geophysical Research Letters*, 20(18):1907–1910.

Jongens, R., Barrell, D. J. A., Campbell, J. K., and Pettinga, J. R. (2012). Faulting and folding beneath the Canterbury Plains identified prior to the 2010 emergence of the Greendale Fault. *New Zealand Journal of Geology and Geophysics*, 55(3):169–176.

Jónsson, S., Zebker, H., Segall, P., and Amelung, F. (2002). Fault slip distribution of the 1999 M_w 7.1 Hector Mine, California, earthquake, estimated from satellite radar and GPS measurements. *Bulletin of the Seismological Society of America*, 92(4):1377–1389.

Jordan, T. H. and Sverdrup, K. A. (1981). Teleseismic location techniques and their application to earthquake clusters in the South-Central Pacific. *Bulletin of the Seismological Society of America*, 71(4):1105–1130.

Kane, D. L., Shearer, P. M., Goertz-Allmann, B. P., and Vernon, F. L. (2013). Rupture directivity of small earthquakes at Parkfield. *Journal of Geophysical Research: Solid Earth*, 118(1):212–221.

Kaneko, Y. and Fialko, Y. (2011). Shallow slip deficit due to large strike-slip earthquakes in dynamic rupture simulations with elasto-plastic off-fault response. *Geophysical Journal International*, 186(3):1389–1403.

Kaneko, Y., Lapusta, N., and Ampuero, J. P. (2008). Spectral element modeling of spontaneous earthquake rupture on rate and state faults: Effect of velocity-strengthening friction at shallow depths. *Journal of Geophysical Research: Solid Earth*, 113(B9):B09317.

Karasözen, E., Nissen, E., Bergman, E. A., and Ghods, A. (2019). Seismotectonics of the Zagros (Iran) From Orogen-Wide, Calibrated Earthquake Relocations. *Journal of Geophysical Research: Solid Earth*, 124(8):9109–9129.

Karasözen, E., Nissen, E., Bergman, E. A., Johnson, K. L., and Walters, R. J. (2016). Normal faulting in the Simav graben of western Turkey reassessed with calibrated earthquake relocations. *Journal of Geophysical Research: Solid Earth*, 121(6):4553–4574.

Karasözen, E., Nissen, E., Büyükakpınar, P., Cambaz, M. D., Kahraman, M., KalkanÂ Ertan, E., Abgarmi, B., Bergman, E., Ghods, A., and Özacar, A. A. (2018). The 2017 July 20 M_w 6.6 Bodrum-Kos earthquake illuminates active faulting in the Gulf of Gökova, SW Turkey. *Geophysical Journal International*, 214(1):185–199.

Kennedy, J., Anderson, R., Biessel, R., Chase, T., Ellis, O., Fairbanks, K., Fleming, C., Horn, W., Johnston, A., Kristenson, H., Logan, T., Meyer, F., Miller, R., Rine, J., Showalter, C., Short, G., Zhu, J., and Player, A. (2021). Skip the Processing: On Demand Analysis-Ready InSAR from ASF. In *AGU Fall Meeting Abstracts*, volume 2021, pages G45B–0395.

Kennett, B. L. N., Engdahl, E. R., and Buland, R. (1995). Constraints on seismic velocities in the Earth from traveltimes. *Geophysical Journal International*, 122(1):108–124.

Kim, T. and Han, H. (2023). Coseismic displacement fields and the slip mechanism of the 2021 Mw 6.7 Hovsgol earthquake in Mongolia constrained by Sentinel-1 and ALOS-2 InSAR. *GIScience & Remote Sensing*, 60(1):2180026.

Kobrick, M. (2006). On the toes of giants–how srtm was born. *Photogrammetric Engineering and Remote Sensing*, 72(3):206–210.

Koehler, R. D., Dee, S., Elliott, A., Hatem, A., Pickering, A., Pierce, I., and Seitz, G. (2021). Field Response and Surface-Rupture Characteristics of the 2020 M 6.5 Monte Cristo Range Earthquake, Central Walker Lane, Nevada. *Seismological Research Letters*, 92(2A):823–839.

Kreemer, C., Blewitt, G., and Klein, E. C. (2014). A geodetic plate motion and Global Strain Rate Model. *Geochemistry, Geophysics, Geosystems*, 15(10):3849–3889.

Kumar, A., Mitra, S., and Suresh, G. (2015). Seismotectonics of the eastern Himalayan and indo-burman plate boundary systems. *Tectonics*, 34(11):2279–2295.

Lacassin, R., Replumaz, A., and Hervé Leloup, P. (1998). Hairpin river loops and slip-sense inversion on southeast Asian strike-slip faults. *Geology*, 26(8):703–706.

Lasserre, C., Peltzer, G., Crampé, F., Klinger, Y., van der Woerd, J., and Tapponnier, P. (2005). Coseismic deformation of the 2001 M_w = 7.8 Kokoxili earthquake in Tibet, measured by synthetic aperture radar interferometry. *Journal of Geophysical Research: Solid Earth*, 110(B12):B12408.

Lauer, B., Grandin, R., and Klinger, Y. (2020). Fault Geometry and Slip Distribution of the 2013 Mw 7.7 Balochistan Earthquake From Inversions of SAR and Optical Data. *Journal of Geophysical Research: Solid Earth*, 125(7):e18380.

Lazecký, M., Spaans, K., González, P. J., Maghsoudi, Y., Morishita, Y., Albino, F., Elliott, J., Greenall, N., Hatton, E., Hooper, A., Juncu, D., McDougall, A., Walters, R. J., Watson, C. S., Weiss, J. R., and Wright, T. J. (2020). LiCSAR: An Automatic InSAR Tool for Measuring and Monitoring Tectonic and Volcanic Activity. *Remote Sensing*, 12(15):2430.

Le Dain, A. Y., Tapponnier, P., and Molnar, P. (1984). Active faulting and tectonics of Burma and surrounding regions. *Journal of Geophysical Research: Solid Earth*, 89(B1):453–472.

Lee, H. C. and Shyu, J. B. H. (2015). Co-seismic deformation of the 16 May 2007 Laos earthquake based on SAR interferometry analysis. In *EGU General Assembly Conference Abstracts*, EGU General Assembly Conference Abstracts, page 8680.

Lee, J., Garwood, J., Stockli, D. F., and Gosse, J. (2009). Quaternary faulting in Queen Valley, California-Nevada: Implications for kinematics of fault-slip transfer in the eastern California shear zone-Walker Lane belt. *Geological Society of America Bulletin*, 121(3–4):599–614.

Lee, J., Stockli, D., Schroeder, J., Tincher, C., Bradley, D., Owen, L., Gosse, J., Finkel, R., and Garwood, J. (2006). *Fault Slip Transfer in the Eastern California Shear Zone-Walker Lane Belt*. Geological Society of America Penrose Conference Field Trip Guide (Kinematics and Geodynamics of Intraplate Dextral Shear in Eastern California and Western Nevada, Mammoth Lakes, California, 21–26 April 2005).

Li, B., Li, Y., Jiang, W., Su, Z., and Shen, W. (2020a). Conjugate ruptures and seismotectonic implications of the 2019 Mindanao earthquake sequence inferred from Sentinel-1 InSAR data. *International Journal of Applied Earth Observation and Geoinformation*, 90:102127.

Li, C., Wang, X., He, C., Wu, X., Kong, Z., and Li, X. (2019). China National Digital Geological Map (Public Version at 1:200 000 Scale) Spatial Database. *Geology in China*, 46(S1):1–10.

Li, K., Li, Y., Tapponnier, P., Xu, X., Li, D., and He, Z. (2021a). Joint InSAR and Field Constraints on Faulting During the Mw 6.4, July 23, 2020, Nima/Rongma Earthquake in Central Tibet. *Journal of Geophysical Research: Solid Earth*, 126(9):e2021JB022212.

Li, K., Tapponnier, P., Xu, X., and Kang, W. (2023). The 2022, Ms 6.9 Menyuan earthquake: Surface rupture, Paleozoic suture re-activation, slip-rate and seismic gap along the Haiyuan fault system, NE Tibet. *Earth and Planetary Science Letters*, 622:118412.

Li, S., Deng, C., Yao, H., Huang, S., Liu, C., He, H., Pan, Y., and Zhu, R. (2013). Magnetostratigraphy of the Dali Basin in Yunnan and implications for late Neogene rotation of the southeast margin of the Tibetan Plateau. *Journal of Geophysical Research (Solid Earth)*, 118(3):791–807.

Li, S., Tao, T., Chen, Y., He, P., Gao, F., Qu, X., and Zhu, Y. (2021b). Geodetic Observation and Modeling of the Coseismic and Postseismic Deformations Associated With the 2020 Mw 6.5 Monte Cristo Earthquake. *Earth and Space Science*, 8(6):e01696.

Li, Y., Bürgmann, R., and Zhao, B. (2020b). Evidence of Fault Immaturity from Shallow Slip Deficit and Lack of Postseismic Deformation of the 2017 M_w 6.5 Jiuzhaigou Earthquake. *Bulletin of the Seismological Society of America*, 110(1):154–165.

Li, Z., Elliott, J. R., Feng, W., Jackson, J. A., Parsons, B. E., and Walters, R. J. (2011). The 2010 M_W 6.8 Yushu (Qinghai, China) earthquake: Constraints provided by InSAR and body wave seismology. *Journal of Geophysical Research: Solid Earth*, 116(B10):B10302.

Lindsey, E. O., Sahakian, V. J., Fialko, Y., Bock, Y., Barbot, S., and Rockwell, T. K. (2014). Interseismic Strain Localization in the San Jacinto Fault Zone. *Pure and Applied Geophysics*, 171(11):2937–2954.

Liu, C., Lay, T., Pollitz, F. F., Xu, J., and Xiong, X. (2021a). Seismic and Geodetic Analysis of Rupture Characteristics of the 2020 M_w 6.5 Monte Cristo Range, Nevada, Earthquake. *Bulletin of the Seismological Society of America*, 111(6):3226–3236.

Liu, G., Qiao, X., Yu, P., Zhou, Y., Zhao, B., and Xiong, W. (2021b). Rupture Kinematics of the 11 January 2021 Mw 6.7 Hovsgol, Mongolia, Earthquake and Implications in the Western Baikal Rift Zone. *Seismological Research Letters*, 92(6):3318–3326.

Liu, X., Xia, T., Liu-Zeng, J., Deng, D., Jia, Z., Wang, P., Yu, P., and Wang, W. (2023). Coseismic and early postseismic deformation of the 2020 Nima Mw 6.4 earthquake, central Tibet, from InSAR and GNSS observations. *Frontiers in Earth Science*, 10:1012773.

Liu, X., Xu, W., Radziminovich, N. A., Fang, N., and Xie, L. (2022). Transtensional coseismic fault slip of the 2021 Mw 6.7 Turt Earthquake and heterogeneous tectonic stress surrounding the Hovsgol Basin, Northwest Mongolia. *Tectonophysics*, 836:229407.

Liu, Z., Li, Z., Yu, C., Zhang, X., and Peng, J. (2024). Stress triggering and future seismic hazards implied by four large earthquakes in the Pamir from 2015 to 2023 revealed by Sentinel-1 radar interferometry. *Geophysical Journal International*, 237(2):887–901.

Locke, A., Billingsley, P., and Mayo, E. B. (1940). Sierra Nevada tectonic pattern. *Geological Society of America Bulletin*, 51(4):513–539.

Lohman, R. B. and Barnhart, W. D. (2010). Evaluation of earthquake triggering during the 2005-2008 earthquake sequence on Qeshm Island, Iran. *Journal of Geophysical Research: Solid Earth*, 115(B12):B12413.

Lozos, J. C. (2022). Dynamic Rupture Modeling of Coseismic Interactions on Orthogonal Strike-Slip Faults. *Geophysical Research Letters*, 49(5):e2021GL097585.

Lu, X., Tan, K., Li, Q., Li, C., Wang, D., and Zhang, C. (2021). Analysis of the current activity of the Red River fault based on GPS data: new seismological inferences. *Journal of Seismology*, 25(6):1525–1535.

Ma, S. T. and Hao, J. G. (1997). The source mechanism solution for July 12, 1995 earthquake with M $_s$=7.3, on the boundary between China and Myanmar. *Acta Seismologica Sinica*, 10(1):133–137.

Mackenzie, D., Elliott, J. R., Altunel, E., Walker, R. T., Kurban, Y. C., Schwenninger, J. L., and Parsons, B. (2016). Seismotectonics and rupture process of the M_W 7.1 2011 Van reverse-faulting earthquake, eastern Turkey, and implications for hazard in regions of distributed shortening. *Geophysical Journal International*, 206(1):501–524.

Magen, Y., Ziv, A., Inbal, A., Baer, G., and Hollingsworth, J. (2020). Fault Rerupture during the July 2019 Ridgecrest Earthquake Pair from Joint Slip Inversion of InSAR, Optical Imagery, and GPS. *The Bulletin of the Seismological Society of America*, 110(4):1627–1643.

Manighetti, I., Campillo, M., Bouley, S., and Cotton, F. (2007). Earthquake scaling, fault segmentation, and structural maturity. *Earth and Planetary Science Letters*, 253(3–4):429–438.

Manighetti, I., Mercier, A., and De Barros, L. (2021). Fault Trace Corrugation and Segmentation as a Measure of Fault Structural Maturity. *Geophysical Research Letters*, 48(20):e95372.

Marchandon, M., Hollingsworth, J., and Radiguet, M. (2021). Origin of the shallow slip deficit on a strike slip fault: Influence of elastic structure, topography, data coverage, and noise. *Earth and Planetary Science Letters*, 554:116696.

Marchandon, M., Vergnolle, M., Sudhaus, H., and Cavalié, O. (2018). Fault Geometry and Slip Distribution at Depth of the 1997 Mw 7.2 Zirkuh Earthquake: Contribution of Near-Field Displacement Data. *Journal of Geophysical Research: Solid Earth*, 123(2):1904–1924.

Marone, C. (1998). Laboratory-Derived Friction Laws and Their Application to Seismic Faulting. *Annual Review of Earth and Planetary Sciences*, 26:643–696.

Marone, C. J., Scholtz, C. H., and Bilham, R. (1991). On the mechanics of earthquake afterslip. *Journal of Geophysical Research: Solid Earth*, 96(B5):8441–8452.

Massonnet, D. and Feigl, K. L. (1998). Radar interferometry and its application to changes in the Earth's surface. *Reviews of Geophysics*, 36(4):441–500.

Massonnet, D., Rossi, M., Carmona, C., Adragna, F., Peltzer, G., Feigl, K., and Rabaute, T. (1993). The displacement field of the Landers earthquake mapped by radar interferometry. *Nature*, 364(6433):138–142.

Matsu'ura, M. (1977). Inversion of geodetic data. Part II. Optimal model of conjugate fault system for the 1927 Tango earthquake. *Journal of Physics of the Earth*, 25(3):233–255.

Maurin, T., Masson, F., Rangin, C., Min, U. T., and Collard, P. (2010). First global positioning system results in northern Myanmar: Constant and localized slip rate along the Sagaing fault. *Geology*, 38(7):591–594.

Metcalfe, I. (2021). Multiple Tethyan ocean basins and orogenic belts in Asia. *Gondwana Research*, 100:87–130.

Meyer, F. J., Arko, S. A., Hogenson, K., McAlpin, D. B., and Whitley, M. A. (2017). A Cloud-Based System for Automatic Hazard Monitoring from Sentinel-1 SAR Data. In *AGU Fall Meeting Abstracts*, volume 2017, pages G33A–03.

Middleton, T. A. and Copley, A. (2014). Constraining fault friction by re-examining earthquake nodal plane dips. *Geophysical Journal International*, 196(2):671–680.

Milliner, C. W. D., Dolan, J. F., Hollingsworth, J., Leprince, S., Ayoub, F., and Sammis, C. G. (2015). Quantifying near-field and off-fault deformation patterns of the 1992 M_w 7.3 Landers earthquake. *Geochemistry, Geophysics, Geosystems*, 16(5):1577–1598.

Morell, K. D., Styron, R., Stirling, M., Griffin, J., Archuleta, R., and Onur, T. (2020). Seismic Hazard Analyses From Geologic and Geomorphic Data: Current and Future Challenges. *Tectonics*, 39(10):e2018TC005365.

Nagorsen-Rinke, S., Lee, J., and Calvert, A. (2013). Pliocene sinistral slip across the Adobe Hills, eastern California–western Nevada: Kinematics of fault slip transfer across the Mina deflection. *Geosphere*, 9(1):37–53.

Namdarsehat, P., Milczarek, W., Bugajska-Jędraszek, N., Motavalli-Anbaran, S.-H., and Khaledzadeh, M. (2024). Uncovering a Seismogenic Fault in Southern Iran through Co-Seismic Deformation of the Mw 6.1 Doublet Earthquake of 14 November 2021. *Remote Sensing*, 16(13):2318.

Nissen, E., Cambaz, M. D., Gaudreau, É., Howell, A., Karasözen, E., and Savidge, E. (2022). A reappraisal of active tectonics along the Fethiye-Burdur trend, southwestern Turkey. *Geophysical Journal International*, 230(2):1030–1051.

Nissen, E., Elliott, J. R., Sloan, R. A., Craig, T. J., Funning, G. J., Hutko, A., Parsons, B. E., and Wright, T. J. (2016). Limitations of rupture forecasting exposed by instantaneously triggered earthquake doublet. *Nature Geoscience*, 9(4):330–336.

Nissen, E., Ghods, A., Karasözen, E., Elliott, J. R., Barnhart, W. D., Bergman, E. A., Hayes, G. P., Jamal-Reyhani, M., Nemati, M., Tan, F., Abdulnaby, W., Benz, H. M., Shahvar, M. P., Talebian, M., and Chen, L. (2019). The 12 November 2017 M_w 7.3 Ezgeleh-Sarpolzahab (Iran) Earthquake and Active Tectonics of the Lurestan Arc. *Journal of Geophysical Research: Solid Earth*, 124(2):2124–2152.

Nualkhao, P., Charusiri, P., Sutiwanich, C., and Pailoplee, S. (2016). Paleoearthquakes along Xaignabouli Fault Zone in Western Lao PDR. *Bulletin of Earth Sciences of Thailand*, 8(1):25–32.

Okada, Y. (1985). Surface deformation due to shear and tensile faults in a half-space. *Bulletin of the Seismological Society of America*, 75(4):1135–1154.

Oldow, J. S., Geissman, J. W., and Stockli, D. F. (2008). Evolution and Strain Reorganization within Late Neogene Structural Stepovers Linking the Central Walker Lane and Northern Eastern California Shear Zone, Western Great Basin. *International Geology Review*, 50(3):270–290.

Oldow, J. S., Kohler, G., and Donelick, R. A. (1994). Late Cenozoic extensional transfer in the Walker Lane strike-slip belt, Nevada. *Geology*, 22(7):637.

Oskin, M. E., Arrowsmith, J. R., Corona, A. H., Elliott, A. J., Fletcher, J. M., Fielding, E. J., Gold, P. O., Garcia, J. J. G., Hudnut, K. W., Liu-Zeng, J., and Teran, O. J. (2012). Near-Field Deformation from the El Mayor-Cucapah Earthquake Revealed by Differential LIDAR. *Science*, 335(6069):702.

Pananont, P., Habangkaem, S., Wongwai, W., Pornsopin, P., Wechbunthung, B., Limpisawad, S., and Kosuwan, S. (2014). Mainshock and Aftershocks Characteristics within 24 hours of the M 6.1 Earthquake on May 5th 2014 in Chiangrai Province, Northern Thailand from the Department of Mineral Resources's Seismic Network. Department of mineral resources thailand seminar report: Lessons from the 2014 mae lao earthquake (in thai), Thailand. Abstract from the report.

Pananont, P., Herman, M. W., Pornsopin, P., Furlong, K. P., Habangkaem, S., Waldhauser, F., Wongwai, W., Limpisawad, S., Warnitchai, P., Kosuwan, S., and Wechbunthung, B. (2017). Seismotectonics of the 2014 Chiang Rai, Thailand, earthquake sequence. *Journal of Geophysical Research: Solid Earth*, 122(8):6367–6388.

Peacock, D. C. P. and Sanderson, D. J. (1991). Displacements, segment linkage and relay ramps in normal fault zones. *Journal of Structural Geology*, 13(6):721–733.

Perrin, C., Manighetti, I., Ampuero, J. P., Cappa, F., and Gaudemer, Y. (2016). Location of largest earthquake slip and fast rupture controlled by along-strike change in fault structural maturity due to fault growth. *Journal of Geophysical Research: Solid Earth*, 121(5):3666–3685.

Perrin, C., Waldhauser, F., and Scholz, C. H. (2021). The Shear Deformation Zone and the Smoothing of Faults With Displacement. *Journal of Geophysical Research: Solid Earth*, 126(5):e20447.

Petronis, M. S., Geissman, J. W., Oldow, J. S., and McIntosh, W. C. (2009). Late Miocene to Pliocene vertical-axis rotation attending development of the Silver Peak–Lone Mountain displacement transfer zone, west-central Nevada. In *Late Cenozoic Structure and Evolution of the Great Basin-Sierra Nevada Transition*, volume 447, pages 215–253. Geological Society of America.

Pierce, I. K. D., Wesnousky, S. G., Owen, L. A., Bormann, J. M., Li, X., and Caffee, M. (2021). Accommodation of Plate Motion in an Incipient Strike Slip System: The Central Walker Lane. *Tectonics*, 40(2):e05612.

Pitarka, A., Dalguer, L. A., Day, S. M., Somerville, P. G., and Dan, K. (2009). Numerical Study of Ground-Motion Differences between Buried-Rupturing and Surface-Rupturing Earthquakes. *Bulletin of the Seismological Society of America*, 99(3):1521–1537.

Pousse-Beltran, L., Nissen, E., Bergman, E. A., Cambaz, M. D., Gaudreau, É., Karasözen, E., and Tan, F. (2020). The 2020 M_w 6.8 Elazığ (Turkey) Earthquake Reveals Rupture Behavior of the East Anatolian Fault. *Geophysical Research Letters*, 47(13):e88136.

Powers, P. M. and Jordan, T. H. (2010). Distribution of seismicity across strike-slip faults in California. *Journal of Geophysical Research: Solid Earth*, 115(B5):B05305.

Press, W. H., Teukolsky, S. A., Vetterling, W. T., and Flannery, B. P. (1992). Downhill Simplex Method in Multidimensions. Numerical Recipes in C: The Art of Scientific Computing.

Radiguet, M., Cotton, F., Manighetti, I., Campillo, M., and Douglas, J. (2009). Dependency of Near-Field Ground Motions on the Structural Maturity of the Ruptured Faults. *Bulletin of the Seismological Society of America*, 99(4):2572–2581.

Ragon, T., Sladen, A., and Simons, M. (2018). Accounting for uncertain fault geometry in earthquake source inversions - I: theory and simplified application. *Geophysical Journal International*, 214(2):1174–1190.

Rezapour, M. and Jamalreyhani, M. R. (2023). Source fault analyses from InSAR data and aftershocks for the Fin doublet earthquakes on 14 November 2021 in Hormozgan province, South Iran. *Journal of the Earth and Space Physics*, 48(4):87–97.

Robertson, E. G. (1983). Relationship of fault displacement to gouge and breccia thickness. *American Institute of Mining Engineering Transactions*, 274:1426–1432.

Rockwell, T. K., Scott, L., Dawson, T., Langridge, R., Lettis, W., and Klinger, Y. (2002). Lateral Offsets on Surveyed Cultural Features Resulting from the 1999 Izmit and Duzce Earthquakes, Turkey. *Bulletin of the Seismological Society of America*, 92(1):79–94.

Rood, D. H., Burbank, D. W., Herman, S. W., and Bogue, S. (2011). Rates and timing of vertical-axis block rotations across the central Sierra Nevada-Walker Lane transition in the Bodie Hills, California/Nevada. *Tectonics*, 30(5):TC5013.

Rosen, P. A., Hensley, S., Joughin, I. R., Li, F. K., Madsen, S. N., Rodriguez, E., and Goldstein, R. M. (2000). Synthetic aperture radar interferometry. *Proceedings of the IEEE*, 88(3):333–382.

Roten, D., Olsen, K. B., and Day, S. M. (2017). Off-fault deformations and shallow slip deficit from dynamic rupture simulations with fault zone plasticity. *Geophysical Research Letters*, 44(15):7733–7742.

Ruhl, C. J., Morton, E. A., Bormann, J. M., Hatch-Ibarra, R., Ichinose, G., and Smith, K. D. (2021). Complex Fault Geometry of the 2020 M_{WW} 6.5 Monte Cristo Range, Nevada Earthquake Sequence. *Seismological Research Letters*, 92(3):1876–1890.

Sadeghi Chorsi, T., Braunmiller, J., Deng, F., Mueller, N., Kerstetter, S., Stern, R. J., and Dixon, T. H. (2021). The May 15, 2020 M 6.5 Monte Cristo Range, Nevada, earthquake: eyes in the sky, boots on the ground, and a chance for students to learn. *International Geology Review*, pages 1–20.

Saikia, C. K. (1994). Modified frequency-wavenumber algorithm for regional seismograms using Filon's quadrature: modelling of Lg waves in eastern North America. *Geophysical Journal International*, 118(1):142–158.

Savage, H. M. and Brodsky, E. E. (2011). Collateral damage: Evolution with displacement of fracture distribution and secondary fault strands in fault damage zones. *Journal of Geophysical Research: Solid Earth*, 116(B3):B03405.

Scholz, C. H. (1987). Wear and gouge formation in brittle faulting. *Geology*, 15(6):493–495.

Schwartz, D. P. and Coppersmith, K. J. (1984). Fault behavior and characteristic earthquakes: Examples from the Wasatch and San Andreas Fault Zones. *Journal of Geophysical Research: Solid Earth*, 89(B7):5681–5698.

Scott, C., Champenois, J., Klinger, Y., Nissen, E., Maruyama, T., Chiba, T., and Arrowsmith, R. (2019). The 2016 M7 Kumamoto, Japan, Earthquake Slip Field Derived From a Joint Inversion of Differential Lidar Topography, Optical Correlation, and InSAR Surface Displacements. *Geophysical Research Letters*, 46(12):6341–6351.

Scott, C. P., Arrowsmith, J. R., Nissen, E., Lajoie, L., Maruyama, T., and Chiba, T. (2018). The M7 2016 Kumamoto, Japan, Earthquake: 3-D Deformation Along the Fault and Within the Damage Zone Constrained From Differential Lidar Topography. *Journal of Geophysical Research: Solid Earth*, 123(7):6138–6155.

Searle, M. P. and Morley, C. K. (2011). Tectonic and thermal evolution of Thailand in the regional context of SE Asia. In *The Geology of Thailand*. Geological Society of London.

Seebeck, H., Van Dissen, R., Litchfield, N., M., B. P., Nicol, A., Langridge, R., Barrell, D. J. A., Villamor, P., Ellis, S., Rattenbury, M., Bannister, S., Gerstenberger, M., Ghisetti, F., Sutherland, R., Hirschberg, H., Fraser, J., Nodder, S. D., Stirling, M., Humphrey, J., Bland, K. J., Howell, A., Mountjoy, J., Moon, V., Stahl, T., Spinardi, F., Townsend, D., Clark, K., Hamling, I., Cox, S., de Lange, W., Wopereis, P., Johnston, M., Morgenstern, R., Coffey, G., Eccles, J. D., Little, T., Fry, B., Griffin, J., Townend, J., Mortimer, N., Alcaraz, S., Massiot, C., Rowland, J. V., Muirhead, J., Upton, P., and Lee, J. (2023). The New Zealand Community Fault Model – version 1.0: an improved geological foundation for seismic hazard modelling. *New Zealand Journal of Geology and Geophysics*, 0(0):1–21.

Sethanant, I., Nissen, E., Pousse-Beltran, L., Bergman, E., and Pierce, I. (2023). The 2020 M_w 6.5 Monte Cristo Range, Nevada, Earthquake: Anatomy of a Crossing-Fault Rupture through a Region of Highly Distributed Deformation. *The Bulletin of the Seismological Society of America*, 113(3):948–975.

Shen, Z.-K., Lü, J., Wang, M., and Bürgmann, R. (2005). Contemporary crustal deformation around the southeast borderland of the Tibetan Plateau. *Journal of Geophysical Research (Solid Earth)*, 110(B11):B11409.

Shi, X., Wang, Y., Sieh, K., Weldon, R., Feng, L., Chan, C.-H., and Liu-Zeng, J. (2018). Fault Slip and GPS Velocities Across the Shan Plateau Define a Curved Southwestward Crustal Motion Around the Eastern Himalayan Syntaxis. *Journal of Geophysical Research: Solid Earth*, 123(3):2502–2518.

Shi, Y., Wang, Y., and Bian, Y. (2023). Coseismic Source Model of the February 2023 Mw 6.8 Tajikistan Earthquake from Sentinel-1A InSAR Observations and Its Associated Earthquake Hazard. *Remote Sensing*, 15(12):3010.

Shipton, Z. K. and Cowie, P. A. (2001). Damage zone and slip-surface evolution over μm to km scales in high-porosity Navajo sandstone, Utah. *Journal of Structural Geology*, 23(12):1825–1844.

Silver, E. A., McCaffrey, R., and Smith, R. B. (1983). Collision, rotation, and the initiation of subduction in the evolution of Sulawesi, Indonesia. *Journal of Geophysical Research: Solid Earth*, 88(B11):9407–9418.

Simons, M., Fialko, Y., and Rivera, L. (2002). Coseismic Deformation from the 1999 Mw 7.1 Hector Mine, California, Earthquake as Inferred from InSAR and GPS Observations. *Bulletin of the Seismological Society of America*, 92(4):1390–1402.

Simons, W. J. F., Socquet, A., Vigny, C., Ambrosius, B. A. C., Haji Abu, S., Promthong, C., Subarya, C., Sarsito, D. A., Matheussen, S., Morgan, P., and Spakman, W. (2007). A decade of GPS in Southeast Asia: Resolving Sundaland motion and boundaries. *Journal of Geophysical Research (Solid Earth)*, 112(B6):B06420.

Socquet, A., Hollingsworth, J., Pathier, E., and Bouchon, M. (2019). Evidence of supershear during the 2018 magnitude 7.5 Palu earthquake from space geodesy. *Nature Geoscience*, 12(3):192–199.

Speed, R. C. and Cogbill, A. H. (1979). Candelaria and other left-oblique slip faults of the Candelaria region, Nevada. *Geological Society of America Bulletin*, 90(2):149.

Stewart, J. H. and Ernst, W. G. (1988). Tectonics of the Walker Lane belt, western Great Basin: Mesozoic and Cenozoic deformation in a zone of shear. *Metamorphism and crustal evolution of the western United States*, 7:683–713.

Stirling, M., Gerstenberger, M., Litchfield, N., McVerry, G., Smith, W., Pettinga, J., and Barnes, P. (2008). Seismic hazard of the Canterbury region, New Zealand: New earthquake source model and methodology. *Bulletin of the New Zealand Society for Earthquake Engineering*, 41(2):51––67.

Stirling, M. W., Wesnousky, S. G., and Shimazaki, K. (1996). Fault trace complexity, cumulative slip, and the shape of the magnitude-frequency distribution for strike-slip faults: a global survey. *Geophysical Journal International*, 124(3):833–868.

Teran, O. J., Fletcher, J. M., Oskin, M. E., Rockwell, T. K., Hudnut, K. W., Spelz, R. M., Akciz, S. O., Hernandez-Flores, A. P., and Morelan, A. E. (2015). Geologic and structural controls on rupture zone fabric: A field-based study of the 2010 Mw 7.2 El Mayor-Cucapah earthquake surface rupture. *Geosphere*, 11(3):899–920.

Thakur, P. and Huang, Y. (2021). Influence of Fault Zone Maturity on Fully Dynamic Earthquake Cycles. *Geophysical Research Letters*, 48(17):e94679.

Thatcher, W. and Hill, D. P. (1991). Fault orientations in extensional and conjugate strike-slip environments and their implications. *Geology*, 19(11):1116.

Thomas, M. Y., Avouac, J.-P., Champenois, J., Lee, J.-C., and Kuo, L.-C. (2014). Spatiotemporal evolution of seismic and aseismic slip on the Longitudinal Valley Fault, Taiwan. *Journal of Geophysical Research: Solid Earth*, 119(6):5114–5139.

Tin, T. Z. H., Nishimura, T., Hashimoto, M., Lindsey, E. O., Aung, L. T., Min, S. M., and Thant, M. (2022). Present-day crustal deformation and slip rate along the southern Sagaing fault in Myanmar by GNSS observation. *Journal of Asian Earth Sciences*, 228:105125.

Tong, X., Sandwell, D. T., and Fialko, Y. (2010). Coseismic slip model of the 2008 Wenchuan earthquake derived from joint inversion of interferometric synthetic aperture radar, GPS, and field data. *Journal of Geophysical Research: Solid Earth*, 115(B4):B04314.

Tun, S. T., Wang, Y., Khaing, S. N., Thant, M., Htay, N., Htwe, Y. M. M., Myint, T., and Sieh, K. (2014). Surface Ruptures of the Mw 6.8 March 2011 Tarlay Earthquake, Eastern Myanmar. *The Bulletin of the Seismological Society of America*, 104(6):2915–2932.

Turkelli, N., Sandvol, E., Zor, E., Gok, R., Bekler, T., Al-Lazki, A., Karabulut, H., Kuleli, S., Eken, T., Gurbuz, C., Bayraktutan, S., Seber, D., and Barazangi, M. (2003). Seismogenic zones in Eastern Turkey. *Geophysical Research Letters*, 30(24):8039.

United Nations Office for the Coordination of Humanitarian Affairs (2011). Myanmar: Earthquake in Shan State Situation Report No. 5. Technical report.

U.S. Geological Survey, Earthquake Hazards Program (2017). Advanced National Seismic System (ANSS) Comprehensive Catalog of Earthquake Events and Products: Various.

Vallage, A., Klinger, Y., Grandin, R., Bhat, H. S., and Pierrot-Deseilligny, M. (2015). Inelastic surface deformation during the 2013 Mw 7.7 Balochistan, Pakistan, earthquake. *Geology*, 43(12):1079–1082.

Vigny, C., Socquet, A., Rangin, C., Chamot-Rooke, N., Pubellier, M., Bouin, M.-N., Bertrand, G., and Becker, M. (2003). Present-day crustal deformation around Sagaing fault, Myanmar. *Journal of Geophysical Research (Solid Earth)*, 108(B11):2533.

Şengör, A. M. C., Tüysüz, O., Imren, C., Sakinç, M., Eyidoğan, H., Görür, N., Le Pichon, X., and Rangin, C. (2005). The North Anatolian Fault: a New Look. *Annual Review of Earth and Planetary Sciences*, 33:37–112.

Walker, R. and Jackson, J. (2002). Offset and evolution of the Gowk fault, S.E. Iran: a major intra-continental strike-slip system. *Journal of Structural Geology*, 24(11):1677–1698.

Walker, R. T., Bergman, E. A., Elliott, J. R., Fielding, E. J., Ghods, A. R., Ghoraishi, M., Jackson, J., Nazari, H., Nemati, M., Oveisi, B., Talebian, M., and Walters, R. J. (2013). The 2010-2011 South Rigan (Baluchestan) earthquake sequence and its implications for distributed deformation and earthquake hazard in southeast Iran. *Geophysical Journal International*, 193(1):349–374.

Walker, R. T., Bergman, E. A., Szeliga, W., and Fielding, E. J. (2011). Insights into the 1968-1997 Dasht-e-Bayaz and Zirkuh earthquake sequences, eastern Iran, from calibrated relocations, InSAR and high-resolution satellite imagery. *Geophysical Journal International*, 187(3):1577–1603.

Walsh, J. J. and Watterson, J. (1988). Analysis of the relationship between displacements and dimensions of faults. *Journal of Structural Geology*, 10(3):239–247.

Wan, Y., Shen, Z. K., Bürgmann, R., Sun, J., and Wang, M. (2017). Fault geometry and slip distribution of the 2008 M_w 7.9 Wenchuan, China earthquake, inferred from GPS and InSAR measurements. *Geophysical Journal International*, 208(2):748–766.

Wang, H., Qiang, Z., Yuan, Z., Wang, Y., Zhang, H., Zhao, X., and Gu, Y. (1991). The distribution of seismic intensities and surface rupture in the Lancang-Gengma (Yunnan Province, China) earthquakes of November 6, 1988. *Acta Seismologica Sinica*, 13(3):344–353.

Wang, K., Zhu, Y., Nissen, E., and Shen, Z.-K. (2021). On the Relevance of Geodetic Deformation Rates to Earthquake Potential. *Geophysical Research Letters*, 48(11):e93231.

Wang, M. and Shen, Z.-K. (2020). Present-Day Crustal Deformation of Continental China Derived From GPS and Its Tectonic Implications. *Journal of Geophysical Research: Solid Earth*, 125(2):e2019JB018774.

Wang, S., Fan, C., Wang, G., and Wang, E. (2008). Late Cenozoic deformation along the northwestern continuation of the Xianshuihe fault system, Eastern Tibetan Plateau. *Geological Society of America Bulletin*, 120(3-4):312–327.

Wang, S., Nissen, E., Pousse-Beltran, L., Craig, T. J., Jiao, R., and Bergman, E. A. (2022). Structural controls on coseismic rupture revealed by the 2020 M_w 6.0 Jiashi earthquake (Kepingtag belt, SW Tian Shan, China). *Geophysical Journal International*, 230(3):1895–1910.

Wang, Y., Lin, Y. N. N., Simons, M., and Tun, S. T. (2014a). Shallow Rupture of the 2011 Tarlay Earthquake (M_w 6.8), Eastern Myanmar. *The Bulletin of the Seismological Society of America*, 104(6):2904–2914.

Wang, Y., Sieh, K., Tun, S. T., Lai, K.-Y., and Myint, T. (2014b). Active tectonics and earthquake potential of the Myanmar region. *Journal of Geophysical Research (Solid Earth)*, 119(4):3767–3822.

Watson, C. S., Elliott, J. R., Ebmeier, S. K., Biggs, J., Albino, F., Brown, S. K., Burns, H., Hooper, A., Lazecký, M., Maghsoudi, Y., Rigby, R., , and Wright, T. J. (2023). Strategies for improving the communication of satellite-derived InSAR data for geohazards through the analysis of Twitter and online data portals. *Geoscience Communication*, 6(2):75–96.

Wechsler, N., Ben-Zion, Y., and Christofferson, S. (2010). Evolving geometrical heterogeneities of fault trace data. *Geophysical Journal International*, 182(2):551–567.

Wegmüller, U., Werner, C., Strozzi, T., Wiesmann, A., Frey, O., and Santoro, M. (2016). Sentinel-1 support in the gamma software. *Procedia Computer Science*, 100:1305–1312.

Wei, S., Barbot, S., Graves, R., Lienkaemper, J. J., Wang, T., Hudnut, K., Fu, Y., and Helmberger, D. (2015). The 2014 Mw 6.1 South Napa Earthquake: A Unilateral Rupture with Shallow Asperity and Rapid Afterslip. *Seismological Research Letters*, 86(2A):344–354.

Wei, S., Fielding, E., Leprince, S., Sladen, A., Avouac, J. P., Helmberger, D., Hauksson, E., Chu, R., Simons, M., Hudnut, K., Herring, T., and Briggs, R. (2011). Superficial simplicity of the 2010 El Mayor-Cucapah earthquake of Baja California in Mexico. *Nature Geoscience*, 4(9):615–618.

Wells, D. L. and Coppersmith, K. J. (1994). New empirical relationships among magnitude, rupture length, rupture width, rupture area, and surface displacement. *Bulletin - Seismological Society of America*, 84(4):974–1002.

Wesnousky, S. G. (1988). Seismological and structural evolution of strike-slip faults. *Nature*, 335(6188):340–343.

Wesnousky, S. G. (2005). Active faulting in the Walker Lane. *Tectonics*, 24(3):TC3009.

Wesnousky, S. G. (2006). Predicting the endpoints of earthquake ruptures. *Nature*, 444(7117):358–360.

Wessel, P., Luis, J. F., Uieda, L., Scharroo, R., Wobbe, F., Smith, W. H. F., and Tian, D. (2019). The Generic Mapping Tools Version 6. *Geochemistry, Geophysics, Geosystems*, 20(11):5556–5564.

Weston, J., Engdahl, E. R., Harris, J., DiÂ Giacomo, D., and Storchak, D. A. (2018). ISC-EHB: reconstruction of a robust earthquake data set. *Geophysical Journal International*, 214(1):474–484.

Weston, J., Ferreira, A. M. G., and Funning, G. J. (2011). Global compilation of interferometric synthetic aperture radar earthquake source models: 1. Comparisons with seismic catalogs. *Journal of Geophysical Research (Solid Earth)*, 116(B8):B08408.

Wetterauer, R. H. (1977). *The Mina deflection—A new interpretation based on the history of the Lower Jurassic Dunlap Formation, western Nevada*. PhD thesis, Northwestern University, Evanston, Illinois.

Wright, T. J., Lu, Z., and Wicks, C. (2003). Source model for the M_w 6.7, 23 October 2002, Nenana Mountain Earthquake (Alaska) from InSAR. *Geophysical Research Letters*, 30(18):1974.

Wright, T. J., Lu, Z., and Wicks, C. (2004). Constraining the Slip Distribution and Fault Geometry of the M_w 7.9, 3 November 2002, Denali Fault Earthquake with Interferometric Synthetic Aperture Radar and Global Positioning System Data. *Bulletin of the Seismological Society of America*, 94(6B):S175–S189.

Wright, T. J., Parsons, B. E., Jackson, J. A., Haynes, M., Fielding, E. J., England, P. C., and Clarke, P. J. (1999). Source parameters of the 1 October 1995 Dinar (Turkey) earthquake from SAR interferometry and seismic bodywave modelling. *Earth and Planetary Science Letters*, 172(1–2):23–37.

Wu, C., Zheng, W., Zhang, P., Zhang, Z., Jia, Q., Yu, J., Zhang, H., Yao, Y., Liu, J., Han, G., and Chen, J. (2019). Oblique Thrust of the Maidan Fault and Late Quaternary Tectonic Deformation in the Southwestern Tian Shan, Northwestern China. *Tectonics*, 38(8):2625–2645.

Xiong, W., Yu, P., Chen, W., Liu, G., Zhao, B., Nie, Z., and Qiao, X. (2022). The 2020 M_w 6.4 Petrinja earthquake: a dextral event with large coseismic slip highlights a complex fault system in northwestern Croatia. *Geophysical Journal International*, 228(3):1935–1945.

Xu, X., Sandwell, D. T., Ward, L. A., Milliner, C. W. D., Smith-Konter, B. R., Fang, P., and Bock, Y. (2020). Surface deformation associated with fractures near the 2019 Ridgecrest earthquake sequence. *Science*, 370(6516):605–608.

Xu, X., Tong, X., Sandwell, D. T., Milliner, C. W., Dolan, J. F., Hollingsworth, J., Leprince, S., and Ayoub, F. (2016). Refining the shallow slip deficit. *Geophysical Journal International*, 204(3):1843–1862.

Yang, H., Wang, D., Guo, R., Xie, M., Zang, Y., Wang, Y., Yao, Q., Cheng, C., An, Y., and Zhang, Y. (2022a). Rapid report of the 8 January 2022 M_s 6.9 Menyuan earthquake, Qinghai, China. *Earthquake Research Advances*, 2(1):100113.

Yang, H. and Yao, S. (2021). Shallow destructive earthquakes. *Earthquake Science*, 34(1):15–24.

Yang, J., Xu, C., Wen, Y., and Xu, G. (2022b). Complex Coseismic and Postseismic Faulting During the 2021 Northern Thessaly (Greece) Earthquake Sequence Illuminated by InSAR Observations. *Geophysical Research Letters*, 49(8):e98545.

Yang, J., Zhu, H., Lay, T., Niu, Y., Ye, L., Lu, Z., Luo, B., Kanamori, H., Huang, J., and Li, Z. (2021). Multifault Opposing Dip Strike Slip and Normal Fault Rupture During the 2020 M_w 6.5 Stanley, Idaho Earthquake. *Geophysical Research Letters*, 48(10):e92510.

Yang, Y. H., Tsai, M. C., Hu, J. C., Aurelio, M. A., Hashimoto, M., Escudero, J. A., Su, Z., and Chen, Q. (2018). Coseismic Slip Deficit of the 2017 Mw 6.5 Ormoc Earthquake That Occurred Along a Creeping Segment and Geothermal Field of the Philippine Fault. *Geophysical Research Letters*, 45(6):2659–2668.

Yao, S. and Yang, H. (2022). Hypocentral dependent shallow slip distribution and rupture extents along a strike-slip fault. *Earth and Planetary Science Letters*, 578:117296.

Ye, T., Chen, X., Liu, Z., Wang, P., Dong, Z., Cui, T., Jiang, F., Cai, J., Zhang, Y., Zhang, J., Zhou, L., and Xie, X. (2022). A magnetotelluric study of 3D electrical resistivity structure underneath the southern segment of the Red River fault zone, South China. *Journal of Asian Earth Sciences*, 225:105056.

Yu, C., Li, Z., and Penna, N. T. (2018a). Interferometric synthetic aperture radar atmospheric correction using a GPS-based iterative tropospheric decomposition model. *Remote Sensing of Environment*, 204:109–121.

Yu, C., Li, Z., Penna, N. T., and Crippa, P. (2018b). Generic Atmospheric Correction Model for Interferometric Synthetic Aperture Radar Observations. *Journal of Geophysical Research: Solid Earth*, 123(10):9202–9222.

Yu, C., Penna, N. T., and Li, Z. (2017). Generation of real-time mode high-resolution water vapor fields from GPS observations. *Journal of Geophysical Research: Atmospheres*, 122(3):2008–2025.

Yu, J., Wang, D., Zhao, B., and Li, Q. (2021). Normal Faulting Movement During the 2020 Mw 6.4 Yutian Earthquake: A Shallow Rupture in NW Tibet Revealed by Geodetic Measurements. *Pure and Applied Geophysics*, 178(5):1563–1578.

Zeng, Y., Petersen, M., and Boyd, O. (2022). Lower Seismogenic Depth Model for Western U.S. Earthquakes. *Seismological Research Letters*, 93(6):3186–3204.

Zhang, H., Thurber, C., and Bedrosian, P. (2009). Joint inversion for Vp, Vs, and Vp/Vs at SAFOD, Parkfield, California. *Geochemistry, Geophysics, Geosystems*, 10(11):Q11002.

Zhang, Y., Shan, X., Gong, W., and Zhang, G. (2021). The ambiguous fault geometry derived from InSAR measurements of buried thrust earthquakes: a synthetic data based study. *Geophysical Journal International*, 225(3):1799–1811.

Zheng, A., Chen, X., and Xu, W. (2020). Present-Day Deformation Mechanism of the Northeastern Mina Deflection Revealed by the 2020 M_w 6.5 Monte Cristo Range Earthquake. *Geophysical Research Letters*, 47(22):e90142.

Zheng, Y., Zebker, H., and Michaelides, R. (2021). A New Decorrelation Phase Covariance Model for Noise Reduction in Unwrapped Interferometric Phase Stacks. *IEEE Transactions on Geoscience and Remote Sensing*, 59(12):10126–10135.

Zhu, C., Wang, C., Zhang, B., Qin, X., and Shan, X. (2021). Differential Interferometric Synthetic Aperture Radar data for more accurate earthquake catalogs. *Remote Sensing of Environment*, 266:112690.

Zinke, R., Dolan, J. F., Van Dissen, R., Grenader, J. R., Rhodes, E. J., McGuire, C. P., Langridge, R. M., Nicol, A., and Hatem, A. E. (2015). Evolution and progressive geomorphic manifestation of surface faulting: A comparison of the Wairau and Awatere faults, South Island, New Zealand. *Geology*, 43(11):1019–1022.

Zinke, R., Hollingsworth, J., and Dolan, J. F. (2014). Surface slip and off-fault deformation patterns in the 2013 M_W 7.7 Balochistan, Pakistan earthquake: Implications for controls on the distribution of near-surface coseismic slip. *Geochemistry, Geophysics, Geosystems*, 15(12):5034–5050.

Zuchiewicz, W., Cuong, N. Q., Bluszcz, A., and Michalik, M. (2004). Quaternary sediments in the Dien Bien Phu fault zone, NW Vietnam: a record of young tectonic processes in the light of OSL-SAR dating results. *Geomorphology*, 60(3):269–302.